2017

Oxygen Transport in Carotid and Stented Coronary Arteries

Eoin A. Murphy
Technological University Dublin, eoin.murphy@tudublin.ie

Oxygen Transport in Carotid and Stented Coronary Arteries

by

Eoin A. Murphy, B.Eng. (Hons)

A thesis submitted to Dublin Institute of Technology in partial fulfilment of the requirements for the degree of

Doctor of Philosophy

2017

Principle Supervisor: Dr. Fergal J. Boyle

Secondary Supervisor: Prof. David M. Kennedy

School of Mechanical and Design Engineering

ABSTRACT

Oxygen deficiency, known as hypoxia, in arterial walls has been linked to increased intimal hyperplasia, which is the main adverse biological process causing in-stent restenosis. Stent implantation can have significant effects on the oxygen transport into the arterial wall. Helical flow has been theorised to improve the local haemodynamics and the oxygen transport within stented arteries.

In this study an advanced oxygen transport model was developed to assess different stent designs. This advanced oxygen transport model incorporates both the free and bound oxygen contained in blood and includes a shear-dependent dispersion coefficient for red blood cells. In two test cases undertaken the results predicted by the advanced oxygen transport model were compared those predicted by simpler models, and in vivo measurements. Two other test cases analysed the predicted oxygen transport in three different stent designs, and the effects of helical flow on the haemodynamics and oxygen transport in stented coronary arteries.

The advanced model showed good agreement with experimental measurements within the mass-transfer boundary layer and at the luminal surface; however, more work is needed for predicting the oxygen transport within the arterial wall. Simplifying the oxygen transport model within the blood produces significant errors in predicting the oxygen transport in arteries. It was found that different stent designs can produce significantly different amounts of hypoxic regions within the stented region. Additionally, helical flow increases the amount of oxygen transferred into the arterial wall, but only in a helical ribbon through the stented region that also experiences high wall shear stress spatial gradients.

DECLARATION

I certify that this thesis which I now submit for examination for the award of Doctor of Philosophy, is entirely my own work and has not been taken from the work of others, save and to the extent that such work has been cited and acknowledged within the text of my work.

This thesis was prepared according to the regulations for postgraduate study by research of the Dublin Institute of Technology and has not been submitted in whole or in part for another award in any other third level institution.

The work reported on in this thesis conforms to the principles and requirements of the DIT's guidelines for ethics in research.

DIT has permission to keep, lend or copy this thesis in whole or in part, on condition that any such use of the material of the thesis be duly acknowledged.

Signature _____ Date _____

ACKNOWLEDGEMENTS

I owe a debt of gratitude to my primary supervisor, Dr Fergal Boyle, who has provided me with consistent, honest, knowledgeable and, at times much-needed, critical advice throughout my research project. His unwavering attention to detail with every piece of research I undertook will serve as a benchmark for all my future work. Without his guidance and motivation I would not have made it this far. I wish to thank my second supervisor Prof David Kennedy, who always had an open door, and gave me support and friendly advice throughout my studies.

My research would not have been possible without funding, under the ABBEST and Fiorsaigh schemes, from Dublin Institute of Technology (DIT) and I am very grateful for the opportunities already presented to me in my career because of this. Within the college there is a wealth of expertise which I always felt was open to me. Particularly I would like to thank Dr Barry Duignan for any modelling queries, and Allen Brereton, Michael Faherty and Simon Farrell for their IT help. Robert Simpson and Dr Marek Rebow were always willing to support me throughout my studies and provide me with helpful words of advice especially with regards to my extracurricular space-related endeavours. I could not have undertaken my research without the ones who preceded me in our research group: Dr David Martin, who provided me with the realistically-deformed stent geometries used herein, and Dr Jonathan Murphy, who previously did extensive research on the local haemodynamics within stented coronary arteries. Both colleagues were always willing to provide helpful advice and friendly banter. Also, Adrian Dunne of CADFEM Ireland provided a wealth of knowledge and expertise in computational modelling that really helped with the finer detail of this work, thanks. The Irish Centre for High-End Computing (ICHEC) provided me with the

computational resources which were essential to my project and their support staff were very helpful.

In parallel to my research I also embarked on a fledgling lecturing career that was helped in many ways by numerous people within the college. I wish to thank Dr Michael Carr, Fr Alan Hilliard, Marisa Llorens Salvador, Eileen Mageean, Ivan Sheridan, Declan Allen, Roisin Murray, and Paul Gorey. I also wish to thank the administrative staff: Orla Hosford, Miriam Daly and Susan Doyle, who made my time in DIT run smoothly. Within the Graduate Research School Gerolmina Di Nardo and Raffaella Salvante both provided me with the support needed throughout my research.

I wish to thank Prof Graeme Houston and Dr Shona Matthew from the University of Dundee for showing faith in me and for their patience as I finished this research as a Marie Curie Experienced Researcher. (This project has received funding from the European Union's Seventh Framework Programme for research, technological development and demonstration under grant agreement no 324487.)

In DIT many of my colleagues there provided me with the moral support and friendly chats vital to such an oft-time lonely endeavour. These are, in no particular order: Dr Zhe Li, Dr David Culliton, Mingzhu Chen, Gerald Gallagher, Brendan Kennedy, Simon Montgomery, Dr Michael Crowley, Neil Branigan, and Martin Byrne. Outside of DIT, Stephen McMullan was kind enough to proofread my thesis and I definitely owe him more than a few pints. All the lads and lassie, Billy, Dave, Pat, Jimmy, Killian, Mosey, Eoin, Neil, and Laura, thanks for knowing when not to ask me when I'll be finished.

Finally, I would never have made it through this without the support of my family. My parents, Tony and Loyola, I owe more than I could ever repay in love and support throughout my life, thank you both. My brother, Neil, and sister, Aoife, are always on-

hand to give some moral support. My wife, Gina, particularly has shown herself to be ever resourceful as we struggled along through financially stressful times. I could always rely on her, and her strength and determination is a tremendous example to me. There's not a day that goes by that I don't feel truly lucky to be her husband. Last, but not least, to my two daughters, Clara and Lucy, you both give me so much joy and happiness that brightens even the darkest day. This is for you.

NOMENCLATURE

Abbreviations

RBC	Red blood cells
VSMC	Vascular smooth muscle cell
EC	Endothelial cell
CFD	Computational fluid dynamics
FEA	Finite element analysis
MI	Myocardial infarction
CABG	Coronary artery bypass graft
PTCA	Percutaneous transluminal coronary angioplasty
BMS	Bare metal stent
DES	Drug eluting stent
CAD	Coronary artery disease
ISR	In-stent restenosis
DAPT	Dual antiplatelet therapy
WSS	Wall shear stress
WSSG	Wall shear stress gradient
WSSAG	Wall shear stress angle gradient
OSI	Oscillatory shear index
RRT	Relative residence time
SS	Shear Stress
IEL	Internal elastic lamina
EEL	External elastic lamina
ICAM-1	intercellular adhesion molecule 1

VCAM-1	Vascular cell adhesion molecule 1
GP	Glycoprotein
NO	Nitric oxide
CO_2	Carbon dioxide
ECM	Extracellular matrix
MAC-1	Macrophage-1 antigen
NIH	Neointimal hyperplasia
IH	Intimal hyperplasia
PDGF	Platelet-derived growth factor
MMP-9	Matrix metalloproteinase-9
bFGF	Basic fibroblast growth factor
G-CSF	Granulocyte colony-stimulating factor
SPC	Smooth muscle progenitor cells
TGF	Transforming growth factor
VEGF	Vascular endothelial growth factor
EC-CFU	Endothelial cell colony forming units
EPC	Endothelial progenitor cells
MTBL	Mass transport boundary layer
Da	Damkohler number
Sc	Schmidt Number
C	Concentration of oxygen
RCA	Right coronary artery
LCA	Left coronary artery
LCX	Left circumflex artery

CT	Computed tomography
MRI	Magnetic resonance imaging
SMAHT	Small amplitude helical technology
ePTFE	expanded polytetrafluorethylene
VFT	Vascular Flow Technologies
ICHEC	Irish Centre for High-End Computing
CPU	Central processing unit
RAM	Random access memory
2D	Two-dimensional
3D	Three-dimensional
CCA	Common carotid artery
ICA	Internal carotid artery
ECA	External carotid artery

Scalars

u,v,w	Velocity magnitudes in x, y, and z directions
t	Time
dt	Infinitesimally small increment of time
$d\alpha, d\beta$	Infinitesimally small angles of rotation
ds	Infinitesimally small surface area
μ	Dynamic viscosity
$\dot{\gamma}$	Shear rate
λ_t	Time constant
n	Power law index (Bird-Carreau)
H_k	Kinetic helicity density

LNH	Local normalised helicity
PO_2	Oxygen tension in plasma
α	Solubility of oxygen in plasma
C	Concentration of free oxygen in plasma
S	Saturation of haemoglobin in RBCs
n	Hill parameter (Hill equation)
D_b	Diffusivity of free oxygen in blood
r	Rate of release of oxygen from haemoglobin
[Hb]	Total oxygen carrying capacity of haemoglobin
D_c	Diffusivity of oxyhaemoglobin in blood
D’	Diffusivity coefficient of PO_2 in blood
M	Michaelis-Menten consumption rate of oxygen
M_0	Maximum consumption rate
D_T	Diffusivity of oxygen in arterial wall tissue
α_T	Solubility of oxygen in arterial wall tissue
Sh	Sherwood number
PO_2	Partial pressure of dissolved oxygen
Dia	Diameter of artery
Da	Damkholer number
ρ	Density
f_b	Body forces exerted on fluid element
g	Gravity constant
φ	Conserved variable
Γ_{eff}	Effective diffusivity

S_φ	Source term
β (Section 3.6.2)	Blend factor
r^n	Residual

Vectors

$\mathbf{V}$	Velocity vector
$\mathbf{i, j, k}$	Cartesian unit vectors
$\boldsymbol{\omega}$	Rate of rotation vector
ζ	Vorticity vector
∇	Del operator
$\mathbf{n}_i$	Normal vector
$\mathbf{r}$	Vector from upwind node to integration point
$[\varphi]$	Solution vector

Second-order tensors

$\boldsymbol{\varepsilon}_{ij}$	Strain rate tensor
$\boldsymbol{\sigma}_{ij}$	Stress tensor
$\boldsymbol{\tau}_{ij}$	Viscous stress tensor

Matrices

[A]	Sparse coefficient matrix

Subscripts

v	Volume
s	Surface
in	Inlet

out	Outlet
w	Wall
up	Upwind node
ip	Current node

Table of Contents

List of Figures

List of Tables

CHAPTER 1

Background Material

1.1 Introduction

This chapter provides the initial background material required for this project. First, the cardiovascular system is introduced with specific reference to the heart, blood, coronary arteries, and cardiac veins. Following this, the burden of coronary artery disease (CAD) is highlighted along with the biological understanding of how atherosclerotic lesions form and their classifications. The available treatments for CAD are listed and described. One treatment option, specifically relevant, is angioplasty with stenting which is considered the standard treatment for patients with CAD presenting with either stable or unstable angina, or with acute myocardial infarction (MI).[178] The history and current status of stent technology is discussed briefly with a mention of one limitation of stent technology which is the re-narrowing of the stented artery post-implantation, known as in-stent restenosis (ISR) (this is discussed in greater detail in Chapter 2). Hypoxia is briefly described followed by the reasoning behind using computational software for prediction of hypoxic regions and in the analysis of stent designs. A brief introduction to helical flow is given which is directly linked to one of the aims of this research. Finally, the aims, structure, novelty and contribution, and relevant publications of this research are highlighted.

1.2 Cardiovascular System

As a whole, the cardiovascular system is responsible for the transportation of oxygen, carbon dioxide (CO_2), nutrients, hormones, chemical messengers, immune cells, stem cells, platelets, proteins, and waste products throughout the body, as well as acting as a system for temperature regulation. The cardiovascular system comprises the heart, approximately five litres of blood and the blood vessels.

1.2.1 Blood

Blood consists of liquid plasma in which three types of cellular elements are suspended: red blood cells (RBCs), white blood cells (leukocytes) and platelets. Plasma is a dilute electrolyte solution mainly composed of water (approximately 95% by volume) which contains about 8% by weight of proteins (fibrinogen, globulin, prothrombin, and albumin), as well as glucose, clotting factors, hormones, and dissolved oxygen and CO_2. About 45% by volume of the blood consists of cellular elements with RBCs constituting about 95% of the cellular elements, leukocytes constituting about 0.13% of the cellular elements, and platelets constituting the remaining 4.9%.[121] RBCs are the main carriers of oxygen in the blood. Leukocytes are responsible for fighting infections and disposing of damaged cells. Platelets are part of the primary response to injury of the arterial wall and form a critical element of the initial healing process following injury.

1.2.2 Heart

The heart is a muscular organ that serves to pump blood around the vessels and beats approximately 100,000 times per day, continuously, for the duration of a person's life. The human heart is approximately the size of two hands entwined and is located just left-of-centre in the upper chest cavity. The heart is comprised of four chambers: the left ventricle and atrium, and the right ventricle and atrium, as shown in Figure 1.1. Both

atria are thin-walled, low-pressure chambers that act predominantly as reservoirs for the two ventricles, which act as the pumping chambers.

The cardiovascular system can be divided into the pulmonary circulation and the systemic circulation, which are linked through these four chambers of the heart. The pulmonary circulation is primarily responsible for the exchange of oxygen and CO_2 with the atmosphere through the lungs, and the systemic circulation delivers oxygenated blood to the body's cells and returns deoxygenated blood back to the heart.

The pulmonary circulation begins in the right ventricle where the blood is propelled into the pulmonary artery. The pulmonary artery feeds into the lungs where the blood is oxygenated and then returns to the left atrium in the heart through the pulmonary veins. From here the oxygenated blood enters the left ventricle, the systemic circulation pumping chamber, which propels the blood out into the aorta. Through a network of connected arteries, arterioles and capillaries it is then distributed to every part of the body. It is predominantly as the blood passes through the capillaries that the oxygen leaves the blood and diffuses out into the surrounding tissue. The deoxygenated blood then returns to the right atrium of the heart through the connected capillaries, venules and veins, completing the systemic circulation. The deoxygenated blood then enters the right ventricle of the heart to begin the pulmonary circulation again.

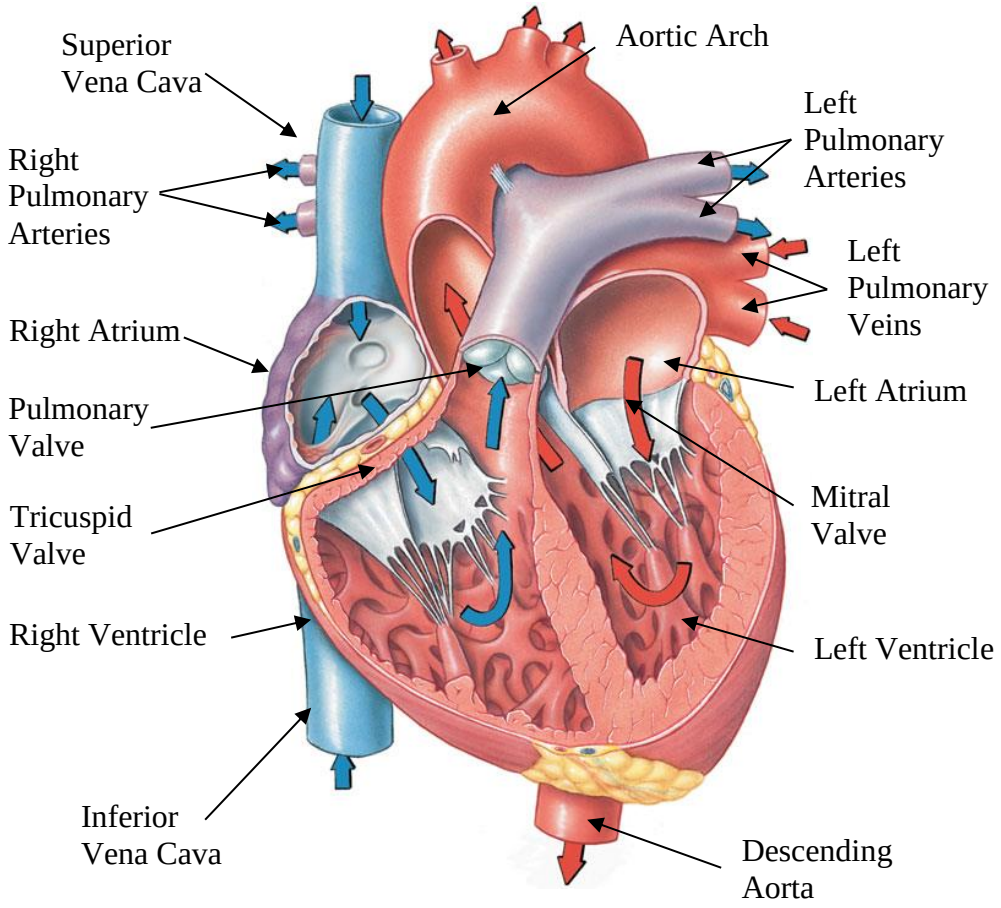

Figure 1.1: A cross-section of the human heart with the relevant chambers, arteries, veins and valves annotated. The path of the blood flow is marked by blue (deoxygenated) and red (oxygenated) arrows.[154]

The four chambers of the heart are separated by four valves which help control the flow of the blood through the heart. The right atrium receives the deoxygenated blood back from the systemic circuit through the superior vena cava and the inferior vena cava. The right atrium is separated from the right ventricle by the tricuspid valve which is composed of three fibrous flaps. These flaps are connected to papillary muscles on the inner wall of the right ventricle which open when the right ventricle is expanding allowing blood to flow through from the right atrium. Once at full capacity the right ventricle then contracts, the tricuspid valve closes preventing blood back-flow into the right atrium and the pulmonic valve opens, allowing the blood to pass into the right and

left pulmonary arteries feeding the lungs. The oxygenated blood then returns to the left atrium through the right and left pulmonary veins. The mitral valve, which is composed of two flaps connected to papillary muscles on the inner wall of the left ventricle and separates the left atrium from the left ventricle, remains closed until shortly after the left ventricle begins to expand. Once the expansion of the left ventricle is complete and it begins to contract, the mitral valve closes, preventing back-flow of the blood into the left atrium, and the aortic valve opens. The blood then flows into the aortic arch and on into the rest of the systemic circulation.

The walls of the heart are composed of three layers: the epicardium, the myocardium and the endocardium. The epicardium is a smooth membrane that covers the outer surface of the heart. The myocardium is the muscular wall of the heart which forms the four chambers. Within this layer is the cardiac muscle, the blood vessels which feed these muscles and the nerves which help control the muscles. The endocardium is a layer of cells, similar to endothelial cells (ECs) discussed later, which covers the inner surfaces of the four chambers and the valves and serves to protect the underlying muscle. The two ventricles differ in size with the muscular walls of the left ventricle thicker than the right. This is because of the extent of the vascular network and its respective resistance which needs to be overcome in order to pump the blood around the body compared with the resistance experienced through the lungs.

1.2.3 The Coronary Arteries

The muscles of the heart need to be constantly supplied with oxygen and nutrients to maintain their functionality, and this is accomplished by the coronary arteries. The coronary arteries originate at the base of the ascending aorta, immediately downstream of the aortic valve, and follow the curvature of the outer surface of the heart muscle.

There are two coronary arteries: the left and the right with their origins in the aortic arch as shown in Figure 1.2. The right coronary artery (RCA) supplies blood to right atrium, portions of both ventricles and areas of the heart which deal with regulating the heart rate. The RCA gives rise to one or more marginal arteries and also supplies the posterior descending artery as shown in Figure 1.3. The left coronary artery (LCA) supplies blood to the left atrium and ventricle, and the wall which divides the two ventricles. The artery itself gives rise to the circumflex artery (LCX) and also the left anterior descending artery (LAD). There are some interconnections between the left and right coronary arteries which help keep the blood supply constant despite fluctuations between heart beats which can be seen in Figure 1.2.

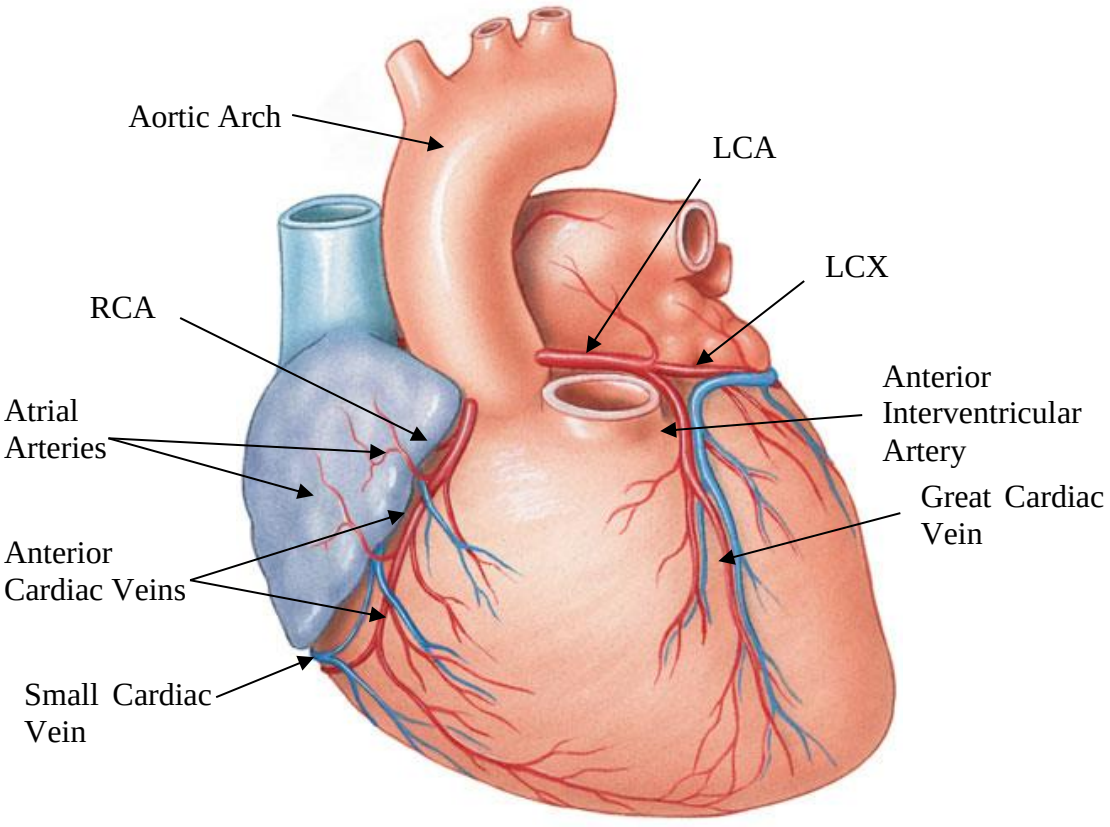

Figure 1.2: Coronary vessels supplying and draining blood to the anterior surface of the heart.[154]

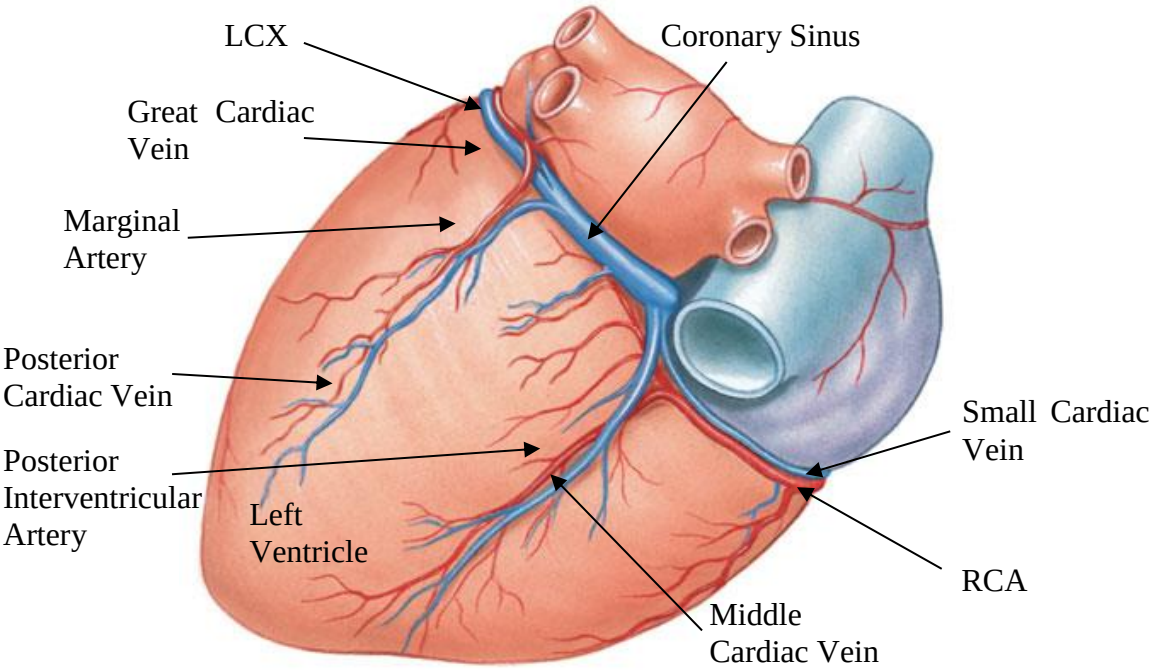

Figure 1.3: Coronary vessels supplying and draining blood to the posterior surface of the heart.[154]

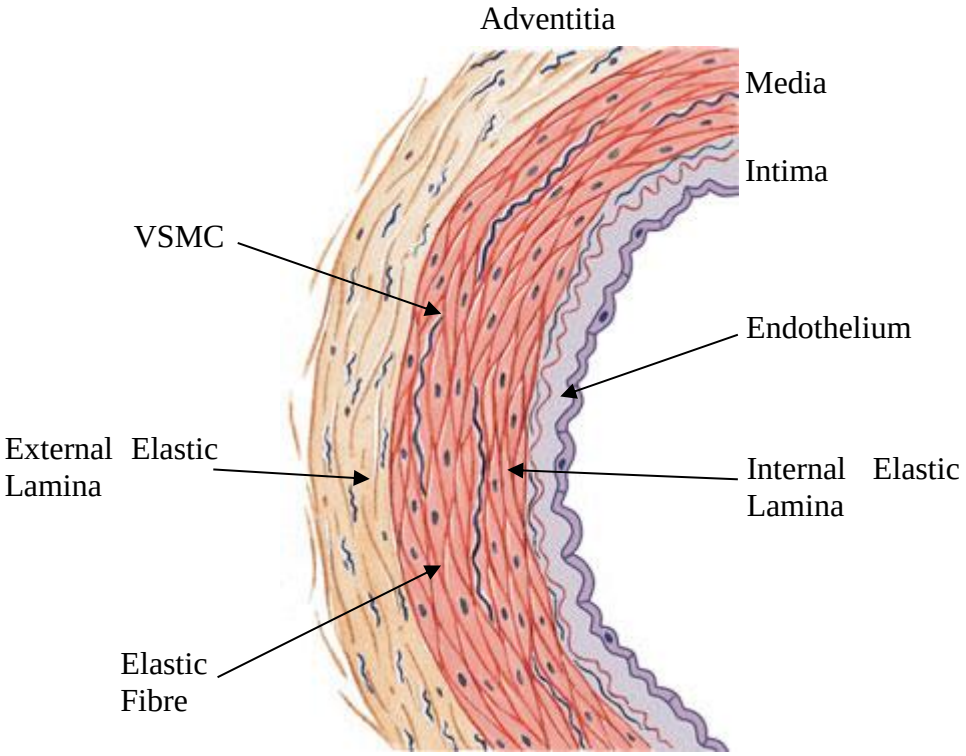

Figure 1.4: Typical arterial wall composition.[154]

All arterial walls, including those of the coronary arteries, are composed of three separate layers: the intima, media and adventitia, as shown in Figure 1.4. The intima is the inner layer of the arterial wall and is comprised of an endothelium, a thin basement membrane and a thin layer of elastic fibres called the internal elastic lamina (IEL). The endothelium, comprised of ECs lining the luminal surface, serves several important functions: to present a smooth surface to the blood flow, regulate the influx of molecules from the blood into the arterial wall, control the tone of the smooth muscle cells within the arterial wall and respond to changes in the local haemodynamic environment.[205] The basement membrane supports the endothelium and regulates molecular movement. The IEL acts as the boundary between the intima and the media. The media is commonly the thickest layer and is comprised of several concentric sheets of vascular smooth muscle cells (VSMCs) contained within a framework of extracellular matrix. The extracellular matrix is predominantly composed of elastin and collagen which provides support for the VSMCs and forms the primary load-bearing components of the arterial wall.[40] The elastin fibres provide a degree of compliance in the artery allowing for the changes in pressure throughout the cardiac cycle. The VSMCs are responsible for changing the calibre of the arteries by contracting, causing vasoconstriction of the vessel, and relaxing, causing vasodilation of the vessel. Chronic vasoconstriction can lead to high blood pressure (hypertension) and excessive vasodilation can occur when a patient goes into shock and leads to low blood pressure. The media is separated from the adventitia by the external elastic lamina. The adventitia consists of elastin and collagen fibres, with nerves and small capillaries running through it. These small capillaries are known as vasa vasorum (vessels within vessels) and are critical in providing oxygen to the cells contained within the media.

1.2.4 The Cardiac Veins

The blood which supplies the heart muscles with oxygen and nutrients is drained away by a series of veins which include the great cardiac vein, the posterior cardiac vein, the middle cardiac vein, the small cardiac vein and the anterior cardiac veins. Each of which drain the blood away from different areas of the heart and empty into the coronary sinus, which in turn empties into the right atrium, near the base of the vena cava. The cardiac veins contain valves to prevent blood backflow and typically are not prone to atherosclerotic plaque development.

1.3 Coronary Artery Disease

In order for the heart to function properly its muscles must receive a constant supply of blood. Restriction of the blood flow to the heart muscles can result in the muscles dying due to lack of oxygen. This is called myocardial infarction, or death of the myocardial muscle, and can be fatal. Coronary artery disease refers to areas within the coronary arteries where the blood flow is partially or fully blocked, and is predominantly caused by atherosclerosis. The risk factors for CAD include, but are not limited to poor diet, smoking, lack of exercise, obesity, diabetes, genetic predisposition to CAD, hypertension and high cholesterol.[77] Atherosclerosis is characterised by the build-up of fatty plaque deposits or lesions within the arterial wall of the coronary artery. Reasons why some regions within arteries are more prone to atherosclerosis compared with others is not known, although it is thought to be related to the haemodynamic features.[24]

To understand the process through which atherosclerotic lesions develop it is first required to look at the formation of lipoproteins in the liver and small intestine. Lipids, of which cholesterol is one, are not commonly water soluble and, consequently, do not dissolve in the blood. The body needs cholesterol for many functions, including the

maintenance of cell membranes and the production of crucial hormones and vitamins. Therefore, it needs to transport it around the body within the blood. To make cholesterol more dissolvable in blood, and hence easier to transport, it is combined with lipoproteins in the liver. The two main lipoproteins are low-density lipoproteins (LDLs) and high-density lipoproteins (HDLs). LDLs have been implicated in the development of atherosclerotic lesions and HDLs, though, remove excess cholesterol from cells and transport it to the liver for elimination.

Figure 1.5 shows the typical progression of an atherosclerotic lesion over time. An atherosclerotic lesion begins when excess LDLs penetrate the arterial wall under the endothelium and accumulate within the intima. This penetration of the endothelium by LDLs has been linked to a dysfunctional endothelium possibly caused by pro-atherogenic local haemodynamics; however, what constitutes pro-atherogenic local haemodynamics is debateable.[161] The lipids and proteins in the LDLs then begin to oxidise, i.e. lose electrons, and bind to sugars within the arterial wall. In response the ECs on the surface and the VSMCs within the media release chemical messengers which attract monocytes (a type of leukocyte) from the blood into the wall, where they change to macrophages. These macrophages then begin consuming the oxidised LDL particles. After a period of time the macrophages become laden with these LDL particles, developing into foam cells. Another type of leukocyte, i.e. T-cells, are also among the first cells to be recruited within the atheroma and by releasing cytokines further increase the inflammatory response.[2]

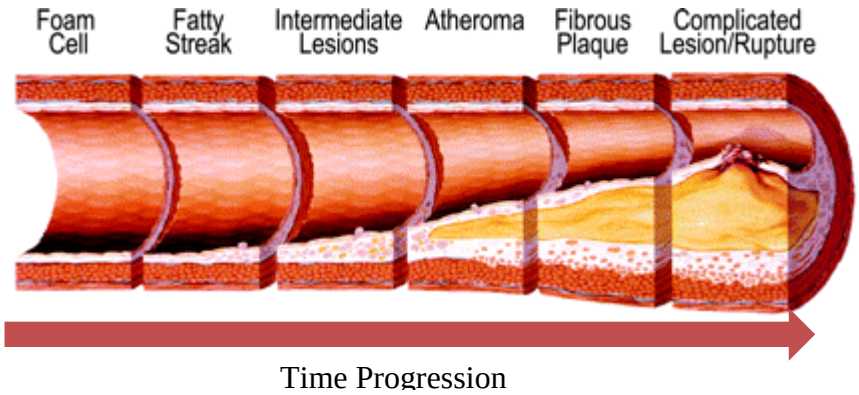

Figure 1.5: A typical progression of an atherosclerotic lesion over time (adapted from Koenig and Khuseyinova.[123]

The cytokines released by the macrophages encourage the proliferation and migration of VSMCs from the media into the intima.[254] The migrated VSMCs can then form a cap over the plaque, separating it away from the lumen. Through this remodelling of the arterial wall the calibre of the lumen can be maintained and the lesion has less impact on the blood flow. However, this method of mitigating the effects of the lesion only functions up to when the lesion occupies 40% of the area encompassed by the IEL.[76] After this, the arterial wall can no longer accommodate the lesion growth and the lesion begins to grow into the lumen; thus, it increasingly restricts the blood flow downstream. In advanced lesions the macrophages undergo apoptosis, i.e. programed death, which can lead to the development of a necrotic core when they are not properly cleared away. The necrotic core can slowly expand over time and result in the disruption of the plaque stability and acute thrombosis.[175] When the fibrous cap over the atherosclerotic plaque ruptures, releasing thrombotic agents from the T-cells into the blood stream, this results in the instigation of a thrombotic cascade and the formation of clots and emboli, which block the vessels downstream, resulting in MI.

1.3.1 Classification of Atherosclerotic Lesions

Stary et al. classified atherosclerotic lesions into eight types according to the stage of development:

- Type I: the lesion contains enough atherogenic LDLs to encourage increased macrophage infiltration and there is evidence of isolated macrophage foam cells
- Type II: the lesions primarily contain layers of macrophages and lipid-laden VSMCs
- Type III: an intermediary stage between Type II and IV, consists of scattered collections of extracellular lipid droplets which can not only disrupt the coherence of the VSMCs but also are precursors to more serious Type IV lesions
- Type IV: presence of lipid core and a fibrous cap
- Type V: lipid core with thick layers of fibrous connective tissue and possibly calcific lesion
- Type VI: lipid core with fissure, hematoma and thrombus
- Type VII: calcification predominates, possibly replacing the accumulated remnants of dead cells and extracellular lipid
- Type VIII: fibrous tissue changes predominate with the normal intima replaced and thickened with fibrous connective tissue.[238]

1.4 Treatment of CAD

The type of treatment to be recommended for CAD is predominantly based on how far the disease has progressed, or essentially how severe the atherosclerotic lesion, or lesions, has developed. In the initial stages of the disease lifestyle changes are the recommended treatment. These include quitting smoking, regular exercise, eating healthily, losing excess weight and reducing stress. Additionally, drugs may be

prescribed, such as statins, which lower the level of LDLs in the blood, or aspirin, which helps to thin the blood, reducing its tendency to clot. If these measures fail to produce satisfactory outcomes further treatment is recommended in the form of a coronary artery bypass graft (CABG) or angioplasty, with or without stenting.

1.4.1 Coronary Artery Bypass Graft

In the case of atherosclerotic lesions in the later stages of development, where the restriction or narrowing of the coronary artery is considerable, more immediate and aggressive treatment is needed. CABG is one of the treatments offered to patients with stable angina and suitable coronary anatomy where their symptoms are not satisfactorily controlled by lifestyle changes and medication.[179] CABG is classed as a major surgery as it is termed open-heart surgery, meaning the risk of infection post-surgery is not negligible. CABG is generally recommended over angioplasty in cases of multi-vessel coronary disease where it is seen to lead to a reduction in long-term mortality, MI and repeat revascularisations.[87,233] Guidelines for managing stable angina recommend that both options are presented and discussed with patients, as there are other factors, such as diabetes, which can affect the decision.[179] The procedure itself involves opening the patient's chest and sternum, exposing the heart, stopping the heart and keeping the blood pumping through a mechanical pump. Once this is achieved a blood vessel is taken from another part of the body and used to bypass the site of the restriction(s). Originally the greater saphenous vein from the leg was the vessel of choice for the bypass graft; however, the internal mammary arteries from the chest or the radial artery from the forearm are currently favoured as they are less likely to re-block. Previously, the only treatment option in the late stages of CAD, CABG has seen a decline in use since the introduction of angioplasty.[233]

1.4.2 Angioplasty

Balloon angioplasty was developed by Charles Dotter in the 1960s as a minimally invasive treatment for arterial narrowing caused by atherosclerotic lesions in the peripheral arteries.[54] Later, in the 1970s, it was applied to renal, coronary and iliac arteries by Andreas Gruentzig and co-workers.[83–85] The procedure is also referred to as percutaneous transluminal coronary angioplasty (PTCA). It involves making a small incision in the groin to gain access to the femoral artery (or in the arm to gain access to the radial artery) whereupon a hollow tube, called a catheter, is threaded up through the femoral artery, the iliac artery, the descending aorta, around the aortic arch, through to the ascending aorta and down into the relevant coronary artery. Once within the coronary artery a contrast agent is injected into the catheter and released into the coronary artery. This helps highlight the site of the restriction or narrowing on an X-ray to the cardiologist, who then feeds the tip of the catheter to the site. Once in position, a balloon on the end of the catheter is inflated, pushing the plaque out against the arterial wall and restoring blood flow to the tissue downstream.

Re-blockage of a treated coronary artery following this procedure, known as restenosis, was reported in 30-60% of patients,[73] with these patients consequently needing re-treatment with either additional percutaneous methods or bypass surgery. Restenosis following balloon angioplasty is attributed to three key responses: acute elastic recoil, negative wall remodelling (reduction in lumen area without a change in wall mass) and arterial wall thickening into the lumen (due to an increase in the number of cells within the arterial wall).

1.4.3 Angioplasty with Stenting

Bare metal stents (BMS) were first used in an angioplasty procedure by Puel and Sigwart in 1986,[230] and were gradually incorporated in the 1990s to serve as a rigid scaffold, thus eliminating elastic recoil and reducing wall remodelling,[92] with some cases of positive remodelling reported.[176] A stent, generally, is a cylindrical metal mesh that is crimped onto the angioplasty catheter, which upon expansion of the catheter balloon is expanded radially out against the arterial wall. BMSs are commonly made of 316L stainless steel, platinum-iridium alloy, tantalum, cobalt-chromium alloy, titanium, pure iron, magnesium alloys or nitinol.[147]

The most common type of stent is balloon expandable, although nitinol stents are self-expanding. Self-expanding stents make use of the superelastic behaviour of the nitinol material, whereby the stent can transition between a strong Austenite phase and a weaker Martensite phase when stressed. For implantation of these stents a balloon is not needed and instead a sheath is withdrawn and the stent expands to a predetermined shape; however, balloon angioplasty may be carried out prior to implantation. Even though stenting reduced restenosis rates to between 22% and 32%,[61,73,223] it still continued to be a burden. Restenosis with stents, known as ISR, is mostly due to arterial wall thickening. Understanding and consequently devising ways of reducing the frequency of ISR has been a continuing goal of research into improved stent designs. From this research drug-eluting stents (DES) were developed which use anti-proliferative, immunosuppressive, pro-healing and anti-inflammatory drugs in an attempt to prevent ISR. DESs have proved effective, with ISR rates at six-month follow-up as low as 2.6-10.1%.[240] As a result, DESs have surpassed BMSs as the preferred stent choice, with 70-80% of stent procedures in the US carried out with DESs by mid-2009.[67,125] However, ISR is still a problem along with stent thrombosis, and

delayed re-endothelialisation (re-growth of the endothelium) due to the anti-proliferative properties of some DES drugs.[70] Newer stents currently in development or undergoing clinical trials are predominantly variations of the DES design with perceived improvements, such as biodegradable polymer and polymer-free coatings, novel coatings which encourage re-endothelialisation, and completely biodegradable platforms.[98,163] However, there are other ideas for reducing ISR which are beginning to show promise, based on the fact that the biological healing response to stent implantation is partially dependent on local haemodynamics in the stented artery. These will be discussed in detail in Chapter 4. BMSs are still implanted in patients with a high bleeding risk or who may not be able to conform to dual antiplatelet therapy (DAPT) required post-implantation. Therefore, research into how to improve the long-term outcomes of angioplasty with stenting using means other than drugs is warranted.

1.5 Hypoxia

The delivery of oxygen to the cells within an arterial wall is crucial to maintaining a healthy artery. The blood passing through the vasa vasorum within the adventitia supplies most of the oxygen needed to the media, and the intima is predominantly supplied through diffusion from the blood contained within the central lumen Hypoxia, a deficiency in the amount of oxygen reaching the cells within the arterial wall, has been found to exacerbate some of the biological processes which can result in ISR.[20,134,215,216] The amount of oxygen diffusing into the arterial wall can be affected by the haemodynamic conditions within the lumen.

The geometry of an implanted stent can have a significant impact on the haemodynamic conditions within the artery. The main beneficial effect is the restoration of blood to the downstream vasculature; however, locally within the stented region recirculation zones can be created around stent struts which can influence the amount of oxygen reaching

the underlying arterial wall cells. Predicting the amount of oxygen that reaches the arterial wall cells is valuable so that the design of stents, and other medical devices, can be improved upon.

1.6 Computational Analysis of Coronary Stents

With the aforementioned dependency of the biological processes that can result in ISR on the local haemodynamics and oxygenation of the arterial wall, analysis of these features is required. Given the small size of the coronary arteries and the scale of the haemodynamic features that takes place within the artery computational analysis techniques have proved to be powerful tools. Considering the complexity of the biological processes that take place within a coronary artery, with a degree of simplification computational techniques can focus on certain aspects of the physical phenomena and help predict the impact of stents on the artery environment. Traditionally, there are two aspects which are focused upon using computational analysis: the structural injury inflicted on the arterial wall and the luminal haemodynamic environment created by stent implantation. The stresses placed upon an arterial wall by stent implantation, which inflict the structural injury, are analysed using advanced finite element analysis (FEA) software and the local haemodynamics are analysed using computational fluid dynamics (CFD).

For predicting the oxygen transport in arteries there are three types of studies which are commonly employed: lumen-free analyses, wall-free analyses and lumen-wall coupled analyses. In lumen-free analyses a constant value for oxygen concentration is imposed on the luminal surface; hence, the impact of the blood flow is neglected. For wall-free analyses a constant oxygen concentration value is applied on the luminal surface and the oxygen flux into the wall is quantified using a dimensionless variable, the Sherwood number (discussed in more detail in Section 3.4). Finally, lumen-wall coupled analyses

are beneficial because the unrealistic assumption of a constant oxygen concentration on the luminal surface is not made and a more detailed indication of oxygen concentration levels, and consequently the extent of hypoxia, within the arterial wall is given.

1.7 Helical Flow

Local hemodynamics have a significant influence on the cellular activity within an arterial wall. Atherosclerosis has been found to preferentially develop in areas of disturbed flow and regions of low wall shear stress (WSS).[59,176,182,183,185] Natural blood flow in the arterial system has been found to be helical in nature, meaning it has a secondary circular motion in addition to the primary forward motion. The beneficial/detrimental implications of helical flow in the cardiovascular system are open to conjecture;[186] however, two novel stent designs are being developed that endeavour to elicit helical flow and take advantage of its beneficial characteristics in terms of inhibiting neo-atherosclerotic lesions (new lesions formed within the stented region) post-implantation and ISR. These two novel stent designs are the BioMimics 3D stent as developed by Veryan Medical Ltd, which is currently undergoing assessment in the MIMICS-2 clinical study with a total of 271 patients, and the Vascular Flow Technologies Ltd spiral flow inducer which originally had some success in synthetic grafts and may also be incorporated into stent designs. Data is available from the first MIMICS study where 76 patients undergoing femoropopliteal artery intervention were enrolled of which 50 were implanted with the BioMimics 3D stent and 26 were implanted with a straight control stent. There were two key findings from this two-year study. First, the Kaplan Meier survival analysis of freedom from loss of primary patency at two years was 72% for the BioMimics 3D subjects vs. 55% for the control group (P=0.0497). Second, there was no increase in the clinically driven target lesion revascularisation rate in the BioMimics arm between 12 and 24 months (9% at both

time-points) compared to an increase of 16% (8% at 12 months and 24% at 24 months) in the control arm.[272] Significantly for this work, the data indicated a correlation between primary patency and stent curvature.[272] Helical flow and these two devices will be discussed in greater detail in Chapter 4 with direct relevance to Test Case 4 presented in Chapter 8 which assesses the effects of helical-flow-inducing stent designs on oxygen transport.

1.8 Aim of this Research

The aim of this research was to develop an advanced oxygen transport model that incorporates both the free oxygen dissolved in plasma and the bound oxygen contained in RBCs, and also accounts for the shear-induced dispersion of RBCs, which could be used to assess stent designs. More detail on the reasoning for this is discussed in Chapter 3. Additionally, this research was undertaken to demonstrate both the limitations of simpler models and also, potential applications of the advanced model; specifically, assessment of oxygen transport in stented coronary arteries. Finally, assessment of the theoretical benefits of helical flow in terms of local haemodynamics and oxygen transport in stented coronary arteries was undertaken.

1.9 Structure of Thesis

Chapter 2 provides the background material to the instigating factors and biological processes involved in ISR. Chapter 3 gives an introduction to fundamental fluid dynamics theory and the haemodynamic variables used, the oxygen transport theory and relevant variables, and also numerical methodologies employed by the CFD software, as used in this study. Chapter 4 is a thorough literature survey of previous work in the areas of oxygen transport, haemodynamic assessment of stent designs, and helical flow. Chapter 5 is a prelude to the four test cases describing the aims of each. Chapter 6 presents the results of Test Case 1 where the results of five different oxygen transport

models were compared with experimental results from dog carotid arteries. The five different oxygen transport models were also compared with experimental results from rabbit aortae in Test Case 2, as presented in Chapter 7, along with Test Case 3 which compares three different coronary stent designs using the most advanced oxygen transport model. Finally in Chapter 8, the predicted haemodynamics and oxygen transport in five helical stent designs are compared with those of a straight stent. The limitations and conclusions of the work undertaken, and also possible future work, are discussed in Chapter 9. Appendix A presents some relevant validation test cases and appendix B describes the required mesh convergence tests.

1.10 Novelty and Contribution

This research contributes to two specific biomedical fields: oxygen transport modelling and assessment of coronary stents. The novelty of the research is that it is the first time that:

1. An oxygen transport model has incorporated the free and bound oxygen along with a variable shear-induced dispersion coefficient.
2. The simplifications of blood oxygen transport models, which are prevalent in the literature, have been assessed in 3D geometries and their effects on the PO_2 profile within the arterial lumen and wall have been analysed.
3. It is the first time that the oxygen transport has been modelled in three different stent designs with the predicted low and hypoxic PO_2 volumes within the arterial wall assessed.
4. An advanced oxygen transport model has been used to assess different helical-flow-inducing stent designs.

1.11 Publications

The work presented in this thesis has led to publications in three peer-reviewed journals:

Oxygen mass transport in stented coronary arteries, Murphy, E.A., Dunne, A.S., Martin, D.M., Boyle, F.J., Annals of Biomedical Engineering, Volume 44, Issue 2, 2016.

Computational fluid dynamics analysis of balloon-expandable coronary stents: influence of stent and vessel deformation, Martin, D.M., Murphy, E.A., Boyle, F.J., Medical Engineering and Physics, Volume 36, Issue 8, 2014.

Reducing in-stent restenosis through novel stent flow field augmentation, Murphy, E.A., Boyle, F.J., Cardiovascular Engineering and Technology, Volume 3, Issue 4, 2012.

Additionally, this work has been presented at several conferences:

Oxygen transport in stented arteries using computational fluid dynamics, Eoin A Murphy, Fergal J Boyle, John G Houston. University of Dundee Medical Symposium, Crieff, February 2016. (Poster)

Assessing the effect of helical flow on the hemodynamic environment post-stent-implantation in the coronary artery, Proceedings of the 20th Annual Bioengineering in Ireland Conference, Co. Limerick, Ireland, 2014

An improved methodology for hemodynamic analysis of stent designs with an application to helical-flow-inducing stents, Proceedings of the 19th Annual Bioengineering in Ireland Conference, Co. Meath, Ireland, 2013

The influence of stent and vessel deformation on wall shear stress and wall shear stress gradient in a stented LAD coronary artery, Proceedings of the Bioengineering Society (UK) Conference, Oxford, England, 2012

CHAPTER 2

In-Stent Restenosis

2.1 Introduction

In this chapter the biological background material relevant to the project is described. This chapter is crucial in detailing the biological processes which take place at a cellular level within the human arterial wall post-stent-implantation, highlighting how they interact, and are influenced by their instigating factors. This offers a justification, in addition to reasons given in Section 1.8, as to why one would be interested in numerically modelling the local haemodynamics and oxygen transport within a stented coronary artery.

2.2 In-Stent Restenosis

A diagram of a healthy arterial wall is shown in Figure 2.1; however, the exact composition of an atherosclerotic artery deviates from this ideal form with plaque, inflammation, and intimal hyperplasia. Stent implantation has three effects on a treated artery: it induces structural injury, introduces a foreign body and alters the local haemodynamics. These three effects instigate and influence four interacting biological processes which can lead to re-narrowing of the stented artery, known as ISR. ISR is defined as angiographic evidence of a loss of greater than 50% of the lumen diameter post intervention.[159]

Structural injury is inflicted on the arterial wall during the implantation procedure. The stent and balloon denude most of the endothelium on contact, exposing the underlying collagen fibres and leaving some damaged ECs directly adjacent to the stent struts.[208] Stent implantation stretches, and therefore stresses, the arterial wall and as a result the cellular structure of VSMCs present in the media can be disrupted, and the IEL and the media can rupture. Atherosclerotic lesions present at an implantation site are inelastic and frequently split rather than stretch upon stent implantation. This combined damage induces a healing response within the arterial wall.

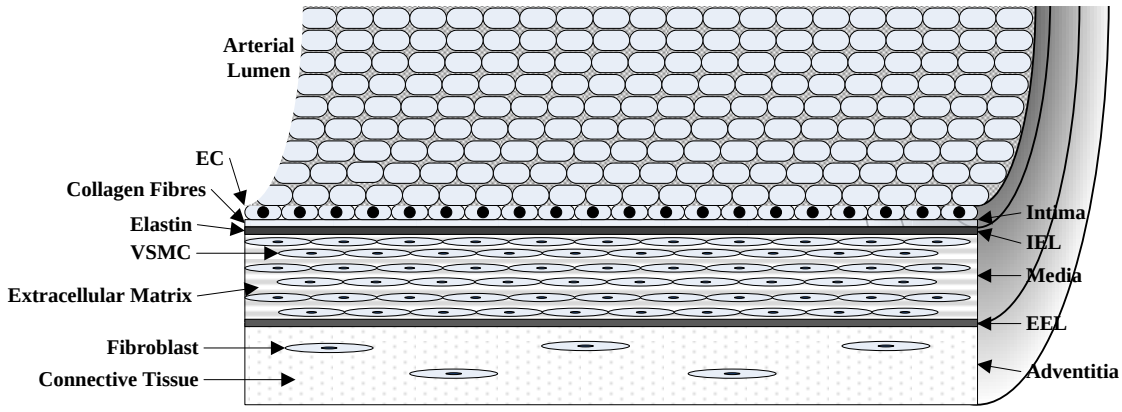

Figure 2.1: Simplified diagram of a healthy artery showing the separate layers and the main cellular components and fibres. Abbreviations: internal elastic lamina (IEL), external elastic lamina (EEL), endothelial cell (EC) and vascular smooth muscle cell (VSMC).

When a stent is inserted in the artery its non-biological surface composition induces a foreign-body response. This response is dependent on properties such as the biocompatibility of the surface material and the surface roughness, along with the existence of contaminants on the surface of the stent. The surface material and roughness of a stent affects how quickly the arterial wall heals over the struts. Contaminants, such as powder from surgical gloves, have been found on a stent surface

due to handling before catheter insertion.[11] The improved biocompatibility of stent materials and the rinsing of stents before implantation reduce the foreign-body response; however, the non-biological nature of stents instigates cells and proteins in the body to react to what they perceive as a foreign invader.

When a stent is implanted in a diseased artery the geometry of the artery is altered, which in turn augments the local haemodynamics. The lesion is compressed out against the arterial wall, clearing the lumen blockage and reinstating blood flow. The stented artery adopts a new geometry based on the stent strut configuration with the struts pressed against the arterial wall and prolapsed tissue between them. In some cases of over-inflation of the balloon, a step-up phenomenon at the ends of the stent can occur, creating recirculation zones at these points. Also, some degree of longitudinal straightening by stent implantation has been reported in curved arteries, although with more flexible stent designs currently on the market this is no longer a serious issue.[86] These changes are a deviation from the smooth surface presented to the blood flow by a healthy artery and lead to disturbed flow within the stented artery. This disturbed flow can encompass flow separation and reattachment, stagnation and recirculation zones, long particle residence times, low and high shear stress (SS) within the blood flow, low and high WSS zones, oscillatory WSS, and high WSS gradient (WSSG) and angle gradient (WSSAG). Cellular components of the arterial wall are impelled to respond to this augmentation of the local haemodynamics in order to return the artery to a circular luminal cross-section with smooth walls. Also, some of the changes in the local haemodynamics are not conducive to the natural healing of the arterial wall and instead hinder or adversely affect it, which consequently can lead to ISR.

It is important to note that historically it was thought that human arteries try to maintain a physiological WSS value of approximately 15dyne/cm^2 (1.5Pa), although this has

since been refuted with one of the current hypotheses being that the WSS varies inversely with vessel radius, becoming larger when the vessel radius decreases.[37] Although, conveniently here, in the case of coronary arteries the basal physiological WSS has been observed to be approximately 1.5Pa.[37] Additionally, physiological WSS values have also been shown to vary across different species which is worth noting as studies involving animals are referenced throughout this section with different values for low WSS values adopted by the researchers involved.

The four interacting biological processes, instigated by these three effects of stent implantation, are thrombus formation, inflammation, neointimal hyperplasia (NIH) and re-endothelialisation. These biological processes, their interactions and the influences of the three instigators on each are described in the following sections. Separate to this, hypoxia and how it affects the biological processes is described in Section 2.3. Also, the influence of stent design on these instigators and biological processes is discussed in Section 2.4.

2.2.1 Thrombus Formation

Thrombus formation, in general, is the body's emergency response mechanism to structural injury and entails primary and secondary haemostasis. Primary haemostasis involves blood-borne platelets quickly adhering to form a plug at an injury site. Occurring in parallel with this is secondary haemostasis which involves the formation of fibrin fibres through the coagulation cascade, and these fibrin fibres bind the adhered platelets together at the injury site.

When structural injury is inflicted on an artery by stent implantation, platelets present in the bloodstream are activated by exposed collagen and plaque, and by proteins expressed by damaged ECs (e.g. fibronectin and von Willebrand factor (vWf)).

Activated platelets are more sensitive to chemical signals and adhere to the collagen, plaque and proteins on the arterial wall, changing their cytoskeleton (cell scaffolding) to become more flexible and capable of spreading out over the injury site. Activated platelets also release platelet activating factor (PAF), adenosine diphosphate (ADP) and thromboxane A2 into the bloodstream which in turn activate more platelets and aid in the aggregation of platelets at an injury site. The coagulation cascade involves several coagulation factors present in the bloodstream and those released by adhered platelets and leukocytes, and VSMCs (e.g. tissue factor). Through the coagulation cascade prothrombin, present in the blood plasma, is converted to thrombin which both activates more platelets and causes soluble fibrinogen molecules in the blood plasma to convert into fibrin monomers. These fibrin monomers form fibrin fibres that bind the platelets that have aggregated together at the injury site, forming a thrombus.

In addition to this response to structural injury, thrombus formation is also initiated by the presence of a foreign body. Blood-soluble proteins adsorb onto the stent surface, forming a thin film which provides a provisional matrix that controls the subsequent biological processes of the foreign-body response.[3] Different proteins (e.g. albumin, fibrinogen, fibronectin, vitronectin and y-globulin) adsorb onto the stent surface depending on the properties of the surface material.[3] These adsorbed proteins produce different effects; fibrinogen for example is pro-thrombotic, promoting activation and adhesion of platelets, whereas albumin reduces platelet adhesion and aggregation.[138] Fibrinogen is adsorbed preferentially over other proteins on many surfaces, especially polymers,[138] and thus facilitates thrombus formation at a stent implantation site.

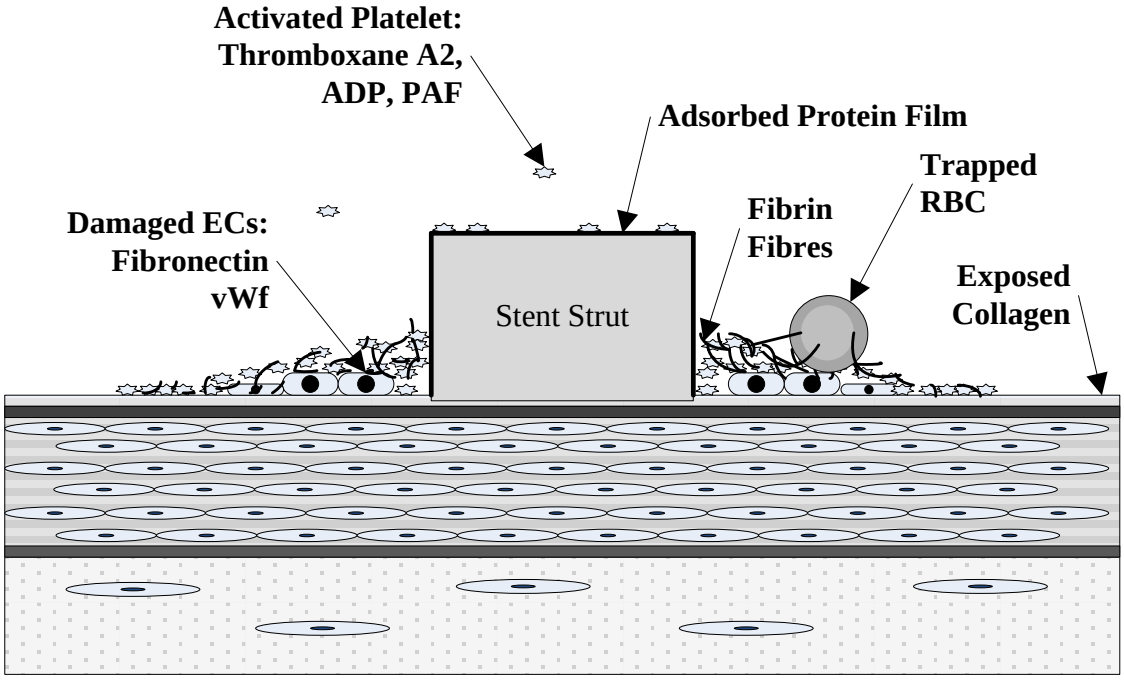

Figure 2.2: Diagram showing the cells, pro-thrombotic agents and proteins involved in thrombus formation at an injury site around a stent strut.

Thrombus formation has been found to be heavily flow dependent. The platelets, coagulation factors and chemical substances involved in thrombus formation are predominantly blood-borne particles and as such their movements are dictated by the local haemodynamics. High particle residence times at the injury site facilitate increased platelet exposure times to thrombotic arterial wall components and activating chemical substances. This increased exposure time results in a greater probability of platelet activation with enhanced platelet activation being observed in low flow conditions.[9] Increased platelet adhesion has been observed downstream of recirculation zones, where the main flow reattaches to the arterial wall, due to the convection of platelets towards the arterial wall.[56,221] RBCs can also get trapped by fibrin monomers in the thrombus within recirculation zones or other low SS regions. Also, in regions of low WSS (<1.0 to 1.2 Pa) ECs respond by down-regulating the release of anti-thrombotic agents and

up-regulating the expression of pro-coagulant and pro-thrombotic agents, thus also instigating thrombus formation. High SS within the blood flow can also activate platelets; this depends on the magnitude of the SS and the exposure time of platelets to the high SS.[31] Figure 2.2 shows the cells (platelets, RBCs and ECs), pro-thrombotic agents and proteins involved in thrombus formation.

2.2.2 Inflammation

Inflammation involving leukocytes (e.g. lymphocytes, monocytes/macrophages, neutrophils, eosinophils and basophils.) is the body's primary defence mechanism against infection. Leukocytes are attracted to an injury site in order to prevent the spread of the tissue damage and infection, and to aid in wound healing and tissue repair.[158]

Structural injury to the arterial wall by stent implantation triggers the expression of several cell adhesion molecules which mediate four steps, shown in Figure 2.3, that each leukocyte undergoes in order to infiltrate an injury site. These four steps are the initial contact (tethering), leading to rolling and activation of the leukocyte, followed by firm adhesion and finally transmigration into the arterial wall. Tethering and rolling are mediated by cell adhesion molecules P-selectin (expressed by adhered platelets and damaged VSMCs) and E-selectin (expressed by damaged ECs) which interact with ligands expressed on the leukocyte surface. Firm adhesion is mediated by platelet glycoprotein (GP) Ib-α, vascular cell adhesion molecule 1 (VCAM-1) and intercellular adhesion molecule 1 (ICAM-1) expressed on the luminal surface of the damaged wall, which interact with integrins expressed on the surface of the leukocytes, e.g. macrophage-1 antigen (MAC-1). The final step is driven by concentration gradients of chemokines (chemotactic cytokines) released by damaged ECs and VSMCs, and by the leukocytes already present at the injury site. Neutrophil infiltration of the injury site represents the initial acute phase of the inflammatory response and they are present up

to, but not beyond, 30 days after BMS implantation.[59] The chronic phase of the inflammatory response involving lymphocyte and monocyte infiltration of the injury site, extends from three days to beyond six months for BMSs.[59] When monocytes migrate across the platelet/fibrin thrombus to the site of initial injury, they differentiate into macrophages. These cells consume the damaged cells around the injury site and also secrete interleukins which attract more leukocytes to the area.

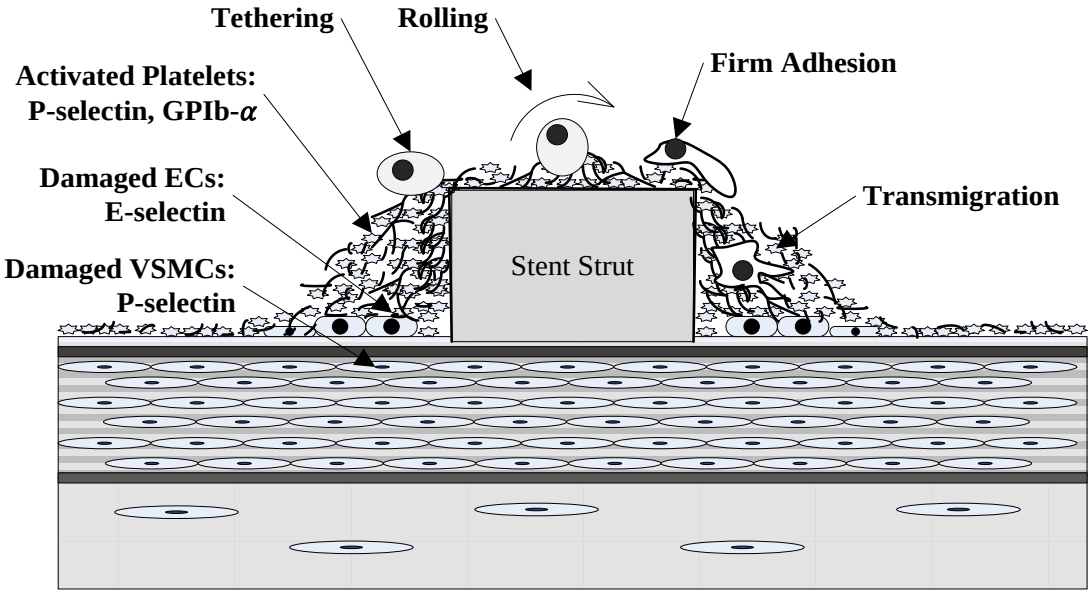

Figure 2.3: Diagram showing the four steps leukocytes undergo in order to infiltrate the injury site.

The thin layer of proteins adsorbed onto the implanted stent surface not only mediates the adhesion of platelets, but also controls the inflammatory phase of the foreign-body response to the stent. The complement system, which consists of more than 20 plasma-based proteins, is a primary contributor to the innate immune system and is activated by the adsorbed protein layer. Activation of the complement system promotes the formation of enzymes and binding proteins which regulate the inflammatory response to a foreign body. Leukocytes, particularly neutrophils and monocytes, follow increased

concentration gradients of chemo-attractant anaphylatoxins, such as C5a, which are fragments produced by activation of the complement system. Other products of complement activation, such as C3b and iC3b, through a process called opsonisation mark foreign particles for phagocytic removal (ingestion) by leukocytes and subsequent proteolysis (digestion) by proteases (cellular enzymes). This is the case for any contaminants on the stent surface; however, in the case of a relatively large foreign body, such as a stent, which cannot be ingested, adhered neutrophils and monocytes undergo a frustrated phagocytosis whereby they release their array of potent oxygen metabolites and proteolytic enzymes.[81] This can lead to an unresolved chronic inflammatory response exemplified by the increased fusion of macrophages into foreign body giant cells around an implanted stent. Platelets which adhere to the adsorbed protein layer on stent struts also release P-selectin to aid leukocyte adhesion and these adhered leukocytes can also encourage thrombus formation through elevated expression of tissue factor.[57] Products of the complement system can interact with proteins involved in thrombus formation and thus, can also regulate each other. Metallic stent struts or the presence of a polymer coating on a stent can induce an allergic inflammatory reaction in some people, which is observed as eosinophil activation and presence at the implantation site.[185]

The local haemodynamics can also mediate the adhesion of leukocytes at an implantation site. With increased thrombus formation due to the haemodynamics in certain regions, e.g. re-attachment areas where flow is directed towards the arterial wall, there is a greater amount of cell adhesion molecules available to capture passing leukocytes. In addition to this, it has been found that local vascular haemodynamics can affect leukocyte ligand expression,[65] shape[46] and consequently interaction with other cells.[246] Leukocyte-EC interaction is heavily influenced by the local haemodynamics

which becomes more relevant as the endothelium reforms over the implantation site. For instance, leukocytes retract their pseudopodia (temporary projections from leukocytes used to adhere to a surface) when exposed to nitric oxide (NO),[160] which is produced by functioning ECs in response to physiological WSS (1.5 to 7 Pa).[32] However, when ECs are exposed to low WSS (<1.0 to 1.2 Pa) or disturbed flow they decrease their expression of anti-inflammatory mediators (e.g. NO) and upregulate cell adhesion molecules (e.g. E-selectin, VCAM-1 and ICAM-1).[32] Increased macromolecule transport across the endothelium, as a result of abnormal endothelial permeability, has been shown to occur in reattachment zones of high WSSG (>0.85Pa/mm).[195] This may lead to increased uptake of monocytes across the endothelium in reattachment zones, for instance, downstream of stent struts. Therefore, the establishment of normal physiological blood flow within a stented artery following the procedure is crucial to avoiding prolonged inflammation and consequently possible ISR.

2.2.3 Neointimal Hyperplasia

NIH takes place up to 18 months post-implantation, results in a thickening of the intimal layer, and is the main cause of ISR. NIH involves the migration and proliferation of VSMCs originating in the media, and also differentiating from fibroblasts in the adventitia and bone-marrow-derived stem cells in the bloodstream. In addition, the VSMCs synthesise extracellular matrix (ECM). The degree of NIH is heavily influenced by the degree of thrombus formation and inflammation which takes place at an implantation site.

Damaged ECs and VSMCs, adhered leukocytes and platelets release cytokines (proteins used for intercellular communication) and mitogens (proteins which encourage a cell to commence the cell-division cycle) which encourage NIH at an injury site. The

migration of the VSMCs is stimulated by cytokines (e.g. tumour necrosis factor (TNF) and interleukin-1 (IL-1)) released by macrophages and also by some of the mitogens (e.g. platelet-derived growth factor (PDGF)). PDGF is capable of stimulating migration at a much lower concentration level than that needed for cell division and therefore, migration is an earlier response than proliferation.[82] In order for migration to occur enzymes (e.g. matrix metalloproteinase (MMP)-9) released by adhered leukocytes and VSMCs help in the dissolution of the IEL and the existing ECM. This dissolution, along with the disruption to the ECM caused by stent implantation, allows the medial VSMCs and myofibroblasts (activated fibroblasts) to migrate through to the neointimal region of the arterial wall. The proliferation of VSMCs is instigated by mitogens (e.g. serotonin, thromboxane A_2, PDGF and basic fibroblast growth factor (bFGF)) which are released by damaged ECs and VSMCs, adhered leukocytes and platelets. This proliferation produces a greater amount of neointimal cells than does migration. In addition to VSMC migration and proliferation, inflammatory and hematopoietic cytokines (e.g. granulocyte colony-stimulating factor (G-CSF)) produced by ECs and leukocytes at the injury site mobilise stem cells from the bone marrow to enter the bloodstream.[108,109] These stem cells can differentiate into smooth muscle progenitor cells (SPCs), which adhere to fibronectin and differentiate into VSMC-like cells in the presence of PDGF-BB (a PDGF isoform) at the injury site.[89,232] The stretching of the original VSMCs in the arterial wall stimulates them to synthesise collagen, a component of ECM, which may serve to alleviate the additional stress caused by stent implantation, but also increases the overall wall volume.[137] This, along with the synthesis of ECM by neointimal VSMCs can contribute up to 80% of the resultant wall thickening.[73]

Leukocytes and platelets attracted to a foreign body can also release cytokines and mitogens which encourage NIH. Macrophages activated by biomedical polymers *in*

vitro have been shown to stimulate fibroblast activity.[3] In addition to this, macrophages and foreign-body giant cells on a biomaterial surface modulate ECM fibrosis. This results in the formation of a fibrous capsule, mainly comprised of collagen fibres and leukocytes, which isolates the stent from the surrounding tissue and blood.[3]

NIH can also be induced and influenced by local haemodynamics within the stented arterial region. Where local haemodynamics cause increased thrombus formation and inflammation, due to the release of mitogens by adhered leukocytes and platelets, this subsequently induces increased NIH. In regions where the endothelium has been denuded and the IEL damaged by stent implantation, underlining VSMCs may be exposed and affected by the local haemodynamics. Human VSMCs exposed to physiological or high WSS, taken as 1.4 and 2.8 Pa respectively in this particular study, for 24 hours show an increase in transforming growth factor (TGF)-β1 expression which inhibits their proliferation, in comparison with a static control.[260] High WSS (>1.5 Pa) also stimulates the release of stored mitogens (PDGF and bFGF) within VSMCs into the bloodstream while low WSS increases VSMC susceptibility to these mitogens.[239] Thus, in a stented artery where there is variability between high and low WSS across the stent and arterial wall, increased proliferation would occur in low WSS zones.[173] In a study by Papadaki et al. into the effects of different shear stresses (0.5, 1.1, 1.5, 1.75 2.15, and 2.5 Pa) on a layer of human aortic VSMCs on glass slides found that above 1.5 Pa the VSMCs showed decreased proliferation over a 24 hour period.[187] In addition, pulsatile turbulent WSS has also been found to stimulate VSMC proliferation,[227] and murine VSMCs exposed to steady laminar WSS of 1.5 Pa have been found to transdifferentiate into ECs.[266] Within the arterial wall, VSMCs and myofibroblasts are exposed to transmural interstitial shear stress, estimated to be normally around 0.1 Pa, which can be increased by endothelium denudation, activating

these cells and promoting their migration into the intima or wound site.[225] ECs present in the stented region downregulate anti-proliferative gene expression and upregulate the release of VSMC growth factors in response to low WSS.[32] Areas experiencing elevated WSSG (>0.2Pa/mm) in the toe region of an end-to-side arterial anastomosis have been found to develop increased NIH.[129,136,184] The oxygen flux from the blood into the arterial wall, which is also heavily flow dependent, has also been found to influence VSMC behaviour. NIH has been found to be reduced in rabbits treated with supplemental oxygen,[135] and areas of low WSS where the oxygen flux into the arterial wall is low are hypothesised to experience increased NIH.[252]

2.2.4 Re-Endothelialisation

The endothelium fulfils several important physiological functions which include acting as a selective permeability barrier, participation in cardiovascular homeostasis and inflammatory responses, regulation of cellular growth and proliferation within the arterial wall, angiogenesis and tumour metastasis.[214] Considering its importance, once denudation by stent implantation has occurred, its reinstatement, i.e. re-endothelialisation, is critical in order for the artery to return to its normal functioning behaviour.

Damaged ECs, adhered platelets, VSMCs and macrophages present at the injury site release mitogens capable of instigating re-endothelialisation. These mitogens include vascular endothelial growth factor (VEGF), PDGF and bFGF and induce the ECs remaining around the stent struts and outside the stented area to migrate and proliferate into the denuded section. In addition, increased levels of VEGF circulating in the bloodstream induce precursors of endothelial cell colony forming units (EC-CFUs) (angiogenic monocytes and lymphocytes) and endothelial progenitor cells (EPCs) derived from bone marrow stem cells, to mobilise, enter the bloodstream and home in

on the injury site. It has been hypothesised that EC-CFUs precursors arrive earlier than EPCs to provide rapid coverage of the injury site and secret angiogenic factors (e.g. VEGF and G-CSF) which encourage EPC homing and proliferation.[186] EPCs attach to proteins and adhesion molecules on the arterial wall and subsequently differentiate into mature ECs.

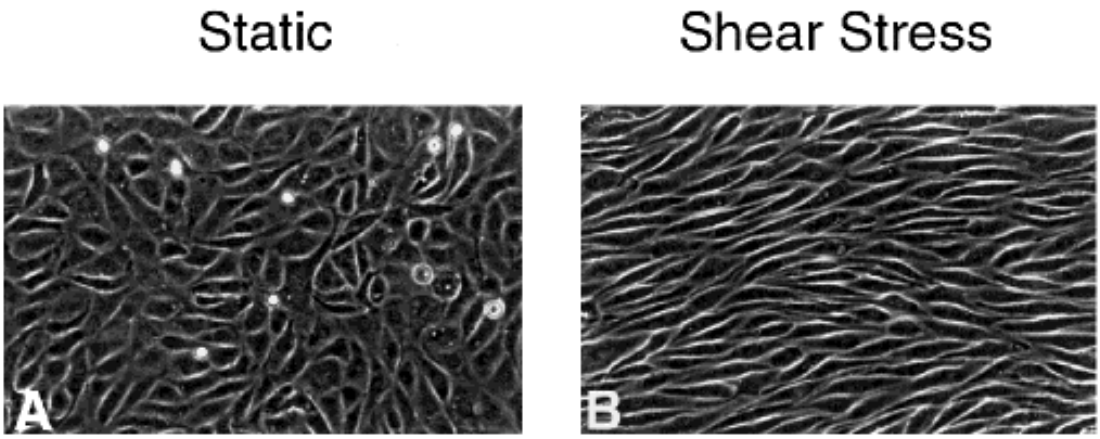

Figure 2.4: Phase-contrast monographs of confluent bovine aortic endothelial monolayers show a distinct difference between ECs under static flow conditions (A) and those exposed to physiological WSS for 24 hours (B). Reproduced and adapted with permission from the Journal of Cell Science.[145]

ECs or EPCs will not adhere directly to, or proliferate over, a normal stent surface and as such re-endothelialisation over the stent struts cannot occur without an adsorbed protein layer and adhesion molecules expressed by cells adhered to the surface.[48] Some stent designs endeavour to promote re-endothelialisation by applying coatings to the stent surface.[13,48,224] The surface texture of a stent also influences re-endothelialisation and thus some new stents are exploring different surface modifications which may aid re-endothelialisation.[17] In addition to this the surface chemical composition also affects re-endothelialisation, e.g. endothelial migration onto stainless steel via interaction with

adsorbed fibrinogen is significantly greater than that observed onto gold surfaces. This could be due to the surface charge, hydrophobicity, or chemical composition of the surface material.[235]

Local haemodynamics at a stent implantation site also have an effect on the initial and continued adherence of ECs and EPCs. Large WSS oscillations over positive and negative values, i.e. 1Hz reversing sinusoidal WSS of mean 2.0 Pa with an amplitude of 4.0 Pa, has been found to cause the detachment of cultured bovine aortic ECs,[94] which would delay re-endothelialisation. ECs have been shown to migrate downstream of an area where the WSSG is above 0.3 Pa/mm.[47,255] The migration of ECs into denuded areas from adjacent areas with an intact endothelium has been shown to be increased when exposed to undisturbed laminar flow as opposed to disturbed laminar flow or static flow.[106] Re-endothelialisation of the stent surface has also been found to be WSS dependent, with low WSS regions experiencing delayed re-endothelialisation and high WSS encouraging EC migration onto stent surfaces.[234] In addition to this, as the healing process progresses and the endothelium layer reforms, ECs can sense and are responsive to WSS conditions. In physiological flow conditions ECs align themselves in the flow direction and are in an atheroprotective state, releasing anticoagulants, antioxidants and vasodilators such as NO. When ECs are in regions of low WSS or high WSSG they switch to an atherogenic state in which they adopt a cobblestone shape in a more random arrangement, shown in Figure 2.4, no longer aligned with the flow and presenting gaps in the endothelial layer, thus encouraging cellular and lipid infiltration.[195,211–213] In this form they also up-regulate inflammatory mediators, adhesion molecules, pro-coagulant and pro-thrombotic agents, and VSMC growth factors, all of which can lead to increased NIH and result in ISR.[144]

2.3 Hypoxia

Oxygen is critical for the maintenance of arterial wall physiology and is supplied to the cells within the arterial wall from both the luminal blood and blood passing through vasa vasorum in the adventitia. The vasa vasorum generally supplies the outer two thirds of the arterial wall, with the inner third supplied by diffusion from the lumen.[95] Oxygen is transported in blood as free oxygen dissolved in plasma and oxygen reversibly-bound to haemoglobin within the RBCs. In the arterial wall oxygen can diffuse up to a maximum of 300μm, and as the thickness of the arterial wall increases due to the formation of atherosclerotic plaque more of the arterial wall is in danger of becoming hypoxic. Hypoxia can contribute in the formation of foam cells from macrophages in atherosclerotic lesions and also causes an increase in the secretion of interleukins.[20,215] Therefore, hypoxia can influence the severity of inflammation in atherosclerotic lesions. Hypoxia has been associated with increased adventitial vasa vasorum[34] and IH in animal studies.[216,218] When VSMCs become hypoxic they express growth factors, such as VEGF and PDGF, that play a critical role in both neovascularisation and IH.[34] VEGF encourages the proliferation of vasa vasorum into the medial layer.[216,262] Although this proliferation of the vasa vasorum may be an adaptive mechanism to counteract hypoxia, it can also promote plaque rupture.[156] When the endothelium is exposed to hypoxic levels of oxygen concentration in the short term it expresses vaso-constricting effectors which results in reversible augmentation of the local blood flow.[58] However, when exposed to chronic hypoxic levels of oxygen concentration growth factors are expressed that result in VSMC proliferation and remodelling of the arterial wall, which have more lasting effects on the artery and local blood flow. Additionally, the growth factor expression can induce EC apoptosis which can increase LDL transport through leaky junctions.[252]

In terms of the augmentation of the haemodynamic environment, stenting produces a predominantly beneficial effect, i.e., restoration of required blood flow to downstream vasculature; however, locally within the stented region, the haemodynamics impact the natural healing processes within the arterial wall. This local augmentation of the haemodynamic environment due to the presence of a stent in turn affects the oxygen flux into the arterial wall which can result in hypoxia in some regions. Conversely, as mentioned earlier, Lee et al. (2001) found that rabbits treated with supplemental oxygen following graft-to-artery anastomosis had reduced NIH.[135] Although, it should be noted that the routine use of high-flow oxygen in uncomplicated MI has been found to result in greater infarct size and possibly increase the risk of mortality and high oxygen partial pressures within blood have been found to act as a vasoconstrictor.[197,269] Therefore, although there may not be any benefit in treatment with supplemental oxygen, the oxygen mass-transfer from the blood into the arterial wall has a crucial role to play in the control of NIH in arteries post stent implantation.

2.4 Influence of Stent Design on ISR

There are many different stents available on the market with varying strut configurations, thicknesses, materials, and deployment mechanisms, and in the case of DESs different coatings, drug types, doses and drug release kinetics. These varying designs produce different degrees of structural injury, foreign-body reactions and haemodynamic flow field alterations, which in turn affect the biological processes taking place within the stented artery and the resultant ISR rates. A study by Kastrati et al. (2001) of 3,370 patients (4,229 stented lesions) who underwent angioplasty with stenting using different BMS types concluded that following vessel size, stent design was the second strongest factor in determining the occurrence of ISR.[118]

The structural injury caused by stent implantation to the arterial wall is assumed to be proportional to the stress induced within the wall, which is dependent, in part, upon the stent design. Self-expanding stents have been found to cause less injury to the endothelium than balloon-expandable stents, because only the stent struts, in contrast with both the struts and an expanded balloon, are in contact with the arterial wall.[90] The injury caused by the balloon depends on the inflation pressure, stent geometry and distance between struts.[209] Stent foreshortening upon expansion, elastic recoil,[55] and deformations of the stent under flexion,[267] have been studied using FEA and are hypothesised to affect the degree of injury inflicted upon the arterial wall. High stresses within the arterial wall can cause increased damage, and in cases of medial injury or lipid core penetration by stent struts there is a propensity for increased inflammation.[59] By reducing the number of strut-strut intersections by one third, disruption of the IEL and the media layer were reduced by nearly one half in a study of steel stents deployed in denuded rabbit iliac arteries.[207] Several clinical studies have linked the degree of arterial wall prolapse between stent struts with the occurrence of ISR.[101,110,199] The amount of prolapse between stent struts is also dependent on the strut spacing. Following implantation, a stent must also be able to withstand additional stresses placed upon it from vessel deformation. In the case of coronary arteries the beating of the heart causes slight movements and deformations of the arteries.[49–51] Also, in peripheral arteries, such as the femoral, popliteal and tibial arteries, deformation is caused by the flexion of the hip, knee or ankle, which in some cases can cause fracture of an implanted stent possibly resulting in renewed injury to the arterial wall and ISR.[219] Therefore, not only does the stent design have an effect on the structural injury inflicted on the arterial wall initially, but the properties of the stent material and its ability to

withstand cyclic loading of the heart beating or a limb moving can also affect the probability of ISR occurring during the lifetime of a stent.

The stent material also has implications for each biological process in the response to a foreign body. Stainless steel, used in most BMSs, is found to oxidise in the body causing varying degrees of cell toxicity.[270] First-generation DES permanent polymer coatings were found to cause delayed healing, impaired stent-strut endothelialisation, and hypersensitivity reactions, which can culminate in stent thrombosis in some cases.[70,75,113,114,182,265] In a study of different DESs implanted in rabbits by Joner et al. it was found that struts lacking endothelial coverage at 14 days showed focal aggregates of platelets and inflammatory cells, including foreign body giant cells.[114] Therefore, in the absence of complete endothelialisation of polymeric strut surfaces increased inflammation and thrombus formation may result. New DES coatings such as phosphorycholine and the co-polymer poly(vinylidene fluoride-co-hexafluoropropylene) mimic the phospholipids on the outer surfaces of RBCs.[151] This improves the biocompatibility of the DES by masking its foreign nature. As a result of the observed detrimental effects of permanent polymers implanted in the body, biodegradable polymer coatings and completely polymer free stents are also being developed.[71]

The resultant local haemodynamics created within the stented lumen are also partially dependent on the stent design. Thrombus formation, as mentioned previously, is heavily flow dependent with highest platelet deposition occurring where flow is directed towards the arterial wall.[56] Monocyte adhesion rates were found to be affected by not only the local WSS, but also the radial component of velocity and the dynamics of the recirculation region and flow reattachment.[201] Flow separation away from the arterial wall and recirculation zones occur both upstream and downstream of rectangular cross-

sectional stent struts. Platelets within these zones experience long particle residence times in proximity to activating substances, which increases their probability of activation. With thinner and more streamlined stent struts, the recirculation zones, and also consequently, the particle residence times can be reduced.[111] WSS, WSSG and WSSAG within an idealised stented artery can be predicted using CFD and different stent designs have been shown to produce significantly different distributions of each.[132,133,173] The angle that stent struts make with the primary direction of blood flow has been shown to strongly influence the amount of intrastrut area of the luminal wall exposed to low WSS.[133] Stents with a greater final diameter than the implanted artery not only cause increased damage within the arterial wall, but also increase the cross-sectional area of the stented artery, reducing the blood flow velocity and as a result reduce the WSS within that region. Alternatively, stent undersizing can result in stent strut malapposition to the arterial wall, thus increasing the resistance to flow and decreasing the WSS.[35]

2.5 Summary

The biological processes: thrombus formation, inflammation, NIH, and re-endothelialisation, that can result in ISR are instigated, and significantly affected by, the damage caused by stent implantation, the presence of a foreign body and the local abnormal haemodynamics created within a stented artery, as summarised in Figure 2.5. The haemodynamics can in turn impact the oxygen transport from the luminal blood into the arterial wall. Analysis of the haemodynamics and the oxygen transport within a stented artery is warranted to elucidate beneficial stent design characteristics that may improve the conditions within a stented artery post-implantation. The next chapter will present the fundamental fluid mechanics and oxygen transport theory relevant to the project.

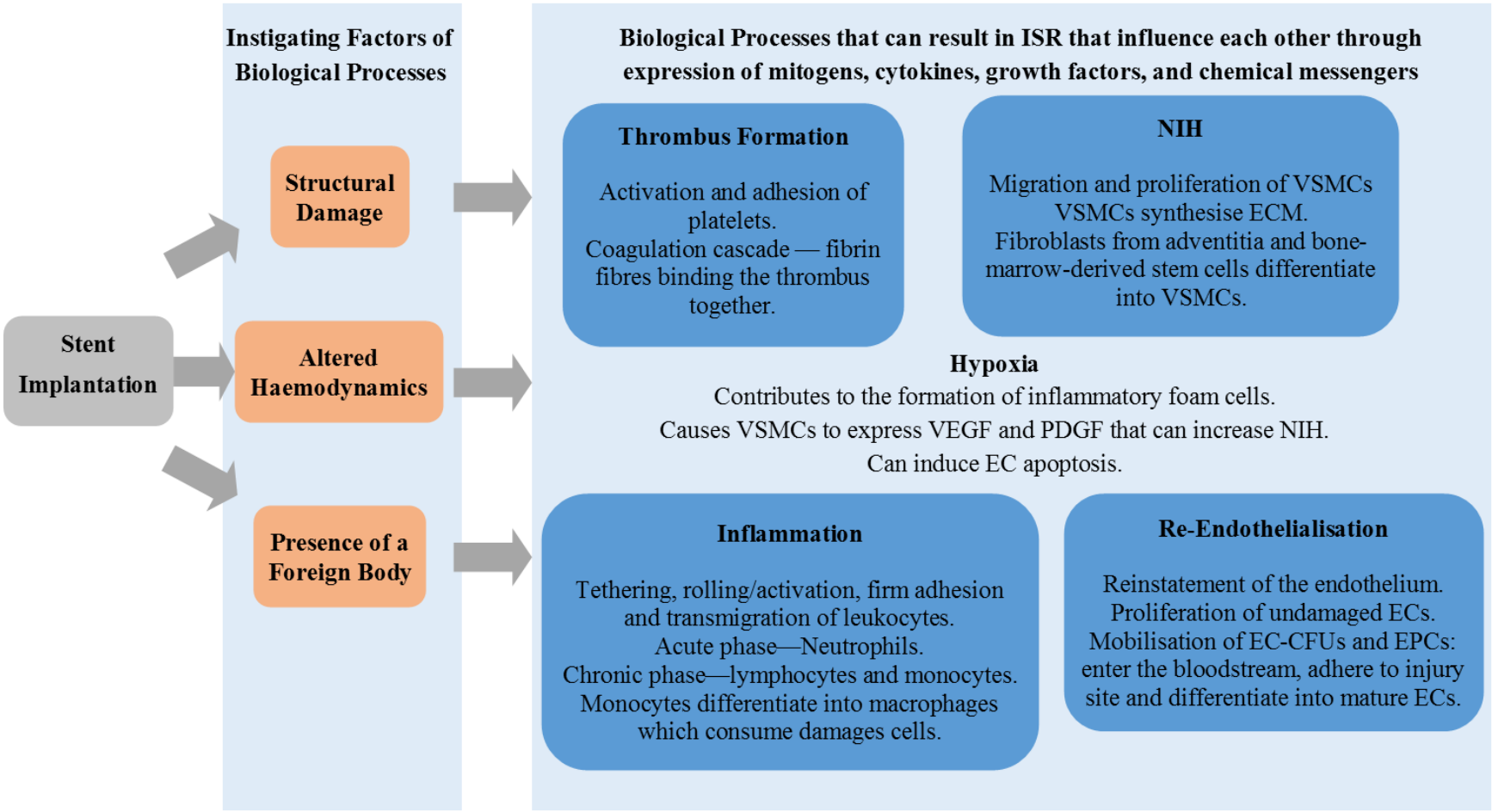

Figure 2.5: Summary of biological processes instigated by stent implantation that can result in ISR.

CHAPTER 3

Fundamental Theory

3.1 Introduction

To study the flow of blood through, and the oxygen transport within, an artery using CFD, it is important to first understand the fundamental theory applicable to both and also how they are modelled in the CFD software. In this chapter the theory will be given which includes the derivation of the fluid stress tensor, the haemodynamic variables of interest to this study, the oxygen transport theory, and the oxygen transport variable of interest. Also the CFD governing equations, discretisation technique, and how the equations are employed in the software are presented.

3.2 Fluid Mechanics Theory

The fluid stress tensor, as described below, is used in the calculation of WSS and WSSG (Section 3.3), and the shear-rate dependent dispersion coefficient (Section 3.4.1). To derive the fluid stress tensor consider a fluid element in a Cartesian coordinate system with side lengths of dx, dy and dz in the x, y, and z direction respectively, and analyse all the forces acting upon it, as shown in Figure 3.1. The forces that act on a fluid element can be classified as body forces and surface forces. Body forces include the forces experienced by the fluid element due to gravity, electromagnetic and nuclear interactions. The surface forces which the fluid element will be subjected to are forces normal and tangential to its surfaces that could result in deformation of the fluid element. Looking at a fluid element in isolation within a flow,

it is understood to possibly undergo four types of deformation: translation, rotation, linear strain and shear strain. Considering that a fluid element may be in constant motion within a flow, and for the purpose of the derivation of the momentum equations, these deformations are studied in terms of rates and a Cartesian coordinate system is used as shown in Figure 3.1.

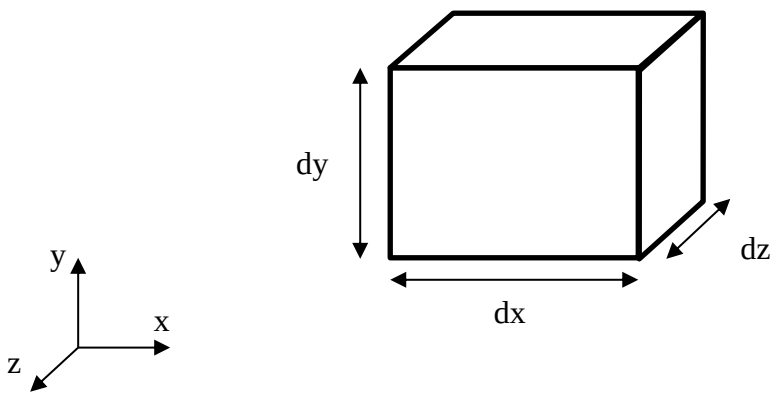

Figure 3.1: Fluid element in a Cartesian coordinate system with side lengths of dx, dy and dz, in the x, y, and z direction respectively, used for analysis of deformations and derivation of momentum equation.

3.2.1 Rate of Translation

Translation is the distance a fluid element has moved through in a certain period of time. The rate of translation is the velocity of a fluid element which is represented by the velocity vector in Cartesian coordinates:

$$\mathbf{V} = u\mathbf{i} + v\mathbf{j} + w\mathbf{k} \tag{3.1}$$

where u, v and w are the velocity magnitudes in the x, y and z directions respectively, with **i**, **j** and **k** defined as the Cartesian unit vectors in these directions also. To calculate the translation distance after an infinitesimally small increment of time dt, the velocity magnitudes are multiplied by dt, i.e. udt, vdt and wdt.

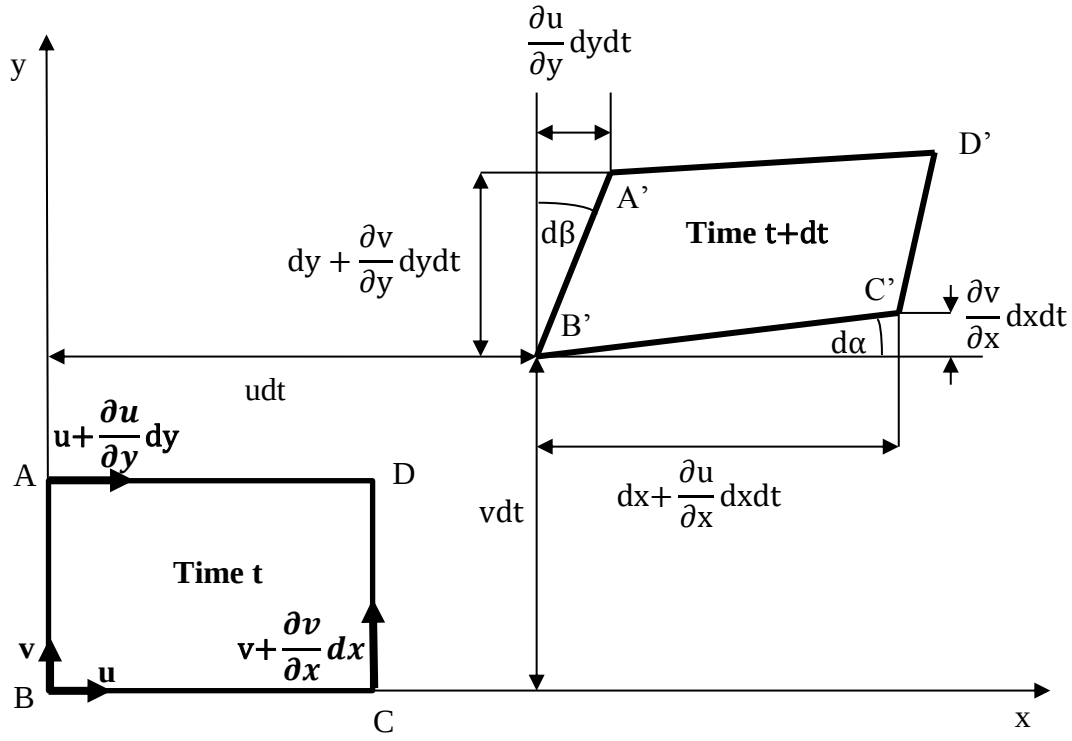

Figure 3.2: The relevant velocities and distances for derivation of the deformations imposed on a two-dimensional (2D) face of a fluid element during time increment dt. The 2D face is shown at time t as ABCD, and time t+dt as A'B'C'D'.

3.2.2 Rate of Rotation

The rate of rotation at a point, also known as the angular velocity, is the average rotation rate of two initially perpendicular lines which meet at that point. For simplicity, here the rate of rotation is derived for a 2D face on the x-y plane of a fluid element in motion from time t to t+dt, as shown in Figure 3.2. For the purpose of this derivation the point B at time t is considered along with the two initially perpendicular lines labelled as AB and BC. The velocity magnitudes in the x and y directions are also shown at point B. Because the velocities vary with position, the velocities at points A and C are slightly different and for clarity only the relevant velocity at both points are shown as first order Taylor series: $u+\frac{\partial u}{\partial y}dy$ at point A and $v+\frac{\partial v}{\partial x}dx$ at point C. At time t+dt the points have

all moved through certain distances as prescribed by these velocities with the assumption that the accelerations do not vary over such small distances within the flow. The four points at time $t+dt$ are labelled as A', B', C' and D'. Lines A'B' and B'C' have rotated through angles $d\beta$ in a clockwise direction and $d\alpha$ in a counter-clockwise direction, respectively, about the z-axis. The average rotation about the z-axis at point B is:

$$d\theta_z = \frac{1}{2}(d\alpha - d\beta) \tag{3.2}$$

where $d\beta$, clockwise, is defined as negative. To derive the rate of rotation the angles are divided by the time increment:

$$\frac{d\theta_z}{dt} = \frac{1}{2}\left(\frac{d\alpha}{dt} - \frac{d\beta}{dt}\right) \tag{3.3}$$

The angles can be calculated based on the inverse tan of the opposite and adjacent sides, as shown in Figure 3.2. For the purpose of this derivation, the angles can be related to the velocity derivatives through the limits of the angles as $dt \to 0$ given as follows:

$$d\alpha = \lim_{dt\to 0}\left(\tan^{-1}\frac{\left(\partial v/\partial x\right)dxdt}{dx + \left(\partial u/\partial x\right)dxdt}\right) = \frac{\partial u}{\partial x}dt \tag{3.4}$$

$$d\beta = \lim_{dt\to 0}\left(\tan^{-1}\frac{\left(\partial u/\partial y\right)dydt}{dy + \left(\partial v/\partial y\right)dydt}\right) = \frac{\partial u}{\partial y}dt \tag{3.5}$$

Substituting Equations (3.4) and (3.5) into Equation (3.3), and cancelling dt on the right-hand-side results in a formula for the rate of rotation about the z axis at point B:

$$\frac{d\theta_z}{dt} = \frac{1}{2}\left(\frac{\partial v}{\partial x} - \frac{\partial u}{\partial y}\right) \tag{3.6}$$

The rate of rotation around the x and y axis can also be derived in a similar fashion and are:

$$\frac{d\theta_x}{dt} = \frac{1}{2}\left(\frac{\partial w}{\partial y} - \frac{\partial v}{\partial z}\right) \tag{3.7}$$

$$\frac{d\theta_y}{dt} = \frac{1}{2}\left(\frac{\partial u}{\partial z} - \frac{\partial w}{\partial y}\right) \tag{3.8}$$

These angular velocities are conventionally written as ω_x, ω_y and ω_z and collectively define the rate of rotation vector in the Cartesian coordinate system as:

$$\boldsymbol{\omega} = \omega_x \mathbf{i} + \omega_y \mathbf{j} + \omega_z \mathbf{k} \tag{3.9}$$

$$\boldsymbol{\omega} = \frac{1}{2}\left(\frac{\partial w}{\partial y} - \frac{\partial v}{\partial z}\right)\mathbf{i} + \frac{1}{2}\left(\frac{\partial u}{\partial z} - \frac{\partial w}{\partial y}\right)\mathbf{j} + \frac{1}{2}\left(\frac{\partial v}{\partial x} - \frac{\partial u}{\partial y}\right)\mathbf{k} \tag{3.10}$$

By defining a new vector ζ, the vorticity of the fluid, the halves can be cancelled:

$$\zeta = 2\boldsymbol{\omega} = \left(\frac{\partial w}{\partial y} - \frac{\partial v}{\partial z}\right)\mathbf{i} + \left(\frac{\partial u}{\partial z} - \frac{\partial w}{\partial y}\right)\mathbf{j} + \left(\frac{\partial v}{\partial x} - \frac{\partial u}{\partial y}\right)\mathbf{k} \tag{3.11}$$

Here, the three components of the vorticity vector are recognised as the curl of the velocity vector **V**, and hence:

$$\zeta = \nabla \times \mathbf{V} \tag{3.12}$$

where ∇ is the gradient operator defined as:

$$\nabla = \frac{\partial}{\partial x}\mathbf{i} + \frac{\partial}{\partial y}\mathbf{j} + \frac{\partial}{\partial z}\mathbf{k} \tag{3.13}$$

With this two types of flow can be defined:

- Rotational flow where $\vec{\zeta} = \vec{\nabla} \times \vec{V} \neq 0$ at every point, and the fluid elements move, deform and rotate.
- Irrotational flow where $\vec{\zeta} = \vec{\nabla} \times \vec{V} = 0$ at every point, and the fluid elements move, and deform, but do not rotate.

3.2.3 Linear Strain Rate

Linear strain is defined as the change in length divided by the original length, and the linear strain rate is the rate of change of the linear strain and can be defined for each Cartesian direction. Referring to the line labelled BC and the deformed line at time t+dt B'C' in Figure 3.2, the x component of the rate of linear strain is defined as follows:

$$\varepsilon_{xx} = \frac{d}{dt}\left(\frac{\left(dx + \frac{\partial u}{\partial x}dxdt\right) - dx}{dx}\right) = \frac{\partial u}{\partial x} \tag{3.14}$$

Conventionally, ε_{ij} corresponds to the strain in the i direction and acting on the surface which has its surface normal vector in the j direction. For example, the notation in this case, ε_{xx} corresponds to the linear strain rate in the x direction which is exerted on a surface which is perpendicular to the direction of the strain. The corresponding rate of linear strain in the z and y direction can also be defined accordingly as:

$$\varepsilon_{yy} = \frac{\partial v}{\partial y} \tag{3.15}$$

$$\varepsilon_{zz} = \frac{\partial w}{\partial z} \tag{3.16}$$

3.2.4 Shear Strain Rate

The shear strain rate in 2D is defined as the average rate of decrease in the angle between two lines, here taken as AB and BC for the face of the fluid element parallel to the xy plane in Figure 3.2, which are initially perpendicular at time t. The average shear strain rate is defined as:

$$\varepsilon_{xy} = \frac{1}{2}\left(\frac{d\alpha}{dt} + \frac{d\beta}{dt}\right) = \frac{1}{2}\left(\frac{\partial v}{\partial x} + \frac{\partial u}{\partial y}\right) \tag{3.17}$$

Likewise, the shear strain rate can be defined for the faces parallel to the yz and zx faces also:

$$\varepsilon_{yz} = \frac{1}{2}\left(\frac{\partial w}{\partial y} + \frac{\partial v}{\partial z}\right) \tag{3.18}$$

$$\varepsilon_{zx} = \frac{1}{2}\left(\frac{\partial u}{\partial z} + \frac{\partial w}{\partial x}\right) \tag{3.19}$$

The shear strain rate is symmetric and hence:

$$\varepsilon_{yx} = \varepsilon_{xy}, \varepsilon_{zy} = \varepsilon_{yz}, \varepsilon_{xz} = \varepsilon_{zx} \tag{3.20}$$

3.2.5 Strain Rate Tensor

The linear strain rate and shear strain rate of the fluid element can be combined into one symmetric second-order tensor:

$$\varepsilon_{ij} = \begin{pmatrix} \varepsilon_{xx} & \varepsilon_{xy} & \varepsilon_{xz} \\ \varepsilon_{yx} & \varepsilon_{yy} & \varepsilon_{yz} \\ \varepsilon_{zx} & \varepsilon_{zy} & \varepsilon_{zz} \end{pmatrix} = \begin{pmatrix} \frac{\partial u}{\partial x} & \frac{1}{2}\left(\frac{\partial v}{\partial x} + \frac{\partial u}{\partial y}\right) & \frac{1}{2}\left(\frac{\partial u}{\partial z} + \frac{\partial w}{\partial x}\right) \\ \frac{1}{2}\left(\frac{\partial v}{\partial x} + \frac{\partial u}{\partial y}\right) & \frac{\partial v}{\partial y} & \frac{1}{2}\left(\frac{\partial w}{\partial y} + \frac{\partial v}{\partial z}\right) \\ \frac{1}{2}\left(\frac{\partial u}{\partial z} + \frac{\partial w}{\partial x}\right) & \frac{1}{2}\left(\frac{\partial w}{\partial y} + \frac{\partial v}{\partial z}\right) & \frac{\partial w}{\partial z} \end{pmatrix} \tag{3.21}$$

A fundamental property of symmetric tensors is that there is at least one coordinate system for which the off-diagonal components of the tensor are reduced to zero. For convenience, the coordinate system here is assumed to be coincident with the principle axes of the strain tensor. Therefore, the principle diagonal terms remain and the off diagonal terms, where $i \neq j$, reduce to zero. Hence the strain rate tensor reduces to:

$$\varepsilon_{ij} = \begin{pmatrix} \varepsilon_1 & 0 & 0 \\ 0 & \varepsilon_2 & 0 \\ 0 & 0 & \varepsilon_3 \end{pmatrix} \tag{3.22}$$

where ε_1, ε_2 and ε_3 are referred to as the principle strain rates.

3.2.6 Fluid Stress Tensor

For an infinitesimally small cubic fluid element fixed within a fluid domain, as shown in Figure 3.3, the total forces acting on it are composed of body and surface forces. Body forces consist of the forces experienced by the fluid element due to gravity, electromagnetic and nuclear interactions.

In the case of surface forces, these comprise of forces due to pressure within the fluid that act normal to the surfaces, and the viscous forces that act tangentially and perpendicularly to the surfaces. For the purpose of this derivation the surfaces of the fluid element are assumed to be parallel with the Cartesian coordinate planes. A second order stress tensor is defined as:

$$\sigma_{ij} = \begin{pmatrix} \sigma_{xx} & \sigma_{xy} & \sigma_{xz} \\ \sigma_{yx} & \sigma_{yy} & \sigma_{yz} \\ \sigma_{zx} & \sigma_{zy} & \sigma_{zz} \end{pmatrix} \tag{3.23}$$

where σ_{ij} correspond to the stress exerted in the i direction and acting on the surface which has its surface normal vector in the j direction. Therefore, the diagonal terms where i=j represent stresses exerted in the same direction as the surface normal vector and when $i \neq j$ the stresses are acting tangentially to the surface, as shown in Figure 3.3. When the fluid is stationary the only stresses acting on the surfaces of the fluid element is the hydrostatic pressure and hence, the stress tensor reduces to:

$$\sigma_{ij} = \begin{pmatrix} \sigma_{xx} & \sigma_{xy} & \sigma_{xz} \\ \sigma_{yx} & \sigma_{yy} & \sigma_{yz} \\ \sigma_{zx} & \sigma_{zy} & \sigma_{zz} \end{pmatrix} = \begin{pmatrix} -P & 0 & 0 \\ 0 & -P & 0 \\ 0 & 0 & -P \end{pmatrix} \tag{3.24}$$

where P is the pressure which acts normal to the surface and inwardly, hence the negative sign.

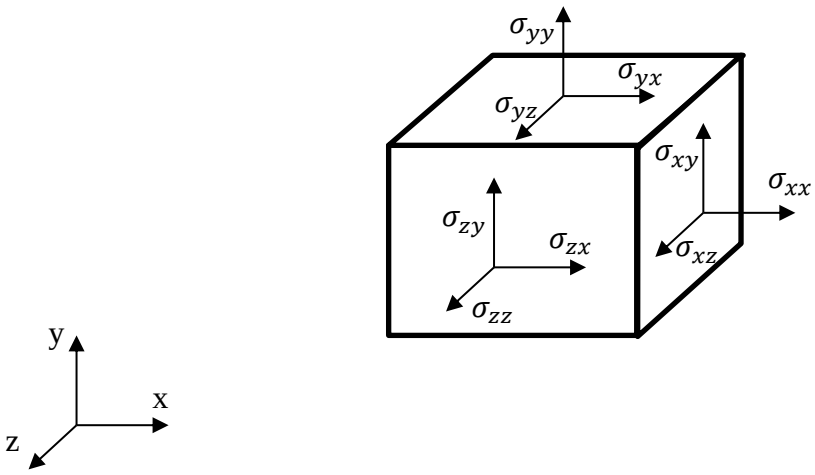

Figure 3.3: The nine positive stresses exerted on a fluid element. An additional nine negative stresses would also act on the other three surfaces of the fluid element.

When the fluid is in motion the total stresses acting on the fluid element are comprised of the hydrostatic pressure stresses, as above, and also the viscous stresses. This is represented by the viscous stress tensor, τ_{ij}, which combined with the hydrostatic pressure stresses gives the total stress on the fluid element as:

$$\sigma_{ij} = \begin{pmatrix} \sigma_{xx} & \sigma_{xy} & \sigma_{xz} \\ \sigma_{yx} & \sigma_{yy} & \sigma_{yz} \\ \sigma_{zx} & \sigma_{zy} & \sigma_{zz} \end{pmatrix} = \begin{pmatrix} -P & 0 & 0 \\ 0 & -P & 0 \\ 0 & 0 & -P \end{pmatrix} + \begin{pmatrix} \tau_{xx} & \tau_{xy} & \tau_{xz} \\ \tau_{yx} & \tau_{yy} & \tau_{yz} \\ \tau_{zx} & \tau_{zy} & \tau_{zz} \end{pmatrix} \tag{3.25}$$

To complete the derivation of the stress tensor it is necessary to relate the viscous stress tensor to the previously derived strain rate tensor. To this end, the fluid is assumed to be incompressible and Newtonian, i.e. the viscous stress tensor is linearly proportional to the strain rate tensor, and isotropic. As a consequence of these assumptions the divergence of the velocity, $\nabla.\mathbf{V}$, is zero and the dynamic viscosity, μ, is constant and therefore, the two tensors are related by:

$$\tau_{ij} = 2\mu\varepsilon_{ij} \tag{3.26}$$

This results in a new equation for the stress tensor:

$$\sigma_{ij} = \begin{pmatrix} -P & 0 & 0 \\ 0 & -P & 0 \\ 0 & 0 & -P \end{pmatrix} + \begin{pmatrix} 2\mu\frac{\partial u}{\partial x} & \mu\left(\frac{\partial v}{\partial x}+\frac{\partial u}{\partial y}\right) & \mu\left(\frac{\partial u}{\partial z}+\frac{\partial w}{\partial x}\right) \\ \mu\left(\frac{\partial v}{\partial x}+\frac{\partial u}{\partial y}\right) & 2\mu\frac{\partial v}{\partial y} & \mu\left(\frac{\partial w}{\partial y}+\frac{\partial v}{\partial z}\right) \\ \mu\left(\frac{\partial u}{\partial z}+\frac{\partial w}{\partial x}\right) & \mu\left(\frac{\partial w}{\partial y}+\frac{\partial v}{\partial z}\right) & 2\mu\frac{\partial w}{\partial z} \end{pmatrix} \tag{3.27}$$

Crucially, this equation allows the viscous stresses to be calculated from the velocity gradients and is directly applicable here to the oxygen transport model used, as discussed in Section 3.4.1, and also the post-processing of the results in the form of the WSS and WSSG, as discussed in Section 3.3.

3.2.7 Shear Rate

The strain rate tensor, as defined in Equation (3.21), has three invariants, one of which is referred to here as the shear rate and is defined by:

$$\dot{\gamma} = \sqrt{2\varepsilon_{ij} : \varepsilon_{ij}} \tag{3.28}$$

where $\dot{\gamma}$ is the local shear rate and ε_{ij} is the strain rate tensor. To find the magnitude of $\dot{\gamma}$ Equation (3.28) is expanded upon, whereby the double product of the strain rate tensor results in:

$$\dot{\gamma} = \left[2\left(\frac{\partial u}{\partial x}\right)^2 + 2\left(\frac{\partial v}{\partial y}\right)^2 + 2\left(\frac{\partial w}{\partial z}\right)^2 + \left(\frac{\partial u}{\partial z}+\frac{\partial w}{\partial x}\right)^2 + \left(\frac{\partial v}{\partial x}+\frac{\partial u}{\partial y}\right)^2 + \left(\frac{\partial w}{\partial y}+\frac{\partial v}{\partial z}\right)^2 \right]^{\frac{1}{2}} \tag{3.29}$$

This is used in both the calculation of the non-Newtonian viscosity of blood using the Bird-Carreau model, as shown below, and the shear-induced dispersion coefficient, as described below in Section 3.4.1.

3.2.8 Bird-Carreau Model

Human blood is a non-Newtonian fluid, in that its viscosity varies non-linearly proportionally to the shear rate being exerted on it. Blood is a shear-thinning fluid where the viscosity increases significantly with decreasing shear rate below a shear rate of $100s^{-1}$.[1,22,66] This effect is modelled using the Bird-Carreau model as described by:

$$\mu = \mu_\infty + (\mu_0 - \mu_\infty)\left[1+\left(\dot{\gamma}\lambda_t\right)^2\right]^{((q-1)/2)} \tag{3.30}$$

where: μ_0 is the low shear dynamic viscosity

μ_∞ is the high shear dynamic viscosity

λ_t is the time constant

n is the power law index

3.3 Haemodynamic Variables of Interest

As discussed in Chapter 2 there are certain key haemodynamic variables which are applicable to the assessment of stented arteries. The biological processes that are instigated by stent implantation, namely thrombosis, inflammation, NIH and re-endothelialisation, are affected by the haemodynamics which take place at the luminal surface of the artery. In the work presented here the predicted WSS and WSSG distributions are analysed. The WSS vector is a measure of the viscous stresses imparted by the flowing blood on the luminal surface and is defined by:

$$\mathrm{WSS} = \mathbf{n}_i \cdot \tau_{ij} \tag{3.31}$$

This can be written as:

$$\begin{aligned}\mathbf{n}_i \cdot \tau_{ij} = \mathbf{i}(n_1\tau_{xx} + n_2\tau_{yx} + n_3\tau_{zx}) + \mathbf{j}(n_1\tau_{xy} + n_2\tau_{yy} + n_3\tau_{zy}) + \\ \mathbf{k}(n_1\tau_{xz} + n_2\tau_{yz} + n_3\tau_{zz})\end{aligned} \tag{3.32}$$

where the normal vector, $\mathbf{n_i}$, is:

$$\mathbf{n}_i \cdot \tau_{ij} = n_1\mathbf{i} + n_2\mathbf{j} + n_3\mathbf{k} \tag{3.33}$$

For the purposes of CFD where the wall cell face normal vector may not be aligned with the Cartesian coordinate frame the normal vector is written as:

$$\mathbf{n}_i \cdot \tau_{ij} = \overline{a_x}\mathbf{i} + \overline{a_y}\mathbf{j} + \overline{a_z}\mathbf{k} \tag{3.34}$$

where

$$\overline{a_x} = \frac{a_x}{\sqrt{\left(a_x^2 + a_y^2 + a_z^2\right)}}, \overline{a_y} = \frac{a_y}{\sqrt{\left(a_x^2 + a_y^2 + a_z^2\right)}}, \overline{a_z} = \frac{a_z}{\sqrt{\left(a_x^2 + a_y^2 + a_z^2\right)}} \tag{3.35}$$

and a_x, a_y, and a_z are the components of the wall cell face area in the x, y, and z directions respectively.

The spatial gradient of the WSS vector with respect to the Cartesian coordinate frame describes the rate of change of each of the three WSS components in the three Cartesian directions. In reference to the study here, the rate of change of the WSS parallel and perpendicular to the local WSS vector is important for analysing the stent geometries, as mentioned in Chapter 2. Therefore, the WSSG variable adopted in this study is the magnitude of the rate of change of the WSS parallel (m-direction) and perpendicular (n-direction) to the local WSS vector, as given by:

$$|\mathrm{WSSG}| = \sqrt{\left(\frac{\partial \tau_{wm}}{\partial m}\right)^2 + \left(\frac{\partial \tau_{wn}}{\partial n}\right)^2} \tag{3.36}$$

where: τ_{wm} is the WSS in the m direction, i.e. parallel to the local WSS vector

τ_{wn} is the WSS in the n direction, i.e. perpendicular to the local WSS vector

Finally, for the purpose of quantifying the strength and extent of the helical flow within the geometries studied in Test Case 4 the helicity of the blood flow is needed. The kinetic helicity density is defined as:

$$H_k = (\nabla \times V) \cdot V \tag{3.37}$$

As described by Morbiducci et al., this variable can be normalised with respect to the vorticity and velocity magnitudes resulting in the local normalised helicity (LNH):[165]

$$LNH = \frac{(\nabla \times V) \cdot V}{|(\nabla \times V)||V|} = \cos\theta \tag{3.38}$$

where θ is the angle between the velocity and vorticity vectors. The LNH is a measure of the alignment/misalignment of the local velocity and vorticity vectors and has a range of $-1 \leq LNH \leq 1$ where positive values are present in left-hand rotating flows and negative values are present in right-hand rotating flows, when viewed in the direction of the forward motion.[38]

3.4 Oxygen Transport Theory

Blood consists of liquid plasma in which three types of cellular elements are suspended: RBCs, white blood cells and platelets. RBCs constitute about 45%, by volume, of whole blood and are the main carriers of oxygen. The coronary arteries act as a conduit for the blood to deliver oxygen and nutrients to the heart muscle downstream. Oxygen is critical for the maintenance of arterial wall physiology and is supplied to the cells within the arterial wall from both the luminal blood and blood passing through vasa vasorum in the adventitia.

3.4.1 Blood Oxygen Transport

Oxygen is transported in blood as free oxygen dissolved in plasma and oxygen reversibly-bound to haemoglobin within the RBCs. The concentration of free oxygen dissolved in plasma is quantified by the oxygen tension, i.e. the partial pressure of oxygen in plasma. The oxygen tension is related to the free oxygen concentration by Henry's law:

$$PO_2 = \frac{C}{\alpha} \tag{3.39}$$

where PO_2 is the oxygen tension, α is the solubility of oxygen in plasma, and C is the concentration of free oxygen in plasma. The amount of bound oxygen contained in the RBCs in the form of oxyhaemoglobin is proportional to the PO_2 within the surrounding plasma and can be approximated using the Hill equation (oxygen dissociation curve, as shown in Figure 3.4):

$$S = \frac{PO_2^n}{PO_2^n + PO_{2,50}^n} \tag{3.40}$$

where S is the ratio of oxyhaemoglobin to total haemoglobin in the RBCs (commonly expressed as a percentage), $PO_{2,50}$ is the PO_2 value at which the haemoglobin is 50% saturated and n is the Hill parameter.

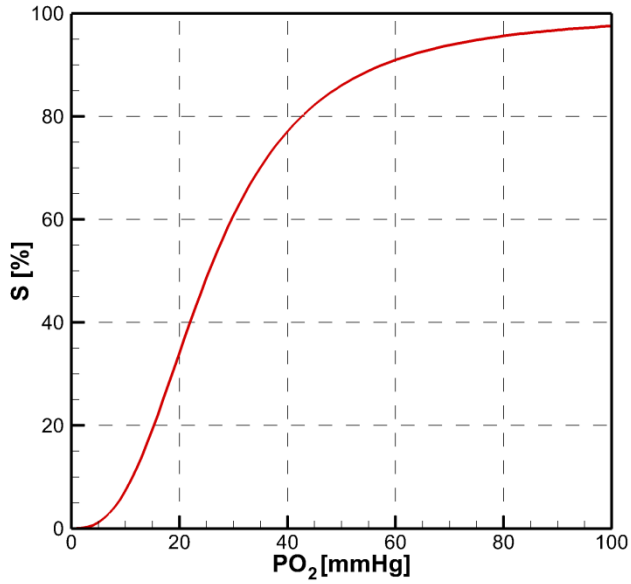

Figure 3.4: Oxygen dissociation curve for n=2.7.

For the purpose of modelling oxygen transport in blood, difficulty arises when the bound oxygen is included in the model because of the non-linear nature of the Hill equation. When included, the transportation of both free oxygen and bound oxygen in the blood can be modelled using two advection-diffusion equations given as Equations (3.41) and (3.42) respectively:

$$\alpha \frac{\mathcal{D}PO_2}{\mathcal{D}t} = \alpha \nabla . \left(D_b \nabla PO_2 \right) + r \tag{3.41}$$

$$[Hb] \frac{\mathcal{D}S}{\mathcal{D}t} = [Hb] \nabla . \left(D_c \nabla S \right) - r \tag{3.42}$$

where $\mathcal{D} / \mathcal{D}t$ is the substantial derivative, D_b is the diffusivity of free oxygen in the blood, r is the rate of release of oxygen from the haemoglobin, [Hb] is the total oxygen carrying capacity of haemoglobin in blood, and D_c is the diffusivity of oxyhaemoglobin

in blood. [Hb] is assumed to be constant, thus ignoring the plasma skimming layer which has little effect on the oxygen transport.[162] Oxyhaemoglobin is encapsulated in RBCs and therefore the D_c value is interpreted as the shear-augmented dispersion coefficient of RBCs in blood flow.

RBCs are present in the blood in high concentrations with approximately 5×10^9 RBCs per cubic millimetre of blood. Due to these high concentrations, there are continuous intercellular collisions and deformation of the RBCs. Through these collisions individual RBCs have been seen to disperse radially within the blood flow. This radial dispersion has been found to be proportional to the shear rate of the blood flow and also improves the diffusion of molecules contained within the blood. Crucially, in the case of oxygen transport, this radial dispersion of RBCs increases the effective diffusion of oxygen within the blood because of the oxygen contained within them in bound form. Because of the size of RBCs and the concentrations commonly found in vessels, quantifying the magnitude of radial dispersion has proved to be difficult. To combat the difficulty in the tracking of individual RBCs in blood flowing through a tube, some researchers have resorted to using ghost RBCs, i.e. RBCs which have had the internal contents, including the haemoglobin, removed through a process known as haemolysis. By using ghost RBCs this improves the signal-to-noise ratio of the detection equipment used, which allows tracer RBCs to be tracked more accurately. There is some debate as to the effects of haemolysis on the mechanical properties of the ghost RBCs membrane and, consequently, their dynamic properties when compared with RBCs.[28,80] Therefore, although the majority of the studies done on the dispersion coefficient of RBCs have been done using ghost cells, there is a degree of uncertainty in the calculated coefficients relative to normal RBCs.

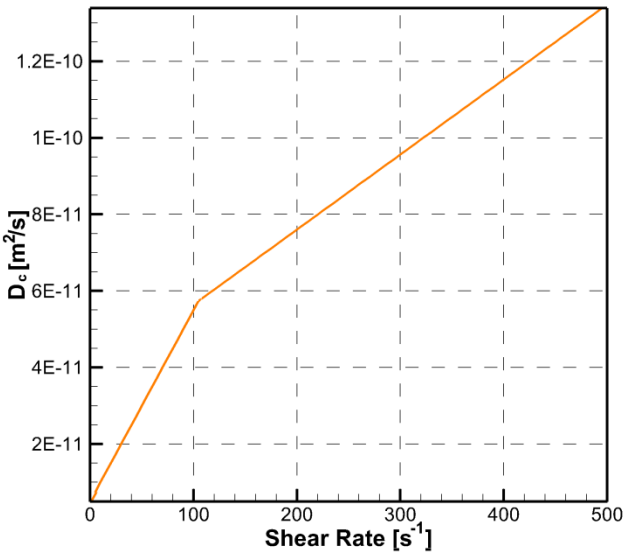

Figure 3.5: D_c as extrapolated from experimental studies for the shear rates ranging from 1 - 500s^{-1}.

In previous studies D_c is taken as 1.5×10^{-11}m^2/s,[162] which is the dispersion coefficient for red tracer cells in a straight glass tube at an approximate shear rate of 20s^{-1}.[28] Higher shear rates are encountered in carotid and coronary arteries and therefore, a variable dispersion coefficient is employed, for the first time, in this work. This was extrapolated from three separate studies by Goldsmith, Goldsmith and Marlow, and Cha and Beissinger, as described in Equations (3.43) & (3.44), with the resultant D_c plotted against the shear rate shown in Figure 3.5:[30,79,80]

$$\text{For } 0 \le \dot{\gamma} \le 100\text{s}^{-1}: \; D_c = 5.00\times10^{-12} + 5.00\times10^{-13}\dot{\gamma} \tag{3.43}$$

$$\text{For } \dot{\gamma} > 100\text{s}^{-1}: \; D_c = 3.68\times10^{-11} + 1.96\times10^{-13}\dot{\gamma} \tag{3.44}$$

where $\dot{\gamma}$ is the local shear rate, as described in Section 3.2. The two constants used in Equation (3.43) are deduced from RBC ghost cell experiments by Goldsmith, and Goldsmith and Marlow between average shear rates of 2-20s^{-1} at haematocrits of 39% and 40% respectively.[79,80] The two constants used in Equation (3.44) were deduced

from the shear-induced particle diffusivity calculated by Cha and Beissinger at shear rates between $200s^{-1}$ and $1000s^{-1}$ at a RBC ghost volume fraction of 0.45 corresponding to the average haematocrit for a human male.[30] It should be noted here that the model is therefore only applicable for haematocrits within this range because the local D_c value has been shown to vary with haematocrit.[139]

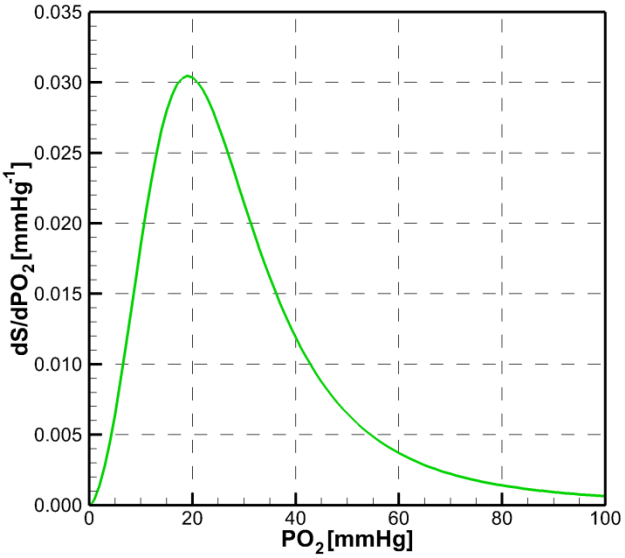

Figure 3.6: The gradient, dS/dPO_2, of the oxygen dissociation curve plotted against PO_2.

To reduce complexity when performing numerical simulations the two advection-diffusion equations given above can be added together to form a single equation, as described in Moore and Ethier:[162]

$$\left(1+\frac{[\mathrm{Hb}]}{\alpha}\frac{\mathrm{dS}}{\mathrm{dPO_2}}\right)\frac{\mathcal{D}\mathrm{PO_2}}{\mathcal{D}t}=\nabla.\left[\left(\mathrm{D_b}\left(1+\frac{[\mathrm{Hb}]}{\alpha}\frac{\mathrm{D_c}}{\mathrm{D_b}}\frac{\mathrm{dS}}{\mathrm{dPO_2}}\right)\right)\nabla\mathrm{PO_2}\right] \tag{3.45}$$

where the term dS/dPO_2, as shown in Figure 3.6, is the slope of the oxygen dissociation curve given by:

$$\frac{dS}{dPO_2} = \frac{1}{PO_{2,50}^n} \frac{nPO_2^{n-1}}{\left[1+\left(PO_2 \middle/ PO_{2,50}\right)^n\right]^2} \tag{3.46}$$

Given the shape of the oxygen dissociation curve, non-linearity enters the oxygen transport equation through this term. In order to implement Equation (3.45) in the commercially-available CFD software package used here it must be rearranged into the form:

$$\frac{\mathcal{D}PO_2}{\mathcal{D}t} = \nabla.\left[D'\nabla PO_2\right] + \{Source\} \tag{3.47}$$

where the diffusivity coefficient D' and the source term {Source} are given in Equations (3.48) and (3.49) respectively:

$$D' = \left(D_b \left(1 + \frac{[Hb]}{\alpha} \frac{D_c}{D_b} \frac{dS}{dPO_2} \right) \middle/ \left(1 + \frac{[Hb]}{\alpha} \frac{dS}{dPO_2} \right) \right) \tag{3.48}$$

$$Source = \left[D_b \left(1 + \frac{[Hb]}{\alpha} \frac{D_c}{D_b} \frac{dS}{dPO_2} \right) \middle/ \left(1 + \frac{[Hb]}{\alpha} \frac{dS}{dPO_2} \right)^2 \right] \nabla PO_2 . \left(\frac{[Hb]}{\alpha} \nabla \frac{dS}{dPO_2} \right) \tag{3.49}$$

Equations (3.47) - (3.49) represent the complete non-linear blood oxygen transport model, referred to herein as Model 1, which incorporates both the free oxygen and bound oxygen.

3.4.1.1 Simplifications of the Blood Oxygen Transport Model

Previous studies have used simpler models in order to reduce computational expense. Firstly, the non-linearity can be removed by replacing dS/dPO_2 with a constant mean value of $\overline{dS/dPO_2}$ calculated as follows:[162]

$$\overline{\frac{dS}{dPO_2}} = \left(\frac{n\bar{S}}{\overline{PO_2}} \right) \left(1 - \bar{S} \right) \tag{3.50}$$

where $\overline{PO_2}$ is a mean reference value fixed at 75mmHg and replaces PO_2 in the Hill equation in order to evaluate $\bar{S}$, as shown in Equation (3.51):

$$\bar{S} = \frac{\overline{PO_2}^n}{\overline{PO_2}^n + PO_{2,50}^n} \tag{3.51}$$

Secondly, the dispersion of the RBCs can be ignored by setting D_c=0, and finally, the bound oxygen can be completely disregarded by setting [Hb]=0.

Similar to the study by Moore and Ethier (1997) the following five models were employed as described below and summarised in Table 3.1:

Model 1: Both the free and bound oxygen are modelled and the non-linearity of the Hill equation is retained.

Model 2: Both the free and bound oxygen are modelled and the non-linear element, dS/dPO_2, is replaced with the constant value $\overline{dS/dPO_2}$ evaluated using Equation (3.50).

Model 3: Both the free and bound oxygen are modelled and the non-linearity of the Hill equation is retained, but D_c=0, thus neglecting the shear-augmented dispersion of RBCs.

Model 4: Both the free and bound oxygen are modelled and the non-linear element, dS/dPO_2, is replaced with the constant value $\overline{dS/dPO_2}$, and D_c=0.

Model 5: Only the free oxygen is modelled, i.e. [Hb]=0.

Models	Free O_2	Bound O_2	D_c	dS/dPO_2
1	Y	Y	Eqn. (3.43 & 3.44)	Eqn. (3.46)
2	Y	Y	Eqn. (3.43 & 3.44)	0.00184 $mmHg^{-1}$
3	Y	Y	0 m^2/s	Eqn. (3.46)
4	Y	Y	0 m^2/s	0.00184 $mmHg^{-1}$
5	Y	N	-	-

Table 3.1: Summary of simplifications adopted for the blood oxygen transport models.

3.4.2 Arterial Wall Oxygen Transport

As previously discussed, the arterial wall consists of three layers: the intima, media and adventitia. In this study only the two inner layers, i.e. the intima and media, are included in the arterial wall models, because the adventitia is supplied with oxygen through the vasa vasorum, with distinct transport parameters assigned to each based on a study by Richardson.[206] In this study, the convection by the interstitial fluid in the arterial wall is ignored as the convective velocity of interstitial fluid is two orders of magnitude lower than the diffusive velocity.[162] It is also assumed that the endothelial cells lining the artery offer no resistance to the oxygen transport,[237] and as oxygen diffuses through the arterial wall it is consumed by the cells within.[252] The consumption rate of oxygen within the wall can be affected by a number of different variables, e.g. thickness of arterial wall, presence of inflammation/atherosclerotic plaque, subject species and age.[206] For the purposes of this study the Michaelis-Menten Kinetics model was employed to model the oxygen consumption within the arterial wall:

$$M = M_0 \frac{PO_2}{PO_2 + PO_{2,M}} \tag{3.52}$$

where M is the consumption rate of oxygen, M_0 is the maximum consumption rate and $PO_{2,M}$ is the value of PO_2 at which the rate of reaction is half-maximal.[200] The resultant diffusion equation employed for the prediction of the transport of oxygen in the arterial wall is:

$$\frac{dPO_2}{dt} = \nabla.\left(D_T \nabla PO_2\right) - \frac{M}{\alpha_T} \tag{3.53}$$

where D_T is the diffusivity of oxygen and α_T is the solubility of oxygen in the arterial wall tissue. Unless otherwise stated the values listed in Table 3.2 are used for the parameters in all simulations and the boundary conditions are given at the end of each test case description.

Symbol	Units	Blood	Intima	Media	Reference
α	$ml_{O_2}/ml_{blood}/mmHg$	3.0×10^{-5}	-	-	198
D_b	m^2/s	1.2×10^{-9}	-	-	162
[Hb]	ml O_2/ml blood	0.2	-	-	198
$PO_{2,50}$	mmHg	26	-	-	162
n	-	2.7	-	-	96
D_T	m^2/s	-	0.9×10^{-9}	1.05×10^{-9}	206
α_T	$ml_{O_2}/ml_{tissue}/mmHg$	-	2.4×10^{-5}	2.4×10^{-5}	206
M_0	$ml_{O_2}/ml_{tissue}/s$	-	2.1×10^{-5}	1.21×10^{-5}	206
$PO_{2,M}$	mmHg	-	1	1	78

Table 3.2: List of parameter values used for the blood and arterial wall oxygen transport model.

3.4.3 Sensitivity Analysis

Of the values listed in Table 3.2 α, D_b, and [Hb] are constant in human blood; although, in reality there is some variability in the other parameter values,[198] except for the solubility of oxygen in the media layer tissue, $\alpha_{T,\,media}$, which is considered to be fixed because the cellular composition of the media does not vary extensively for the arteries assessed here.[206] To assess the impact of variability of the other values on the oxygen transport a sensitivity analysis was carried out whereby a simplified straight coronary artery segment was modelled as shown in Figure 3.7. The radius of the lumen was 2.70 mm and the thickness of the intima and media were 0.24 mm and 0.32 mm, respectively. Model 1, as defined in , was used to model the oxygen transport with boundary conditions as follows: $PO_{2,in}$=100 mmHg, $PO_{2,adventitia}$=45 mmHg, $PO_{2,out}$=0

mmHg. An entry region was placed at the inlet to allow for development of the flow with a zero oxygen flux boundary condition placed on the luminal wall surface.

Each parameter was assessed separately and varied according to minimum and maximum values as listed in Table 3.3 while all other values were fixed at the values defined in Table 3.2. Additionally, two other simulations were carried out where, first, a fixed D_c value of 1.5×10^{-11} m^2/s was used, as adopted by Moore and Ethier (1998),[162] and second, intima layer properties were set which represented a high fat content in line with a late-stage atherosclerotic plaque lesion, although the thickness was not increased. To represent the effect of varying the parameter value in one number the difference between the test and standard minimum PO_2 value predicted in the intima domain is shown in Figure 3.8.

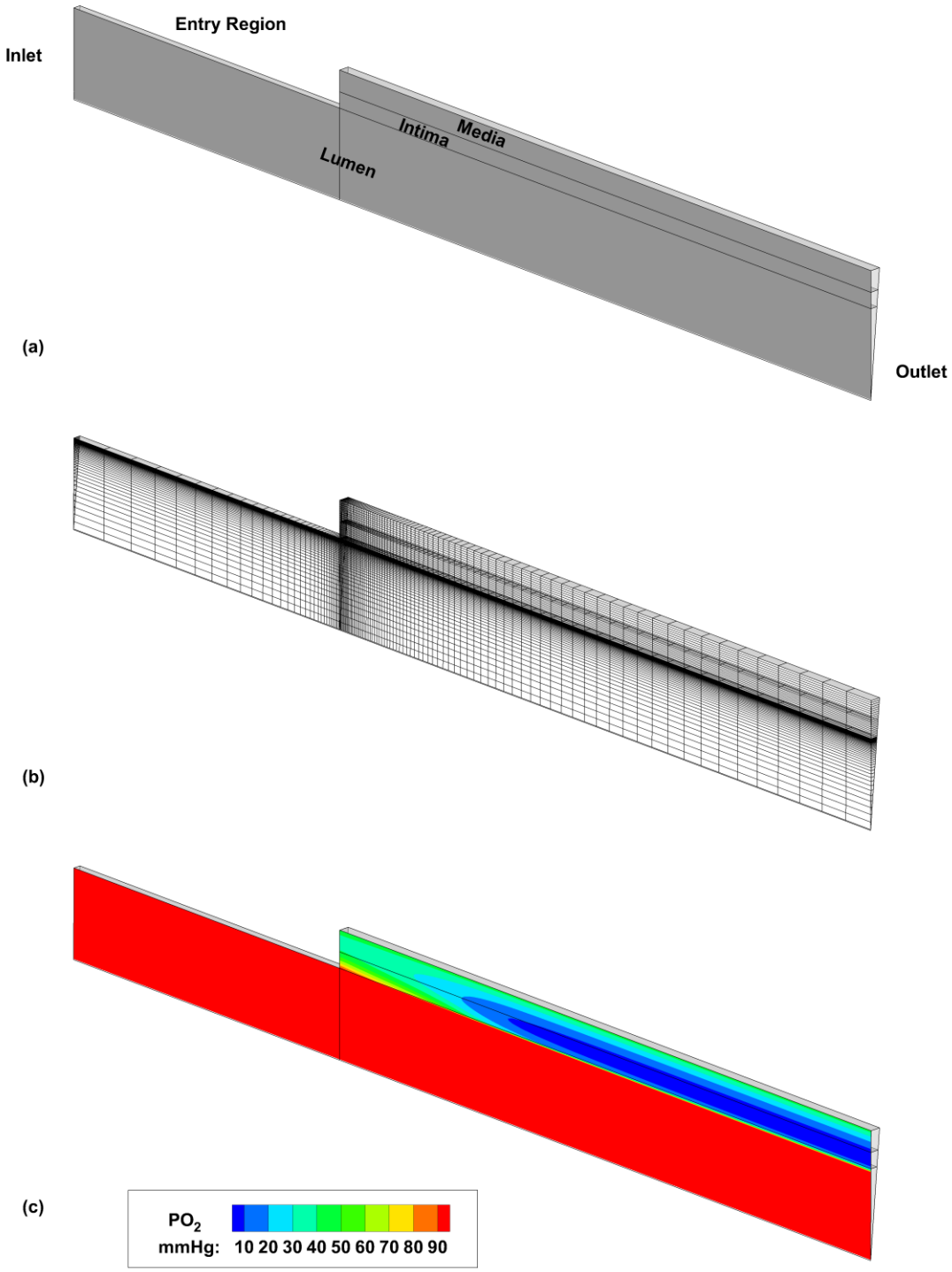

Figure 3.7: (a) Geometry and domain set up used for sensitivity analysis, (b) mesh employed and (c) typical contour plot of PO_2 along a slice within the lumen, intima, and media.

Parameter	Value used	Min	Max
$PO_{2,50}$	26.6	23.1	30.6
n	2.7	1.7	3.2
$D_{T,\ intima}$	0.9×10^{-9}	0.72×10^{-9}	0.9×10^{-9}
$D_{T,\ media}$	1.05×10^{-9}	0.75×10^{-9}	1.05×10^{-9}
$\alpha_{T,\ intima}$	2.4×10^{-5}	2.4×10^{-5}	3.8×10^{-5}
$M_{0,\ intima}$	2.1×10^{-5}	1.68×10^{-5}	2.9×10^{-5}
$M_{0,\ media}$	1.21×10^{-5}	1.21×10^{-5}	1.89×10^{-5}
$PO_{2,M}$	1	0.5	1

Table 3.3: List of parameter values that were assessed for the sensitivity analysis. For each parameter the value used in the Test Cases 1, 2, 3 & 4 is given along with the minimum and maximum values possible in the human vasculature.

3.4.3.1 Results of Sensitivity Analysis

The oxygen dissociation curve is affected by several factors: blood temperature, pH, and carbon dioxide concentration, and is defined by two values: the $PO_{2,50}$ and n. $PO_{2,50}$ is the PO_2 value at which the haemoglobin within the RBCs is at 50% saturation.[88] The typical value within the arterial system is 26.6 mmHg, although it can vary depending on the pH of the blood which is affected by the amount of carbon dioxide (CO_2) dissolved in the blood. This is known as the Bohr effect and is actually useful in the body because when CO_2 dissolves in the water within the blood carbonic acid is formed and the pH of the blood decreases resulting in the haemoglobin exhibiting less affinity for oxygen, thus releasing oxygen to tissues most in need of oxygen that are producing the CO_2 as a waste product.[174] The effects of changes in the partial pressure of CO_2 and pH in blood on $PO_{2,50}$ was assessed by Hamilton et al. (2004),[88] and the minimum and

maximum $PO_{2,50}$ values shown in Table 3.3 correspond to the range observed and are taken here as 23.1 mmHg and 30.6 mmHg, respectively. As can be seen in Figure 3.8 the variation of $PO_{2,50}$ has a small effect on the oxygen transport with a slightly increased amount of oxygen reaching the intimal tissue in the case when $PO_{2,50}$ is minimum and the opposite with $PO_{2,50}$ in maximum.

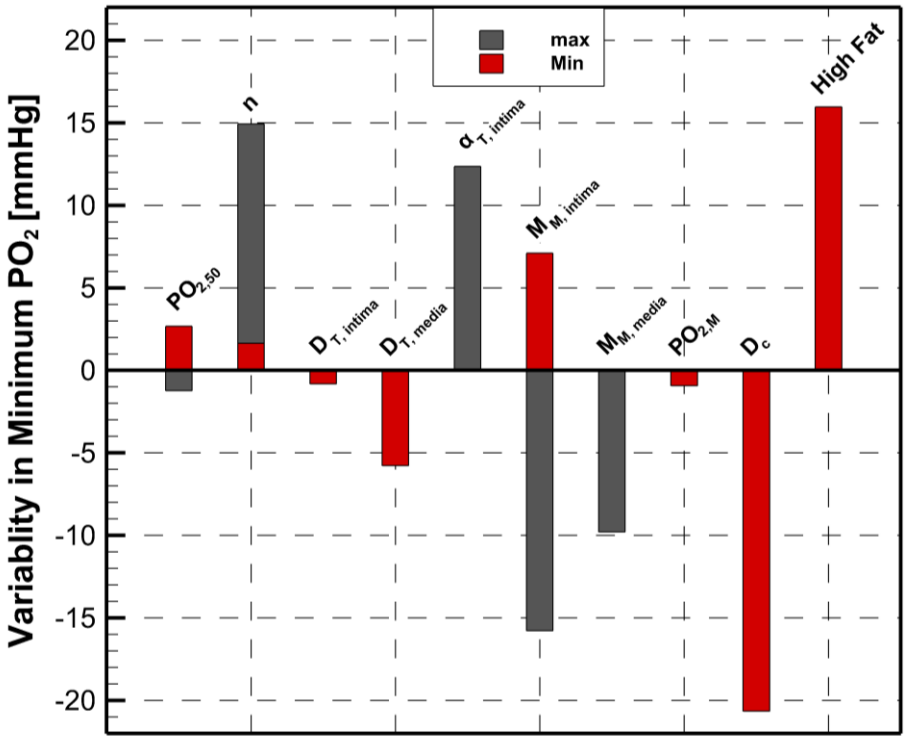

Figure 3.8: Variability in minimum PO_2 within the intima domain with respect to standard case.

Conversely, n is shown to have a significant effect on the amount of oxygen reaching the arterial wall as shown by a significant increase in the minimum PO_2 in the intima. This can be explained by the considerable increase in the slope of the dissociation curve, dS/dPO_2, when n=3.2 which means that for a small change in PO_2 there is a

large change in S. Therefore, the oxygen transport is sensitive to small changes in the n value.

In the case of $D_{T,\ intima}$ the minimum value of 0.72×10^{-9} m^2/s, which corresponds to the lower diffusivity experienced in a six month old baby's intima, has an almost negligible effect on the oxygen transport into the arterial wall, as shown in Figure 3.8. $D_{T,\ media}$ has a more noticeable effect with the minimum value of 0.75×10^{-9} m^2/s, which likewise corresponds to the lower diffusivity experienced in a six month old baby's media, exhibiting a drop in the minimum PO_2 value in the intima of 5.77 mmHg. The standard values of both $D_{T,\ intima}$ and $D_{T,\ media}$ are both the maximum values recorded in the literature which do not vary significantly throughout the life of the arterial wall even in the presence of a lesion.[206]

The maximum value of $\alpha_{T,\ intima}$, which represents the predicted solubility in an intima with a high fat and calcium content, i.e. with a significant plaque lesion present,[206] produces a significant change in the minimum PO_2 levels within the intima with an increase of 12.36 mmHg, as shown in Figure 3.8. This may on initial inspection appear to mean that the presence of a plaque lesion in the intima produces a positive outcome in terms of oxygen transport, but it should be noted that this simulation assumes everything else remains equal which it would not in the case of a plaque lesion with the consequence of increased intimal thickness increasing the diffusion distance and eventually resulting in a necrotic plaque core. Nevertheless, $\alpha_{T,\ intima}$ does have a significant effect on the oxygen transport.

In the case of $M_{0,\ intima}$ this shows the largest effect on the oxygen transport into the arterial wall, as shown in Figure 3.8, with maximum value producing a drop in the minimum PO_2 value of 15.78 mmHg, and the minimum value of $M_{0,\ intima}$ producing an

increase of 7.11 mmHg. The maximum value of $M_{0,\ intima}$ corresponds to the value predicted by Richardson (2008) in a 24 year old human with no plaque lesion present.[206] Also noted in that study was that the oxygen consumption is predicted to decrease over time in human arterial wall free of atherosclerosis. As such, the minimum $M_{0,\ intima}$ value corresponds to the value predicted in a 70 year old with an 88% stenosis. It should be noted again that this simulation assumes everything else remains constant including the intimal thickness. However, it is clear that $M_{0,\ intima}$ has a significant impact on the oxygen levels in the arterial wall. Likewise, the maximum value of $M_{0,\ media}$ also produces a predicted decrease of 9.79 mmHg in the minimum PO_2 value; however, it should be noted that this value is theorised to only exist in a 6 month old baby.[206] The $PO_{2,\ M}$ minimum value of 0.5 mmHg is shown to have an almost negligible effect on the oxygen levels, as would be expected considering the standard value used is 1 mmHg.

To demonstrate the effect of including a variable shear-induced dispersion coefficient, D_c, a simulation was run with $D_c=1.5\times10^{-11}$ m^2/s. As shown in Figure 3.8, by ignoring the increase in D_c caused by the higher shear rates experienced in coronary arteries there is a significant decrease of 20.65 mmHg in the predicted minimum PO_2 value within the intima. This provides an initial support for the use of a variable D_c value and shows one disadvantage of simplification of the blood oxygen transport model.

Finally, a simulation was carried out to assess the effects of combining the two relevant consequences of the presence of a 88% stenosis, i.e. an increased $\alpha_{T,\ intima}$ value of 3.8×10^{-9} $ml_{O_2}/ml_{tissue}/mmHg$ and a decreased $M_{0,\ intima}$ value of 1.68×10^{-5} $ml_{O_2}/ml_{tissue}/s$. This is predicted to have a positive effect with a significant increase of 16 mmHg in the minimum PO_2 value in the intima shown in Figure 3.8. This is again with the stipulation that the increased intimal thickness is not factored in, but

demonstrate how the plaque lesion properties could potentially affect the PO_2 levels in the arterial wall.

3.5 Oxygen Transport Variable of Interest – Sherwood Number

The Sherwood number (Sh) is a dimensionless mass-transfer coefficient and is used in Test Cases 2 and 3, discussed in Chapter 6, along the luminal surface using:

$$Sh = -\frac{Dia\left(dPO_2 / dn\right)}{\left(PO_{2,in} - PO_{2,w}\right)} \tag{3.54}$$

where Dia is the diameter of the artery, dPO_2/dn is the gradient of PO_2 normal to the wall, $PO_{2,in}$ is the PO_2 set at the inlet and $PO_{2,w}$ is the PO_2 predicted at the arterial wall luminal surface. Low Sh highlights potential areas on the luminal surface where the underlining cells may be in danger of hypoxia. To establish what constitutes low Sh the Damkholer number (Da), a dimensionless reaction rate coefficient, is first calculated using:

$$Da = \frac{M_0 T Dia}{\alpha_T D_T PO_{2,in}} \tag{3.55}$$

where T is the arterial wall thickness. Using the assigned parameters for the coronary artery models presented here the calculated $Da \approx 17$. When $Sh \gg Da$ the supply exceeds the demand within the arterial wall; however, as $Sh \rightarrow Da$ the PO_2 levels become increasingly dependent upon the blood oxygen transport.[252] Therefore, as the Sh drops towards this calculated value of Da the PO_2 levels within the arterial wall will decrease to possible hypoxic levels.

3.6 Computational Fluid Dynamics

All simulations for this study were carried out in the commercial CFD software ANSYS CFX 15.0 (ANSYS Inc., Canonsburg, PA, USA) which uses an element-based finite volume method. ANSYS CFX makes the assumption of a continuum medium where the

fluid is assumed to be evenly distributed throughout the domain. The information presented here is adapted from the ANSYS Theory Guide with additional information from books on the topic as referenced throughout.

3.6.1 Governing Equations

CFD is based on three fundamental governing equations of fluid dynamics: the continuity, momentum and energy equations, which are based on three physical laws:

1. Continuity equation – mass is conserved, i.e. Law of Conservation of Mass
2. Momentum equation – net force on a body is equal to the mass of the body multiplied by the acceleration, i.e. Newton's Second Law
3. Energy equation – energy is conserved, i.e. Second Law of Thermodynamics

The energy equation is neglected in this instance as the process taking place is assumed to be adiabatic and no mechanical energy is exchanged. If the flow is assumed to be incompressible; i.e., there is no change in density, the continuity and momentum equations in Cartesian coordinates can be presented as:

$$\nabla \cdot \mathbf{V} = 0 \tag{3.56}$$

$$\rho\left(\frac{\partial \mathbf{V}}{\partial t} + \mathbf{V} \cdot \nabla \mathbf{V}\right) = \nabla \cdot \sigma_{ij} + f_b \tag{3.57}$$

The left hand side of Equation (3.57) represents the density multiplied by the acceleration of the fluid element and the right hand side is the sum of all the forces acting on the fluid element. Within the first term on the right σ_{ij} represents the stress tensor, as derived earlier in Section 3.2.6, and f_b represents the body forces exerted on a fluid element, which in this case is assumed to only consist of the force due to gravity, ρg. In accordance with Equation (3.25), the first term on the right of Equation (3.57), $\nabla \cdot \sigma_{ij}$, becomes $(-\nabla P + \nabla \cdot (\mu_{eff} \nabla \mathbf{V}))$ for a Newtonian fluid, where μ_{eff} is the effective viscosity. Thus, the momentum equation is expressed as:

$$\rho\left(\frac{\partial \mathbf{V}}{\partial t}+\left(\mathbf{V}\cdot\nabla\right)\mathbf{V}\right)=-\nabla P+\nabla\cdot\left(\mu_{eff}\nabla\mathbf{V}\right)+\rho\mathbf{g} \tag{3.58}$$

Equation (3.58) is known as the Navier-Stokes equation and can be expressed in the form of the transport (advection-diffusion) equation, Equation (3.59). The transport equation is also used for modelling the transport of a passive scalar, such as PO_2.

$$\rho\left(\underbrace{\frac{\partial \varphi}{\partial t}}_{\text{transient}}+\underbrace{\nabla\cdot\varphi\mathbf{V}}_{\text{advection}}\right)=\underbrace{\nabla\cdot\left(\Gamma_{eff}\nabla\varphi\right)}_{\text{diffusion}}+\underbrace{S_{\varphi}}_{\text{source}} \tag{3.59}$$

where φ is the conserved variable, Γ_{eff} is the effective diffusivity and S_{φ} is the source term. Each of the terms in the transport equation represent a different component of the overall transport of the conserved variable as signified by the notation under each. The first term, $\frac{\partial \varphi}{\partial t}$, is called the transient term and represents how the conserved variable changes with time. The second term, $\nabla\cdot\varphi\mathbf{V}$, is the advection term and describes how the conserved variable is affected by the velocity of the fluid. The third term, $\nabla\cdot\left(\Gamma_{eff}\nabla\varphi\right)$, is the diffusion term and describes how the conserved variable is affected by diffusion due to gradients in values between neighbouring control volumes. In the case of the Navier-Stokes equation **V** is the conserved variable, μ_{eff} (dynamic viscosity) is the effective diffusivity and the source term is the sum of the pressure and gravity forces. In the case of the transport of PO_2, D' is the effective diffusivity and the source term is as described in Section 3.4.1.

3.6.2 Discretisation

As mentioned previously, ANSYS CFX uses an element-based finite volume method and in order to solve the governing equations they need to discretised according to this method. Firstly, the computational domain is spatially discretised into control volumes

using a mesh. The mesh is comprised of nodes, where all solution variables and fluid properties are stored, and these are surrounded by the control volumes. A control volume is formed around a node by joining the centre points of all the surrounding mesh elements and edge midpoints, as shown in a basic 2D mesh in Figure 3.9. Once the computational domain is spatially discretised the governing equations are integrated over each control volume. Taking the general transport equation, Equation (3.59), as representative of all three governing equations, it can be integrated over the control volume as follows:

$$\int_v \frac{\partial}{\partial t}(\rho\varphi)\,dv + \int_v \nabla\cdot(\rho\varphi\mathbf{V})\,dv = \int_v \nabla\cdot(\Gamma_{eff}\nabla\varphi)\,dv + \int_v S_\varphi dv \tag{3.60}$$

where v denotes the volume. Using the divergence theorem the second and third terms can be converted from volume integrals to surface integrals:

$$\int_v \frac{\partial}{\partial t}(\rho\varphi)\,dv + \int_s (\rho\varphi\mathbf{V})\cdot n\,ds = \int_s (\Gamma_{eff}\nabla\varphi)\cdot n\,ds + \int_v S_\varphi dv \tag{3.61}$$

where n represents the surface normal vector. The surface integrals represent a summation of all the fluxes crossing the boundaries of the individual control volumes and the volume integrals represent source or accumulation terms. Once these integrals have been derived they must be numerically discretised, essentially replacing each integral with an algebraic equation.

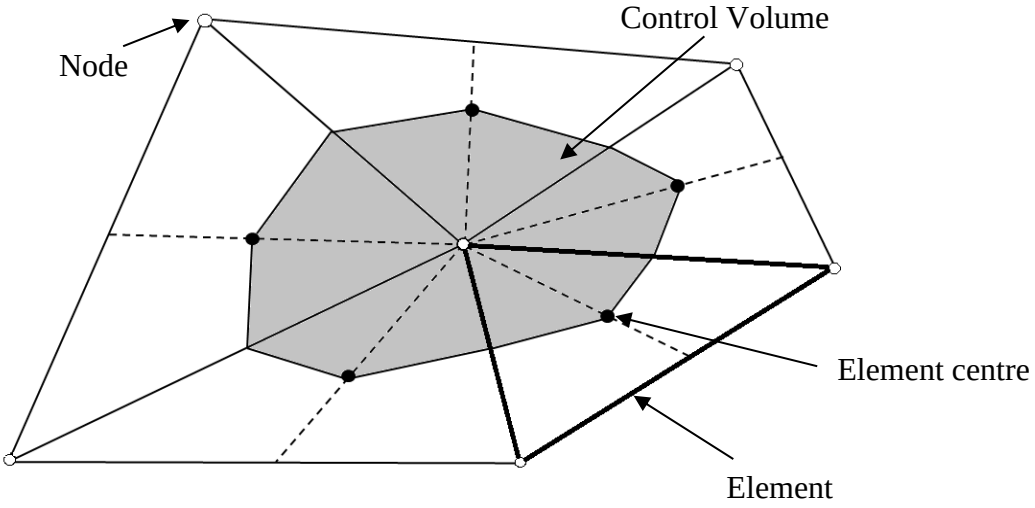

Figure 3.9: Sample 2D mesh with control volume defined around node.

Looking at Equation (3.61) there are four terms, two of which have volume integrals and two of which have surface integrals. Volume integrals are discretised within each element sector and then the total for each control volume is a summation of all the sector values within that control volume. The surface integrals are discretised at integration points, located at the midpoint of sector edges as shown in Figure 3.10, and then distributed to the adjacent control volumes. The surface integrals are equal in magnitude and opposite in sign for the two control volumes to which they are distributed to.

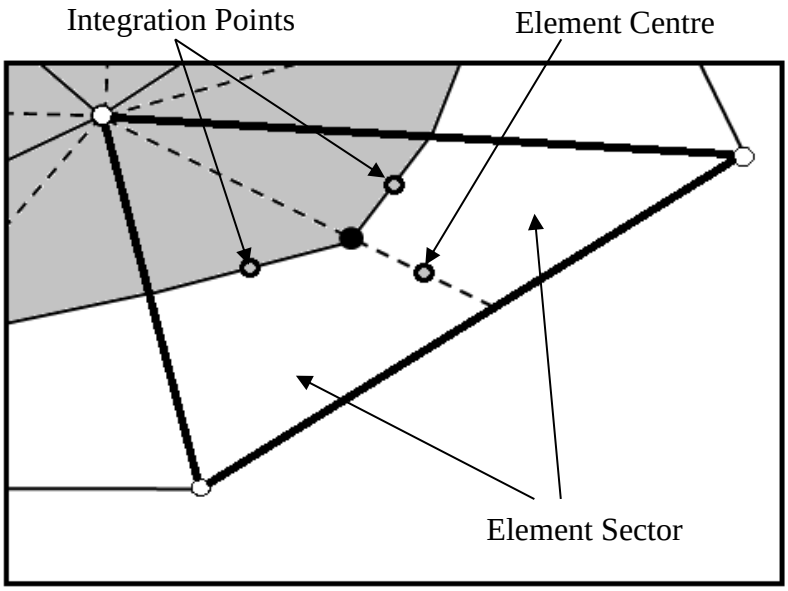

Figure 3.10: 2D Mesh element taken from Figure 3.9 with integration points and element sector highlighted.

The transient term in Equation (3.61) is a volume integral and discretising it using the second-order backward Euler method results in the algebraic equation:

$$\int_v \frac{\partial}{\partial t}(\rho\varphi)\,dv = \frac{v}{\Delta t}\left[\frac{3}{2}(\rho\varphi)^n - 2(\rho\varphi)^{n-1} + \frac{1}{2}(\rho\varphi)^{n-2}\right] \tag{3.62}$$

where v represents the control volume, Δt is the time step, and the superscripts n, n-1 and n-2 represent the current, previous and second previous time steps respectively. The advection term in Equation (3.61) is a surface integral and is discretised as the sum of fluxes over all the faces of the control volume:

$$\int_s (\rho\varphi\mathbf{V})\cdot\mathbf{n}ds = \sum_{ip=1}^{a}(\rho\mathbf{V}\cdot\mathbf{n}ds)_{ip}\,\varphi_{ip} \tag{3.63}$$

where $\rho\mathbf{V}\cdot\mathbf{n}ds$ represents the mass flow rate normal to the control volume face containing the integration point (ip) and φ_{ip} is the conserved variable at that integration point (total number of integration points represented by a). The solution variables are

stored at the nodes and therefore, the face values are approximated at the integration points using:

$$\varphi_{ip} = \varphi_{up} + \beta \nabla\varphi \cdot \Delta \mathbf{r} \tag{3.64}$$

where φ_{up} is the value of the conserved variable at the node directly upwind from the integration point, β is the blend factor, $\nabla\varphi$ is the gradient of the conserved variable and $\mathbf{r}$ is the vector from the upwind node to the integration point. The high resolution scheme was implemented in all simulations herein, for which $0 \leq \beta \leq 1$ and a nonlinear recipe is used to calculate β at each node based on the boundedness principles used by Barth and Jesperson.[8] The gradients of conserved variable is calculated using shape function which are linear in terms of the parametric coordinates. The diffusion term is also a surface integral and is approximated as:

$$\int_s \left(\Gamma_{eff} \nabla\varphi\right) \cdot \mathbf{n} ds = \sum_{ip=1}^{a} \left(\Gamma_{eff} \nabla\varphi\right) \cdot \mathbf{n} ds \tag{3.65}$$

The source term is a volume integral and is approximated as follows:

$$\int_v S_\varphi dv = \bar{S}_\varphi v \tag{3.66}$$

where $\bar{S}_\varphi$ is the average value of the source term within the control volume and v is the volume of the control volume. When all four terms are discretised the resultant equation is:

$$\frac{v}{\Delta t}\left[\frac{3}{2}(\rho\varphi)^n - 2(\rho\varphi)^{n-1} + \frac{1}{2}(\rho\varphi)^{n-2}\right] + \sum_{ip=1}^{a} (\rho \mathbf{V} \cdot \mathbf{n} ds)_{ip} \varphi_{ip} = \sum_{ip=1}^{a} \left(\Gamma_{eff} \nabla\varphi\right) \cdot \mathbf{n} ds + \bar{S}_\varphi v \tag{3.67}$$

By putting the diffusion term on the right hand side, the equation becomes:

$$\frac{v}{\Delta t}\left[\frac{3}{2}(\rho\varphi)^n - 2(\rho\varphi)^{n-1} + \frac{1}{2}(\rho\varphi)^{n-2}\right] + \sum_{ip=1}^{a} (\rho \mathbf{V} \cdot \mathbf{n} ds)_{ip} \varphi_{ip} - \sum_{ip=1}^{a} \left(\Gamma_{eff} \nabla\varphi\right) \cdot \mathbf{n} ds = \bar{S}_\varphi v \tag{3.68}$$

When this equation is applied to all control volumes throughout the computational domain all of the algebraic equations can be combined into a matrix of the form:

$$[A][\varphi] = [b] \tag{3.69}$$

where [A] represents the sparse coefficient matrix, [φ] is the solution vector containing the variable values at the nodes and [b] is the right hand side of Equation (3.68).

3.6.3 Solution

The discretised algebraic equations are solved in ANSYS CFX using an implicitly coupled multigrid accelerated incomplete lower upper factorisation technique. This is an iterative technique that involves the solution converging towards an exact solution over the course of numerous iterations. The multigrid process comprises of early iterations being solved on a fine mesh and later iterations being solved on progressively courser virtual meshes.[4] The results are then transferred from the coarsest mesh back to the original fine mesh. This technique has the advantage of decreasing the time taken to reach a converged solution.

Looking at Equation (3.69) above, the solution is reached by first using an approximate solution of φ, φ^n, and improving this by a correction, φ', which results in the solution after a time step, φ^{n+1}, being closer to the exact solution, where:

$$\varphi^{n+1} = \varphi^n + \varphi' \tag{3.70}$$

The correction term is calculated using:

$$A\varphi' = r^n \tag{3.71}$$

where r^n is the residual of the previous time step calculated using:

$$r^n = b - A\varphi^n \tag{3.72}$$

The residuals are normalised for monitoring the solution and setting the convergence criteria.

3.7 Summary

In this chapter the fundamental theory relevant to the study was presented. First, the derivation of the fluid stress tensor was shown along with the haemodynamic variables of interest to this study. Second, the oxygen transport theory relevant to both the blood and the arterial wall was described along with the oxygen transport variable of interest, Sh. The results of a sensitivity analysis of the oxygen transport model were presented with variation of several parameters shown to have a significant effect on the amount of oxygen reaching the arterial wall. Specifically, the Hill coefficient (n), the solubility of oxygen in the intima ($\alpha_{T,\ intima}$), and the consumption of oxygen in both the intima ($M_{0,\ intima}$) and media ($M_{0,\ media}$) all play a dominant role in the oxygen transport. These also are the parameters that would vary the most in diseased arterial walls and their effects were previously assessed by Richardson (2008); however, the luminal oxygen transport was ignored with a constant PO_2 value fixed on the luminal surface.[206] The effect of using a constant D_c value of 1.5×10^{-11} m^2/s as done previously by other researchers was assessed and showed to have a significant effect on the oxygen transport in coronary arteries where the shear rates are much higher than the shear rate where the fixed D_c value is valid, i.e. 20 s^{-1}. Finally, the CFD governing equations, discretisation technique, and how the equations are employed in the software was presented. In the next chapter a thorough review of the literature particular to this study is discussed.

CHAPTER 4

Literature Survey

4.1 Introduction

In this chapter literature reviews of previous studies in the areas of oxygen transport in arteries and haemodynamic analysis of stents are presented. In addition to this, with specific relevance to Test Case 4, a thorough review of helical flow in the cardiovascular system is given along with the studies related to two stent devices being developed that not only re-establish blood-flow in an obstructed artery but establish haemodynamics that theoretically inhibit ISR.

4.2 Oxygen Transport Analyses

The biological processes that can result in ISR are instigated by the effects of stent implantation and include structural damage to the arterial wall, augmentation of the local haemodynamic environment and the presence of a foreign body.[171] In terms of the augmentation of the haemodynamic environment, stenting produces a predominantly beneficial effect, i.e. restoration of required blood flow to downstream vasculature; however, locally within the stented region, the haemodynamics impact the natural healing processes within the arterial wall. This local augmentation of the haemodynamic environment due to the presence of a stent in turn affects the oxygen flux into the arterial wall which can result in a deficiency of oxygen, known as hypoxia, in some regions. Hypoxia has been associated with increased adventitial vasa vasorum[34] and IH in animal studies.[216,218] Therefore, given that hypoxia and increased IH may result in

ISR, investigation of the local oxygen transport within stented artery models using CFD is important in order to elucidate the effects of stenting on the arterial wall cellular components and also to aid in the design of future coronary stents.

Hypoxia is known to cause atherosclerosis in large arteries.[252] Because of this, the majority of numerical studies of oxygen transport in three-dimensional (3D) arteries have been in relation to arteries with no implanted device. Many of these numerical studies fall into the category of wall-free models where only the oxygen transport in the blood is modelled and a constant value of oxygen concentration/PO_2 value is specified on the luminal surface.[45] Another category of oxygen transport studies employs fully coupled blood and arterial wall models, where diffusion and consumption of oxygen in the arterial wall are modelled, and a constant flux or concentration/PO_2 value boundary condition is specified on the media/adventitia boundary interface.[23,248] These models offer the advantage of a more realistic representation of the oxygen transport conditions; however, in these simulations the arterial wall was modelled as homogeneous which is not physiologically correct. In contrast, a third analysis type is lumen-free models which ignore the haemodynamic conditions within the lumen and assume a constant oxygen concentration/PO_2 value on the luminal surface. As an example, Richardson modelled the oxygen transport within heterogeneous coronary arterial walls only, with varying parameters according to age and stenosis, while ignoring the flow within the lumen.[206] Considering the influence of haemodynamics on the oxygen transport into the arterial wall, the wall-free and coupled analyses are discussed below.

4.2.1 Wall-Free Analyses

Wall-free models are the simplest models as they just account for the mass transport within the blood. The effects of the transport into the arterial wall are accounted for by applying an appropriate set of boundary conditions. In oxygen mass transport studies this is generally a PO_2 value of 60mmHg, or equivalent in concentration/normalised concentration values, being imposed on the luminal surface. This simplification essentially ignores the oxygen consumption and diffusion in the arterial wall and is used when the study of the haemodynamic effects are preferred. In these cases the Sh is valuable as it can be calculated based on the spatial gradient of the PO_2 normal to the wall surface. For interpretation of the Sh there are three different scenarios where the flow is: directed towards the wall, flowing parallel to the wall, and directed away from the wall. In case (1), the mass transport boundary layer (MTBL) is relatively narrow which results in a high PO_2 gradient normal to the wall and consequently a high Sh. In case (2), the MTBL is free to develop and will gradually increase until a constant thickness is reached. For the PO_2 gradient and Sh this results in a gradual transition from high values to low values longitudinally along the wall. In case (3), a relatively thicker MTBL is created and consequently, both the PO_2 gradient and the Sh are reduced. Areas of low Sh are then interpreted as areas which are prone to hypoxia occurring in the underlying tissue and possibly increased IH and atherosclerosis.

One of the earliest numerical studies of oxygen transport in arteries was carried out by Friedman and Ehrlich and published in 1975.[64] They modelled the oxygen transport in a 2D arterial bifurcation in steady flow conditions and analysed the effects of spatial variations in shear on the oxygen flux to the wall. It was found that there was as much variation in the wall flux and concentration values as there was in shear. In a study published in 1977 Back et al. examined the oxygen transport in 2D representations of

partially obstructed human coronary arteries and found that the oxygen flux into the arterial wall was reduced in the flow separation region downstream of plaque locations.[5] One of the recommendations of this study was that *in vivo* measurements with oxygen microelectrodes in animals were needed to learn more about the variations in oxygen transport in plaque regions. Two such studies carried out by Santilli et al. in 1995 and 2000 are used in Test Case 1 and 2 (Chapters 6 and 7) to compare the transport models adopted in this work.[217,218]

In terms of 3D studies, Rappitsch et al. (1997) presented a numerical scheme for the simulation of unsteady flow and mass transport in large arteries where the flow is unsteady and the resistance of the arterial wall to transmural transport is governed by a shear-dependent wall permeability model.[204] The methodology is demonstrated in a 90° arterial bend and the key observation noted is that the mass transfer flux is reduced on the inner wall of the bend, which is critical in the modelling of not only oxygen transport, but also of macromolecules such as LDLs and albumin. The shear-dependent wall permeability model adopted was noted to not be valid for oxygen transfer through the wall, but it would be important for future studies in the mass transport of macromolecules such as albumin or LDL.[204]

In the same year Ma et al. (1997) published a study where they conducted a 3D simulation of steady flow and oxygen transport in an idealised carotid bifurcation with a constant PO_2 value imposed at the arterial wall surface and predicted the oxygen flux distribution over the inner wall surface.[142] The geometry used was based on measurements of biplanar angiograms of 57 patients by Bharadvaj et al. (1982a, b)[15,16] which were also used in studies by Tada and Tarbell, discussed below.[248,249] The mass transfer was found to be five times lower along the outer wall of the carotid sinus in comparison with the arterial wall immediately upstream or downstream of the sinus.

Areas of predicted low mass transfer was found to correlate strongly with areas prone to intimal thickening in humans, as shown in Figure 4.1. This study was important in that it supported the relatively new hypothesis put forward by Simanonok in 1996 that non-ischemic hypoxia of the arterial wall is the primary cause of atherosclerosis.[231] This hypothesis was proposed to replace the dominant model of atherosclerosis at the time which was the response-to-injury hypothesis which was originally proposed by Ross and Glomset in 1976.[210] This is a reoccurring theme in CFD simulations, in that there are assumptions made throughout the process including in geometry generation which affect the perceived accuracy of the simulations.

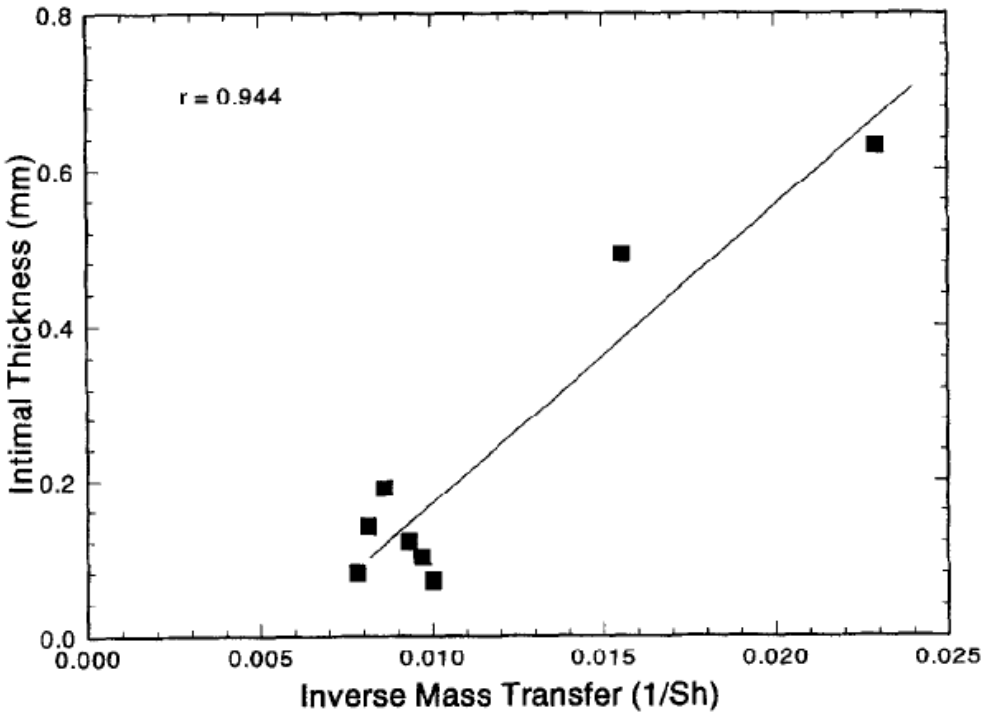

Figure 4.1: Low mass transfer rate is directly related to measured intimal thickness with a correlation coefficient of 0.944. Thus, low mass transfer may be an indication of plaque localisation and atherogenic growth.[142]

Qiu and Tarbell (2000) modelled the oxygen mass transfer in a compliant curved tube model of a coronary artery.[202] In this study they modelled the movement of the coronary artery arterial wall as predicted would occur due to the motion of the heart. In this study the curvature of the coronary artery caused a difference between the Sh value on the inner and outer, in terms of the centreline curvature, luminal surface of several magnitudes which implied that the oxygen content of the arterial wall could be limited by the flow conditions in this region. Interestingly, the effects of the movement of the coronary artery caused by the motion of the heart on the results was not discussed by the authors. In this study the authors neglected the bound oxygen transport and reasoned that the Sh with the bound oxygen would be 2.5 times the predicted Sh without the bound oxygen. This assumption is based on the results from the paper by Moore and Ethier (1997) which compared five different models, similar to the models discussed in Chapter 3. The validity of this assumption will be revisited in Chapter 9.

These results from Qui and Tarbell (2000) were found to be in agreement with a separate study by Kaazemput-Mofrad and Ethier (2001) analysing the oxygen transport within an anatomically realistic human RCA.[116] The results of this study showed how the oxygen concentration field within the RCA closely followed the primary and secondary flow features. The secondary flow features mentioned are two Dean vortices which are formed due to the curvature of the RCA centreline. As the flow develops further one vortex becomes more dominant and as a result the concentration field is pulled away from the inner wall leaving a zone of reduced oxygen concentration near the inner wall. The importance of the secondary flow structure is a reoccurring issue in the study of oxygen mass transport and will be elaborated on later. In this study the Sh was found to vary by 800 fold from the inner to the outer wall of the curved RCA; however, it was noted that with the addition of flow pulsatility and diameter reduction

of the artery, this may be reduced to 23 fold. In comparison with the study by Qui and Tarbell, the range of Sh was smaller and this was deemed to have been caused by the enhanced mixing produced in a more realistic geometry.[116]

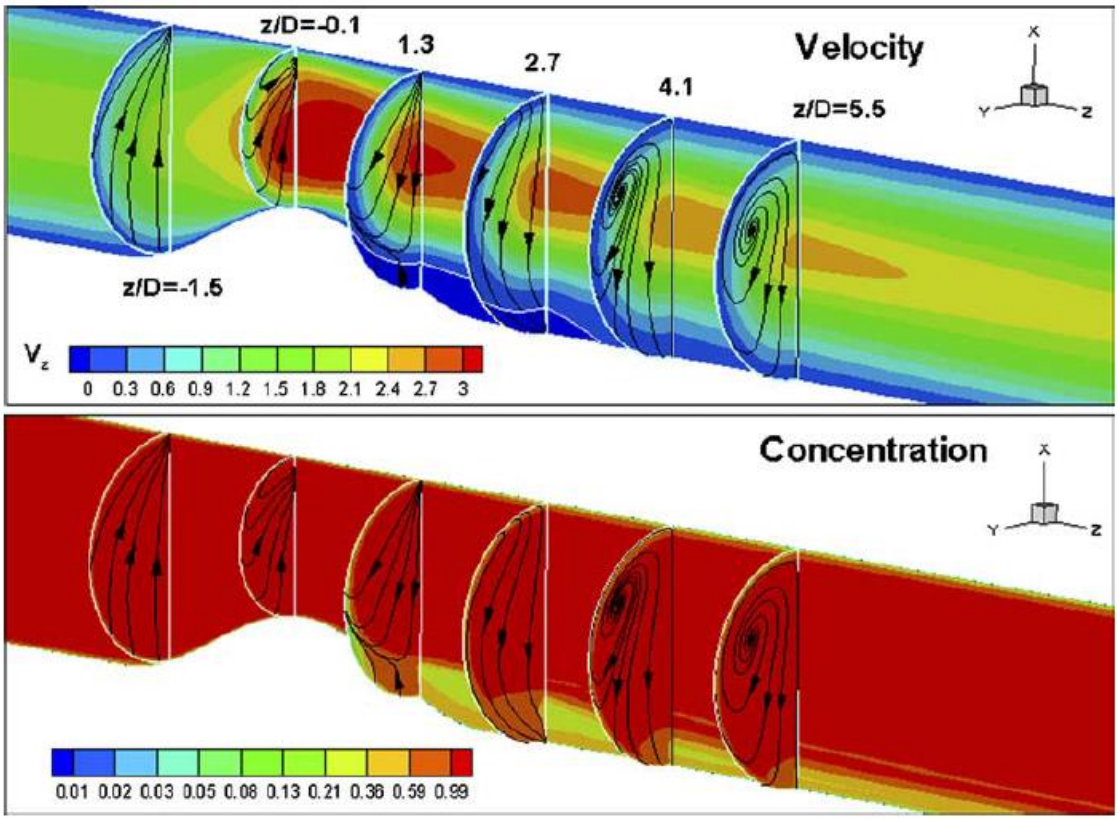

Figure 4.2: Velocity and concentration profiles in the non-symmetric stenosis model.[117]

In 2005 Kaazempur-Mofrad and Ethier published a study where they analysed the difference in terms of oxygen transport within a coronary artery partially obstructed by axisymmetric and asymmetric plaque lesions, as shown in Figure 4.2.[117] This again was a wall-free model where the oxygen concentration was fixed on the arterial wall luminal surface and the flux was analysed using the local Sh. The results indicated that there is a considerable difference in mass transfer patterns between both models, concluding that

accurate representations of the arterial geometries is essential in order to predict the mass transfer in partially obstructed arteries.

Kolandavel et al. (2006) modelled both the LDL and oxygen mass transport in an idealised moving coronary artery model under both steady and pulsatile flow conditions.[124] A physiological velocity profile was imposed at the inlet and the curvature of the artery was varied according to a sinusoidal waveform over the period of a cardiac cycle. In comparison with the steady flow simulation, the pulsatility was found to decrease the oxygen flux to the inner wall. Conversely, with the addition of wall motion an increase in oxygen flux in the distal region of the inner wall was observed. Overall the oxygen wall flux was found to not vary appreciably over the course of a cardiac cycle.

Tada and Tarbell (2006) modelled the oxygen transport in a compliant carotid bifurcation model with realistic blood flow waveforms and PO_2=0mmHg imposed on the luminal surface.[250] As with previous papers, the Sh was used to quantify the oxygen flux into the arterial wall. A region of low Sh was predicted on the outer wall of the carotid sinus where the flow separates away from the wall. Therefore, it was concluded that flow separation provides a very strong haemodynamic barrier to oxygen transport. Dramatic differences in the Sh were seen during the cardiac cycle between the compliant model and rigid model; however, crucially, these transient differences did not translate into significant differences in the time-mean Sh, as shown in Figure 4.3. Additionally, the time-mean Sh values did not show considerable difference with the transient models. Thus, neglecting the compliance of the arterial wall and the pulsatility of the flow in simulations of oxygen transport in arteries is justifiable.

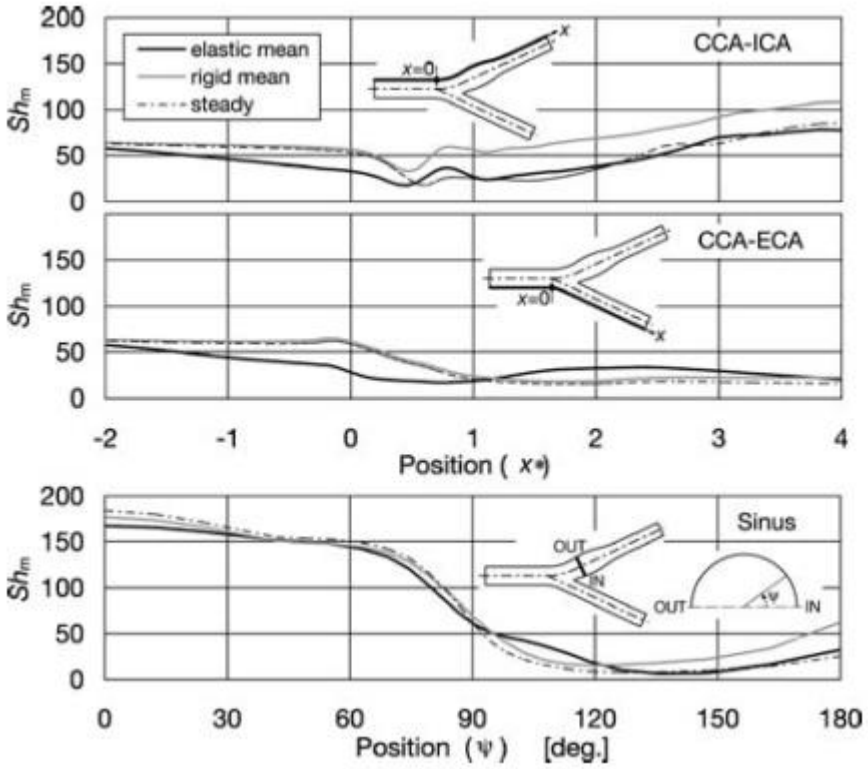

Figure 4.3: Profiles of the time-mean Sh along the outer wall of the common carotid artery and internal carotid artery, the outer wall of the CCA and external carotid artery, and the periphery of the ICA sinus for three different haemodynamic models: transient with compliant arterial walls (elastic mean), transient with rigid walls (rigid mean) and steady state with rigid walls (steady) from Tada and Tarbell (2006).[250]

Although slightly off topic, in terms of simulating oxygen transport in arteries, a 2D study by Zierenberg et al. (2007) analysing the oxygen transfer from a circular cylinder filled with an oxygen source to surrounding blood is worth mentioning.[275] The investigation was a fundamental study into the gas exchange and haemodynamic conditions needed for the proper working of an artificial lung. In this particular study the authors used an oxygen transport model which incorporated the bound oxygen as well as the free oxygen present in the plasma. This is similar to the oxygen transport

model adopted here, although a constant shear-augmented dispersion coefficient ($1.5\times10^{-11}m^2/s$) of RBCs was used and also the calculated Schmidt number (Sc) was lower (1000) compared with other studies (~3600). Sc is a dimensionless number that is defined as the ratio of the viscous diffusion rate and the mass diffusion rate, $Sc=\frac{\nu}{D}$, where in this case ν is the kinematic viscosity of blood and D is the mass diffusivity of oxygen in blood. This study demonstrates some of the other applications of an accurate oxygen transport model in the design of medical devices.

Coppola and Caro (2008) analysed the oxygen mass transport in two U-bends: one with a straight centreline and one with a helical centreline.[43] The adopted oxygen transport model only incorporated the free oxygen, with the effect of the bound oxygen accounted for by using the same correction factor of 2.5 as used by Qiu and Tarbell (2000)[203] based on results from Moore and Ethier (1997).[162] They observed that the WSS and oxygen supply uncoupled downstream of planar bends, and that secondary motion resulting from the 3D geometry can influence both the WSS and Sh distribution.[44] In 2009 Coppola and Caro analysed the WSS distribution and oxygen mass transport in an artery with a helical section with a pulsatile inlet velocity.[45] The pulsatile flow was sinusoidal in nature with the effects of variation of the amplitude and frequency studied. It was found that there is a sweeping motion of the Dean Vortices and with increasing amplitude the WSS and oxygen flux increases. Increasing the frequency of the pulsatile waveform increased the WSS, but had no effect on the oxygen mass transfer.

Liu et al. (2010) analysed the effect of spiral flow on the oxygen mass transfer in the aorta.[140] The simulations were carried out in four difference models of the aorta: a realistic model constructed from MRI images with all geometrical features of the aorta intact, and three other models with decreasing amounts of features included. They

concluded that spiral flow may have physiological significance and enhance oxygen flux into the arterial wall, which will be discussed further in Section 4.4.

Carroll et al. (2010) conducted an experimental validation of advection-diffusion discretisation schemes used for solving mass transport numerically.[29] In this study the authors simulated the mass-transport of a species concentration in an idealised aneurysm geometry solved using four different discretisation schemes: first-order upwind, power law, second-order upwind and quadratic upstream interpolation for convective kinetics (QUICK). The results of these simulations were then compared with the experimental results taken from fluid samples extracted from a glass aneurysm model. They concluded that second order or QUICK discretisation schemes are most appropriate and produce the most accurate prediction of the mass transfer field when compared with the experimental results.[29]

One interesting study was conducted by Biasetti et al. (2014) who assessed four patient-specific geometries for low oxygen mass flux into the arterial wall by locating regions of low haematocrit.[18] This was interesting because instead of modelling the oxygen transport the authors modelled the RBC transport and from the results induced that areas where the haematocrit was low must coincide with areas that the oxygen flux into the arterial wall was low. The RBCs were modelled using the Phillips' shear-induced-model for RBC dispersion where the RBCs are assumed to be rigid particles.[196] The areas located matched with areas know to be prone to formation of atherosclerotic lesions with an example shown in Figure 4.4. The authors also found that the shear-induced migration of the RBCs away from the arterial wall surface could be enhanced or dampened by secondary flows within the blood flow that convect RBCs away or towards the arterial wall. With the exception of this study by Biasetti et al. and the previously mentioned study by Zierenberg et al. all of the above studies only included

the free oxygen in their blood oxygen transport models. Additionally, the oxygen concentration at the arterial wall surface was assumed to be constant with the Sh used to analyse the oxygen flux. The test cases presented in Chapters 6 and 7 will consider the advantages and disadvantages of this approach.

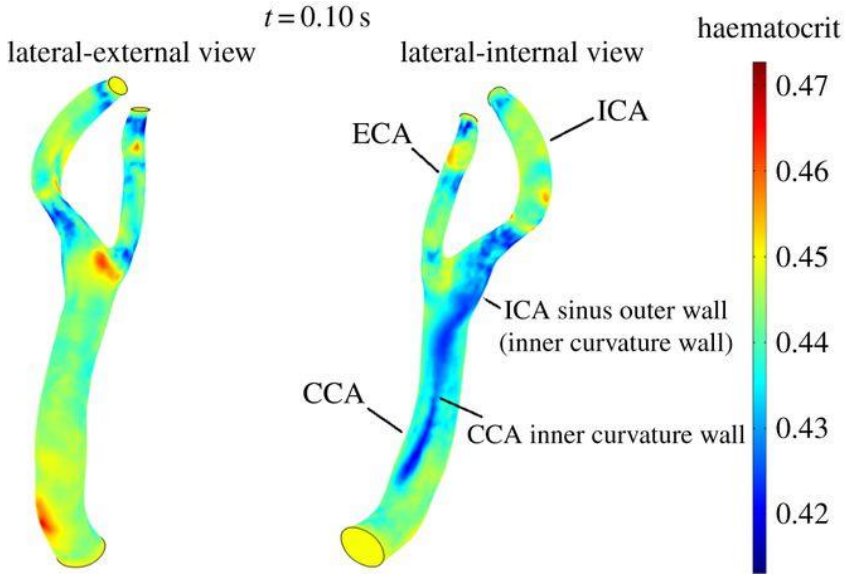

Figure 4.4: Wall haematocrit in the patient-specific normal carotid bifurcation during the cardiac cycle at t=0.10s from Biasetti et al. (2014).[18]

4.2.2 Coupled Blood-Arterial Wall Analyses

Oxygen transport models which incorporate the blood and the arterial wall have an advantage over the previous wall-free models in that the interaction between the mass transport processes ongoing in both domains can be studied. These also offer the advantage of predicting the effects of haemodynamic conditions on the oxygen concentration in the wall more accurately in comparison with using the Sh. The disadvantage of these models is that there are many factors that affect the oxygen consumption and diffusion within the wall which could lead to a lot of variability in the oxygen levels in reality. For the purpose of analysis, the standard approach is to use

constant consumption and diffusion parameters for the arterial wall. The results obtained in this case are only varied according to the set parameters, the haemodynamic conditions, the thickness of the arterial wall and the boundary conditions. Thus the effects of different cell composition, atherosclerotic lesion progression, inflammatory cellular activity and vasa vasorum penetration are ignored.

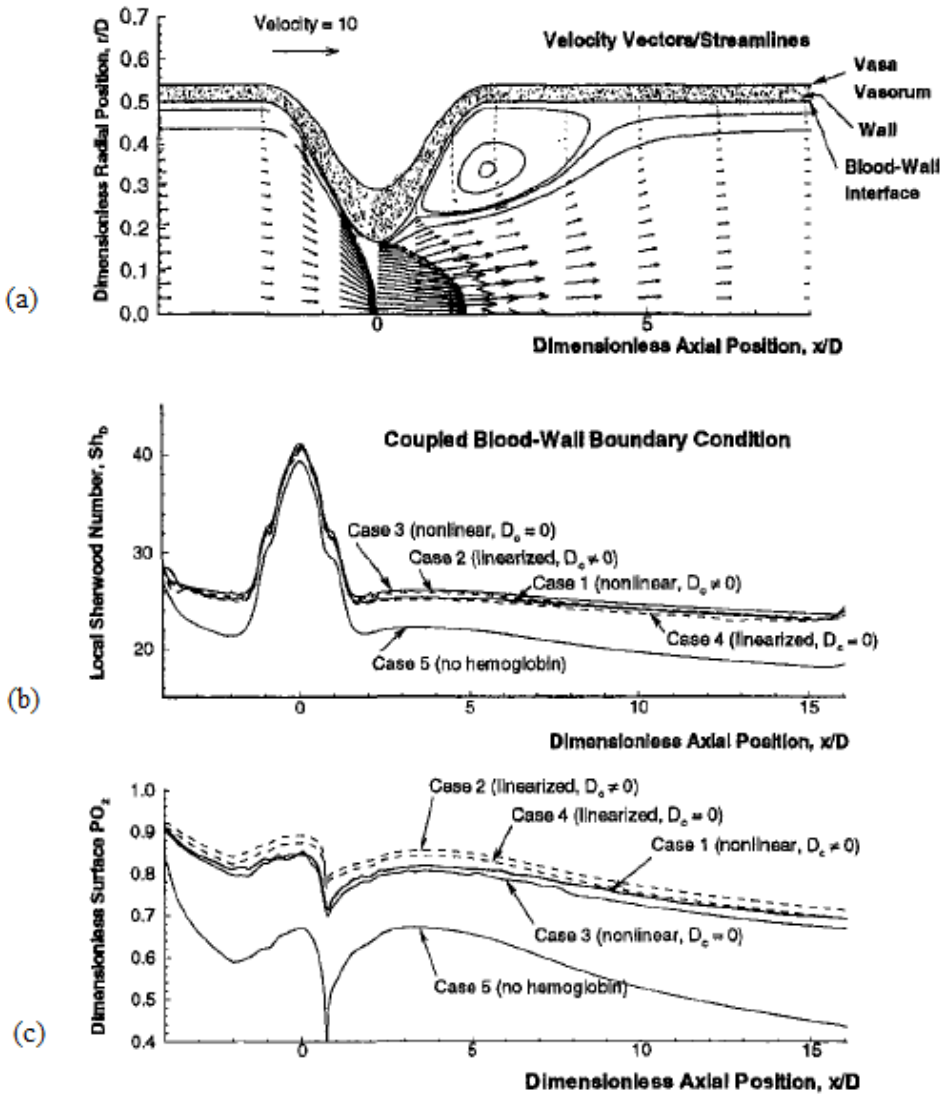

Figure 4.5: (a) Model geometry and velocity vector plot for steady flow through the stenosis (b) Local Sh and (c) dimensionless surface PO_2, $(PO_2-PO_{2,w})/(PO_{2,in}-PO_{2,w})$, as a function of dimensionless axial position for all five cases with fluid side

transport coupled to an oxygen consuming wall. Adapted from Moore and Ethier (1997).[162]

Coupled wall-lumen models of oxygen transport have the advantage over wall-free models in that they can provide information on the concentration profiles within the arterial wall. Moore and Ethier (1997) analysed the oxygen transport within a 2D geometry of a 89% area reduction axisymmetric stenosis under steady flow conditions, as shown in Figure 4.5.[162] The consumption of oxygen in the arterial wall is included along with the non-linear oxygen binding properties of haemoglobin. As part of the study the authors analysed the effects of simplifying the blood oxygen transport model used, and of artificially decreasing Sc. As well as demonstrating the disadvantages of simplifying the blood transport model, the authors concluded that further studies of oxygen transport in large arteries must include the oxygen transport into an accurate model of the arterial wall. This study is important for the work presented here because the blood oxygen transport models, as described in Chapter 3, were based on those used by Moore and Ethier. How their study differed was that they assumed a constant shear-induced RBC dispersion coefficient, $1.5\times10^{-11}m^2/s$, whereas the models used here adopted a variable dispersion coefficient that was dependent on the shear rate. This is more reflective of the range of shear rates experienced in the arteries modelled here. As mentioned previously, many subsequent studies reference Moore and Ethier's results when simplifying their oxygen transport models, for instance neglecting the bound oxygen. The validity of this is debated in the conclusions section of Chapter 7.

Perktold et al. (2002) modelled the oxygen transport, along with wall and suture mechanics, in anatomically-correct bypass configurations.[193] Three different types of anastomosis were modelled: conventional, Taylor-patch and Miller-cuff with venous

interposition grafts of different modifications. The haemodynamic conditions were assessed for each geometry and it was found that there was a correlation between low WSS and reduced oxygen flux into the arterial wall.

One particular study published by Banerjee et al. (2008) modelled the oxygen transport in a simplistic 2D avascular arterial wall of a coronary artery stenosis before and after angioplasty.[7] The stenosis pre- and post-angioplasty was found to have a significant impact on the luminal PO_2 values along the arterial wall and the calculated flux into the arterial wall. The geometries did not include stent struts, and the arterial wall was assumed to be homogeneous and of constant thickness.

Tada (2010) continued his previous work modelling the oxygen transport and transient blood flow in a carotid bifurcation model by including a homogeneous arterial wall and neglecting the effects of a compliant arterial wall, as modelled previously by Tada and Tarbell (2006).[248,250] The geometry was constructed from averaged dimensions taken from several previous studies: Ma et al. (1997), Bharadvaj et al. (1982), and Perktold and Rappitsch (1995).[15,142,194] Three PO_2 profile locations were adopted for comparison from *in vivo* measurement locations used by Santilli et al. in dog carotid arteries.[217] One simplification implemented was that the curvature of the ICA was ignored which would produce a swirling flow within the ICA. This would not alter the WSS or oxygen flux within the carotid sinus, where two of the three measurement locations are situated. The region of low oxygen flux on the outer wall of the carotid sinus, as observed by previous authors, was predicted in this study also. In addition, it was found that the effect of oscillatory blood flow on the PO_2 levels in the arterial wall was negligible. The three PO_2 profile plots exhibited a considerable difference when compared with Santilli et al. as shown in Figure 4.6. A steep gradient at the luminal surface present in the results presented by Santilli et al. was not reproduced in these results. Additionally, the

results failed to predict the minima point in all three plots. The geometry used by Tada was adapted for use in Test Case 1, as described in Chapter 6.

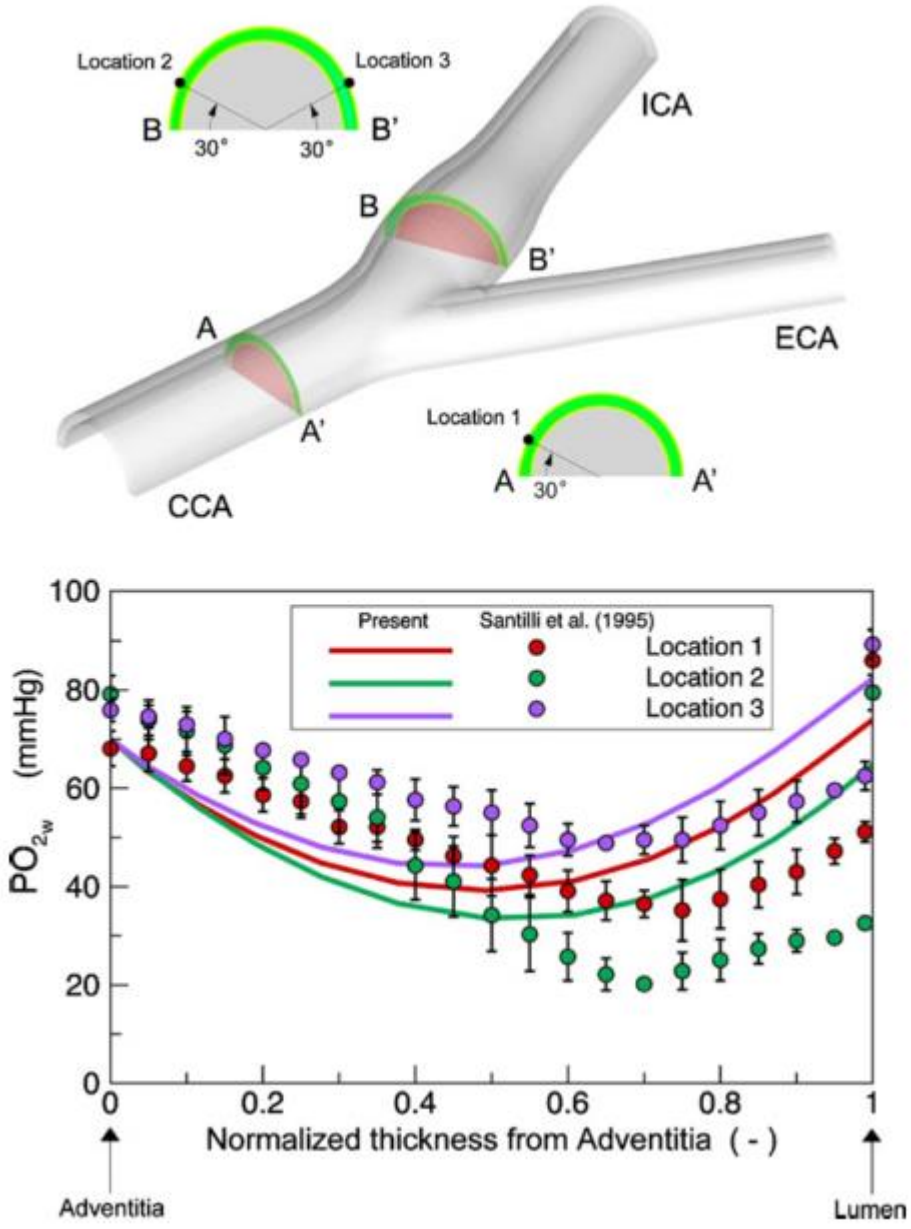

Figure 4.6: Transarterial wall PO_2 profiles at three locations from Tada (2010).[248]

Caputo et al. (2013) conducted an analysis of the haemodynamic conditions and oxygen transport in three geometries of stented coronary arteries with different centreline

curvatures.[23] Initially, a stainless steel, balloon-expandable stent was implanted in a healthy RCA at a balloon-to-artery ratio of 1.4:1. After 14 days the stented artery was harvested and the stent was imaged using high resolution micro-CT scans. The stent geometry was then imported into a commercial FEA software where an idealised arterial wall was over-expanded and allowed to relax onto the stent geometry. This was done to obtain an accurate representation of the arterial wall prolapse without the neointimal growth present. The resultant geometry had a straight centreline that extended proximal and distal to the stented region. Two additional geometries were constructed whereby the proximal and distal regions had a curved centreline. The two radii of curvature were 36 and 20mm (labelled as CU36 and CU20 in Figure 4.7), which corresponded to the range of curvatures of human and porcine RCAs obtained from angiographic data. The simulations were steady-state and the bound oxygen was ignored. When the predicted results were compared with the histological data, areas of predicted low WSS (defined by Caputo as <0.4Pa) and low oxygen concentration were found to match with areas of increased NIH, with some sample plots shown in Figure 4.7. This is the only 3D study of oxygen transport in stented arteries carried out to date which incorporates the stent struts, which were found to have a considerable impact on the local haemodynamics and oxygen transport. Because of the limitations in the oxygen transport model adopted it is possible that the extent of the hypoxic regions in the arterial wall was under-predicted.

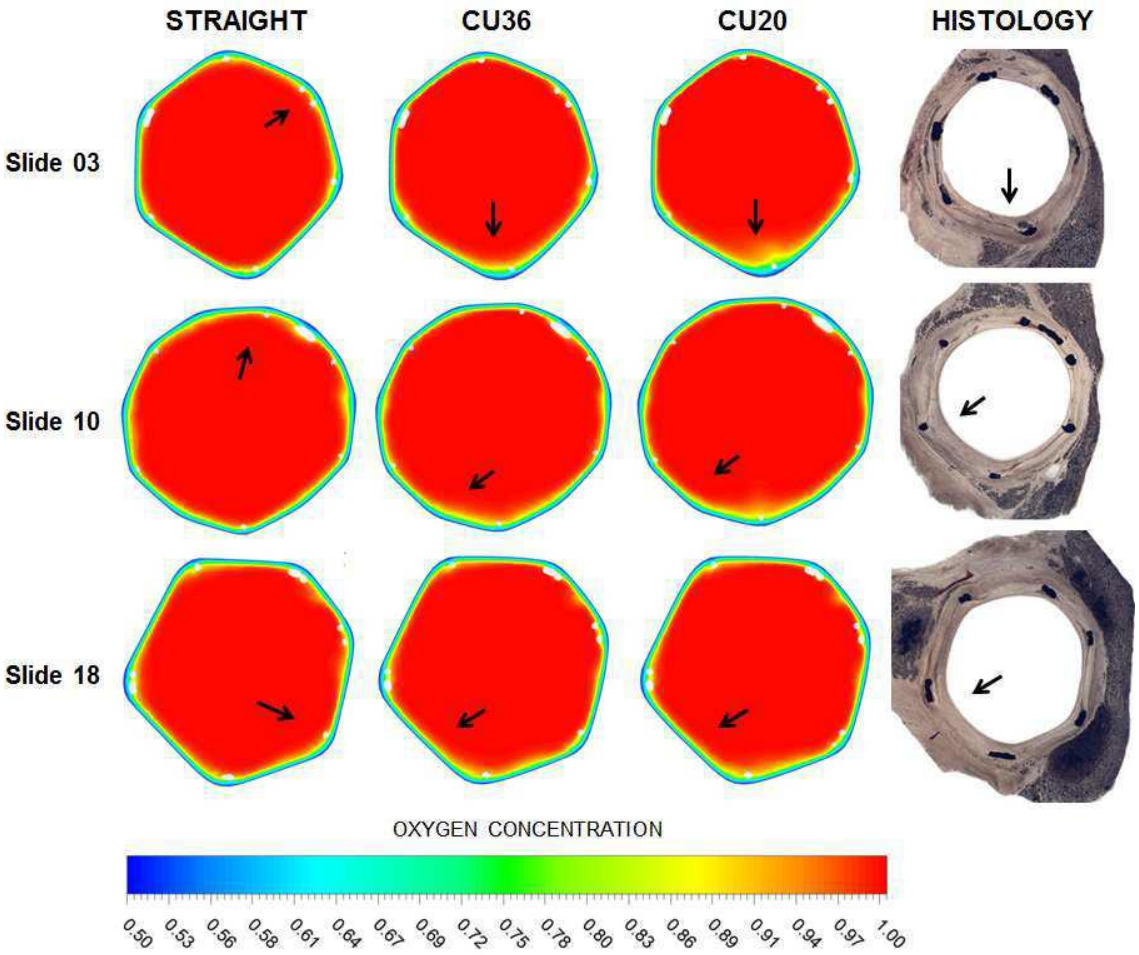

Figure 4.7: Qualitative comparison of the oxygen concentration between the computational models: straight, and with a radius of curvature of 36 and 20 mm, labelled as CU36 and CU20, respectively, as modelled by Caputo et al. (2013).[23] Also shown on the right are the corresponding histological images at three selected sections. Black arrows indicate the wall region with the lowest oxygen concentration in the computational models and the greatest neointimal thickness in the histologies.[23]

4.3 Haemodynamic Analyses of Stented Arteries

The local haemodynamics present in arteries have been shown to affect the biological processes which take place following stent implantation, as discussed in Chapter 2. CFD simulations are required for analysing the local haemodynamics within a stented artery because of the size of the arteries concerned and consequently, the difficulty in analysing the blood flow *in vivo* or *in vitro*. Additionally, the incidence and severity of ISR has been found to vary with stent type and therefore, comparison of stent types using CFD is warranted. Throughout the relatively short history of CFD analysis of stents there are three reoccurring themes: how stent design affects the local haemodynamics within the stented region, how realistic are the geometries used, and what haemodynamic variables are used to assess the designs. The first theme was discussed in Chapter 2. The second theme is common to the oxygen transport studies above and will also be apparent in relevant studies below. In reference to the third theme the range of haemodynamic variables used in assessing stent geometries, which endeavour to capture the flow features more accurately, is ever expanding and a select amount will be mentioned throughout this section and Section 4.4.

LaDisa et al. (2003) were among the first to analyse the haemodynamic impact of stenting a coronary artery using CFD.[130] In their study the arterial wall surface was modelled as a straight cylinder and the stent investigated was similar to the Palmaz-Schatz stent (Johnson & Johnson, Fremont, CA, USA). They compared the WSS distribution within the stented geometry with that of an unstented geometry. The simulations were based on previous *in vivo* measurements of canine LAD coronary artery diameter and blood flow velocities before and after stent implantation.[131] The results of this study showed that the stent geometry had a dramatic effect on the WSS distribution along the luminal surface including that the minimum WSS value decreased

by 77% in comparison with an unstented artery, and stagnation zones were localised around stent struts. Following this study LaDisa et al. conducted several more studies into how stent designs and deployment ratios affect the WSS and spatial WSSG distributions within stented coronary arteries. Following this, in a paper published in 2004, LaDisa et al. assessed the impact of deployment diameter and stent strut properties including number, width and thickness, on the WSS distribution. Increasing the deployment ratio from 1.1:1 to 1.2:1 increased the area of the stented luminal surface exposed to low WSS (defined as <0.5Pa) 12-fold. Doubling the number of struts from four to eight resulted in a 2.75-fold increase in the luminal surface area exposed to low WSS. Reducing the strut thickness from 0.096 to 0.056mm caused the total area exposed to low WSS to decrease by approximately 87%. A reduction in stent strut width resulted in an increase of 9% of the stent area being exposed to low WSS. This study confirmed that stent design properties and deployment ratio could influence the local haemodynamic conditions and consequently, affect the biological processes post-stent implantation.

In a paper published in 2005 LaDisa et al. assessed the impact of a more realistic representation of the arterial wall deformation on the transient WSS. The hypothesis was that in reality the arterial wall would straighten circumferentially between stent struts and if modelled this would produce different WSS distributions in comparison with idealised cylindrical stented arteries. To derive the circumferentially straightened geometries an automated construction algorithm was used. The WSS and the WSSG were assessed for two different geometries based on the Palmaz-Schutz stent and they concluded that the arterial wall deformation is important in determining the WSS distribution.

He et al. conducted a parametric study, published in 2005, of stent strut geometries using geometries comprising of just two stent struts in a flat configuration with and without a link strut.[93] The authors assessed the geometries in terms of the normalised axial WSS and the percentage of the arterial wall luminal surface exposed to a low WSS threshold value of <0.5Pa. This was done for a variety of stent strut configurations and carried out under high and low flow conditions. The study confirmed that stent strut configuration could influence the local haemodynamics and, specifically, that struts should be, wherever possible, orientated parallel to the vessel axis to reduce flow recirculation and low WSS zones.

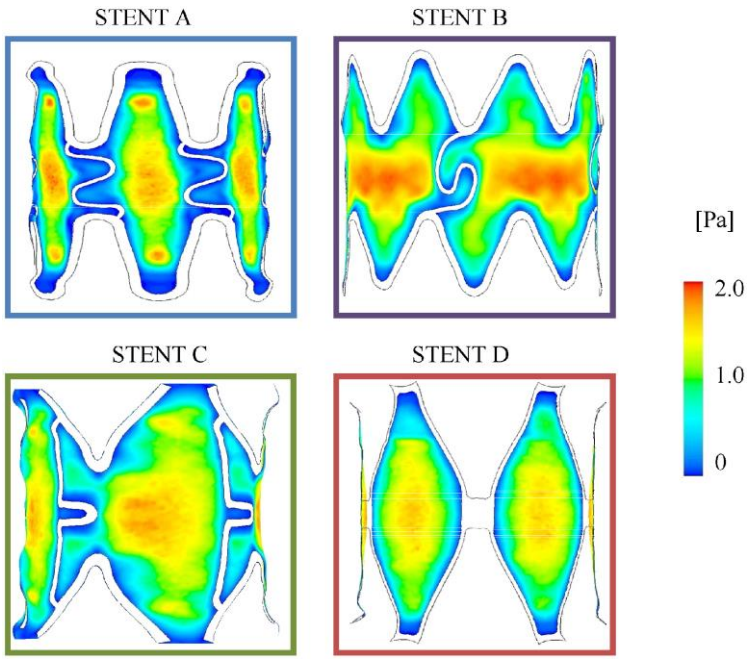

Figure 4.8: Contour plots of the WSS magnitude on the arterial wall portion delimited by the links and the stent struts at the diastolic peak (0.16s) for each stent model, from Balossino et al. (2009).[6]

Balossino et al., in a paper published in 2008, compared the effects of four different stent designs, similar to four commercially available stents, on the local haemodynamics within stented coronary arteries. Single units of each stent design were expanded

virtually using FEA in idealised arteries with simplified arterial plaque and the resultant geometries were analysed using a transient velocity inlet boundary condition. Given that the CFD geometries used were derived using FEA, and also included the presence of plaque, they were more representative of what would happen *in vivo*. The percentage area of the arterial wall luminal surface exposed to a low WSS threshold value of 0.5Pa at six time instants during the cardiac cycle was used to compare the four different stent designs, with the contour plots of the WSS magnitude at diastolic peak for each stent shown in Figure 4.8. Additionally, the effect of stent strut thickness on the WSS was assessed and interestingly, it was found that a thicker strut, in this instance, results in less of the arterial wall being exposed to low WSS. The authors note that this observation disagrees with previous studies and may be the result of modelling the pulsatile flow with a FEA-derived geometry; i.e. more realistic geometries than previous studies. The authors also analysed the peak WSS and noticed that the greater the distance between stent struts the higher the peak WSS values are. This study further confirmed the link between stent design parameters and the WSS distribution within a stented coronary artery.

Murphy and Boyle in 2008 assessed the effects of increasing levels of physiological realism on the WSS and WSSG in stented coronary arteries. Similar to LaDisa et al. (2005), where the arterial wall was modelled with circumferentially straight sections between stent struts, Murphy and Boyle developed a novel methodology to predict the tissue prolapse occurring between stent struts to increase the accuracy of how the arterial wall surface was represented. Using Young's equation and distance between the struts, a curved surface was generated to represent the tissue prolapse. Additionally, the effect of stent oversizing, where stents are typically implanted with a stent-to-artery diameter ratio of 1.1-1.2:1, was also assessed. Modelling the tissue prolapse and the

stent oversizing were both shown to affect the WSS and WSSG distributions in the stented coronary arteries in comparison with simplified straight cylindrical artery wall models. Therefore, increasingly realistic arteries were deemed necessary to accurately assess the haemodynamic conditions in stented coronary artery models. Following on from this study, Murphy and Boyle in 2010 carried out a transient CFD comparison study of three stent designs, as shown in Figure 4.9. The four variables used in the comparison were WSS, WSSG, wall shear stress angel gradient (WSSAG), and oscillatory shear index (OSI), and a detailed statistical analysis of the results was carried out. One of the key conclusions of this study was that just applying the threshold assessment technique to stent comparison was insufficient in elucidating the effects of stent implantation on coronary artery haemodynamics and further studies should include statistical analysis of the results.

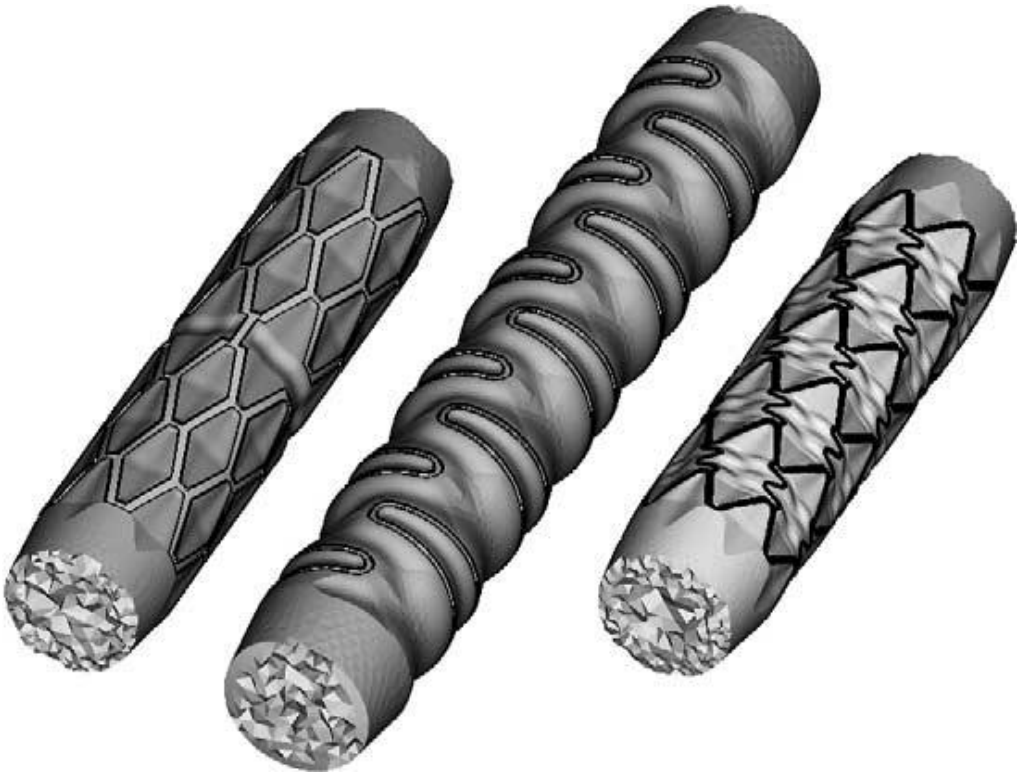

Figure 4.9: Solid models of the LAD arteries implanted with (from left to right) the PS stent, the GR-II stent and the Bx stent from Murphy and Boyle (2010).[172]

In a paper published in 2010, Pant et al. compared the haemodynamic conditions induced by five stent designs, similar to commercially available stents, in idealised stented coronary arteries. All simulations had a transient inlet velocity, the arterial wall was modelled as a straight cylinder and the only a quarter of the stented domain was modelled to exploit the periodic symmetry of the stents to reduce computational expense. The WSS and the modified oscillatory shear index (MOSI) were assessed and it was found that the length of the link struts in the cross-flow direction and their alignment with the main flow were critical factors in the haemodynamic performance of the stent designs.

In terms of the generation of the geometries required for the CFD simulations of stented arteries there have been a variety of avenues pursued by different studies. Gundert et al., in a paper published in 2011, described a rapid and computationally inexpensive method to virtually implant stents in patient-specific artery models rendered from medical imaging data. According to this method, a parameterised version of the stent is geometrically flexed until its centreline follows the centreline of the implanted artery. This gives an idealised stent geometry which includes the stent struts in a patient-specific model but neglects the stent and vessel deformation. Morlacchi et al. in a paper published in 2011 utilised a sequential approach of FEA followed by CFD to investigate the final kissing balloon technique for stenting a coronary bifurcation. A stent model was virtually expanded in an idealised atherosclerotic bifurcation model using FEA and the resultant geometry was analysed using CFD. Additionally, Chiastra et al. in two papers in 2012 and 2013 continued this work with a similar CFD analysis of stented coronary bifurcation models. The stents were virtually expanded using FEA within artery models constructed from pre-operative computed tomography angiography and conventional coronary angiography images. Transient CFD simulations were then

carried out and the TAWSS, relative residence time and OSI were assessed. In these studies the feasibility of virtually implanted patient-specific coronary bifurcation geometries for haemodynamic assessment was demonstrated. In terms of assessing the impact of using more realistic stented geometries, Martin et al. (2014) compared the transient haemodynamics within three stented geometries generated using FEA or purely idealised. The authors found that stent and vessel deformation had a significant impact on the local haemodynamics within a stented artery. Critically though, the computational cost of virtually expanding stent geometries using FEA is significant and therefore, in most instances the hardware and time expense would make this method unfeasible, at least for the time being.

4.4 Helical Flow

Experiments conducted by Caro on the dispersion of indicator flowing in simplified models of the circulatory system showed that large secondary motions were induced by bends in the models.[25] It was postulated that these secondary motions had particular physiological importance in circulation, listing possible advantages as being the prevention of stagnation zones and flow separation at the arterial walls. Inspired by observations of spiral folds on the inner endoluminal surface of arteries using fibre-optic angioscopy by Stonebridge and Brophy,[241] postulated by Caro et al. as being helical distributions of lesions due to low WSS zones,[27] Stonebridge et al. went on to show that blood flows in the right common and distal superficial femoral and the left common femoral arteries with a secondary rotational motion which produces an overall spiral (helical) flow. This was detected using Doppler ultrasound with the probe aligned perpendicular to the axial flow, as shown in Figure 4.10 along with a sample ultrasound image.[245]

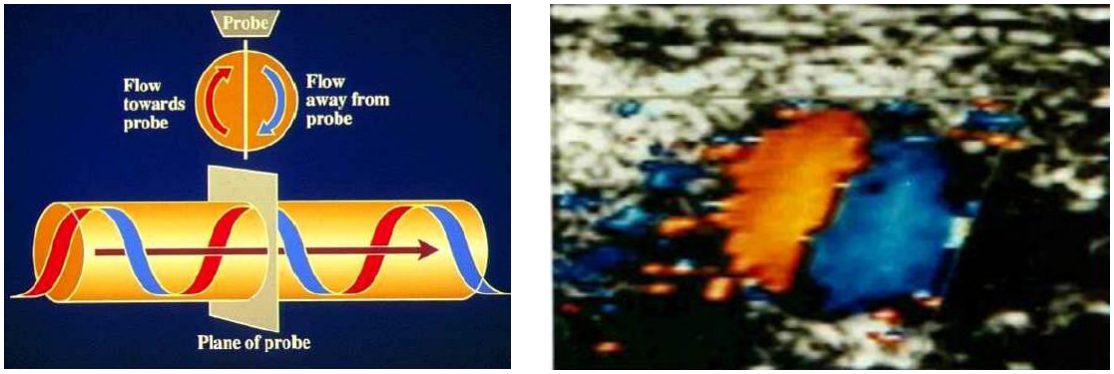

(a) (b)

Figure 4.10 (a): The Doppler ultrasound set up used in the experiment described by Stonebridge et al.[245] (b): This sample image clearly shows the characteristic red/blue split signifying helical flow as observed *in vivo*.[244] Reproduced with permission from Vascular Flow Technologies.

The terms spiral flow and helical flow are used interchangeably in the literature, but for the purpose of this literature survey, helical flow is the term used. The helical flow in arteries is induced by their non-planar curvature and the heart itself. It has been proposed that the secondary motion, i.e. the rotational motion, of the blood flow is induced by the twisting of the left ventricle during contraction,[149] and then accentuated upon entering the aortic arch.[63,119] This twisting is, in part, due to the structure of the ventricular myocardial band of the heart which has been found by Torrent-Guasp to be spatially orientated in the form of a helix.[257] Brecher also observed that there existed a continuous negative pressure within the ventricle[21] which Marinelli cited as evidence of a perpetual vortex within the ventricle,[148] which provides the ventricular suction during the diastolic period, and possibly incites the initial helical flow. Helical flow had been observed before in the human aorta by Segadel and Matre[222] and again by Kilner and Yang using magnetic resonance imaging (MRI),[119] and by Frazin et al. in canine

thoracic and abdominal aortae using Doppler ultrasound,[63] but the studies by Stonebridge et al. were the first to show that the helical flow was maintained in the peripheral arteries also. Suo concluded, following MRI and CFD analysis, that helical flow in the aorta could only be produced by including the specific aortic motion caused by the beating heart.[247] Caro et al. published observations from MRI data of flow through healthy human arteries with non-planar curvature and branching which showed how these features appeared to significantly affect the haemodynamics, including WSS.[27]

Many of the beneficial effects of helical flow in the arteries were originally only postulations by researchers in the area; however, there is growing evidence which support these postulations. Stonebridge et al. discuss how there are theoretical advantages to helical flow, including rotationally-induced stability, reduced turbulence, and a beneficial effect on mechanisms of endothelial damage.[245] In a paper by Caro et al. it was highlighted that greater mixing and more uniform WSS was expected in the cardiovascular system which was found to be commonly non-planar.[27] Doorly et al. found through CFD analysis that a simple modification to the geometry of an end-to-side anastomosis, where the graft is rendered approximately helical, produced a profound effect on the flow, enhancing the swirling motion of the flow downstream.[52] Zabielski and Mestel concluded from a CFD analysis into helical flow around arterial bends that the non-planar curvature limits the severity of flow separation at the inner bend and reduces variation of the WSS.[271] This was confirmed in a CFD analysis by Papaharilaou et al. of planar and non-planar end-to-side anastomoses where it was found that the introduction of an out-of-plane curvature produced a significant change in the spatial distribution of WSS and a 10% reduction in the time-averaged peak WSS magnitude.[189] The spatial extent of the elevated oscillatory WSS regions was reduced in

the non-planar model in comparison with the planar model and, given that Ku et al. found a correlation between elevated oscillatory WSS and NIH, there are effectively less areas exposed to unfavourable, in terms of disease progression or ISR, flow conditions in the non-planar geometry.[128] In a numerical study of vortical flow identification and flow transport in arterial graft geometries, Doorly et al. found that significantly greater particle mixing was prevalent in the non-planar geometry compared with the planar geometry, with continual transport of particles away from the wall, thus lessening near-wall particle residence times.[53] Stonebridge et al. compared helical and non-helical flow patterns through stenoses using MRI *in vitro* and CFD modelling.[243] In this study it was found that near-wall turbulence energy was considerably less with helical flow ($0.025 m^2/s^2$) than non-helical flow ($0.16 m^2/s^2$) beyond the stenosis, with turbulence being associated with substantial WSS fluctuations in both space and time.[146] The degree of helical flow has been found by Houston et al. to be reduced in atherosclerotic arteries, although a direct relationship between atherosclerotic lesions and the absence of helical flow has not been proven, and within these arteries the turbulent nature of the resulting flow encourages further development of the disease.[103] A study by Morbiducci et al. indicated that helical flow dampened WSS temporal gradients in aortocoronary bypass grafts.[164] Morbiducci et al. also conducted an *in vivo* investigation into the helical flow patterns in the aortic region of five healthy humans using 4D phase-contrast MRI, and CFD analyses of the reconstructed aortic geometries. It was found that helical-blood-flow dynamics is common to healthy individuals, and that helical flow might be caused by natural optimisation of fluid transport processes in the cardiovascular system, aimed at obtaining efficient perfusion of blood and nutrients therein to the organs and tissue.[166] In predicting these transport processes, and also those involved in atherogenesis, a paper by Chiastra et al. highlighted that flow properties

such as velocity, helicity and vorticity are primarily responsible, and that researchers should consider these bulk flow properties in addition to the WSS variables.[39] Liu et al. conducted a CFD study of the transport of LDL in four models of human aortae and found that the helical flow induced in the aortic arch had a beneficial effect on LDL concentration at the arterial wall.[141] Helical flow has also been shown to be instrumental in moderating shear-induced activation of platelets, which is a problem for some cardiovascular implants.[155,165,191,273] Massai et al. found through CFD simulations of a reconstructed model of a left carotid bifurcation that an inverse relationship existed between the helical flow index (a variable for measuring the helical structure of the flow) and the probability of shear-induced activation of platelets.[155]

An analysis by Paul and Larman using CFD of helical flow downstream of a 75% stenosis found that turbulent kinetic energy was reduced post stenosis.[191] The helical motion provides rotational stability to the flow, reducing flow disturbance and turbulence, which is a beneficial effect. Conversely, as noted by Paul and Larman, helical flow also produced oscillating WSS in the post-stenosis model,[191] which is considered a detrimental effect possibly causing damage to the endothelium. In addition to this, other researchers have speculated on whether the effects of helical flow are entirely beneficial. Frazin et al. considered that although the rotational element of the flow may be important physiologically for organ perfusion, pathologically, there may be a relation between the shear forces induced by helical flow and plaque deposition.[62] A paper by Texon showed that "serpentine flow" in relatively straight vessels may also produce zones of diminished lateral pressure and atherosclerosis.[256] A CFD study of helical grafts by Zheng et al. found that along with the benefits of increased WSS and swirling flow, there was also an enlarged pressure drop and low velocity concentrated in one area in a helical graft model which could lead to increased NIH or thrombosis.[274]

Pressure drop was found to be proportional to the helicity of an inlet flow into an idealised stented artery in a CFD study by Chen et al.[36] CFD simulations conducted in this study showed pressure drops for the stent with swirling flow to be 164, 167 and 173 Pa for inlet helicities of 3.5, 6.4 and 14.5 m/s^2, respectively, whereas for the stent with normal inlet flow the pressure drop was 163 Pa. Beneficial effects of helical flow also noted in this paper were that the average lengths of the recirculation zones between the stent struts and OSI, a measure of the change in direction and magnitude of the WSS vectors during the cardiac cycle, were reduced with increasing helicity of the inlet flow, which enhanced the average WSS in comparison with normal flow.[36]

Considering the correlation between adverse flow conditions and increased NIH,[10,74,91,97,122,188] and the effects of the local haemodynamics on the other biological processes leading to ISR, discussed in Section 2, there are two particular stents which are embracing the beneficial theoretical effects of helical flow, i.e. increasing particle mixing, reducing areas of disturbed flow and providing a more uniform WSS, and endeavouring to restore this natural blood flow pattern in a stented artery.

4.4.1 BioMimics 3D Helical Stent

The BioMimics 3D helical stent, as shown in Figure 4.11, is being developed by Veryan Medical Ltd which has its head office in Horsham, West Sussex, UK and research and development based in Galway, Ireland. This stent appears to have evolved from a helical bypass graft, marketed as SwirlGraft, which incorporated Small Amplitude Helical Technology (SMAHT), developed at Imperial College London. The theory behind this technology is that a normal planar bend induces two equal but opposite Dean vortices within the flow, whereas in a non-planar bend, as found in SMAHT, one

of the vortices begins to dominate the other as the flow progresses through the bend, producing helical flow.

Figure 4.11: BioMimics 3D helical stent. Reproduced with permission from Veryan Medical Ltd.

Caro et al. compared SwirlGraft devices with conventional expanded polytetrafluorethylene (ePTFE) arteriovenous shunts in two pigs.[26] Even though the experiment was limited by the number of pigs employed, the results of this study were still positive with consistently less thrombus formation and NIH in SwirlGraft devices compared with the conventional devices. Interestingly, when the porcine arterial sections were analysed, two seemingly helical ribbons of NIH were found which seemed to match with the predicted areas of low WSS in a CFD model of SwirlGraft. A clinical trial was carried out by Huijbregts et al. in which 20 patients requiring vascular access grafts were implanted with SwirlGraft.[107] It was found that the graft was prone to thrombosis, possibly due to the loss of the helical geometry of the graft upon implantation. It was concluded by Huijbregts et al. that with modifications to

implantation techniques and the SwirlGraft design that the product might advance to a randomised controlled trial.[107]

Veryan Medical has taken this same SMAHT technology and applied it to peripheral stent design in the form of the BioMimics 3D helical stent, shown in Figure 4.11. In addition to the helical flow benefits, the stent also includes design features such as tapered radial stiffness and collinear stent ends which, in theory, help in providing a more gradual change in the wall stress and luminal area between the unstented and stented portion of the artery, as opposed to a dramatic change which could form a stagnation zone in the flow, encouraging thrombus and neointimal formation. For peripheral stent implantation, in the femoral artery particularly, as the leg bends the stent must be flexible enough to allow movement and longitudinal slackening of the artery without stent fracture or the infliction of damage on the arterial wall. The BioMimics 3D helical stent has been assessed in this regard through a human cadaver study as stated on the company website (http://www.veryanmed.com/). In this study the BioMimics 3D stent and control straight stents were implanted in the lower and mid superficial femoral artery and the upper popliteal fossa of three cadavers and the knee joint was flexed over a range of angles. It was observed that the BioMimics 3D helical stent could increase its helicity and thus take up the slack in the artery upon flexion of the knee, while also avoiding permanent deformation, unlike the straight stents. This ability is deemed a valuable characteristic which could prolong the life of a peripheral stent by absorbing stresses which ordinarily could cause fracture.

As mentioned earlier, studies by Lee et al. into the effects of supplemental oxygen on NIH and by Tarbell into mass transport of molecules, e.g. oxygen, into arterial walls and localisation of atherosclerosis and NIH, highlight the importance of flow conditions and oxygen flux into the arterial wall on the development of NIH.[135,252] Coppola and

Caro, citing Tarbell and the link between a local lack of oxygen and both atherosclerosis and NIH, used CFD to examine the effects of arterial three-dimensionality on the distribution of WSS and the mass transport of oxygen from the blood flow into the arterial wall in a U-bend by modelling the blood vessels as either a cylindrical or helical conduit.[44] It was shown that a helical geometry can reduce both the range and extent of low WSS regions and substantially increase the oxygen flux through the walls.

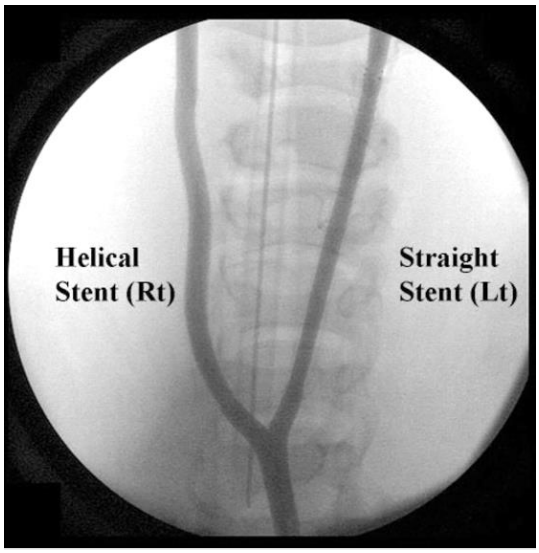

Figure 4.12: Angiograph showing the BioMimics 3D helical stent and the conventional straight stent inserted in the contralateral (left) and common carotid artery (right) respectively.[228] Reproduced with permission from Veryan Medical Ltd.

Shinke et al. presented results from a pilot porcine trial where two pigs were implanted with a conventional stent in one common carotid artery and the BioMimics 3D helical stent in the contralateral artery, as shown in the angiograph in Figure 4.12.[228] Comparisons were made between the histological sections taken at three locations in the two arteries, as shown in Figure 4.13. As can be seen from these sections the extent of

NIH with the helical stent was far less than with the conventional one and thus it was concluded that the helical stent's improved flow regime helped in minimising NIH.

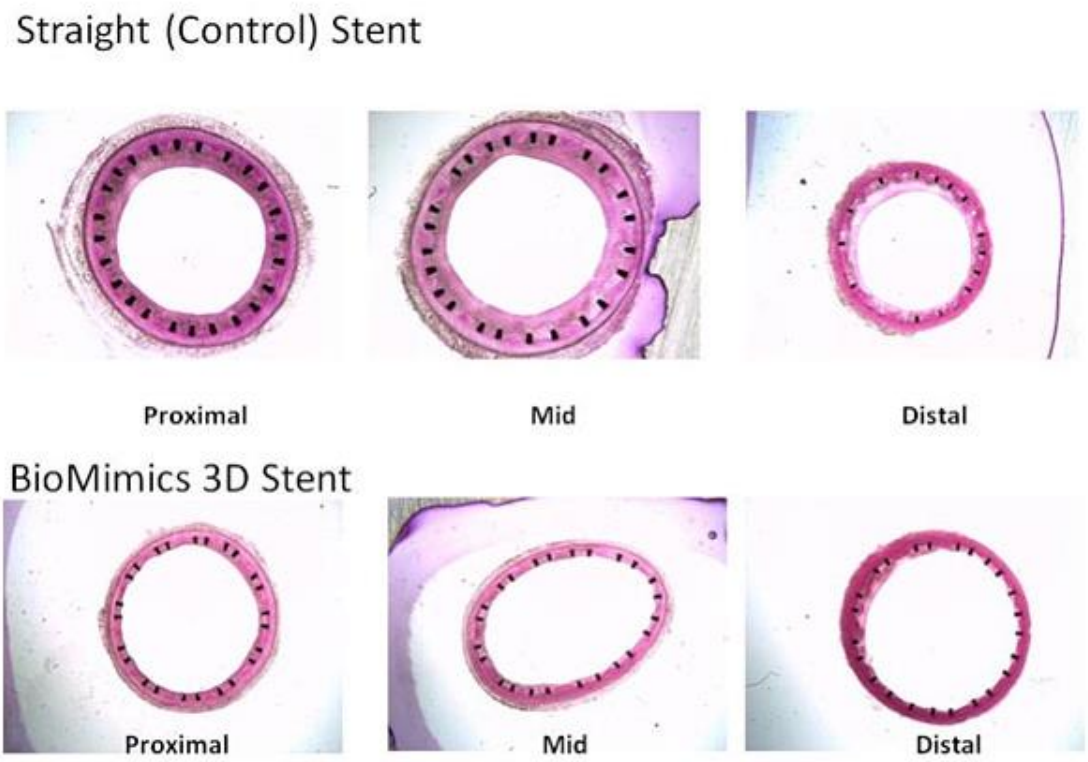

Figure 4.13: Histological sections of the stented arteries for the straight (control) stent and the BioMimics 3D helical stent one month post implantation. The sections shown correspond to proximal, middle and distal locations to the stented region.[228] Reproduced with permission from Veryan Medical Ltd.

The *in vivo* results from this porcine study were compared with CFD predictions by Coppola and Caro and the effects of varying the geometrical parameters, i.e. the amplitude and frequency of the helical shape, on the flow pattern, WSS, and oxygen flux to the arterial wall were studied.[45] It was expected that the increased mixing effects of the geometry-induced secondary flows would modify the distribution of WSS and produce higher oxygen flux levels to the arterial wall. Results showed that increasing the amplitude of the helical geometry increased the WSS and oxygen flux to the vessel

wall, and that increasing the frequency increased the WSS but had no effect on the oxygen flux.[45] Oddly, the results indicated that the inner curvature regions of the helical model are exposed to lower oxygen flux than in the corresponding straight stent case, and yet the development of NIH is lower in these regions, as shown by the porcine trial. The reasons for this were inconclusive; however, the overall results of the study were positive.

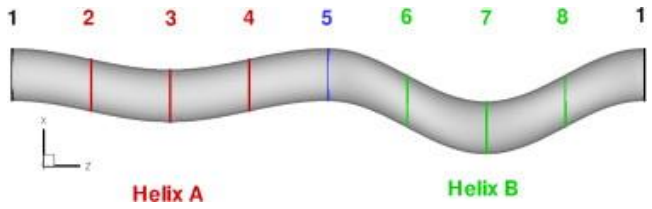

Figure 4.14: Diagram of the helical geometry employed by Cookson et al. in a CFD analysis of the mixing behaviour in a helical pipe with two different helical geometries.[42]

Cookson et al. conducted a CFD investigation of the mixing behaviour of a small amplitude helical pipe incorporating two different helical geometries, as shown in Figure 4.14.[42] Helix A has an amplitude of 0.2 times the diameter of the pipe and Helix B has an amplitude of 0.5 times the diameter. This investigation was based on the hypothesis that increased mixing, induced by helical geometries, reduced thrombosis in grafts incorporating SMAHT and that by joining together two helical geometries of different amplitudes the mixing effect could be enhanced further without an excessive pressure loss across the device. This study followed on from a previous numerical study of single helical geometries by Cookson et al.[41] The results of the investigation indicated that the mixing effect was improved upon in the combined helical geometry in comparison with the single helical geometry and that the pressure drop was found to be less in the combined helical geometry. These results show a possible improvement in

the original SMAHT design on which SwirlGraft and the BioMimics 3D helical stent are based.

4.4.2 Vascular Flow Technologies Ltd Stent

The BioMimics 3D helical stent induces a helical flow by imposing a helical geometry on the treated artery, while another stent technology, currently in development at Vascular Flow Technologies Ltd (VFT) based in Dundee, Scotland, induces helical flow through the use of a helical ridge placed on the inner surface of the stent. VFT (formerly Tayside Flow Technologies) is a spin-out company set up in 1998 from Tayside University Hospitals NHS Trust. The stent technology being developed by VFT is based on research by Stonebridge et al. into the naturally occurring helical flow found in studies of the cardiovascular system using Doppler ultrasound, as mentioned previously.[241,242,245] The benefits of helical flow, discussed earlier, led VFT to design a bypass graft, which was similar to SwirlGraft in that its goal is to induce helical flow; however, instead of shaping the graft in a helical form which could be lost on implantation, this bypass graft incorporated a helical ridge at the distal end of the graft, which restored helical flow. Early clinical results from a first-in-man study were presented by Vermassen and Stonebridge in which 40 patients with peripheral arterial disease had the graft implanted.[263] 10 patients were assessed for the presence of helical flow at six months and in all 10 helical flow was evident, confirming that the graft induced helical flow. In addition, a patency-rate of 88% at one year follow-up was found for the 40 patients treated.[263]

The company is currently developing a helical-ridge insert for stents, similar to the graft design, in order to induce helical flow in a stented artery. Two patents which have been filed give some details of this technology: European Patent EP1314406 (B1) and US

Patent US7721767 (B2).[104,105] The former describes a partially helical-shaped ridge insert for a stent as shown in Figure 4.15, while the latter gives details of a method for determining the helix angle of a helical formation for a conduit.

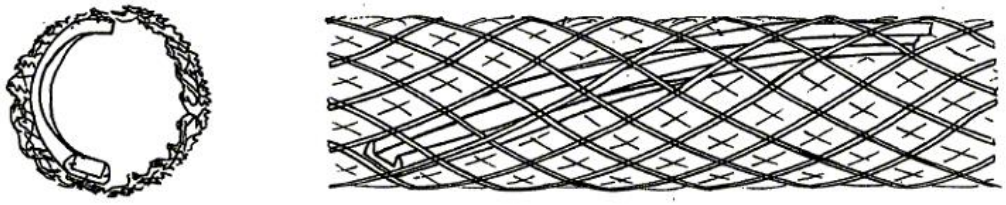

Figure 4.15: Axial and longitudinal views of the proposed helical-ridge insert for stents, adapted from European Patent EP1314406 (B1).[105] Reproduced with permission from Vascular Flow Technologies.

A conduit, as described in the US Patent, includes natural blood-flow tubing, stents, and artificial industrial equipment, e.g. a hose or pipe.[104] The method described in this patent allows the determination of the optimum helix angle through the use of two characteristic curves. As shown in Figure 4.16, for a given mass flow rate in a given conduit the experimentally determined non-dimensional pressure drop and turbulent kinetic energy are plotted against the helix angle. The optimum helix angle would normally correspond to the angle at which the non-dimensional pressure drop and the non-dimensional turbulent kinetic energy are equal to zero, in this case at approximately 7.5 degrees (notated as 52 in Figure 4.16); however, this may not always be the case.[104]

In a preclinical porcine study by Houston et al., an unmodified control stent and a modified stent incorporating the helical-ridge insert were compared in a 45 day carotid cuff stenosis model.[102] The cuff model is designed to mimic lesions that may occur downstream of a stent and to induce cell proliferation and ECM synthesis, both of which contribute to neointimal thickening. There was a statistically significant reduction

in intima/media ratios distal to the implanted region in the modified stent porcine models, with a high ratio indicating significant neointimal thickening, in comparison with the control stent porcine models. Using Doppler ultrasound it was confirmed that the modified stent maintained the natural helical flow within the arteries of all eight pigs, whereas, the control stent did not. An idealised plain-wall tube was compared with a tube with a helical ridge using CFD and results obtained predicted a reduction in turbulent kinetic energy downstream of a 50% stenosis in the helical-ridge model.

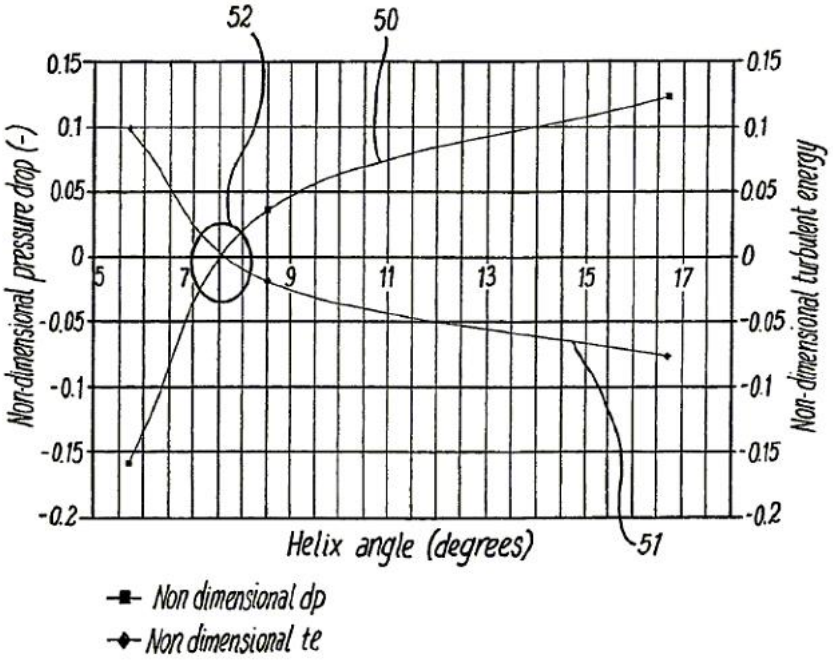

Figure 4.16: Graph taken from US Patent US7721767. The variation of non-dimensional pressure drop with the helix angle is notated as 50 and the variation of non-dimensional turbulent kinetic energy with the helix angle is notated as 51. The helix angle when both variables are equal to zero is notated as 52.[104] Reproduced with permission from Vascular Flow Technologies.

4.5 Summary

In this chapter a review of the existing literature was presented on the relevant topics for this study. The topics reviewed were oxygen transport analyses, haemodynamic analyses of stented arteries, and helical flow. Oxygen transport analyses vary in complexity with computationally-cheap wall-free analyses and simplified blood oxygen transport models that do not incorporate the bound oxygen common within the literature. Coupled blood-arterial wall analyses allow accurate assessment of the resultant oxygen distribution within the arterial wall, as also achieved in the test cases presented in Chapters 6, 7, and 8. Haemodynamic analyses of stented arteries are generally limited to WSS variables, but by analysing the oxygen transport also, one of the secondary effects of the abnormal haemodynamics within a stented artery can be investigated. In theory, helical flow, as reviewed here, could have beneficial effects on both the local haemodynamics and oxygen transport within stented arteries.

Key points from this chapter include:

- *In vivo* measurements with oxygen microelectrodes in animals are needed to learn more about the variations in oxygen transport.
- Shear-dependent wall permeability model adopted by Rappitsch et al. (1997) was noted to not be valid for oxygen transfer through the wall.
- Areas of predicted low mass transfer were found to correlate strongly with areas prone to intimal thickening in humans.[143]
- Some previous studies neglected the bound oxygen transport and reasoned that the Sh with the bound oxygen would be 2.5 times the predicted Sh without the bound oxygen. This assumption will be assessed in Chapter 9.

- Moore and Ethier (1997) previously concluded that further studies of oxygen transport in large arteries must include the oxygen transport into an accurate model of the arterial wall.[162]
- Several previous studies have noted that accurate representations of the arterial geometries is essential in order to predict the mass transfer.
- Neglecting the compliance of the arterial wall and the pulsatility of the flow in simulations of oxygen transport in arteries is justifiable.
- Helical flow is theorised to produce more uniform WSS, reduced high oscillating flow regions, greater particle mixing, reduced near-wall particle residence times, dampened WSS temporal gradients, and increased oxygen transport. Further analysis of this is presented in Chapters 8 and 9.

CHAPTER 5

Prelude to Test Cases

5.1 Introduction

As discussed in Section 3.4, Model 1 is the most advanced blood oxygen transport model which incorporates the oxygen bound within RBCs, the non-linearity of the oxygen exchange between the free and bound oxygen, and a variable shear-induced RBC dispersion coefficient. There are four additional models which have varying degrees of simplifications with the most simple of these, Model 5, most commonly used in the literature. To compare the five different models, two separate test cases were devised. Test Case 1 compared the transarterial wall PO_2 profiles predicted in an idealised carotid bifurcation using the five models with measurements recorded by Santilli et al. in dog carotid bifurcations.[217] In Test Case 2 the maximum and minimum transarterial wall PO_2 profiles in a stented coronary artery predicted using the five models were compared with measurements from a separate study by Santilli et al. In this separate study transarterial wall PO_2 profile measurements were taken within rabbit aortae, of similar size to human coronary arteries, which had been implanted with 3mm diameter stents.[218] Additionally, the PO_2 and the local Sh on the stented artery luminal surface predicted by each model were compared, along with the percentage volume of the arterial wall exposed to low and hypoxic levels of PO_2.

Following these two test cases a third test, Test Case 3, was constructed in which the most advanced model, Model 1, was applied to three sample stents to demonstrate how

different stent designs can impact the oxygen transport within a stented coronary artery. Finally, in Test Case 4 the predicted oxygen transport in a variety of helical stent geometries were assessed using Model 1. The goal of this test case was to elucidate the effects of increasing helical radius on the PO_2 levels within the arterial wall of idealised stented coronary arteries. This will further build on previous studies on helical flow by analysing its impact on the local haemodynamics and oxygen transport within a stented artery, and assess helical flow in terms of its theoretical benefits, as reviewed in Chapter 4.

5.2 Modelling the Blood Flow

For all simulations carried out as part of this study the meshes, generated in ANSYS ICEM meshing software (ANSYS Inc., Canonsburg, PA, USA), were imported into the CFD commercial software ANSYS CFX 15 (ANSYS Inc., Canonsburg, PA, USA) where the Navier-Stokes equations were solved to predict the blood flow within the luminal domain. All simulations were steady state as pulsatility has been shown to have a minimal effect on oxygen transport to the arterial wall.[124] The density of blood was taken as 1060kg/m^3 and the non-Newtonian nature of blood was modelled using the non-Newtonian Bird-Carreau model, with assigned values based on experimental data from Jung et al.[115] The continuity and momentum equations were solved with a high resolution advection scheme and the convergence criteria were set to a maximum residual tolerance of 1×10^{-6}.

All simulations were carried out on the Irish Centre for High-End Computing (ICHEC) Fionn supercomputer using a maximum of five nodes, each with 2×12 2.4GHz Intel Ivy Bridge core processors and 64GB of RAM. The computer processor unit (CPU) time to reach convergence for each model in Test Cases 1 & 2 are given in Table 5.1 and there

is a clear pattern whereby Model 5 almost halves the CPU time required on the same meshes. This may be significant when computational resources are an issue, although, as will be demonstrated by these test cases simplification of the oxygen transport model has considerable limitations. The CPU run times for each stent in Test Case 3 are 4.13×10^6 s, 6.55×10^6 s and 5.17×10^6 s for Stent A, B and C, respectively, and for Test Case 4 the typical CPU time was ~5.0×10^6 s.

	Test Case	
Model	1	2
1	1.90×10^6 s	4.13×10^6 s
2	1.07×10^6 s	4.56×10^6 s
3	1.73×10^6 s	4.49×10^6 s
4	1.09×10^6 s	4.50×10^6 s
5	6.49×10^6 s	2.62×10^6 s

Table 5.1: CPU run times in seconds for each simulation to reach convergence for all five models in Test Cases 1 & 2.

5.3 Modelling the Oxygen Transport

The PO_2 in the blood and the arterial wall is modelled in ANSYS CFX 15 using an additional variable. Additional variables are defined in ANSYS CFX as non-reacting scalar components that are transported through a flow field but do not affect the continuity or momentum equations. The transport of the PO_2 within the blood flow is governed by Equation 3.47 with flow variables affecting the transport through the substantial derivative term ($\mathcal{D}PO_2/\mathcal{D}t$). The diffusivity coefficient, D', is represented by Equation 3.48 and the source term is controlled by Equation 3.49. Both D' and the source term are evaluated explicitly, based on the previous time-step value for PO_2, and

a time-step independence study found no difference in the predicted PO_2 results at smaller time-step increments. The PO_2 is transported via diffusion only in the arterial wall with a fixed diffusivity coefficient, D_T, and consumption modelled via a source term. The advection/diffusion equation for PO_2 in the lumen domain was solved with a high resolution advection scheme, in line with recommendations by Carroll et al.,[29] and the convergence criteria were set to a maximum residual tolerance of 1×10^{-6} in all domains.

CHAPTER 6

Test Case 1 – Carotid Bifurcation

6.1 Introduction

To assess the accuracy of the oxygen transport models, as described in Chapter 3 and summarised in Table 3.1, experimental measurements are needed for comparison. Santilli et al. used an oxygen microelectrode to measure the transarterial wall PO_2 profiles in 11 dog carotid bifurcations.[217] An idealised human carotid bifurcation geometry was constructed from detailed measurements taken from several studies.[128,142,248] A dog carotid bifurcation geometry would be ideal for comparison; however, Santilli et al. reported that they used mongrel dogs, and only the wall thicknesses were reported with no luminal diameters given.[217] The size of the arteries and the oxygen transport parameters within the arterial wall would vary according to different breeds of dogs. Therefore, the PO_2 measurements by Santilli et al. are used here, as done previously by other researchers,[248–250] for comparison with the predicted results for a human with the distance through the arterial wall scaled according to the thickness of the human artery. The five different models were used to simulate the oxygen transport in an idealised human carotid bifurcation, shown in Figure 6.1, adapted from Tada with, for the first time, the addition of a heterogeneous arterial wall.[128,142,248] The carotid bifurcation offers two advantages for this study: there are different flow patterns present in it which will affect the oxygen transport, and because

the carotid sinus is prone to atherosclerotic plaque build-up it is an area of interest for oxygen transport modelling.

6.1.1 Geometry Creation

The geometry was constructed in Rhinoceros 3-D (McNeel, Indianapolis, IN, USA) and comprised of the common carotid artery (CCA) which bifurcates into the internal carotid artery (ICA) and the external carotid artery (ECA). To reduce computational expense half of the geometry was used with symmetry assumed along the centreline of the carotid arteries, thus ignoring the secondary curvature of the ICA.[248] The secondary curvature has the greatest effect downstream of the measurement locations and therefore, would have no consequence on the results presented here. The thickness of the arterial wall in the carotid arteries, particularly the intima in the carotid sinus, has been shown to vary with location in human subjects.[128] Accordingly, a variable intimal thickness ranging from 0.10 to 0.63mm was used, as shown in Figure 6.1. The intimal thicknesses correspond to the mean values of measurements from bi-planar angiographs from 57 patients, as listed in Table 6.1 with reference to Figure 6.2 (which shows the orientation of the polar coordinates in each arterial segment), adopted from Ku et al.[128] The media was assumed not to experience any thickening and was assigned a constant thickness of 0.60mm.

The predicted and measured transarterial wall PO_2 profiles were then compared at three of the six measurement locations as outlined by Santilli et al.[217] One of the benefits of these locations numbered 1 - 3, in terms of assessing the blood oxygen transport models, is that they cover three distinct flow patterns: straight shear flow parallel to a wall, low shear recirculation flow and high shear flow directed towards the wall, respectively.

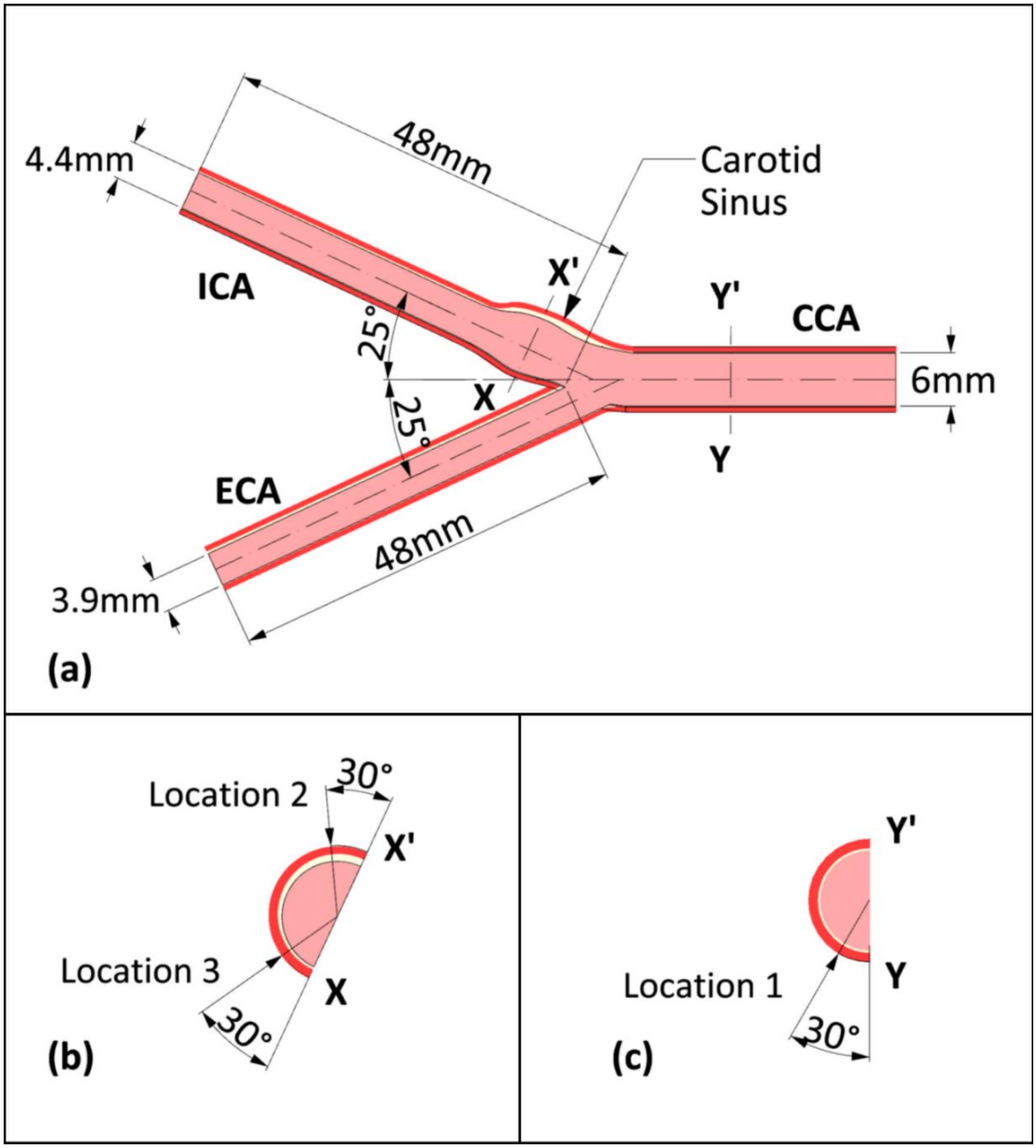

Figure 6.1: (a) Plan of the carotid bifurcation model with (b) cross-section X-X' and (c) cross-section Y-Y'. The intima thickness is approximately 0.12mm throughout the common carotid artery (CCA) and the internal carotid artery (ICA), except in the outer wall of the carotid sinus and proximal to the ICA where it gradually increases to a maximum of 0.63mm in accordance with Ku et al.[128] This can be seen clearly in the cross-section X-X'.

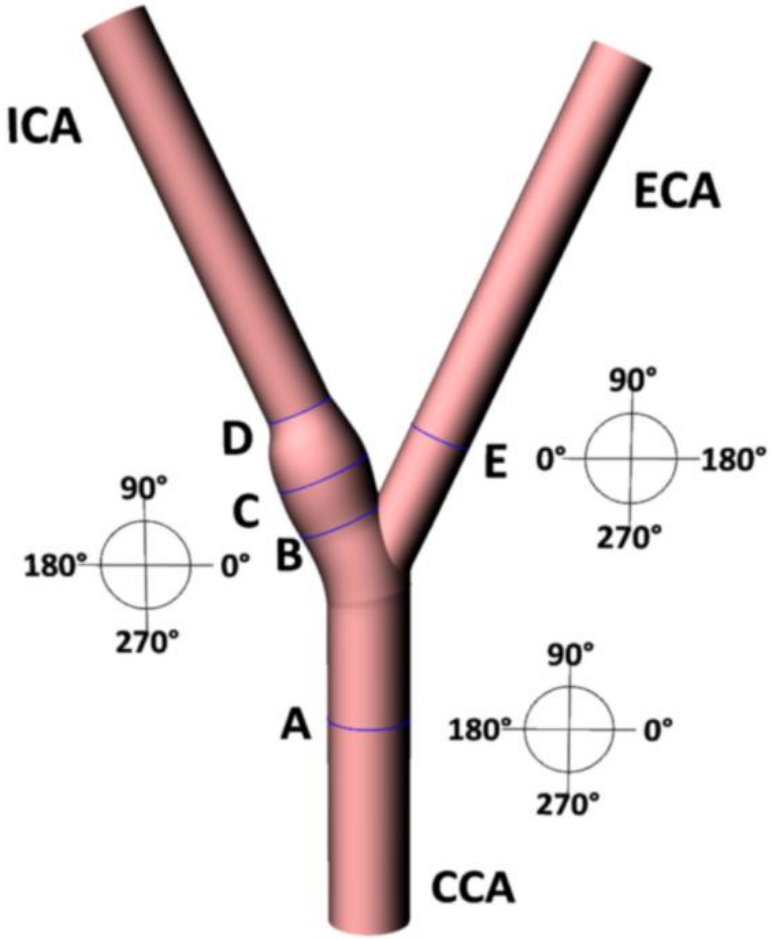

Figure 6.2: Schematic representation of the locations at which the intimal thickness data from human carotid arteries were recorded along with the polar coordinate orientation used in each artery segment. It should be noted that in keeping with the original data from Ku et al. the orientation of the polar coordinates is different at location E compared with all other locations.[128]

Cross-Section Location	Polar Position (°)	Intimal Thickness (mm)
A. CCA	0	0.10 ±0.02
	90	0.15 ±0.03
	180	0.12 ±0.03
	270	0.10 ±0.02
B. Proximal ICA	0	0.14 ±0.05
	90	0.47 ±0.13
	180	0.63 ±0.17
	270	0.37 ±0.10
C. Midpoint Carotid Sinus	0	0.19 ±0.07
	90	0.24 ±0.05
	180	0.49 ±0.10
	270	0.31 ±0.07
D. Distal Internal Carotid	0	0.07 ±0.02
	90	0.06 ±0.01
	180	0.08 ±0.04
	270	0.09 ±0.04
E. External Carotid	0	0.27 ±0.15
	90	0.08 ±0.02
	180	0.12 ±0.05
	270	0.15 ±0.05

Table 6.1: Intimal thicknesses as adopted from Ku et al.[128] Only half of the bifurcation geometry used and therefore, only the measurements at 270° were used normal to the plane of symmetry. The polar positions for each segment are shown in Figure 6.2.

6.1.2 Geometry Discretisation

The mesh for Test Case 1 was generated using ANSYS ICEM meshing software (ANSYS Inc., Canonsburg, PA, USA). It comprised of hexahedral elements and was inflated into the luminal domain from the arterial wall surface with the height of the initial element set at 3μm in order to accurately capture the MTBL. This is in line with both the Validation Test Case 2 presented in Appendix A and from previous literature in the area of oxygen transport modelling.[203,248] Following a mesh convergence study, as

discussed in Appendix B, the resultant mesh had a total of 973121 nodes broken down as follows: 501546 in the lumen domain, 295075 in the intima domain and 176500 in the media domain.

6.1.3 Boundary Conditions

A mass flow rate boundary condition of 0.00375kg/s, taken from a study by Tada,[248] was placed at the inlet of the CCA which corresponds to the averaged mass flow rate over the cardiac cycle, divided by two for the half geometry. Additionally, at the inlet $PO_{2,in}$=100mmHg, which corresponds to the typical arterial value found in human arteries,[200] and also the average luminal value recorded by Santilli et al.[217] At both outlets $PO_{2,out}$=0mmHg, a boundary condition that allows ANSYS CFX to automatically replace this value with the value attained iteratively from the solution process, and an entrainment boundary condition was imposed with a zero relative pressure. The mass flow rates at the two outlets were compared with the calculated transient mass flow rates from Tada and found a maximum difference of 5.68% in the averaged flow rate over the cardiac cycle at the ECA outlet. At the external wall boundary, which corresponds to the medial/adventitia interface, a constant PO_2=75mmHg was imposed, which was the averaged PO_2 value recorded at the adventitia by Santilli et al. At the arterial wall surfaces located at the inlet and outlets a zero flux PO_2 boundary condition was imposed.

6.2 Results and Discussion

Figure 6.3 shows the predicted PO_2 levels on the luminal surface for each of the models. The flow patterns are the exact same in each simulation; however, the predicted PO_2 levels clearly vary significantly depending on which blood oxygen transport model is adopted. In the following sections the results at the three prescribed locations are

compared with experimental results from Santilli et al., specifically, the transarterial wall PO_2 profiles. The oxygen MTBL at each location was analysed in detail for each of the five models.

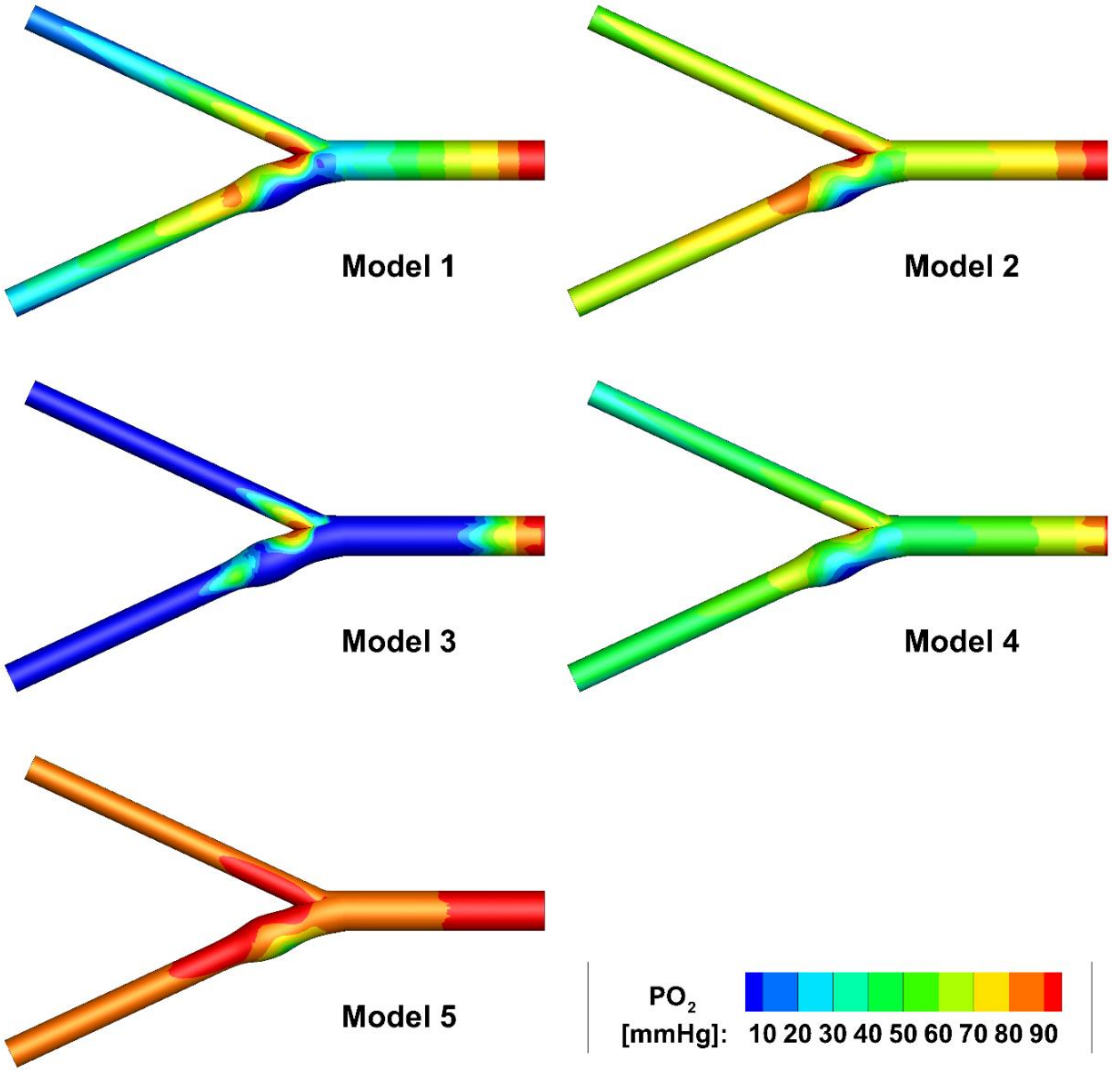

Figure 6.3: Predicted PO_2 levels along the luminal surface using the five different models, as summarised in Table 3.1.

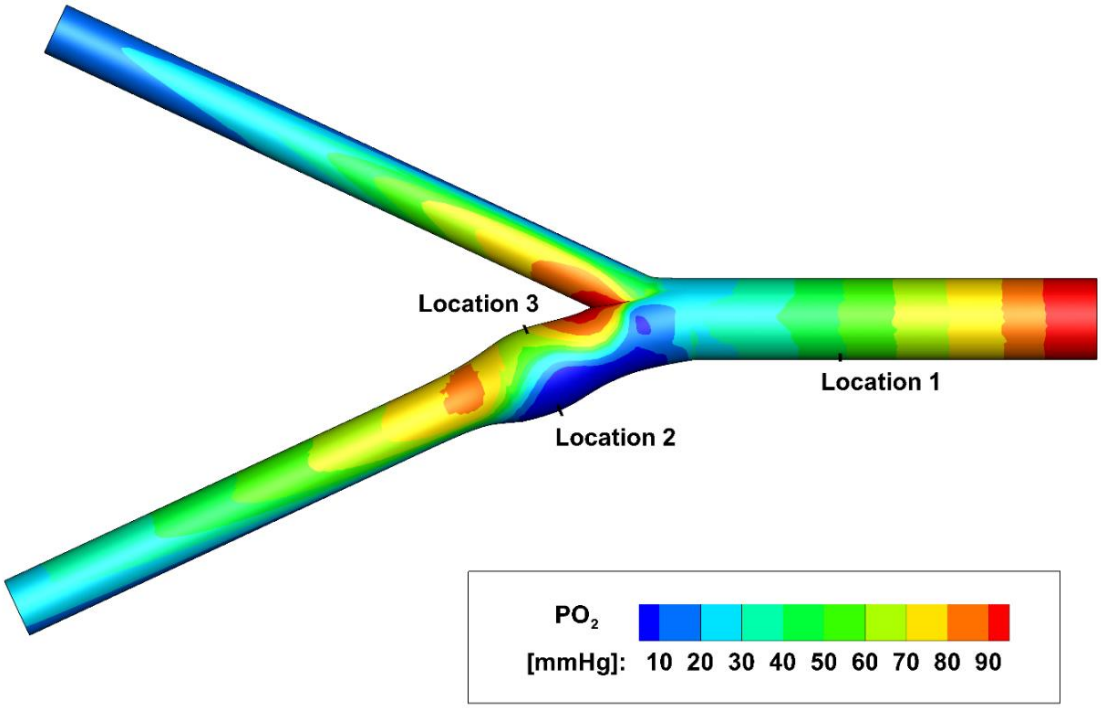

Figure 6.4: Locations of transarterial wall PO_2 profiles along with the predicted PO_2 levels on the luminal surface using Model 1.

For reference, Figure 6.4 shows the luminal surface PO_2 levels as predicted by Model 1 along with the locations of the three transarterial wall PO_2 profiles. Location 1 is within a developing MTBL with a uniform distribution of PO_2 circumferentially around the luminal surface with no flow disturbances. Location 2 is in a recirculation zone within the carotid sinus where the PO_2 levels are significantly depleted. Looking at Figure 6.3 it is clear that this low PO_2 region is present in each simulation with all five models except for Model 3 where it is imperceptible because most of the luminal surface is exposed to low/hypoxic PO_2 levels. Location 3 is adjacent to a high PO_2 region at the bifurcation divide. A detailed analysis of each location for each model follows.

6.2.1 Location 1

Location 1 is situated in the CCA where the flow is parallel to the luminal surface and within a developing MTBL, as shown in Figure 6.4. Figure 6.5 shows a cross-sectional slice at Location 1 with a contour plot of the predicted velocity magnitude. As shown, the blood flow at this location is undisturbed and is flowing parallel to the luminal surface. This means that the oxygen transport is predominantly diffusive perpendicular to the luminal surface at this location. For Models 1 and 2 D' is affected by the local shear rate through the variable D_c. Figure 6.6 shows the predicted shear rate and D_c at Location 1. The shear rate is a typical shape for developing pipe flow with a maximum value of $437s^{-1}$ at the luminal surface. The D_c value correspondingly varies between a minimum value of $8.0\times10^{-12}m^2/s$ within the centre of the lumen and a maximum value of $1.2\times10^{-10}m^2/s$ within the MTBL at the luminal surface.

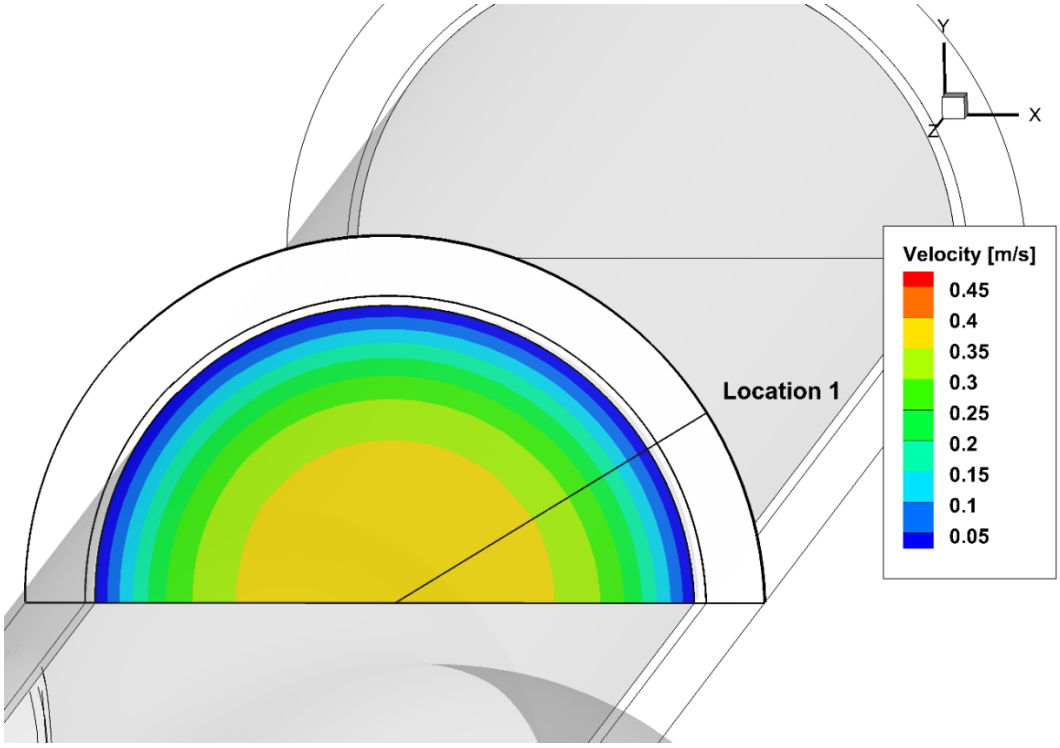

Figure 6.5: Cross-sectional slice at Location 1 showing a contour plot of the predicted velocity magnitude.

The effect of a relatively high D_c value within the MTBL can be seen by comparing the results of both Models 1 and 3, and Models 2 and 4. Figure 6.7 shows the predicted PO_2, dS/dPO_2, D', and S along a line at Location 1 for each model. Looking at Figure 6.7(c) there is a clear difference in the predicted D' values within the MTBL for Models 1 and 3 where the only difference between the two models is that a variable D_c value is used for Model 1, and $D_c=0m^2/s$ for Model 3 (essentially ignoring the dispersion of RBCs). For Model 3, ignoring the dispersion of RBCs leads to lower PO_2 values within the MTBL, and at the luminal surface, which is compounded by resultant higher dS/dPO_2 values within the MTBL. This is also seen when comparing Models 2 and 4; however, the effect of neglecting the dispersion of RBCs is not as pronounced because the dS/dPO_2 value is constant. Completely ignoring the contribution of the oxyhaemoglobin contained within the RBCs, i.e. Model 5, results in a higher D' value and consequently, a higher luminal surface PO_2 value compared with the other four models. The saturation of the oxyhaemoglobin, S, is shown in Figure 6.7(d) to follow a similar trend to the PO_2 for each model with Model 3 showing the largest decrease. Interestingly though, S begins to decrease much closer to the luminal surface than PO_2 because of the slope of the oxygen disassociation curve is relatively low until PO_2 begins to fall below 60mmHg, Figure 6.7(b), as demonstrated best with Model 3. A high dS/dPO_2 means that for a relatively large change in PO_2 there is a corresponding large change in S; whereas, if dS/dPO_2 is low, then a similarly large change in PO_2 will only produce a small change in S.

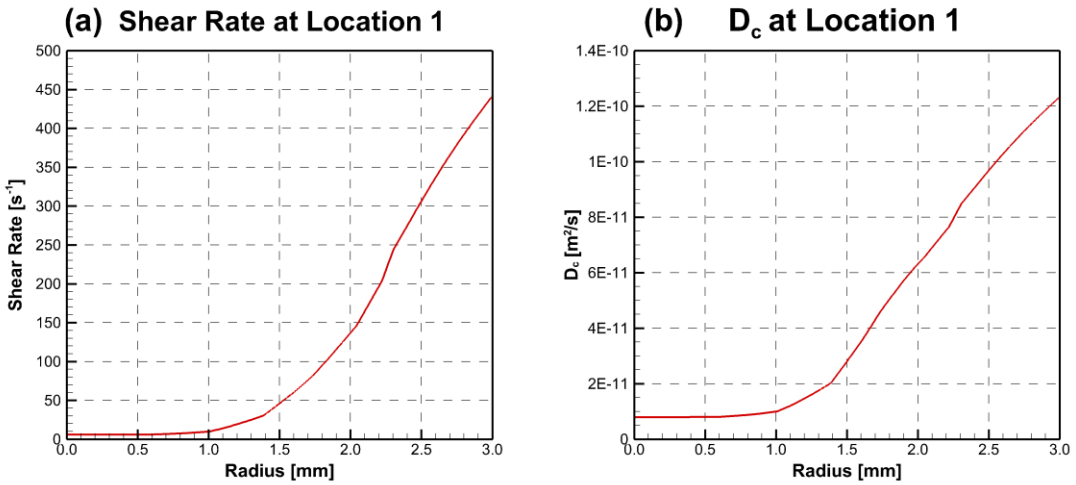

Figure 6.6: Predicted (a) shear rate and (b) D_c along a line within the blood flow from the centre of the artery to the luminal surface at Location 1.

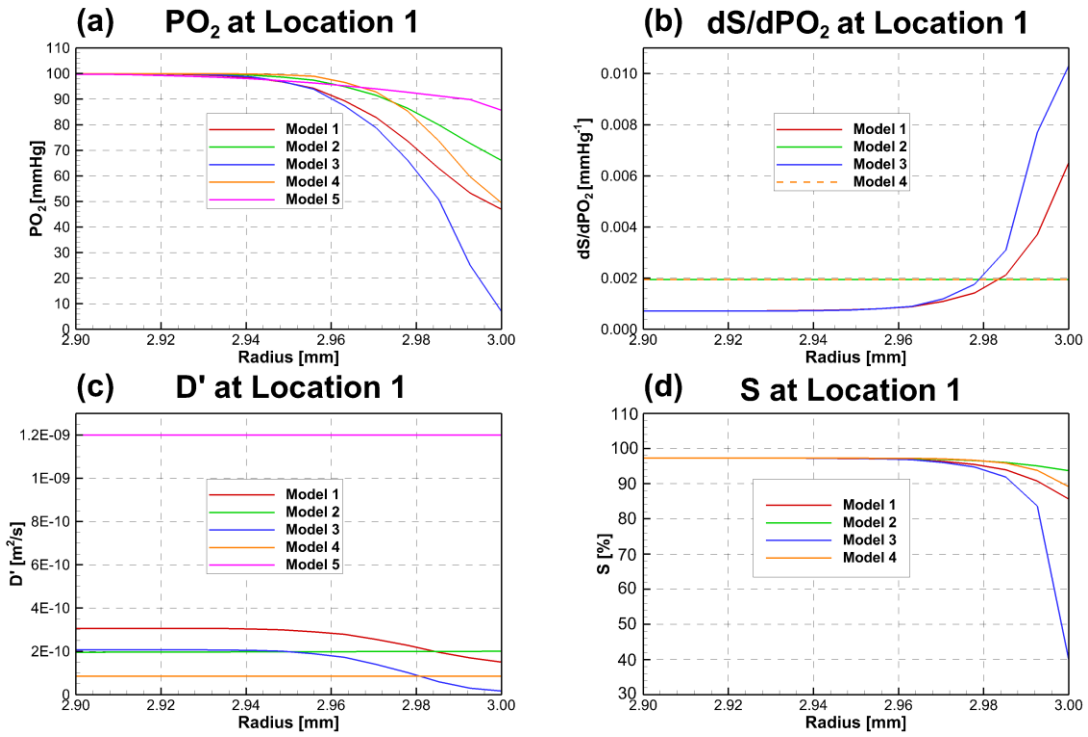

Figure 6.7: Predicted (a) PO_2, (b) dS/dPO_2, (c) D' and (d) S values along a line within the blood flow from a radius of 2.90mm to the luminal surface at a radius of 3.00mm at Location 1.

Figure 6.8 shows the cross-sectional slice at Location 1 with a contour plot of the predicted PO_2 levels using Model 1 which shows the PO_2 levels within the arterial wall are circumferentially uniform due to the uniformity of the flow in this region. In terms of the transarterial wall PO_2 profiles for Model 1 at Location 1, the predicted PO_2 values show reasonable agreement with the experimental results in capturing the overall trend, as shown in Figure 6.9. The radial position of the predicted nadir in the PO_2 levels is different to the nadir of the Santilli et al. experimental results. This may be due to different diffusion and consumption parameters within the dog arterial wall compared with the adopted values based on human arteries. Crucially though, at this location at least, the predicted PO_2 levels do not fall below the hypoxic or low PO_2 levels of 10mmHg and 30mmHg. The predicted results using the other four models show a broad variation in comparison with Model 1. Model 2 gives a higher luminal surface value than Model 1 and consequently, overall higher PO_2 values across the arterial wall. The predicted PO_2 profile from Model 4 is very close to that predicted by Model 1 because taking $D_c=0m^2/s$ decreases the D' value within the MTBL, and conversely, taking a constant value for dS/dPO_2 at this location has the opposite effect of increasing the D'. This results in a D' value for Model 4 adjacent to the luminal surface which is close to the D' value predicted by Model 1, as shown in Figure 6.7(c). Model 3 predicts the lowest PO_2 values on the luminal surface, and consequently, across the arterial wall. Model 5, on the other hand, predicts the highest PO_2 values on the luminal surface and across the arterial wall. Crucially, it fails to predict the high PO_2 gradient within the MTBL that is seen with Models 1-4. This will be discussed in greater detail separately in Section 6.2.4.

From analysing the results at Location 1, where the blood flow is parallel to the wall, laminar and undisturbed, it can be concluded that inclusion of the bound oxygen has a

significant effect on the predicted PO_2 levels within the MTBL. Counterintuitively, inclusion of the bound oxygen predicts lower PO_2 levels when compared with a simpler model, Model 5. In addition, both neglecting the dispersion of RBCs and the variability of the slope of the oxygen disassociation curve also significantly impact the predicted results.

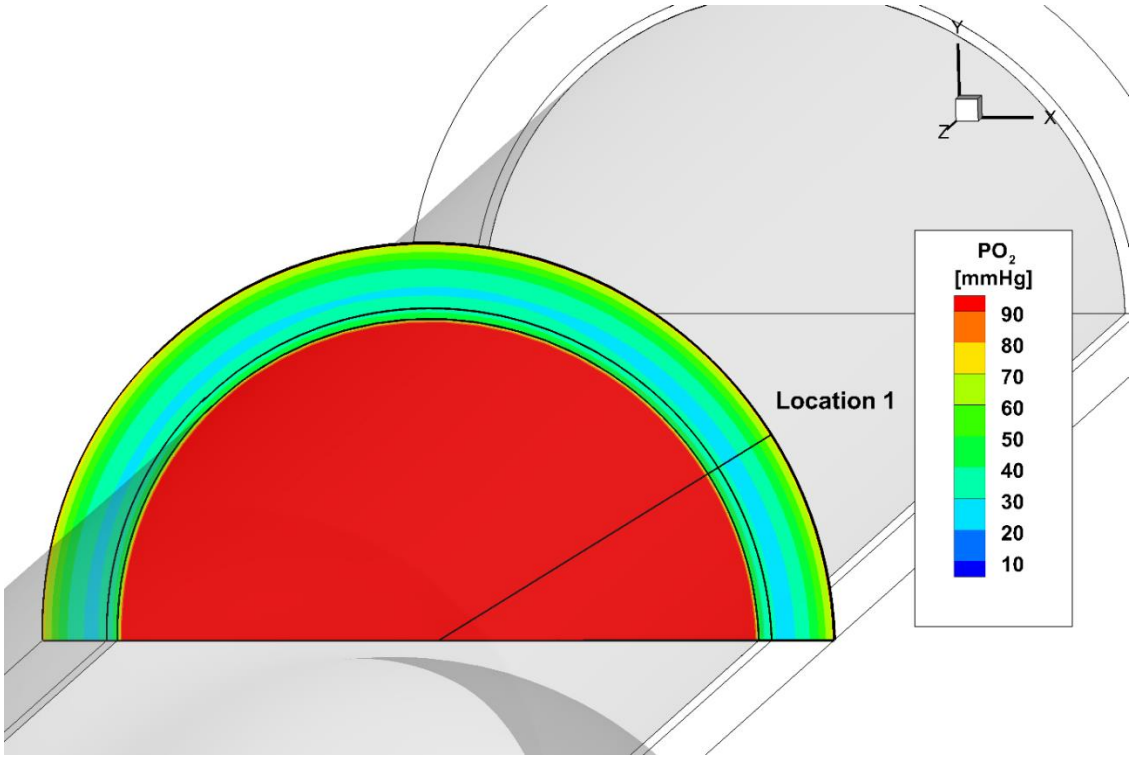

Figure 6.8: Cross-sectional slice at Location 1 showing a contour plot of the predicted PO_2 levels in all three domains.

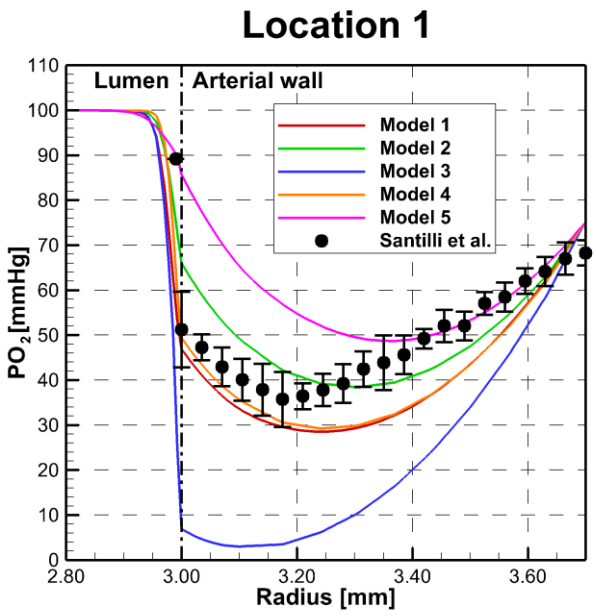

Figure 6.9: Comparison of predicted and measured transarterial wall PO_2 profiles at Location 1. Measurements adapted from Santilli et al. are shown for comparison and the distances through the arterial wall for these have been scaled to the size of a human carotid artery.

6.2.2 Location 2

Location 2 is situated on the outer side of the carotid sinus within the ICA where the flow is considerably different to that at Location 1. As shown in Figure 6.10, the velocity magnitude peak value is offset to the bifurcation side of the sinus with a relatively large low velocity recirculation zone present on the side of Location 2. The tangential velocity vectors on the slice surface are also shown in Figure 6.10 to highlight the presence of secondary motion within the sinus. This secondary motion is similar to that seen in previous studies of flow patterns in the human carotid bifurcation such as experimental work by Motomiya and Karino (1984) using transparent segments prepared from a human subject post-mortem.[168] This is also demonstrated in Figure 6.11 using streamtraces coloured according to PO_2 levels which highlights how previously

oxygen depleted blood is turned over towards the outer surface of the carotid sinus where it enters a low velocity recirculation zone and further depleted.

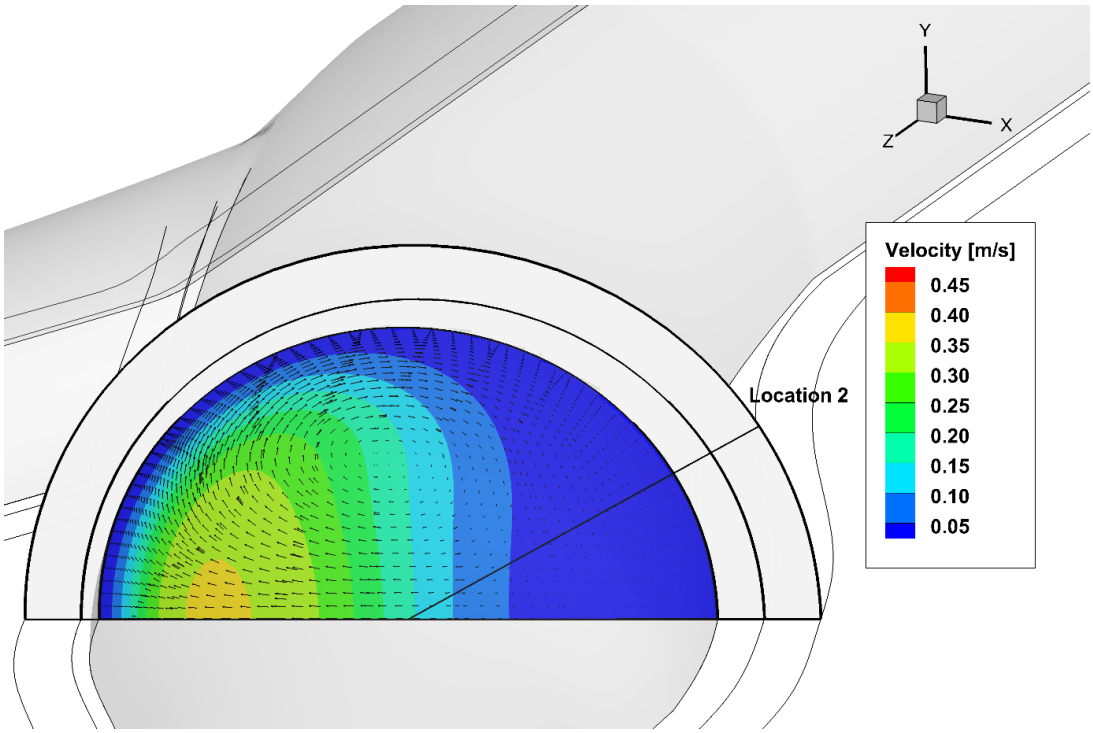

Figure 6.10: Cross-sectional slice at Location 2 showing a contour plot of the predicted velocity magnitude. The velocity vectors tangential to the slice plane are shown, with arbitrary length, to highlight the secondary motion present within the sinus.

As mentioned before, D' is affected by the local shear rate through the variable D_c for both Models 1 and 2. Figure 6.12 shows the predicted shear rate and D_c along a line at Location 2. The shear rate is maximum, for Location 2, at the centre of the artery with a value of $140s^{-1}$ and minimum adjacent to the luminal surface with a value of $9s^{-1}$. The D_c value correspondingly varies between a maximum value of $6.4\times10^{-11}m^2/s$ within the centre of the lumen and a minimum value of $9.4\times10^{-12}m^2/s$ within the MTBL adjacent to the luminal surface. Consequently, there is no significant increase in D' caused by the shear rate and D_c. Physiologically, this means that the shear-induced dispersion of

RBCs does not increase the effective diffusivity of oxygen within the low velocity zone on the outer side of the carotid sinus, as would be expected. Note: the change in the slope of the plot of D_c at Location 2, Figure 6.12(b), is a reflection of the change in governing equation for D_c for values above and below a shear rate value of $100s^{-1}$.

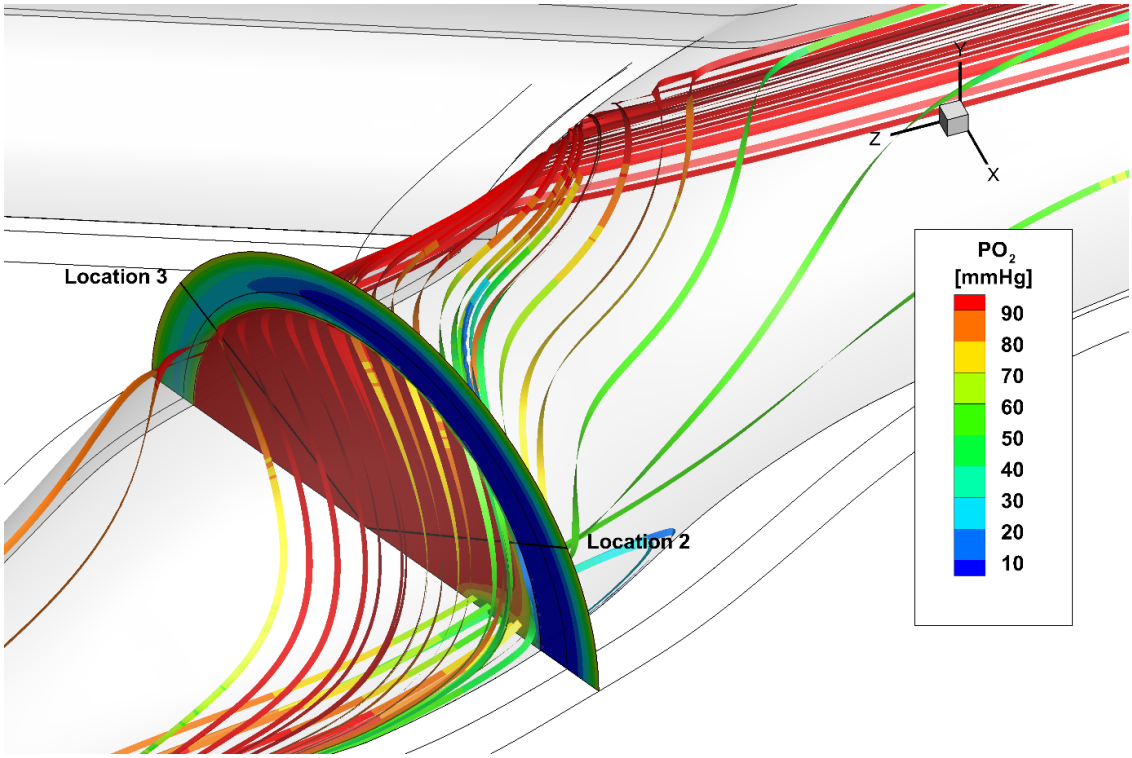

Figure 6.11: Streamlines passing through the cross-sectional slice at Location 2 and 3 coloured according to predicted PO_2 values using Model 1 along the streamlines.

The effect of a relatively low D_c value within the MTBL can be seen by comparing the results of both Models 1 and 3, and Models 2 and 4. Figure 6.13 shows the predicted PO_2, dS/dPO_2, D', and S along a line at Location 2 for each model. Looking at Figure 6.13(c) Models 1 – 4 all predict very low D' values within the MTBL and consequently, low luminal surface PO_2 values. For Models 3 and 4, which ignore the dispersion of RBCs, show no difference in luminal surface PO_2 values in comparison with Models 1

and 2 because D_c, as modelled in Model 1, has little effect on D' as seen in Figure 6.13(c). This is opposite to Location 1, as demonstrated by Figure 6.7(b), where a considerable difference was visible between the D' values within the MTBL between the models that included D_c (Models 1 & 2) and those that did not (Models 3 & 4). Completely ignoring the contribution of the oxyhaemoglobin contained within the RBCs, i.e. Model 5, again here at Location 2 results in a significantly higher D' value and consequently, a higher luminal surface PO_2 value compared with the other four models. The saturation of the oxyhaemoglobin, S, is shown in Figure 6.13(d) to follow a similar trend to the PO_2 for each model where it is included (Models 1 - 4). As seen at Location 1 as shown in Figure 6.7, S begins to decrease much closer to the luminal surface than PO_2; however, unlike Location 1, all four models predict a significant drop in the S within the MTBL. Physiologically, this means that the bound oxygen content has a particularly significant contribution to the oxygenation of the arterial wall at this location; although because of the low velocity of the flow the PO_2 levels fail to be kept sufficiently high to maintain the required supply to the arterial wall.

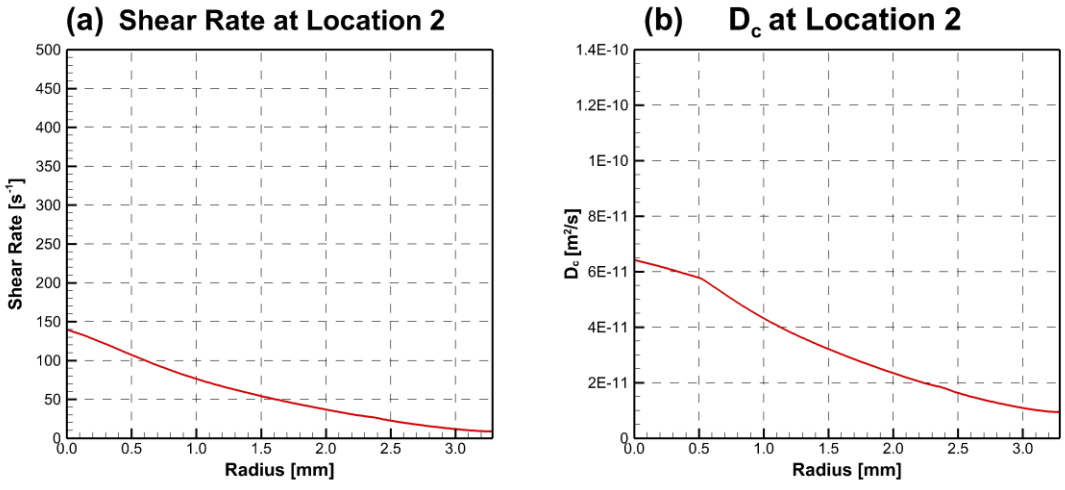

Figure 6.12: Predicted (a) shear rate and (b) D_c within the blood flow at Location 2 from centre of artery to the luminal surface.

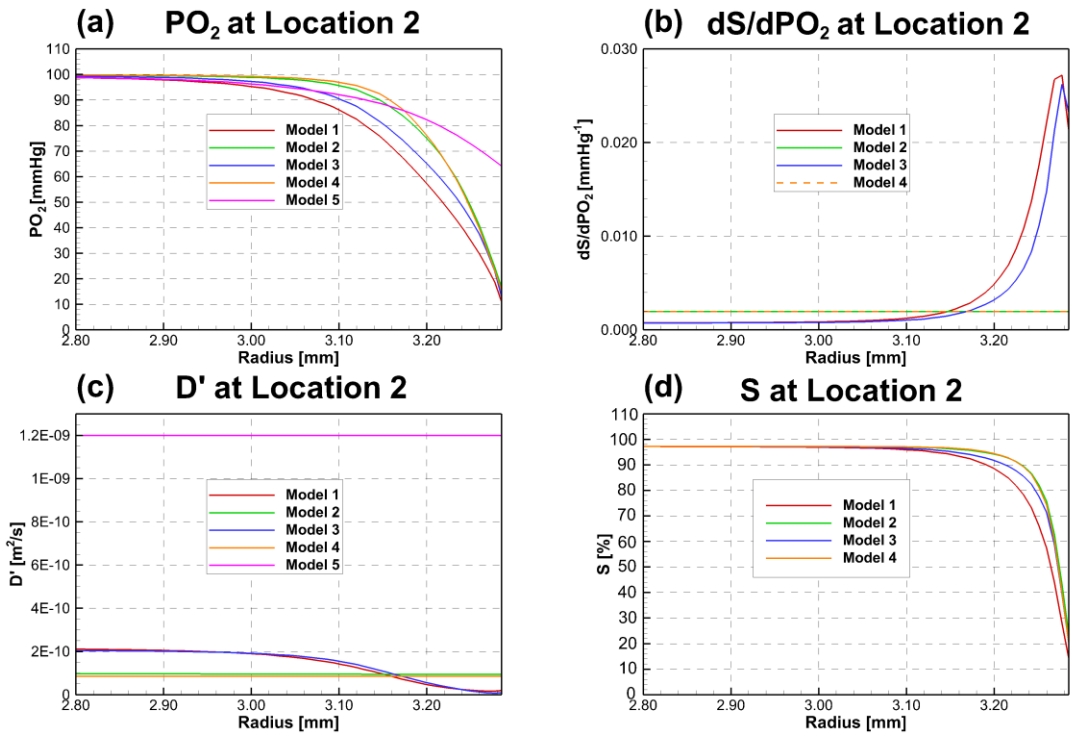

Figure 6.13: Predicted (a) PO_2, (b) dS/dPO_2, (c) D' and (d) S values along a line within the blood flow from a radius of 2.80mm to the luminal surface at a radius of 3.29mm at Location 2.

Figure 6.14 shows the cross-sectional slice at Location 2 with a contour plot of the predicted PO_2 levels using Model 1. Because of the low velocity and recirculation zone in the sinus on the side of Location 2 the PO_2 levels are hypoxic across the intima and a substantial portion of the media. Looking at Figure 6.15 there is a considerable difference between the predicted PO_2 values and the experimental results from Santilli et al. There are several reasons for this, all stemming from the fact that the carotid bifurcation geometry used here is based on measurements from humans and the experimental results from Santilli et al. are from dog carotid arteries. In humans this location is commonly a site of intimal thickening, caused by atherosclerotic plaque

build-up, as included here with the total arterial wall thickness varying between 1.09mm and 0.84mm within the cross-sectional slice shown in Figure 6.14. Conversely, in dogs, as studied by Santilli et al., the wall thicknesses recorded were considerably thinner at 154.0 ±4μm at Location 2.[217] The effect of the intimal thickening in humans on the oxygenation of the arterial wall can be seen here with extensive hypoxic regions where cells would express VEGFs resulting in the penetration of vasa vasorum into the medial layer to increase the oxygen supply to the cells at this site.[262]

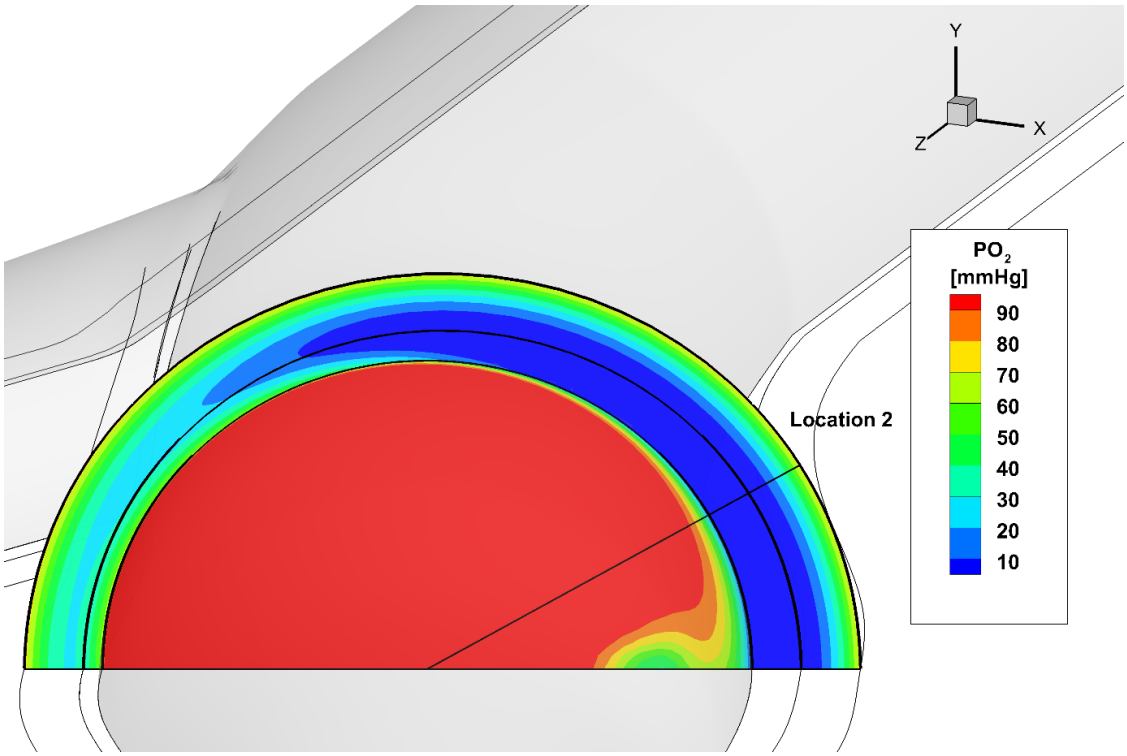

Figure 6.14: Cross-sectional slice at Location 2 showing a contour plot of the predicted PO_2 levels in all three domains.

Analysing Figure 6.15, there is no significant difference between Models 1 and 3 because the relatively low D_c has a negligible effect on the D' within the MTBL for Model 1. This is also true for the small difference between Models 2 and 4. Model 5 again predicts a much higher luminal surface PO_2 value, although there is still a portion

of the arterial wall exposed to low and hypoxic PO_2 levels. Interestingly, because all five models reach a nadir of 0mmHg the extent of the influence of the oxygen diffusing in from the adventitia is noticeable with the PO_2 levels rising from a radius of 3.7mm up to the medial/adventitial interface at 4.35mm. This gives an effective range of oxygen diffusion at this location of 0.65mm; however, the PO_2 levels become hypoxic at approximately half this distance. A similarly high PO_2 gradient is observed at the location also which Models 1 – 4 predict but Model 5 does not.

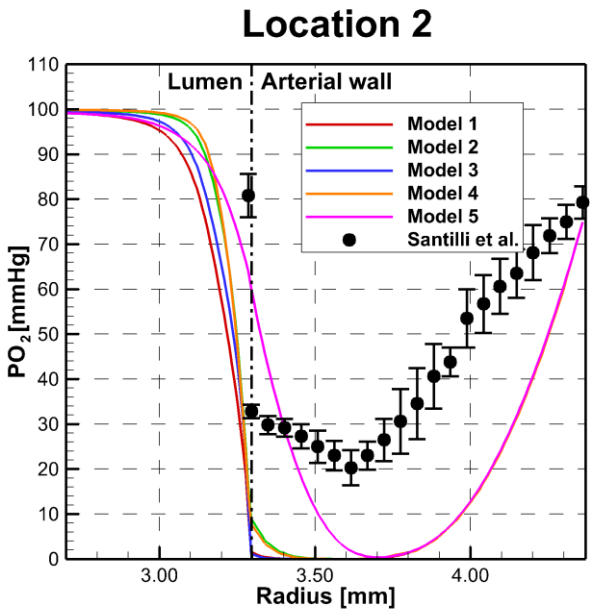

Figure 6.15: Comparison of predicted and measured transarterial wall PO_2 profiles at Location 2. Measurements adapted from Santilli et al. are shown for comparison and the distances through the arterial wall for these have been scaled to the size of a human carotid artery.

6.2.3 Location 3

Lastly, Location 3 is situated on the inner side of the carotid sinus within the ICA where the flow is different to both previous locations. Figure 6.16 shows a cross-sectional slice at Location 3 with a contour plot of the predicted velocity magnitude and Figure 6.17 shows the predicted shear rate and D_c at Location 3. The velocity magnitude peak value is offset to the inner side of the sinus, as shown in Figure 6.16, which has a noticeable effect on the shear rate as shown in Figure 6.17(a). The tangential velocity vectors on the slice surface are again shown in Figure 6.16 to highlight the presence of secondary motion within the sinus that has the effect of replenishing the oxygen at this location. This means that the oxygen transport has a greater contribution from the advection term of the transport equation in comparison with Locations 1 and 2. Additionally, for Models 1 and 2, D' is affected by the local shear rate through the variable D_c. The shear rate is a reflection of the rate of change of velocity so looking at Figure 6.17(a) in combination with Figure 6.16 gives an understanding of why the shear rate along the line at Location 3 has a particular shape. In Figure 6.16 the closeness of the velocity contours reflect the rate at which the velocity is changing in a given region of flow. Within the first 1.0mm, going from the centre out, the shear rate is consistently above $100s^{-1}$ which is reflective of the relatively gradual change in velocity in this region of flow. Moving radially out along the line the next 1.5mm sees very little change in the velocity as the line passes through the region of flow coloured according to the velocity range of 0.30 to 0.35m/s. The shear rate dips to a nadir value of $50s^{-1}$ within this region. Following this, with the peak velocity skewed towards the inner side luminal surface, the velocity changes rapidly from approximately 0.30m/s down to 0.00m/s at the luminal surface. This relatively rapid transition is reflected in the closeness of the velocity contours in Figure 6.16. The shear rate correspondingly rises to a peak value of

$547s^{-1}$ and then drops to a value of $336s^{-1}$ at the luminal surface. The D_c value similarly varies between a minimum value of $3.2\times10^{-11}m^2/s$ within the low shear rate region and a maximum value of $1.4\times10^{-10}m^2/s$ at the peak shear rate point. Importantly, the D_c value drops to a value of $1.0\times10^{-10}m^2/s$ within the MTBL at the luminal surface. Physiologically, this means that the dispersion of RBCs has a significant effect on the oxygen transport at this location.

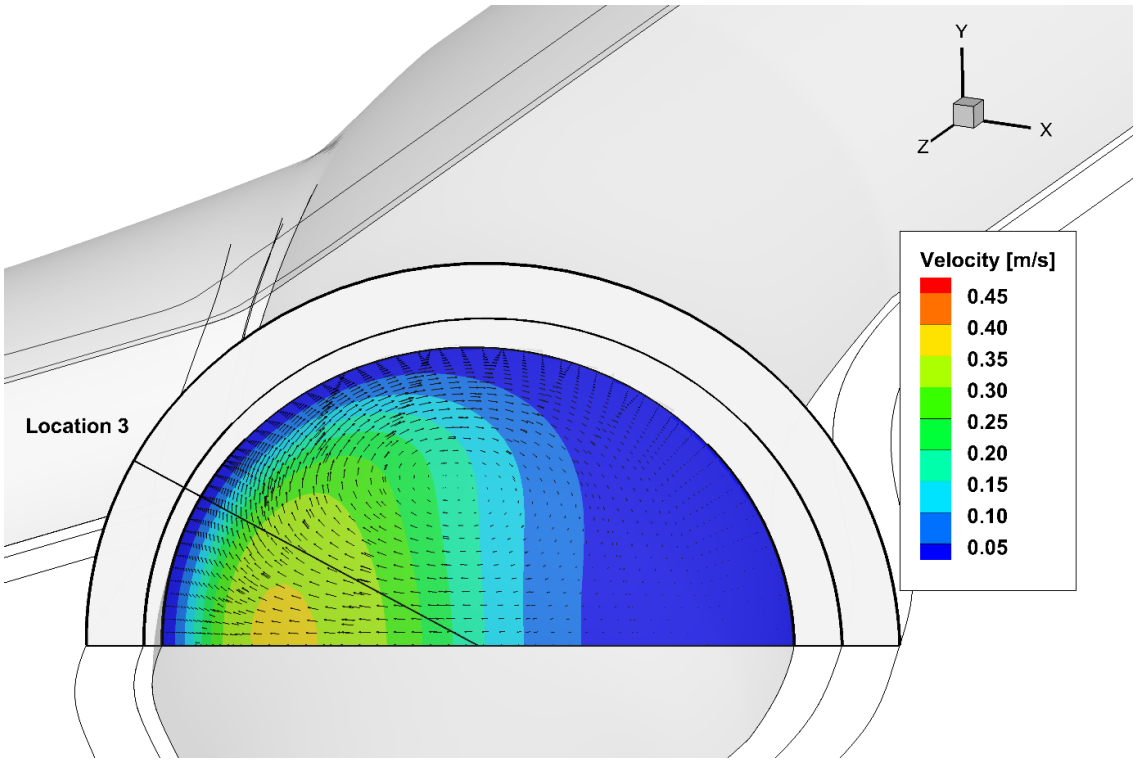

Figure 6.16: Cross-sectional slice at Location 3 showing a contour plot of the predicted velocity magnitude. The tangential velocity vectors are shown, with arbitrary length, to highlight the secondary motion present within the sinus.

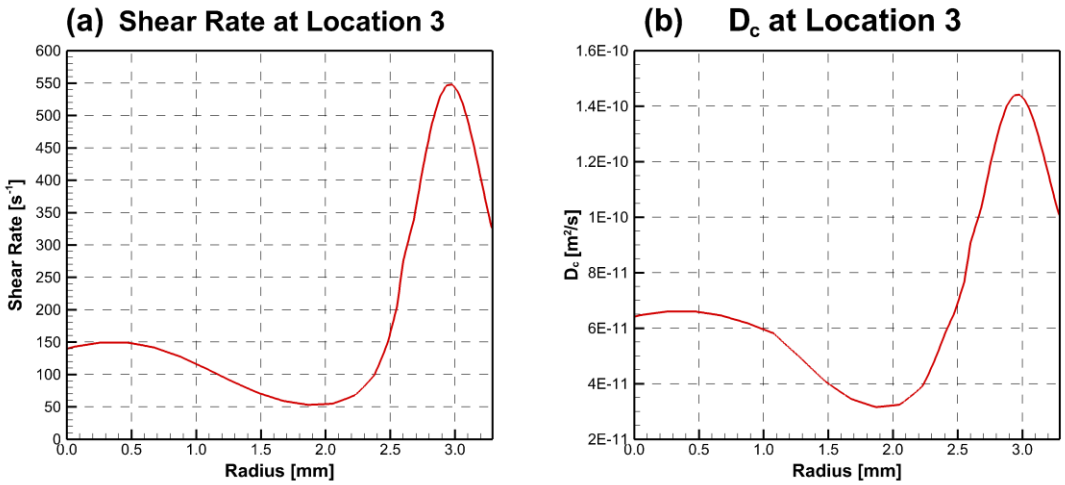

Figure 6.17: Predicted (a) shear rate and (b) D_c within the blood flow at Location 3 from centre of artery to the luminal surface.

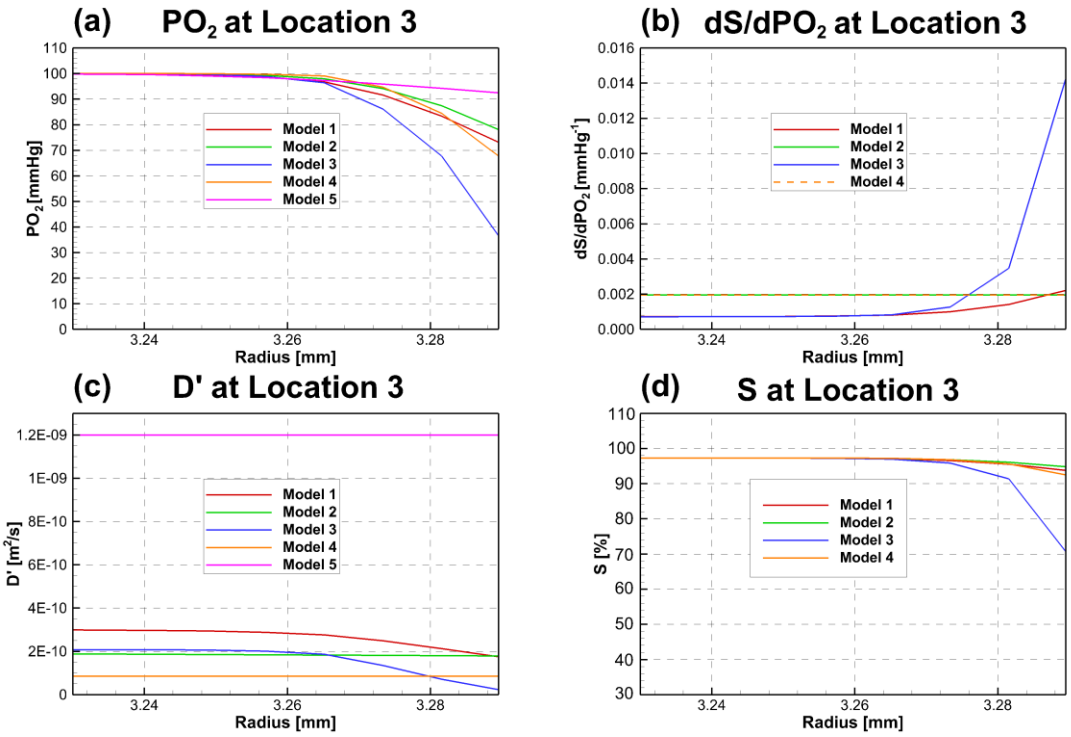

Figure 6.18: Predicted (a) PO_2, (b) dS/dPO_2, (c) D' and (d) S values along a line within the blood flow from a radius of 3.23mm to the luminal surface at a radius of 3.29mm at Location 3.

Figure 6.18 shows the predicted PO_2, dS/dPO_2, D', and S along a line at Location 3 for each model. The relatively high D_c value increases D' within the MTBL which can be seen by comparing the D' values of both Models 1 and 3, and Models 2 and 4. Looking at Figure 6.18(c) there is almost no difference in the predicted D' values within the MTBL for Models 1 and 2 (a minimum of $1.78\times10^{-10}m^2/s$ and $1.79\times10^{-10}m^2/s$, respectively, at the luminal surface), that results in similar luminal surface PO_2 values (74mmHg and 79mmHg, respectively). This is also the case with their respective dS/dPO_2 values at the luminal surface ($0.0022mmHg^{-1}$ and $0.0019mmHg^{-1}$, Model 1 and 2 respectively). Model 3 again predicts a relatively low luminal surface PO_2 value (39mmHg) with high dS/dPO_2 and low D' values within the MTBL. Model 4 predicts a lower luminal surface PO_2 value (69mmHg) than Model 1. Completely ignoring the contribution of the oxyhaemoglobin contained within the RBCs, i.e. Model 5, again results in a higher D' value and consequently, a higher luminal surface PO_2 value (93mmHg) compared with the other four models. The saturation of the oxyhaemoglobin, S, as shown in Figure 6.18(d), is very similar in Models 1, 2, and 4 because the PO_2 levels are very similar and are all in a region on the oxyhaemoglobin curve that has a low slope and consequently, there is little change in S over small changes in PO_2. Model 3 again predicts a greater drop in S, similar to the drop in PO_2. Physiologically, this means that the bound oxygen content has less of an effect on the oxygenation of the arterial wall at this location in comparison with the other two locations, but the dispersion of the RBCs does play a crucial part in the overall oxygen transport at this location.

At Location 3 the predicted PO_2 value (66mmHg) for Model 1 just within the arterial wall matches well with the experimental results from Santilli et al. (64mmHg), as shown in Figure 6.19; however, the PO_2 values across the arterial wall differ with those

recorded experimentally, which again are due to differences in consumption, diffusion and solubility of the oxygen in humans and dogs. Looking at Figure 6.20 it is clear how thin the MTBL is at Location 3 in comparison with Location 2 (approximately 0.05mm vs 0.5mm, respectively), which is caused by the off-centre velocity profile. There is little difference between the transarterial wall PO_2 profiles predicted by Models 1 and 2 because the dS/dPO_2 value predicted by Model 1 adjacent to the luminal surface is similar to the constant value taken for Model 2. Model 3 again predicts a very low transarterial wall PO_2 profile at this location. The transarterial wall PO_2 values predicted by Model 4 are lower than those predicted by Model 1 because of the effect of the increased D_c value, as modelled by Model 1, is not included. Model 5 again predicts a much higher luminal surface PO_2 value. As with the other two locations a high PO_2 gradient is observed at Location 3 using Models 1 – 4 but not with Model 5.

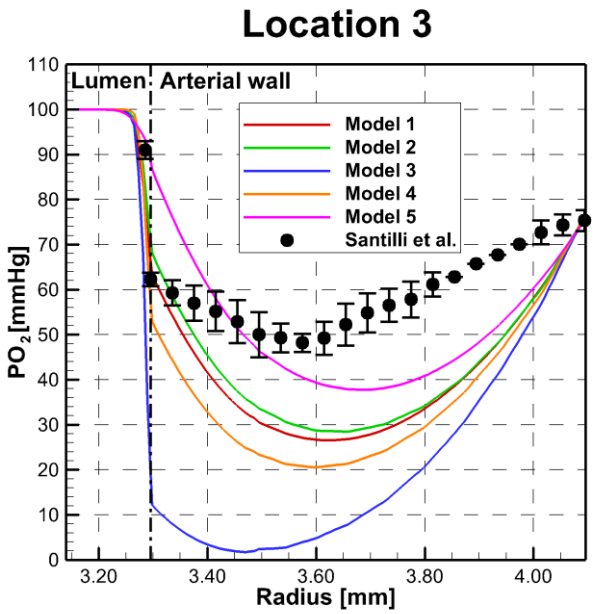

Figure 6.19: Comparison of predicted and measured transarterial wall PO_2 profiles at Location 3. Measurements adapted from Santilli et al. are shown for

comparison and the distances through the arterial wall for these have been scaled to the size of a human carotid artery.

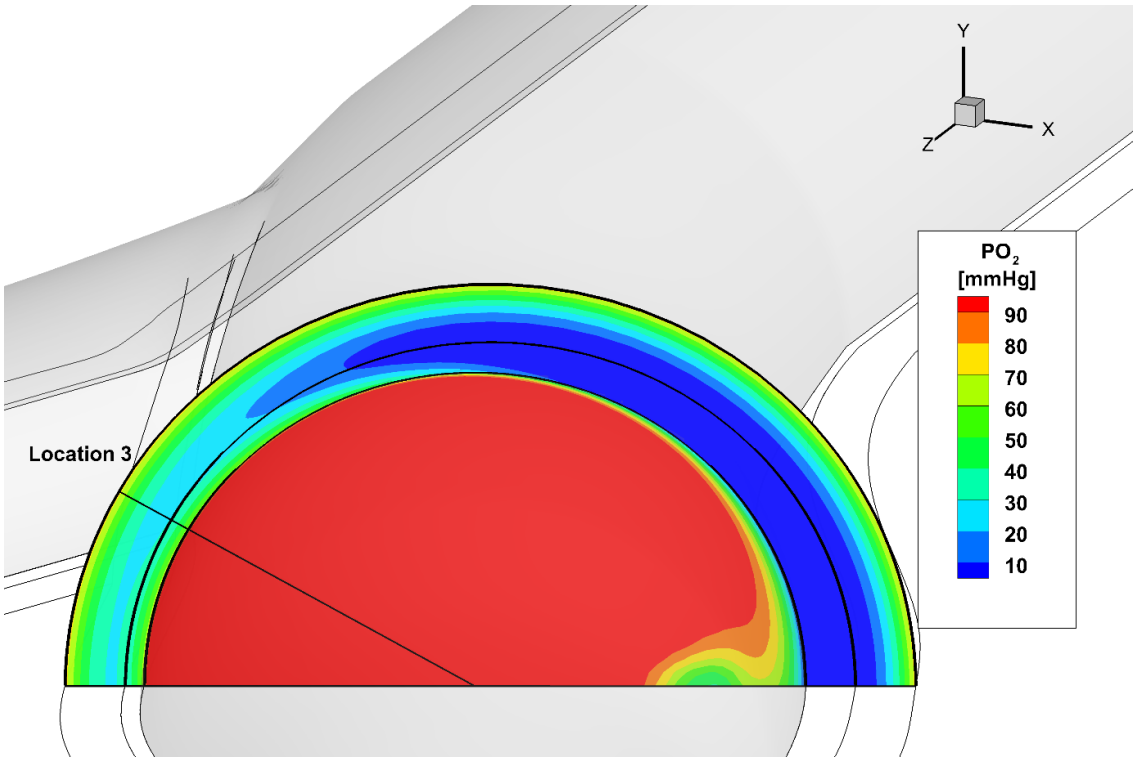

Figure 6.20: Cross-sectional slice at Location 2 showing a contour plot of the predicted PO_2 levels using Model 1 in all three domains.

6.2.4 High PO_2 Gradient in MTBL

The results of each model at Locations 1, 2 and 3 within the human carotid bifurcation are presented in Figure 6.9, Figure 6.15 and Figure 6.19 respectively, along with experimental values recorded by Santilli et al. in dog carotid bifurcations. Models 1 - 4, which include the bound oxygen, predict a high gradient within the MTBL at all three locations that is also observed between the luminal and first arterial wall PO_2 values in the experimental results from Santilli et al. Model 5, which does not include the bound oxygen, fails to predict this steep gradient. Previous studies have hypothesised that this high gradient in PO_2 between the lumen and arterial wall is due to high oxygen

consumption by the endothelium,[259] and this is currently an unresolved controversy in this field because it is not corroborated by *in vitro* studies. This controversy is covered in depth by both Vadapalli et al. and Tsai et al.[258,261] In the results presented here, predictions by Model 1 show that the high gradient seen experimentally could be due to the complex balance between the free and bound oxygen contained within the MTBL, and the consumption within the arterial wall. This could be a very important consideration for future oxygen transport studies.

To analyse this phenomenon in further detail the PO_2, dS/dPO_2, D' and S values for each model at Location 1, as shown in Figure 6.7, are referred to again. Model 1 and 3 include the varying gradient of the dissociation curve, dS/dPO_2, in the calculation of D'. As shown in Figure 6.7(b), dS/dPO_2, increases rapidly within the boundary layer which numerically results in a decreased D' within this region for both Model 1 and 3. What this means physiologically is that there are two exchanges taking place: the exchange of oxygen between the blood and the arterial wall, and the exchange of oxygen between the RBCs and the plasma, i.e. the bound and free oxygen. The free oxygen only constitutes 1.5% of the total oxygen contained within the blood,[200] and therefore, the bound oxygen can have a significant effect on the exchange of oxygen between the blood and the wall by either acting as a large PO_2 reservoir. This is exemplified by the difference in PO_2 between the models that include the bound oxygen, Models 1 - 4, and the one that does not, Model 5. It is clear from the results that the high gradient is not a result of modelling just the RBC dispersion (Models 1 and 2) or by assigning a variable dS/dPO_2 value within the domain (Models 1 and 3), but just by including the bound oxygen only.

6.3 Conclusion

This test case was undertaken to assess the five blood oxygen transport models in an idealised artery and to compare the predicted results to experimental measurements at three locations taken in dog carotid arteries. When the results were analysed the most significant observation was that the most advanced model, Model 1, predicted a high PO_2 gradient at the luminal surface. This is the first time that this has been observed in computational models and matches well with experimental measurements. Critically, this may help settle a controversial issue in the area of oxygen transport modelling which is explained in a paper by Tsai et al. (2010).[258] Specifically, the high gradient in the PO_2 levels adjacent to the arterial wall luminal surface were observed experimentally which led to some researchers to assume that the endothelium consumes vastly more oxygen than the typical VSMCs in the arterial wall. This assumption is not backed up by experimental data on cultured ECs. Here, for the first time, the high PO_2 gradient has been predicted and appears to be a consequence of the balance between the free and bound oxygen, and the consumption within the arterial wall.

In addition to the above conclusion, this test case also confirms that simplifying the blood oxygen transport model leads to significant differences in the predicted PO_2 levels on the luminal surface and also within the arterial wall. Critically, Model 5, the most commonly used blood oxygen transport model in the literature, failed to predict the steep PO_2 gradient adjacent to the luminal surface and significantly over-predicted the amount of oxygen diffusing into the arterial wall. This will be further demonstrated in Test Case 2 in the following chapter.

Finally, an obvious limitation of this work is evident in the results, namely that the arterial wall oxygen transport model is not accurate with predicted PO_2 values across the arterial wall falling below the experimental measurements. This may be in part due

to the difference between physiological differences between dogs and human arteries. Also, the intima and media are modelled as homogeneous materials with different consumption, diffusivity and oxygen solubility. In reality, macrophages, plaques and penetrating vasa vasorum which could exist *in vivo* would alter these values significantly. Certainly, at Location 2, an area which is prone to lesion development, could have a cellular composition and consequently, oxygen transport governing parameters very different to those which exist in a healthy artery.

6.4 Summary

In this test case the oxygen transport within an idealised geometry of a human carotid bifurcation was predicted using five different oxygen transport models with varying degrees of simplification. The results were compared with experimental results from a study of oxygen levels across the arterial wall of carotid arteries at three locations in 11 mongrel dogs.

The results indicate that:

- Simplifying the blood oxygen transport model has significant effects on the predicted arterial wall oxygen levels.
- Further work is needed in deriving crucial parameters for the oxygen diffusion and consumption within the arterial wall to vacillate more accurate prediction of oxygen levels.
- A high PO_2 gradient observed in experimental studies was recreated here for the first time using the oxygen transport models that incorporate both bound oxygen and free oxygen. This may have important implications for future work in this area.

The next chapter describes Test Cases 2, where the same five models were used in analysing the oxygen transport in a stented coronary artery, and Test Case 3, where Model 1 is used to compare three different stent designs.

CHAPTER 7

Test Cases 2 & 3 – Stented Coronary Arteries

7.1 Introduction

ISR is a continuing problem for coronary artery stent design. NIH is one of the key biological processes that can result in ISR, and has been found to be exacerbated by hypoxia and disturbed haemodynamics within the stented region.[134,135] Test Case 2 assesses the predicted PO_2 levels and Sh using the five blood oxygen transport models, as summarised in Table 3.1, within a realistically-deformed stented coronary artery. As part of this assessment the maximum and minimum PO_2 transarterial wall profile plots within the stented region are compared with *in vivo* experimental measurements from stented rabbit aortas of similar size from Santilli et al.[218] Test Case 3 then compares the predicted PO_2 levels and Sh, as modelled using the most advanced blood oxygen transport model, within the realistically-deformed stented coronary arteries of three different stent designs.

7.2 Geometry Creation

Three different stent designs, shown in Figure 7.1, were investigated in this study and are referred to as Stent A, Stent B and Stent C with their differing geometrical properties listed in Table 7.1.[153] Stent A resembles the BX Velocity stent (Cordis of Johnson & Johnson, Fremont, CA, USA), Stent B resembles the S7 AVE stent (Medtronic, Fridley, MN, USA) and Stent C resembles the thick strut Multilink RX Ultra stent (Abbott Laboratories, Lake Bluff, IL, USA). The tri-folded balloon-tipped

catheter, used in the structural analysis described below, resembles the configuration of the Raptor balloon-tipped catheter (Johnson & Johnson).

Stent	A	B	C
Stent configuration	Closed-cell	Open-cell	Open-cell
Strut thickness	0.14 mm	0.10 mm	0.13 mm
Strut width	0.13 mm	0.10 mm	0.10 mm
Link configuration	Peak-to-peak	Peak-to-peak	Peak-to-valley
Link type	Flexible	Non-flexible	Non-flexible
Link shape	N-shaped	Straight	Straight
Link width	0.10 mm	0.08 mm	0.10 mm

Table 7.1: Geometrical properties of the three investigated stents.[153]

The realistically-deformed stented artery geometries were obtained from non-linear finite element analyses (FEA) carried out using ABAQUS (Dassault Systèmes, Providence, RI, USA). These structural analyses consisted of the expansion of the sample stents using the realistic model of a tri-folded balloon-tipped catheter within an idealised coronary artery as shown in Figure 7.2. Each of the three stents were assumed to be manufactured from 316L stainless steel and a rate-independent elastic-plastic material model with isotropic hardening was adopted to describe their mechanical behaviour. The elastic-plastic response was modelled on the basis of data reported by Murphy et al., who conducted uniaxial tension tests of 316L stainless steel struts.[170] Likewise, the mechanical behaviour of the guide wire, catheter shaft, and angioplasty balloon was described using isotropic linear elastic material models with their linear elastic response described using data from Mortier et al., who employed a realistic model of the Raptor balloon-tipped catheter to evaluate the mechanical impact of stent

deployment within a bifurcated coronary artery.[167] The thicknesses of the intima, media and adventitia were 0.24, 0.32, and 0.34mm respectively, and their mechanical behaviour was described using isotropic hyperelastic material models with their non-linear elastic response adopted from data reported by Holzapfel et al.[100] Holzapfel et al. carried out experimental analysis of 13 human LAD coronary arteries harvested within 24 hours of death.

The computational domain was 20mm long with the arterial lumen set at a stent-free diameter of 2.7mm and external arterial wall diameter of 4.5mm. The stents had an 8.0mm unexpanded length and were expanded using a pressure load, which varied with each stent design, within the balloon to achieve a deployment ratio of 1.1:1. Once expanded, depending on the stent strut configuration, the overall length of the stent changes: Stent A 7.7mm, Stent B 7.4mm, and Stent C 8.3mm. This can be seen clearly in Figure 7.3 where Stent C is noticeably longer than the other two stents when completely expanded. As a side note, also noticeable in Figure 7.3 is the apparent corrugation of the arterial wall luminal surface, i.e. the surface is not completely smooth. This is because of the mesh size and type used for discretising the arterial wall for the FEA, and has a perceptible effect on the variables of interest which use gradients in their calculation, namely WSSG and Sh. For the purpose of this study though the overall distributions are still clear for both variables.

The mechanical behaviour of the coronary arterial wall is highly non-linear, predominantly because of the collagen fibres within, which stiffen the arterial wall at higher stress levels.[72] This non-linearity is accounted for by using third-order Ogden hyperelastic material models for each layer of the arterial wall. These hyperelastic material models were fit to the appropriate experimental data from Holzapfel et al. with different hyperelastic material constants adopted for each layer, which showed good

agreement with experimental data, as described by Martin.[150] The FEA solution was carried out using ABAQUS/Explicit solver with multiple contact surfaces and friction included. As shown in Figure 7.2(b), as the pressure load is increased the ends of the stent begin to expand first. This is referred to as dog-boning, because of the shape, and is commonly observed in the literature.[152,236,251] Once the fully expanded configuration is reached, as in Figure 7.2(c), the balloon was deflated, Figure 7.2(d), and the stent recoils slightly and settles into its final expanded configuration. Further details of these analyses are discussed elsewhere.[150,153] The final expanded configuration of both the stent and the arterial wall was then exported from ABAQUS to Rhinoceros 3-D where the geometry was adapted for CFD analysis. This adaption involved removal of small sliver regions, which would disrupt the mesh generation, where the stent surface would be malapposed to the luminal surface that are caused largely by mismatched mesh patterns. Entry and exit regions, 32mm in length, were added proximal and distal to the stented region to ensure that the haemodynamics were not affected by the boundary conditions. These regions also included 4mm length of intima and media to ensure that the oxygen MTBL had developed adequately. Only the intima and media layers of the arterial wall were needed for the oxygen transport analysis as the adventitia is supplied with oxygen by vasa vasorum within it, as discussed in previous chapters. The stented region itself for each stent was defined as the 12mm long region where the diameter of the artery at the extremities has returned to its unstented value. The stented region for each stent is shown in Figure 7.3.

Only Stent A was used for comparison of the five different blood oxygen transport models in Test Case 2. All three stents were compared using the most advanced model, i.e. Model 1, in Test Case 3 for the purpose of demonstrating the effects of different stent designs on the PO_2 values on and within the arterial wall.

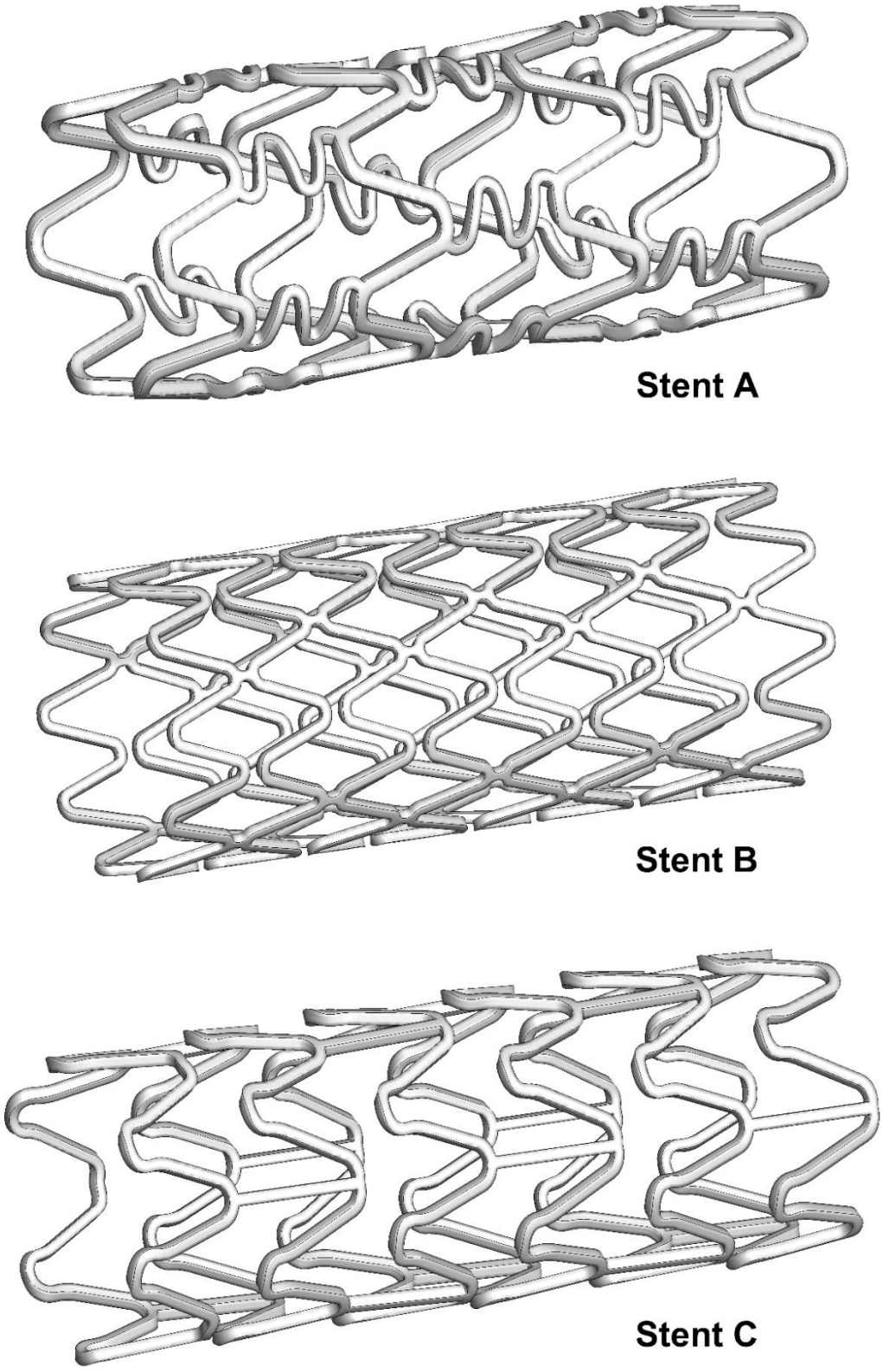

Figure 7.1: The three stents analysed. The final deformed configuration is shown.

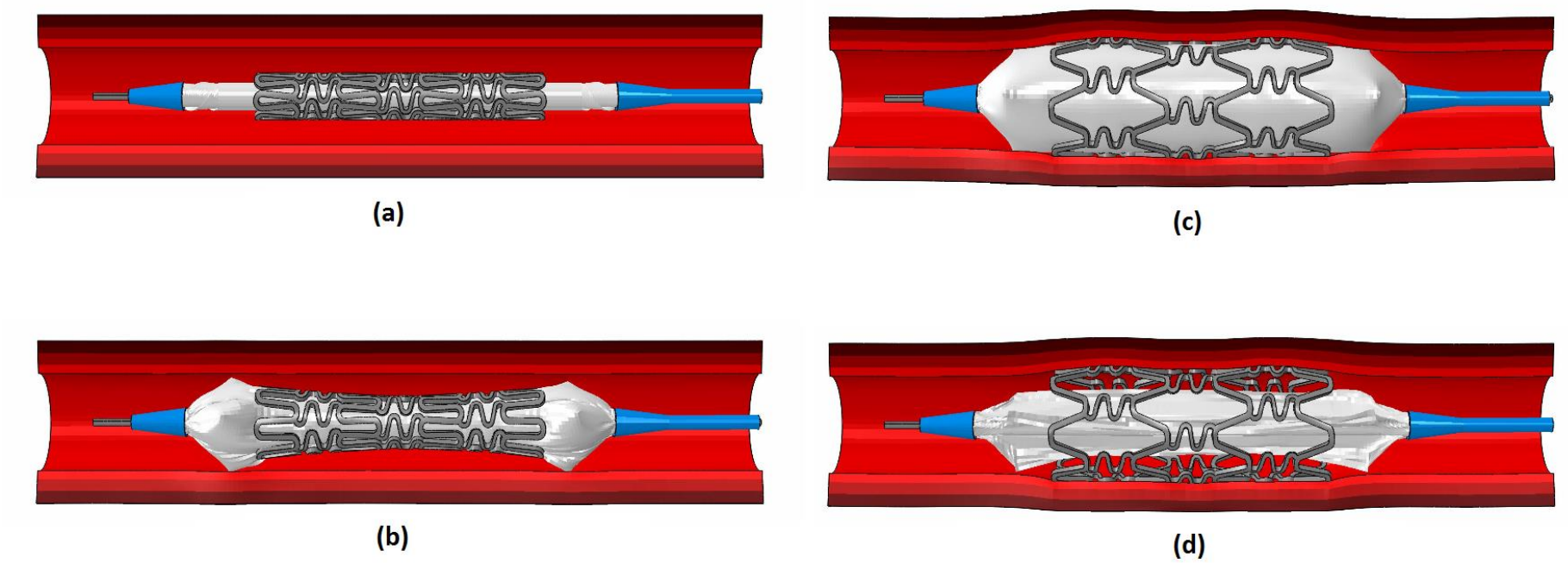

Figure 7.2: FEA-predicted deployment of Stent A, as carried out by Martin et al. (2014), using a tri-folded balloon-tipped catheter within an idealised coronary artery with a heterogeneous multi-layered arterial wall incorporating an intima, media and adventitia.[153] **(a) Initial configuration with a pressure load=0.00MPa, (b) expansion of balloon with a pressure load=0.50MPa, (c) maximum expansion with a pressure load=1.10MPa, and (d) the final deformed configuration with a pressure load=-0.01MPa.**

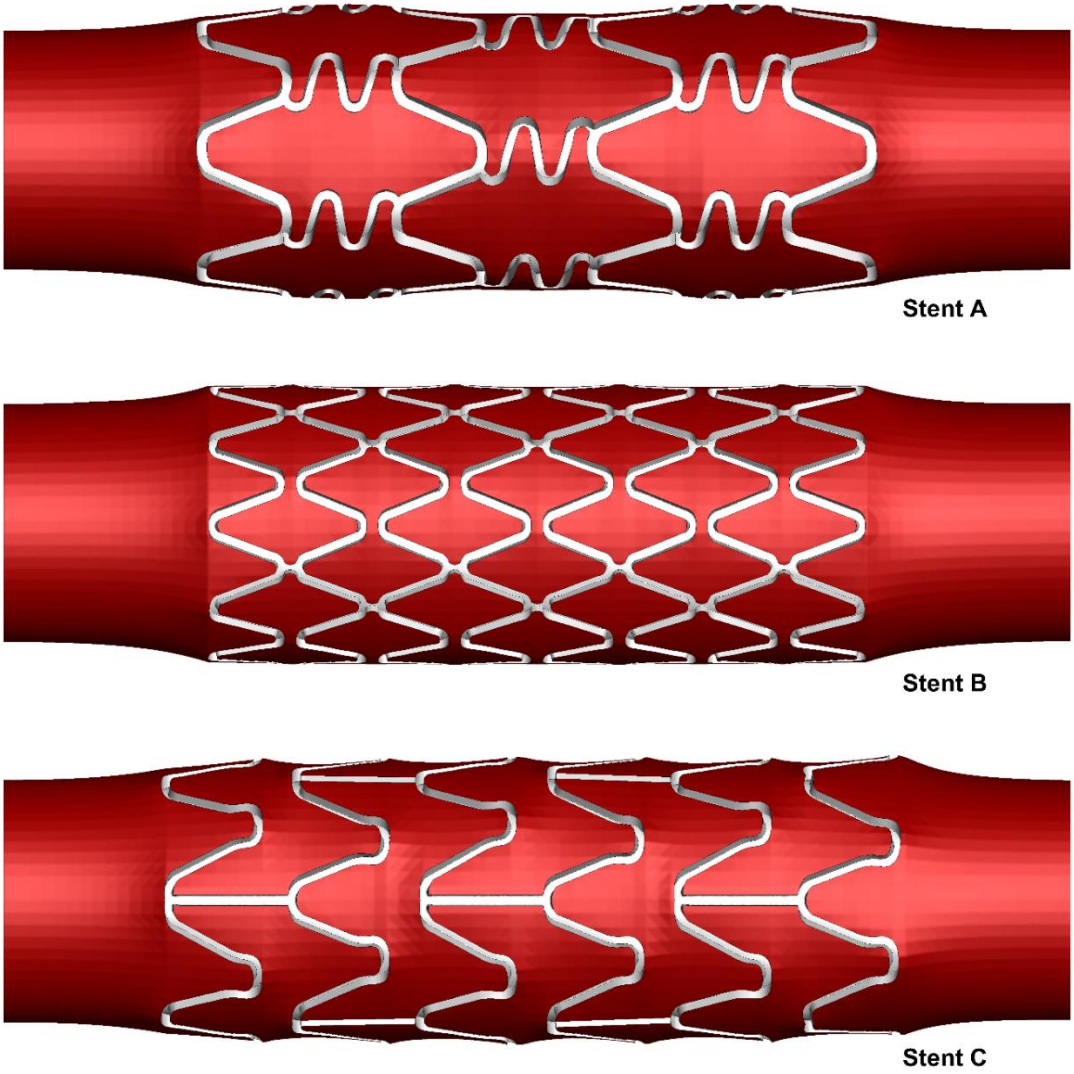

Figure 7.3: The stent and luminal surface within the stented region for the three stents analysed.

7.2.1 Geometry Discretisation

Similar to Test Case 1 the geometry was imported into ANSYS ICEM meshing software for discretisation. An unstructured mesh topography was adopted for all three stented artery geometries comprising of tetrahedral and prism elements. The mesh inflation parameters established in the validation test case were taken as a basis for the mesh convergence studies of the stented coronary artery geometry. The surface mesh

was generated using the Octree Method which was used as a basis for the volume mesh created using the Delauney Method. Finally, prism layers were added at the luminal surface (eight layers) and within the media (eight layers). This meshing procedure is recognised for its generation of good quality meshes for CFD using ANSYS ICEM mesh generation software. The Octree Method is a robust method that is reliable for complicated geometries and the Delauney Method produces a volume mesh which has a smoother volume mesh transition between adjacent elements. This smoother transition results in improved aspect ratios, which in turn helps with solution convergence. The prism layers are required for accurate prediction of both the haemodynamics and the PO_2 boundary layer at the luminal surface. Recommendations by previous researchers in this area were taken into account in the mesh generation and also confirmed by the mesh convergence study, the results of which are presented in Appendix B. For instance, it was found that for accuracy in predicting the oxygen transport at the luminal surface at least three layers of prisms off the luminal surface within the MTBL are required. This is in agreement with previous work by Tada, and Coppola and Caro in this area.[43,248] For the meshes generated here eight prism layers were used because areas of flow disturbance resulted in a thickened MTBL which required additional prism layers, in comparison with previous authors, for it to be accurately captured. Figure 7.4 shows a cross-section of the mesh employed for Stent A.

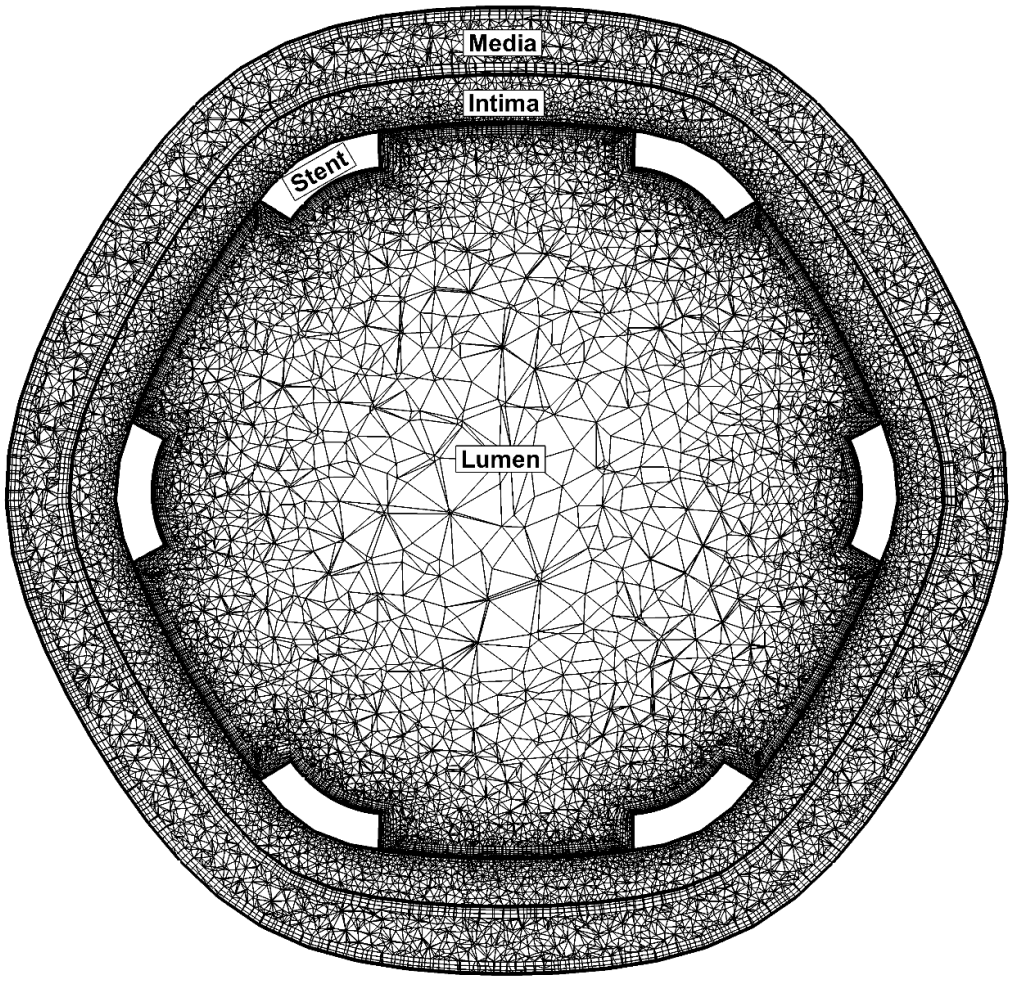

Figure 7.4: Cross-section of mesh employed for Stent A at mid-point of stented region. Refinement was applied on the stent surface and prism layers were used on the luminal surface, and also within the arterial wall, to ensure accurate capture of both the haemodynamic and PO_2 transport features.

7.2.2 Boundary Conditions

For the stented artery models the following boundary conditions were implemented. At the inlet of the fluid domain a fully developed Hagen-Poiseuille velocity profile was imposed with V_{mean}=0.2313m/s, which results in an average volume flow rate of 40ml/min which is within the range of typical basal values seen in human LAD coronary arteries *in vivo*.[112] Also, at the inlet $PO_{2,in}$=100mmHg, which is normal arterial

blood PO_2.[200] At the outlet an entrainment boundary condition with a zero relative pressure was set with $PO_{2,out}$=0mmHg. PO_2 was free to transfer across the luminal/arterial wall surface, and across the intima/media interface surface. On the stent surface a PO_2 zero-flux condition was imposed. On the media/adventitia interface surface PO_2=45mmHg, as used by Richardson,[206] and on the wall surfaces located either end of the arterial wall section a zero flux boundary condition was imposed.

7.3 Results and Discussion - Test Case 2

Figure 7.5(a) and (b) show the maximum and minimum PO_2 transarterial wall profile plots within the stented domain for all five models which were taken at the position of maximum and minimum luminal surface values. For comparison the measurements by Santilli et al. from rabbit aortic arteries on day 1 following stent implantation with 3mm internal-diameter stents are also shown.[218] The stents used by Santilli et al. were manufactured by Cordis, although it was not stated specifically that the BX Velocity stent was used. The balloon used was a 3.0mm outer diameter balloon, which was also used in the FEA simulations presented here. In their study, the exact measurement location within the stented domain is not provided and therefore, the maximum and minimum profiles for each model are presented here alongside the experimental results. Assuming the experimental results are taken as being reflective of the PO_2 values present in a similar size human coronary artery, as modelled here, then Model 1 is again shown to produce the steep PO_2 gradient and is within the range of luminal surface PO_2 values observed experimentally. Model 5 again over-predicts the amount of oxygen being transported to the luminal surface and there is an absence of the steep PO_2 gradient at both locations. Models 2 and 4 also over-predict the oxygen flux into the arterial wall, and Model 3 again significantly under-predicts it. Both Models 1 and 3, and Models 2 and 4 are quite similar at the minimum location because the minimum

luminal surface PO_2 values for all five models are within a low velocity recirculation (almost stagnate) zone next to a stent strut and the shear rate is low which consequently means the D_c value is also low, i.e. almost negligible in this case. The uneven section of the transarterial curves within the lumen in Figure 7.5(b) are also attributed to this recirculation zone downstream of the stent strut at this location.

Differences in the PO_2 transarterial wall profile predicted by the simulations and the experimental results from Santilli et al. are attributed to differences in arterial wall properties of different species. For example, looking in more detail at the PO_2 transarterial wall profiles it would appear that the diffusion of oxygen through the intima of the rabbit aortae may be higher than in the human coronary arteries as modelled here. This would be supported by looking specifically at the maximum PO_2 transarterial wall profile of Model 1 which shows the closest luminal surface PO_2 value to the experimental results. A higher diffusivity would shift the curve (in red in Figure 7.5(a)) over towards the experimental measurements by Santilli et al.; additionally, the consumption value would also vary. Further work would need to be carried out to confirm this and could again highlight the differences in arterial wall tissue properties observed across different species.

The effect of the higher consumption value for the human coronary artery as adopted in the intima domain in these simulations is clearly distinguishable in Figure 7.5(a) with a considerably steeper curve in the first approximately 0.15mm (less than 0.24mm set for the intima because of stretching caused by the stent implantation) from the luminal surface to an approximate radius of 1.70mm in comparison with the slope of the PO_2 transarterial wall profile from this point to the outer boundary.

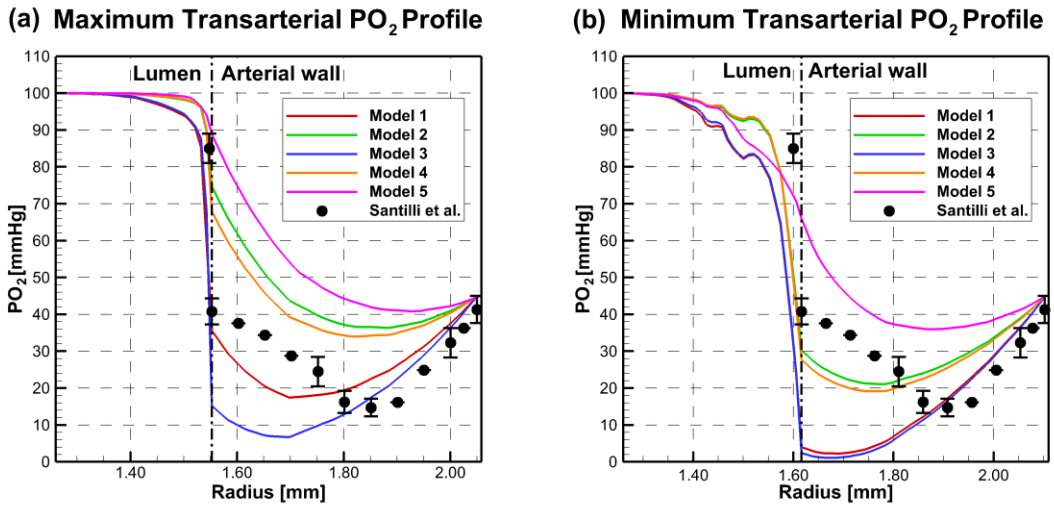

Figure 7.5: (a) Maximum and (b) minimum transarterial PO_2 profiles for each model applied to the deformed coronary artery geometry virtually implanted with Stent A. Measurements adapted from Santilli et al. are shown for comparison and the distances through the arterial wall for these have been scaled to the size of a human coronary artery.[218] The minimum PO_2 luminal surface value for each model is located within a recirculation zone immediately downstream of a stent strut which produces a severe drop and variable slope in PO_2 profile in Figure 7.5(b). The luminal surface is shown as a vertical dashed-dotted line. Note: locations of maximum and minimum PO_2 transarterial profiles for each model are shown in Figure 7.6.

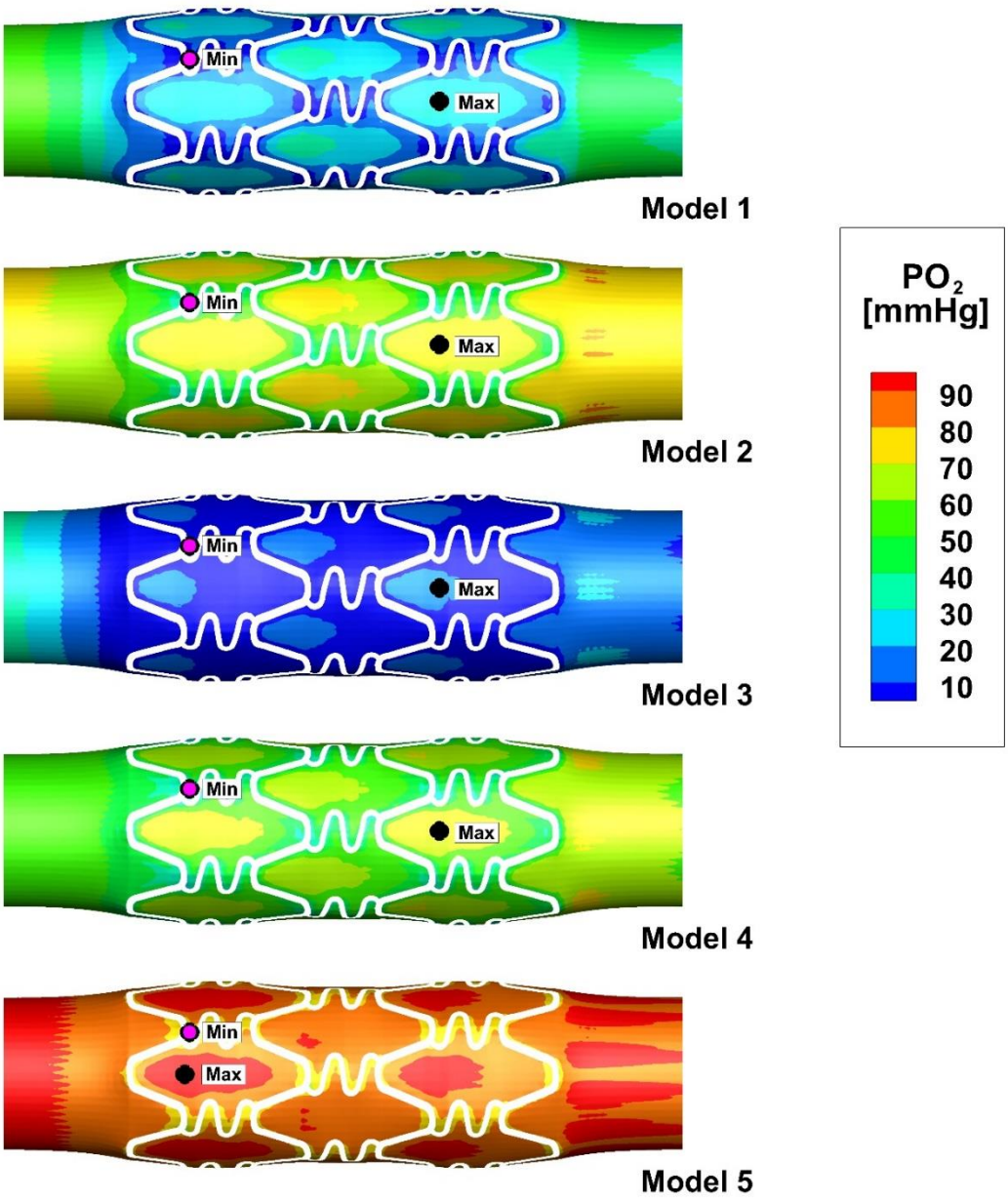

Figure 7.6: Locations of predicted maximum and minimum luminal surface PO_2 values within the stented region for each model which were used for the profile plots in Figure 7.5. To give an indication of the gradient of the PO_2 along the surface at the maximum locations Figure 7.8 shows a line plot of the PO_2 along line A-A'.

Contour plots of the PO_2 and Sh are shown in Figure 7.7(a) and (b) respectively. When analysed in conjunction with the line plots along the axial cross-section A-A' (Figure

7.8) the effects of each model become apparent. The difference between Model 1 and the simpler models is striking. Firstly, the plots of the PO_2 values along the luminal surface in Figure 7.7(a) show quite a large variability across the five models with the extent of the difference clear in the PO_2 line-plot in Figure 7.8. The areas of low PO_2 values (<30mmHg) around the stent struts which are apparent with Model 1 do not appear with Models 2, 4 and 5, with Model 5 predicting very little variation in PO_2 on the luminal surface with the lowest value being 64mmHg. Model 3, which neglects the RBC dispersion, predicts very low PO_2 levels on the luminal surface that translate into very little oxygen diffusing into the arterial wall. Interestingly though, Model 3 predicts very high Sh values along the surface because the Sh is based on the gradient of PO_2 normal to the surface, which is very high for Model 3 as seen previously in Figure 7.5. This highlights a possible disadvantage in using the Sh as a basis for analysis in the form adopted here as it uses the PO_2 gradient normal to the wall.

	Hypoxic PO_2 (<10mmHg)	**Low PO_2 (<30mmHg)**	**D'_{min}**	**D'_{max}**
Model 1	12.6%	72.8%	1.12E-11	3.51E-10
Model 2	0.0%	14.3%	9.05E-11	2.56E-10
Model 3	36.6%	80.8%	6.13E-12	2.08E-10
Model 4	0.0%	33.9%	8.58E-11	8.58E-11
Model 5	0.0%	0.0%	1.20E-09	1.20E-09

Table 7.2: Percentage volume of the arterial wall exposed to hypoxic and low PO_2 within the stented region for each model along with the minimum and maximum D' values present within the blood flow.

The relatively small variation in PO_2 values observed along the luminal surface for Model 5 translates to very little variation predicted in the local Sh also. For Models 1 –

4 there is a similarity in the regions of low and high Sh, with low Sh (values tending towards the calculated Da≈17) predicted in regions where the flow is separating away from the luminal surface and high Sh predicted in regions where the flow is reattaching, i.e. where the flow is directed towards the wall and oxygen transport through convection is high. The peaks of high Sh observed with Models 1 – 4 are dampened considerably for Model 5 to the extent that the reattachment points are unrecognisable on the luminal surface plots. Da itself could not be used as a threshold value in this case since none of the models actually predicted the local Sh to drop below 17 on the luminal surface even though significant portions of the arterial wall were predicted to be exposed to hypoxic PO_2 levels. This may highlight a limitation of using Da as a threshold value for low Sh.

Greater amounts of neointimal thickening have been shown to occur in areas with PO_2 values of less than 30mmHg, and hypoxia exists where the PO_2 levels drop to below 10mmHg.[34,218] Thus, how much of the arterial wall is exposed to PO_2 values below these two thresholds is of importance in predicting the possibility of excessive neointimal thickening and potential ISR. As shown in Table 7.2, the five models studied here predict a broad range of percentage volumes of the arterial wall exposed to low PO_2 (<30mmHg). For example, Model 5 predicts that none of the stented arterial wall is exposed to low PO_2, as opposed to Model 1 predicting 72.8% of the stented arterial wall is exposed to low PO_2 with 12.6% exposed to hypoxic conditions. Model 2, which neglects the non-linearity of the oxygen disassociation curve, differs significantly in the amount of hypoxic and low PO_2 regions (0% and 14.3% respectively) within the arterial wall compared with Model 1. Model 3, which neglects the shear-dependent dispersion of RBCs, predicts extensive hypoxic and low PO_2 regions within the stented region (36.6% and 80.8% respectively). The PO_2 levels drop off severely within the MTBL for Model 3 because the slope of the oxygen disassociation curve, dS/dPO_2, increases

significantly, reducing the D', as demonstrated in the analysis at each location in Test Case 1. This results in the lowest D' value of the five models, as shown in Table 7.2, which in turn results in the lowest PO_2 luminal surface values throughout the stented region, as shown in Figure 7.7. Model 4 is similar to Model 2 in the regard that it predicts that none of the arterial wall within the stented region is exposed to hypoxic PO_2 levels. Critically, this broad variability in predicted hypoxic and low PO_2 regions within the stented region again highlights the disadvantages of simplifying the blood oxygen transport model.

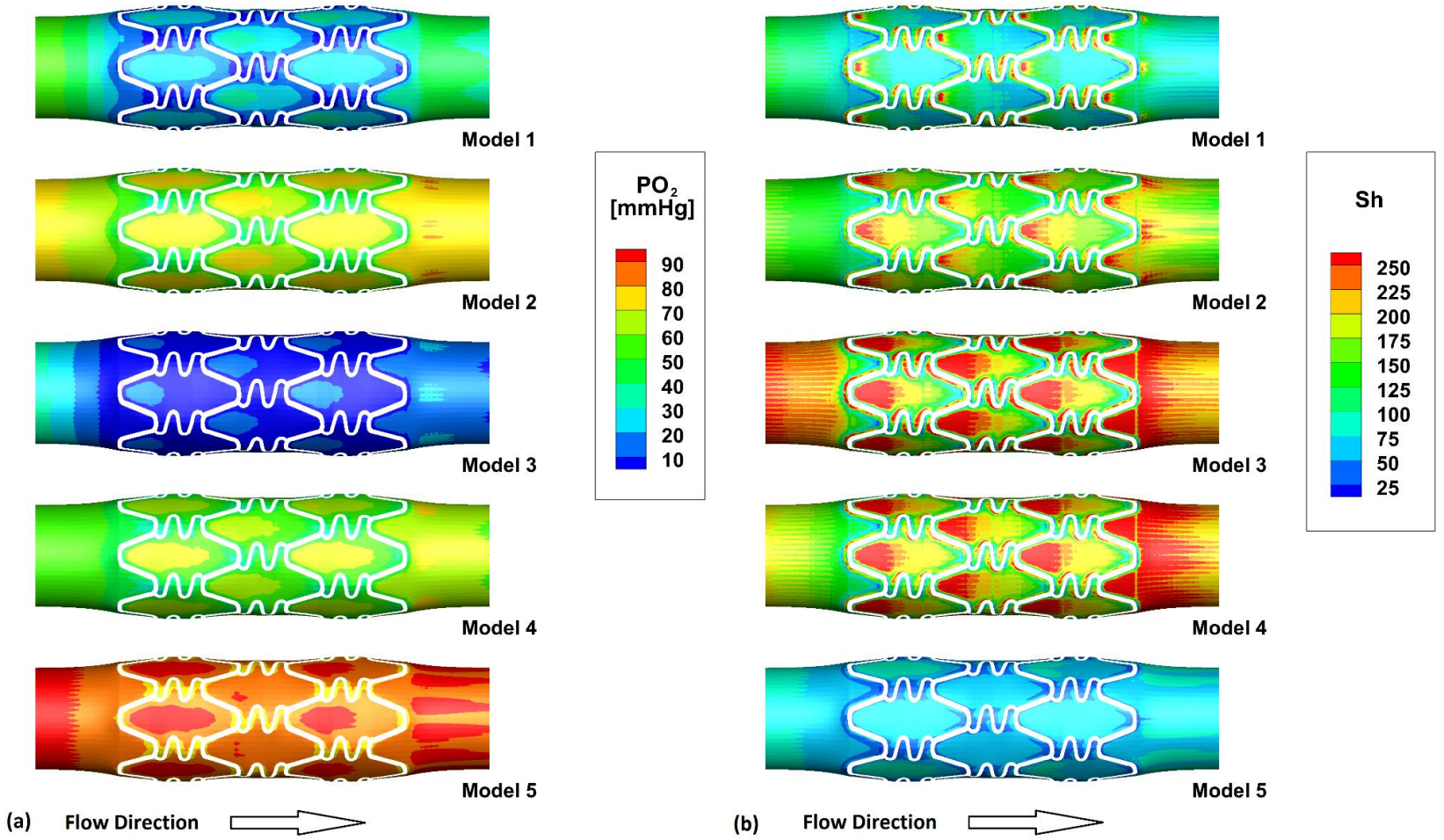

Figure 7.7: Predicted (a) PO_2 and (b) Sh on the luminal surface within the stented region.

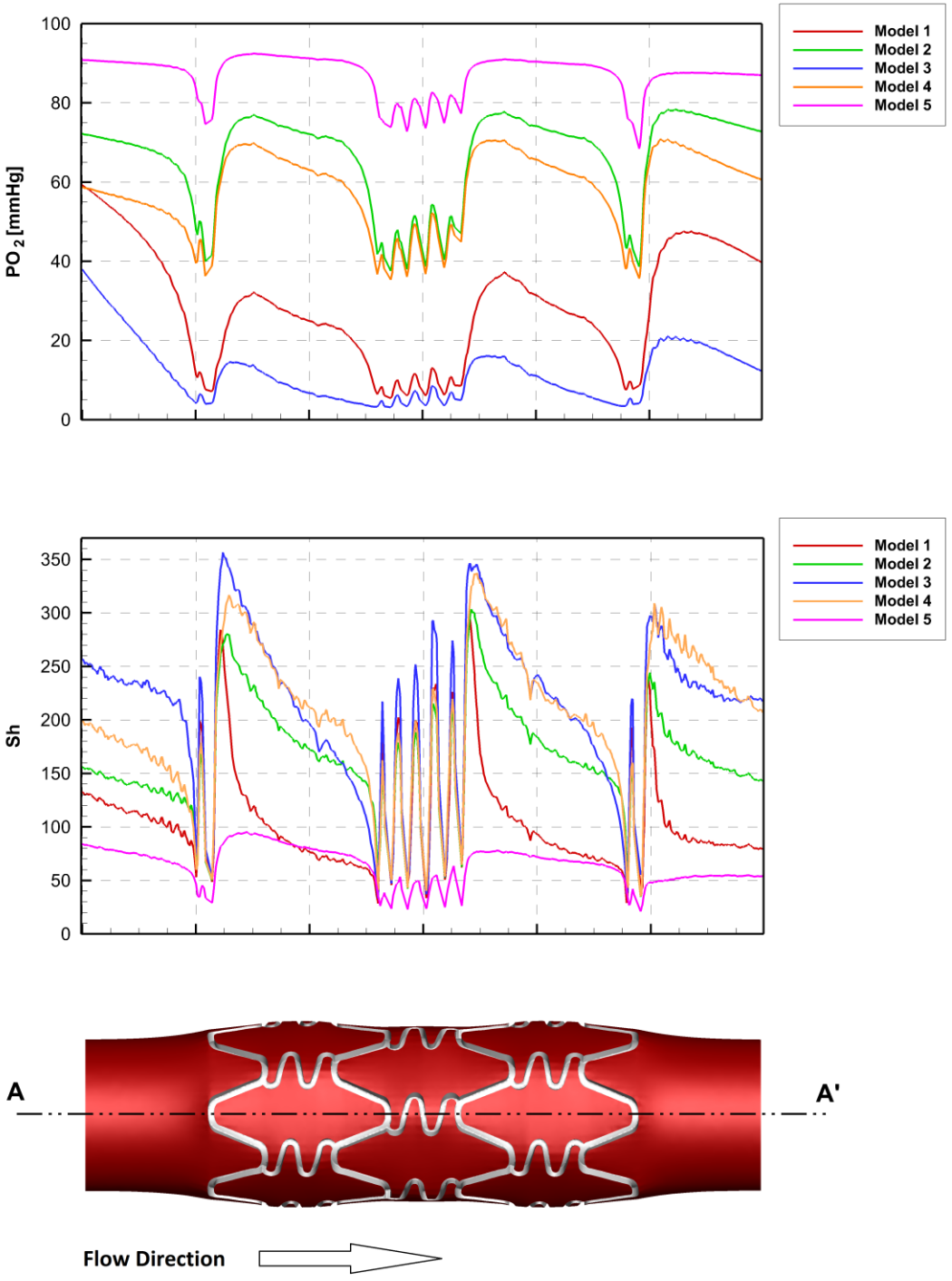

Figure 7.8: Predicted PO_2 and Sh along line A-A'.

7.4 Results and Discussion - Test Case 3

Investigating the results from all three stented arteries requires first to analyse the haemodynamics, and then the oxygen transport within each domain and how it's affected by the haemodynamics and arterial wall deformation. Finally, the predicted haemodynamics and oxygen transport results are compared alongside the restenosis rates for each stent.

7.4.1 Haemodynamics

Figure 7.9 shows the predicted WSS and WSSG within the stented region for each stent. Table 7.3 shows the percentage luminal area of the stented region which is exposed to low WSS <0.5 Pa. Low WSS is correlated with increased NIH.[127] As reviewed in Chapter 2, previous studies have shown that increased expression of pro-thrombotic agents, inflammatory cell adhesion molecules, and VSMC growth factors by ECs occurs in response their exposure to WSS below 1.0 – 1.2 Pa, although the effects are considered more severe below 0.5 Pa. Also, as mentioned in Chapter 2, a study of stent implantation in rabbits showed that ECs are still present adjacent to stent struts immediately post-implantation. This is crucial here because as shown in Figure 7.9(a) the areas that experience WSS values below 0.5 Pa are predominantly adjacent to stent struts. Stent A is predicted to perform the best of the three stents with 31.3% of the luminal area within the stented region exposed to low WSS, in comparison with 35.4% and 36.3% for Stent B and Stent C, respectively. Where the endothelial layer is destroyed within the stented region, in interstices between stent struts, VSMCs can be exposed to the blood flow.[208] According to the predicted WSS distributions for each stent here, as shown in Figure 7.9(a), any areas where VSMCs may be exposed to the

blood flow the WSS is below physiological WSS values, ranging from 0.5 – 1.0 Pa, which encourages VSMCs to proliferate.

The WSSG is also plotted for each stent in Figure 7.9(b). High WSSG (>0.85 Pa/mm) has been shown to increase endothelial permeability that causes increased macromolecule uptake.[195] It is assumed here that the endothelium offers no resistance to oxygen transport; however, increased endothelial permeability could lead to increased uptake of leukocytes causing increased inflammation in areas predominately around stent struts. The percentage of the luminal surface within the stented region which is exposed to WSSG values above 0.85 Pa/mm are shown in Table 7.3 for each stent. Significantly less of the luminal area is exposed to high WSSG values for Stent A (42.0%) than both Stent B (53.1%) and Stent C (53.9%). Therefore, the ECs within the stented region for Stent A would experience, in theory, less endothelial permeability in comparison with Stent B and Stent C.

Stent	A	B	C
Low PO_2 (<30mmHg)	72.8%	74.2%	68.9%
Hypoxic PO_2 (<10mmHg)	12.6%	14.3%	5.3%
Luminal Low PO_2 (<30mmHg)	62.7%	64.1%	57.2%
Luminal Hypoxic PO_2 (<10mmHg)	11.9%	5.0%	2.4%
Low WSS (<0.5Pa)	31.3%	36.3%	35.4%
High WSSG (>0.85Pa/mm)	42.0%	53.1%	53.9%
Interface Area	99.75mm^2	95.43mm^2	99.11mm^2
Restenosis Rate	31.4%	10.1%	25.8%

Table 7.3 Percentage volume of the arterial wall exposed to low and hypoxic PO_2 within the stented region for each stent along with the lumen/arterial wall interface area within the stented region and restenosis rate, as taken from the following clinical trials at 6-month follow-up: Stent A, ISAR-STEREO-II, Stent B, DISTANCE and Stent C, ISAR-STEREO-I, and discussed in Section 7.4.3.

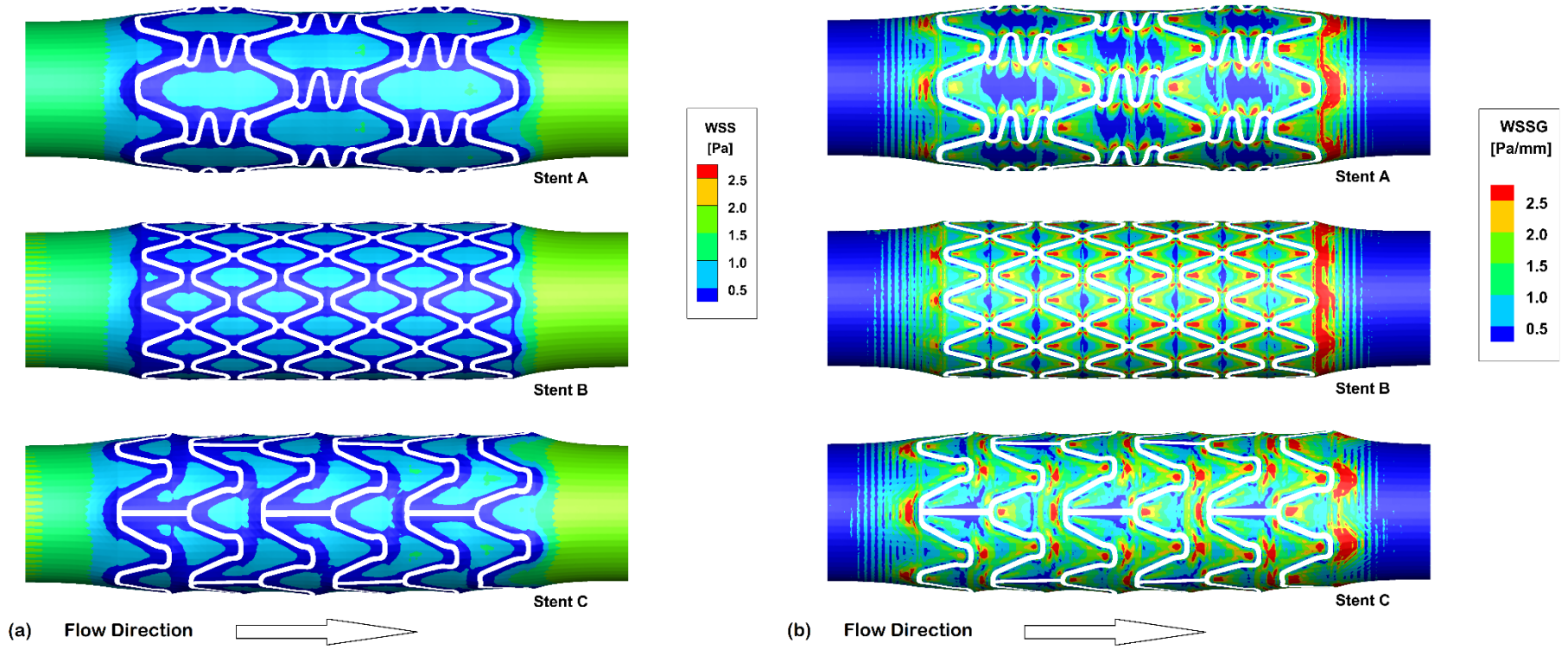

Figure 7.9: Predicted (a) WSS and (b) WSSG on the stented artery luminal surface for the three stents analysed.

7.4.2 Oxygen Transport

Comparing the three stent designs by concentrating solely on the percentage luminal area exposed to low WSS or high WSSG does not give sufficient detail on how the haemodynamics can affect the biological processes taking place within the arterial wall post-implantation. In this study here the inclusion of the oxygen transport allows analysis of the effects of the haemodynamics post-stent implantation on one aspect that can directly affect the cells within the arterial wall, not just on the luminal surface. Table 7.3 lists the predicted percentage volume of the arterial wall for each stent exposed to low and hypoxic PO_2 values. Stent C is predicted to perform the best of the three stents with only 68.9% of the arterial wall exposed to low PO_2 and only 5.3% exposed to hypoxic conditions. For Stent A 72.8% exposed to low PO_2 and 12.6% of the arterial wall is predicted to be exposed to hypoxic conditions. Stent B has the highest percentage volume exposed to low PO_2 at 74.2% and 14.3% of the arterial wall is exposed to hypoxic PO_2 levels. Figure 7.10(a), (b), and (c) show the distribution of the percentage volume of the arterial wall within the stented region exposed to PO_2 values in bins of 5 mmHg. Comparing the three stents, it is predicted that none of the arterial wall for Stent C is exposed to PO_2 values below 5 mmHg, compared with 1.1% and 3.1% of the arterial wall for Stent B and Stent A, respectively. Included in these histograms are the percentage volume of the arterial wall that is present in the intima for each PO_2 bin range. This analysis shows that in the case of these idealised arterial walls, with no plaque present, only the intima experiences hypoxic PO_2 levels, with the assumption that the intima remains intact. This would be in agreement with previous studies that found that the media is predominantly supplied with oxygen from the adventitial vasa vasorum. In this case, with hypoxia present within the intima, penetration of the media by the vasa vasorum would be induced.

To ascertain why each stent performs differently, in terms of oxygen transport, further investigation is warranted. Looking again at the WSS and WSSG luminal surface plots presented in Figure 7.9, along with the PO_2 and Sh luminal surface plots, and PO_2 axial cross-sectional plots for Stents A, B and C, as shown in Figure 7.11, and Figure 7.12. When Figure 7.12 is analysed it becomes apparent that the design of Stent C, with stent struts that are well-spaced out and link struts which are aligned with the flow, results in reduction in the size of the low and hypoxic PO_2 zones. Interestingly, the prolapse of the arterial wall between the struts allows increased oxygen convection into the wall downstream of each strut, which is apparent in Figure 7.11(b) with high Sh in these regions. This detail would not have been captured effectively with an idealised non-deformed arterial wall. Immediately apparent in Figure 7.11(a) and Figure 7.12 is that the N-shaped link struts in Stent A, which are predominantly aligned perpendicular to the flow, cause an extended region of recirculation zones and consequently low PO_2 values on the luminal surface. This further suggests the dominance of the augmented haemodynamic environment caused by stent implantation on the oxygen flux. For Stent B, the smaller interstrut areas relative to Stents A and C mean that the arterial wall does not prolapse into the lumen to the same extent as with the other two stents, as seen in Figure 7.13 and Figure 7.14. Additionally, the lumen/arterial wall interface area, i.e. the area exposed to the blood flow within the stented region, for Stent B is less than both Stents A and C because of the greater number of stent struts. It would appear that these particular design features of Stent B cause more of the arterial wall to be exposed to low and hypoxic PO_2 levels in comparison with Stent C.

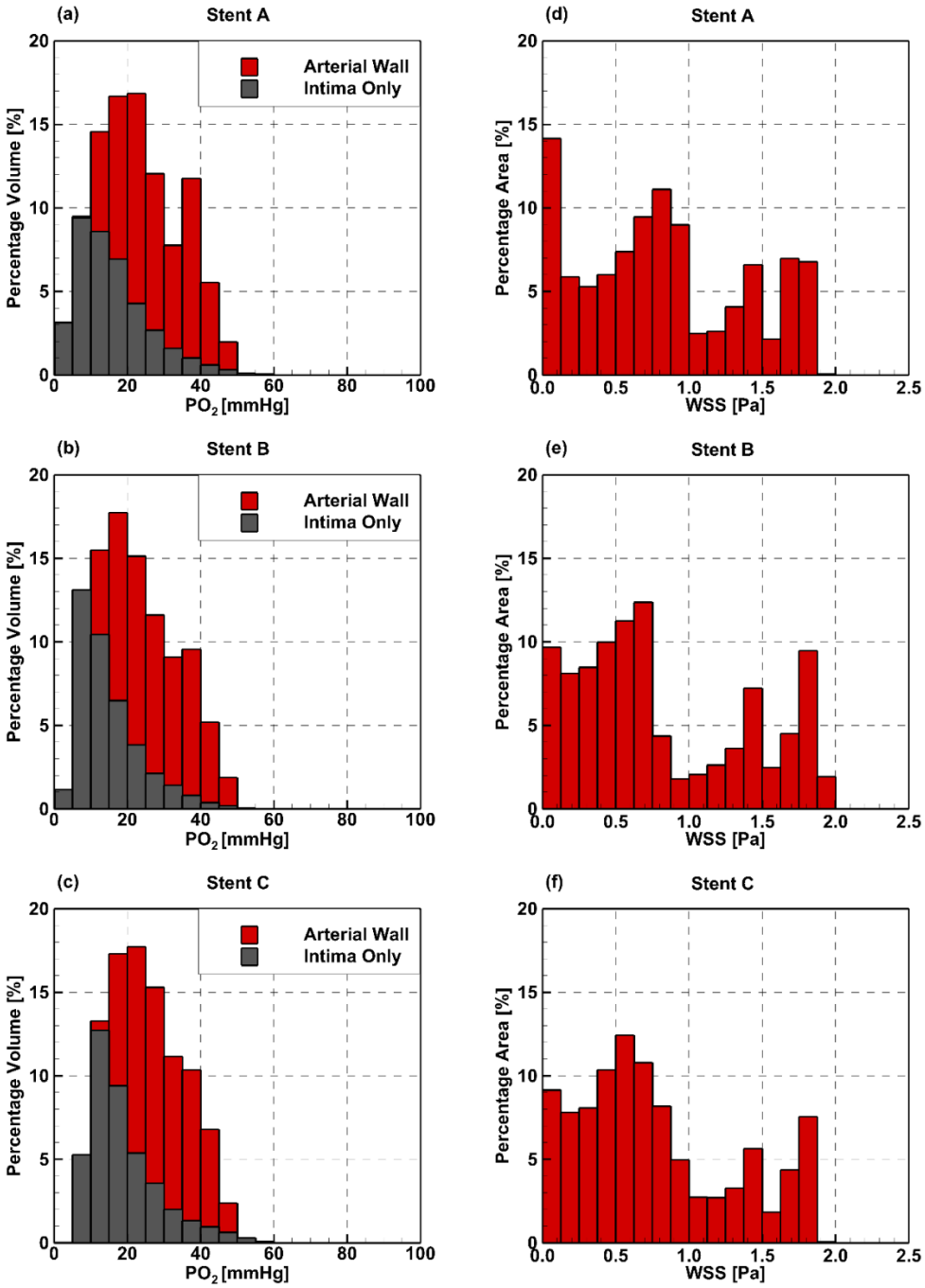

Figure 7.10: (a, b & c) Predicted percentage volume of the arterial wall and intima, both normalised with respect to the arterial wall volume within the stented region, exposed to PO_2 values in bins of 5mmHg for each stent. (d, e & f) Predicted percentage area of the stented luminal surface exposed to WSS values in bins of 0.125Pa normalised with respect to the total luminal area within the stented region for each stent.

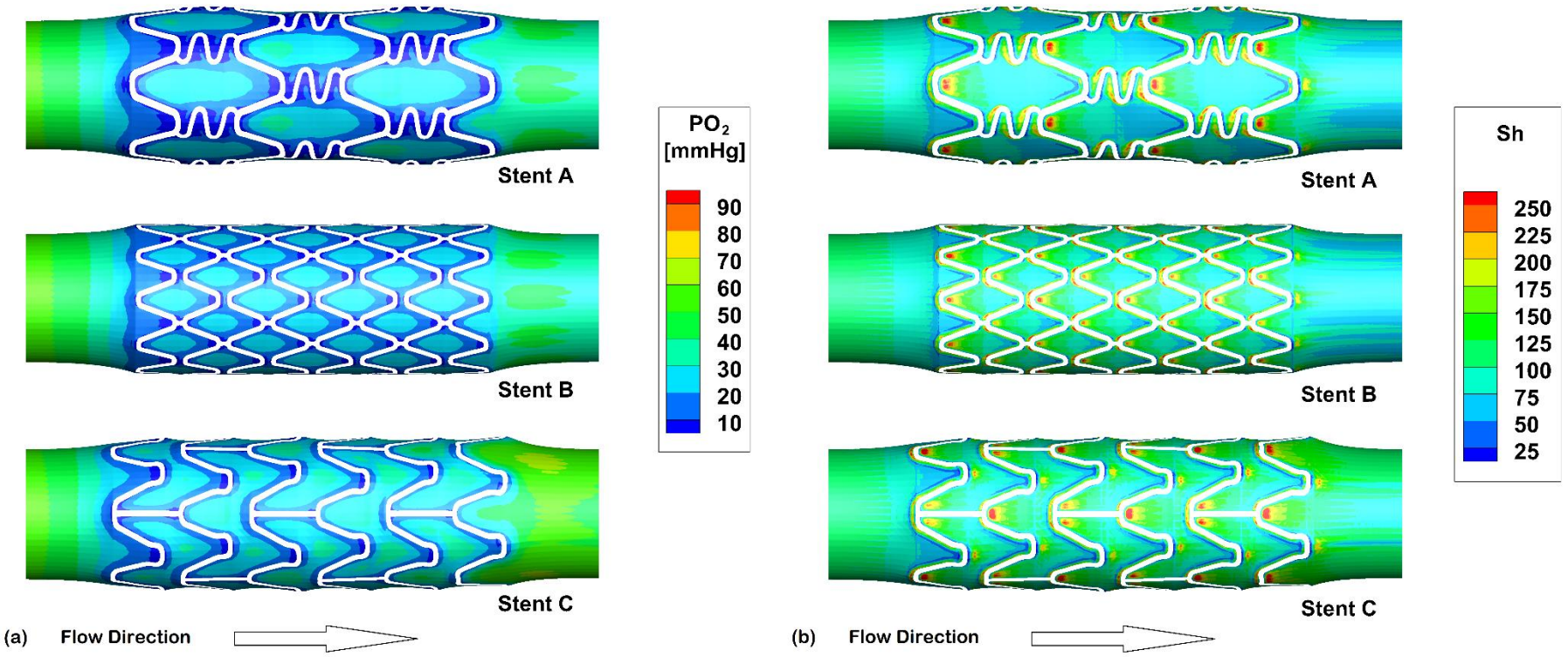

Figure 7.11: Predicted (a) PO_2 and (b) Sh on the stented artery luminal surface for the three stents analysed.

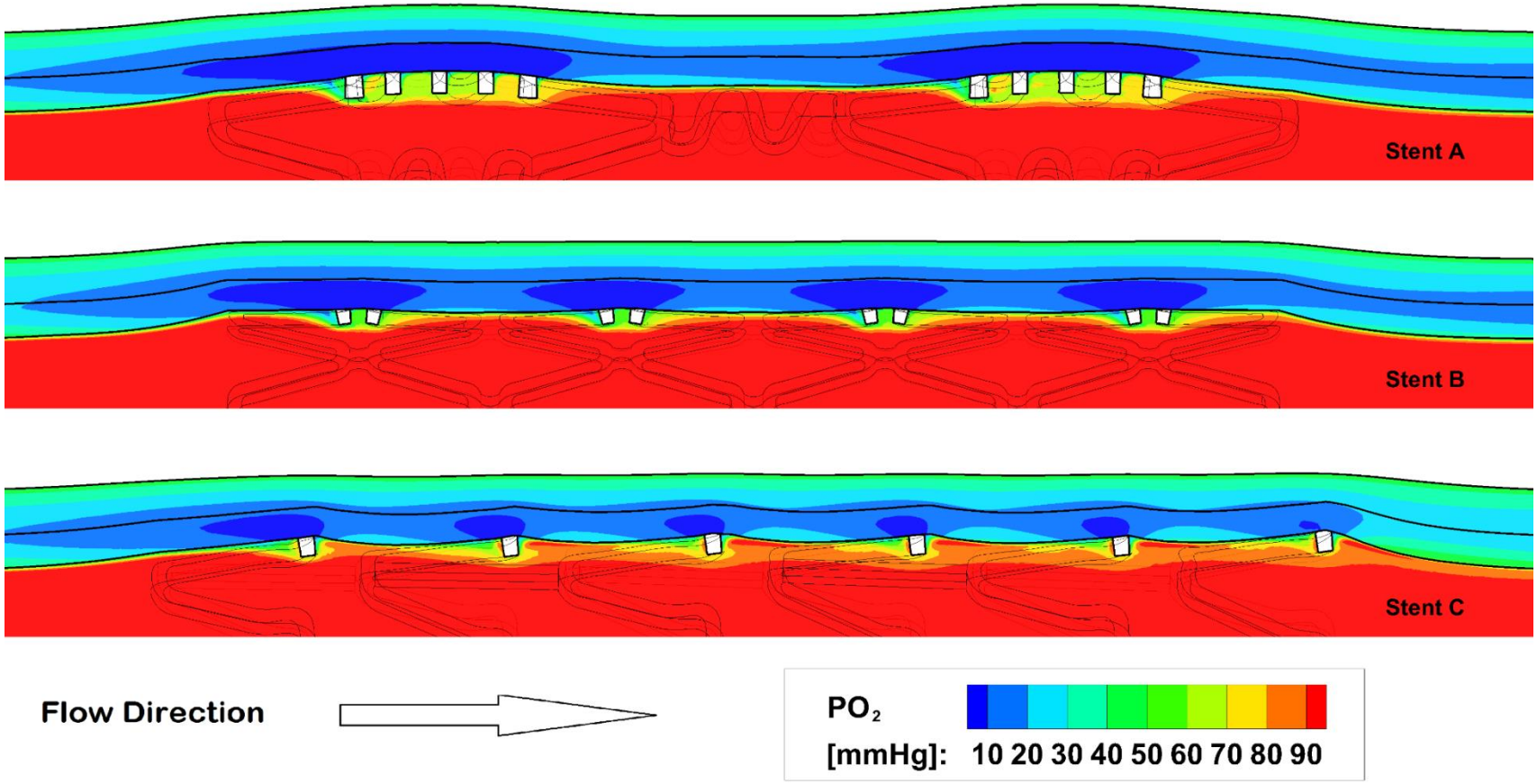

Figure 7.12: Axial cross-section of predicted PO_2 in both the arterial wall and lumen within the stented region for the three stents analysed. The interfaces between all three domains are clearly outlined.

Although, it is clear that it is not simply a case of decreased lumen/arterial wall interface area which impinges the PO_2 flux into the arterial wall since Stent A has a similar interface area to Stent C, as shown in Table 7.3, but produces low and hypoxic PO_2 percentage volumes only marginally better than Stent B. Therefore, there are additional factors involved. Particular to this study here, the realistically-deformed arterial wall is different for each stent, specifically the medial and intimal thicknesses vary within the stented region for each stent.

Figure 7.13 and Figure 7.14 show these thicknesses along two axial cross-sections for each stented artery geometry. When these are analysed it is clear that the arterial wall stretches when the stent is implanted, and that this stretching reduces the thickness of the arterial wall within the stented region to different extents depending on the stent design. The stretching acts circumferentially and axially, and for Stent C, which elongates in the axial direction from a length of 8.0mm crimped to a length of 8.3mm in final deployment configuration, it appears that the axial stretching thins the arterial wall, specifically the media, within the stented region. The percentage change in the volume of the arterial wall within the stented region for Stent A is -0.2%, for Stent B -2.5% and for Stent C -7.0%. Therefore, for Stent C there is a significant difference in the amount of the arterial wall that requires oxygen delivery. The media shows a -11.6% reduction for Stent C compared with -0.4% and -4.7% for Stents A and B, respectively. This comparative reduction is clear in Figure 7.13 and Figure 7.14 where Stent C shows a much lower medial thickness along two different axial cross-sections. This hypothesis is supported by the fact that the luminal surface PO_2 threshold percentage values, as shown in Table 7.3, do not directly match the arterial wall PO_2 threshold values. For instance Stent B has 5.0% of the luminal surface exposed to hypoxic PO_2 levels, compared to 11.0% and 2.4% for Stents A and C respectively. Yet, Stent B has the

highest percentage volume of the arterial wall exposed to hypoxic PO_2 levels (14.3%) compared with 12.6% and 5.3% for Stents A and C respectively. Note: the arterial wall volume displaced out of the stented region is still present in the computational domain as the arterial wall is modelled in the structural analysis as almost incompressible, it is just pushed out of the stented region. This is indicated by the slightly higher thickness of the media (0.33mm) on the extremities of the stented region in Figure 7.14. This would not be captured by a non-deformed idealised geometry.

On inspection of Figure 7.15, Figure 7.16, and Figure 7.17 it can be seen that higher values of Sh coincide with reattachment zones where both the WSSG is high and the WSS is increasing in the direction of flow. It is possible that within these reattachment zones increased infiltration of cytokines, mitogens, leukocytes, and thrombotic elements into the arterial wall could also occur leading to increased NIH. Therefore, increased oxygen transport by convection may come at a price of increased convection of pro-restenotic agents within the blood stream into the arterial wall at these locations. Also clear from Figure 7.15, Figure 7.16, and Figure 7.17 is that the predicted PO_2 luminal surface values are closely related to the WSS; however, the percentage volumes exposed to low and hypoxic PO_2 levels in the arterial wall do not match the percentage luminal areas exposed to low WSS, as shown in Table 7.3 and is also clear by comparing the histograms in Figure 7.10. This draws the conclusion that even though the WSS and luminal PO_2 values seem to follow similar trends along the luminal surface in Figure 7.15, Figure 7.16, and Figure 7.17, the percentage of low WSS cannot act as a predictor of the extent of low and hypoxic PO_2 levels within the arterial wall.

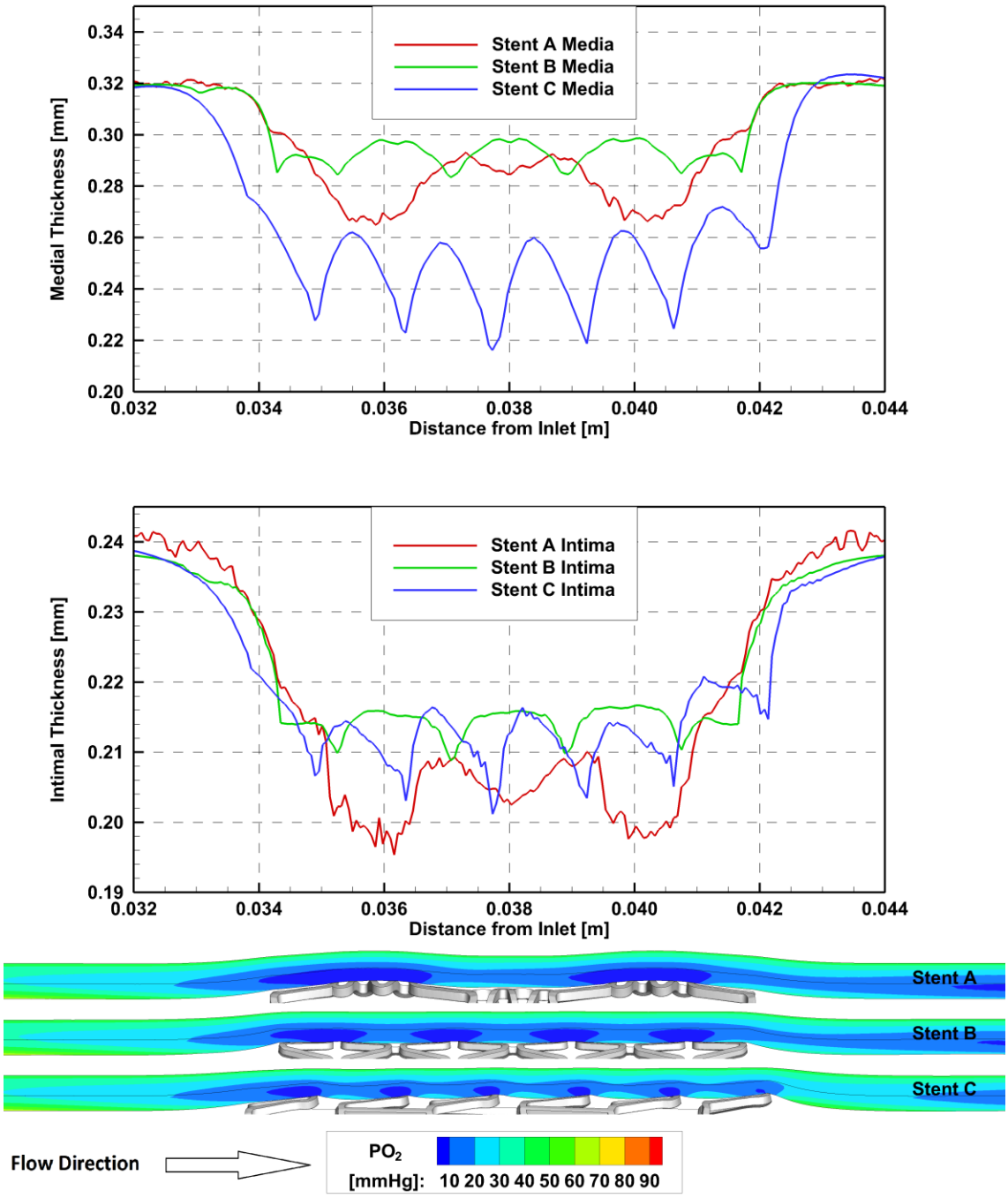

Figure 7.13: Line plots of the medial and intimal thicknesses within the stented region for each stent along an axial cross-section with the corresponding predicted PO_2 values within the arterial wall. Cross-sections are taken at same location as A-A', B-B' and C-C' as shown in Figure 7.15, Figure 7.16, and Figure 7.17, respectively.

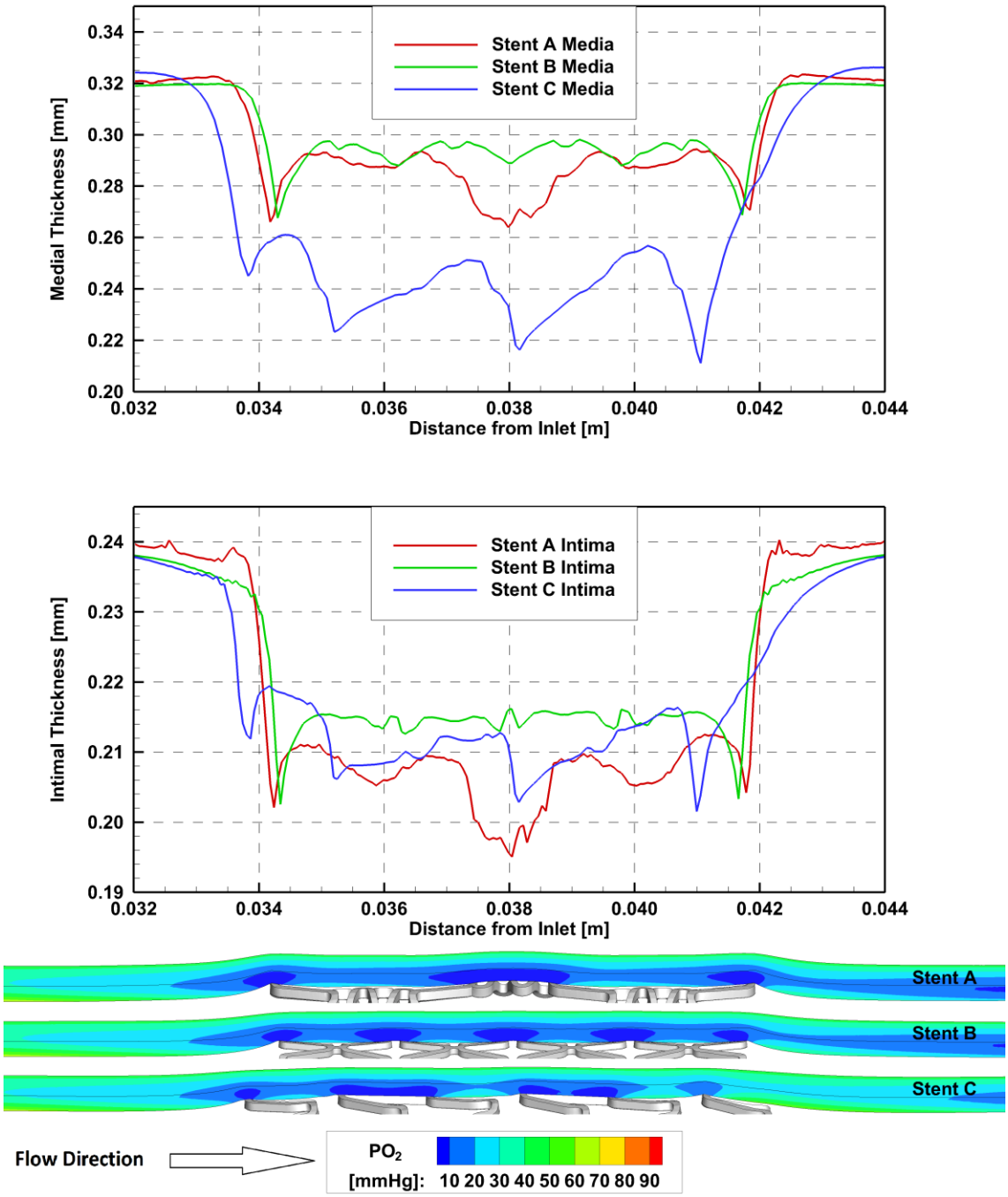

Figure 7.14: Line plots of the medial and intimal thicknesses within the stented region for each stent along an axial cross-section with the corresponding predicted PO_2 values within the arterial wall. These cross-sections were taken perpendicular to the previous set in Figure 7.13.

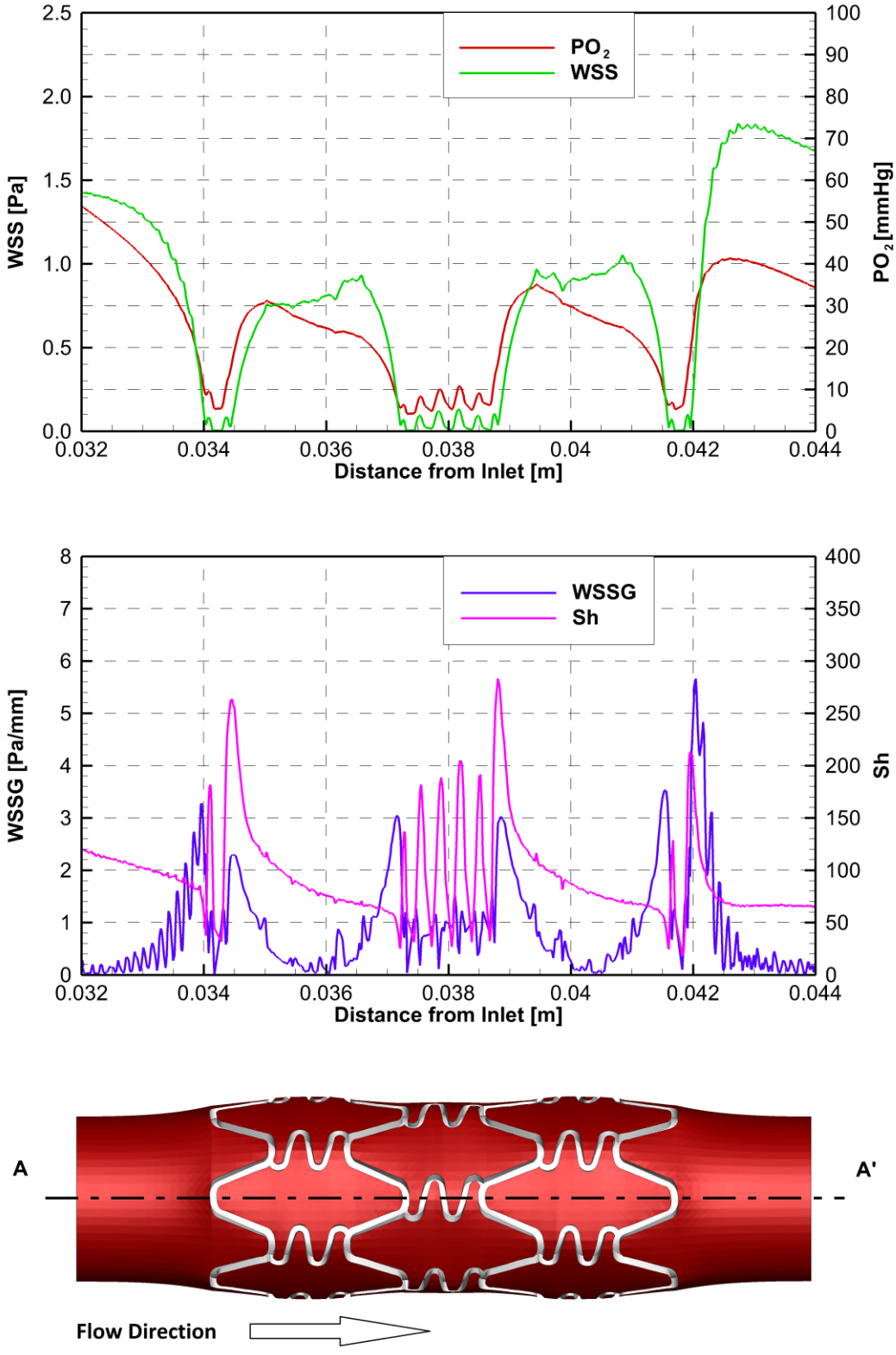

Figure 7.15: Predicted PO_2 and WSS, and Sh and WSSG along line A – A'.

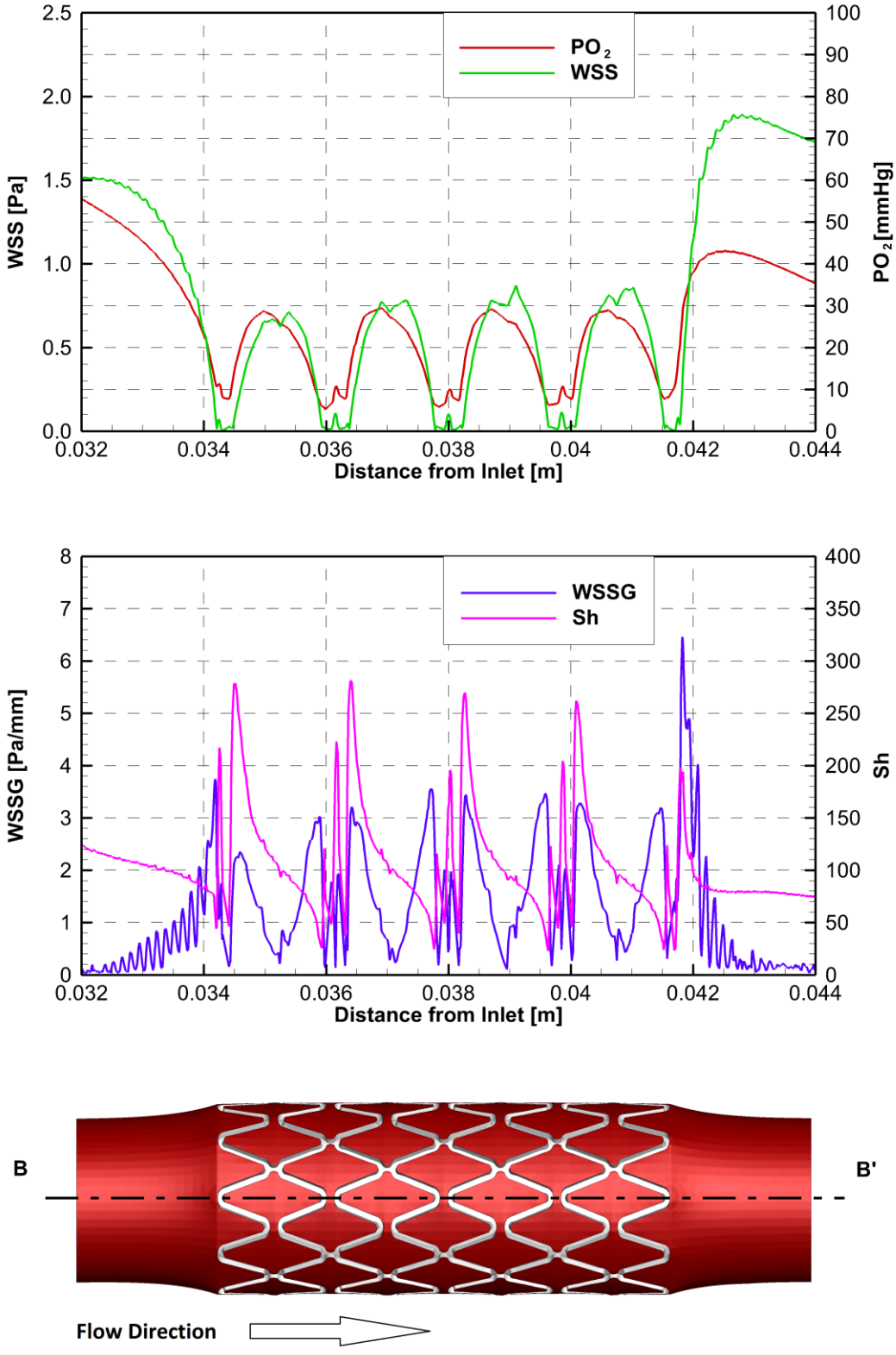

Figure 7.16: Predicted PO_2 and WSS, and Sh and WSSG along line B – B'.

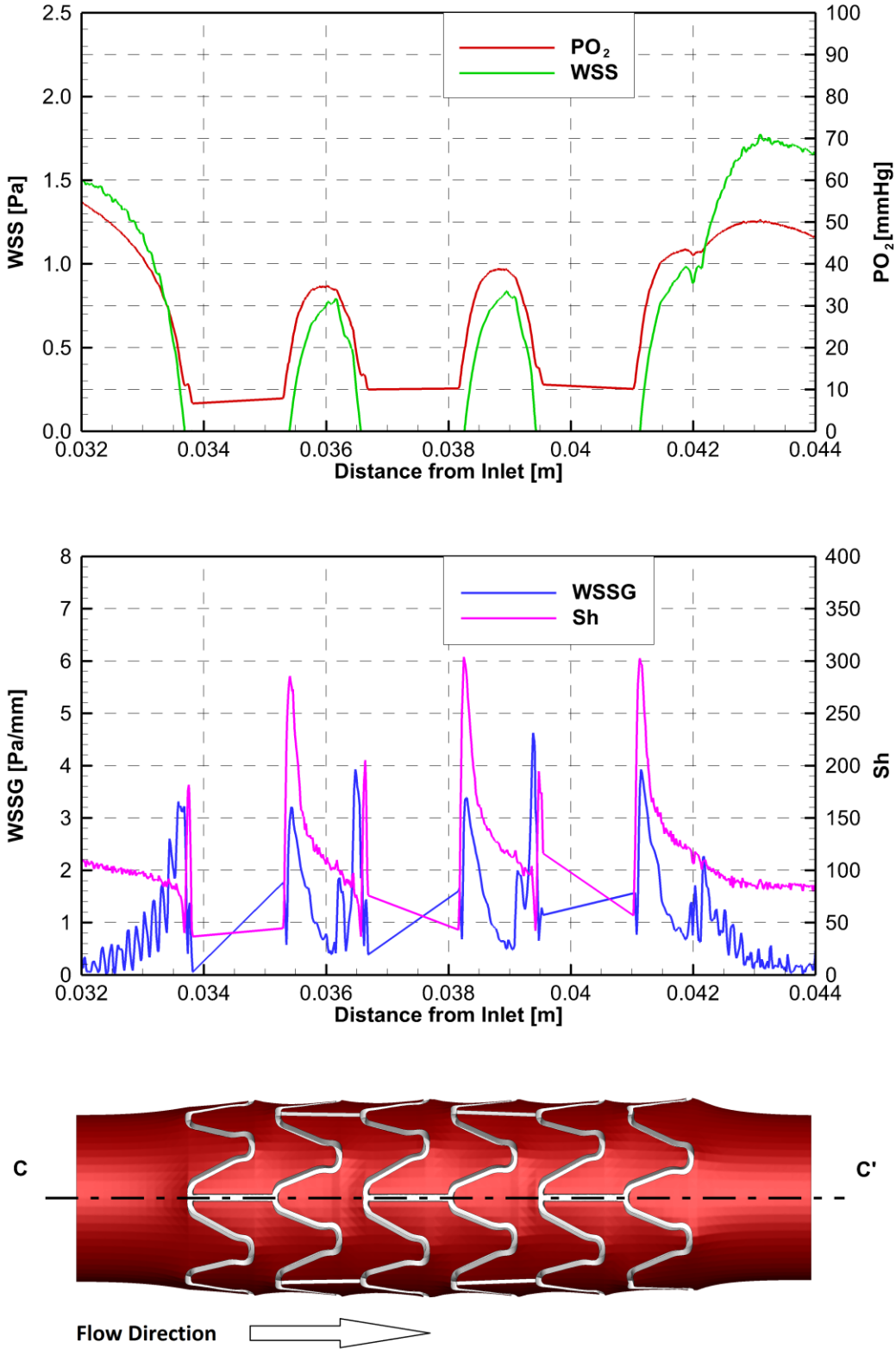

Figure 7.17: Predicted PO_2 and WSS, and Sh and WSSG along line C – C'.

7.4.3 Comparison with Restenosis Rates

The angiographic restenosis rates for each commercially available coronary stent that resemble the three stents are presented in Table 7.3, along with the percentage volume of the arterial wall exposed to low and hypoxic PO_2 levels. These rates were taken from the following clinical trials at 6-month follow-up: Stent A, ISAR-STEREO-II, Stent B, DISTANCE and Stent C, ISAR-STEREO-I. Stent B is predicted to perform the worst, in terms of volumetric percentages of low (74.2%) and hypoxic (24.3%) PO_2 within the arterial wall, but shows the lowest restenosis rate (10.1%). Stents A has slightly lower percentage volumes of low (72.8%) and hypoxic (12.6%) PO_2 within the arterial wall and has the highest restenosis rate (31.4%). Stent C is predicted to have significantly less percentage volume of the arterial wall exposed to low (68.9%) and hypoxic (5.3%) PO_2 levels but has a lower restenosis rate (25.8%) in comparison with Stent A, but significantly higher than Stent B (10.1%). Looking solely at the amount of the arterial wall exposed to low and hypoxic PO_2 levels Stent C is predicted to perform the best out of the three stents; however, this does not match with the restenosis rates. Considering ISR is a multifactorial process, there may be some other issue with this stent, e.g. structural damage of the arterial wall or areas of low wall shear stress, which is not captured by oxygen transport models alone. With all these elements that can affect the biological processes within an implanted artery, it is difficult to determine which element dominates.

Possibly the extent of damage inflicted on the arterial wall by stent implantation may also play a role in the risk of ISR. Martin (2014) analysed the equivalent stress (ES), time-averaged WSS, OSI and RRT using the same three stent geometries (along with an additional three). Of the three stents presented here, Stent A had the highest maximum ES (83.84 kPa) and the highest mean ES (10.7 kPa). Stent B was predicted to exert a

maximum ES of 58.98 kPa and a mean ES of 8.83 kPa on the arterial wall, and Stent C a maximum ES of 74.37kPa and a mean ES of 9.21kPa. Plots of the ES distribution within the arterial wall and on the luminal surface are shown in Figure 7.18. For Stent A, for example, which is predicted to perform the worst in terms of ES, the area exposed to the highest ES is around the N-shaped link struts. This area is also shown to experience hypoxic PO_2 levels, low WSS and high WSSG. Possibly the combined effects of the high stress exerted on the arterial wall, the adverse local haemodynamics and hypoxic PO_2 levels within a focussed area of the stented region for Stent A leads to higher restenosis rates. This is conjecture at this point and for significant statistical power more geometries would need to analysed than just the three presented here.

One difference between Stents A and C, and Stent B is that Stent B is predicted to create a more uniformly circular luminal cross-section, as opposed to more polygonal cross-section with Stents A and C. A typical transverse cross-section is shown for each stent in Figure 7.19. In a study by Garasic et al. the authors found that stent geometries with 12 struts per cross-section had 50% to 60% less mural thrombus, and two-fold less neointimal area than identical stents with only eight struts after 28 days in rabbits.[69] The authors also observed increased macrophage numbers in the 12-strut stented arteries which was explained by the observation that leukocytes cluster around stent struts.[69] This would support the theory that the leukocyte adhesion is increased in regions of recirculation and low WSS which are generally located adjacent to stent struts. Interestingly, in their study the increased macrophage cell count in the 12-strut stented arteries did not translate into increased NIH at 28 days. Possibly, the inflammatory cells impact is only noticeable after the 28 day period in rabbits as noted by the authors.

Given that factors, in addition to the oxygen transport and the local haemodynamics, that also affect the biological processes that can result in ISR, possibly a more complete

and comprehensive assessment methodology is necessary in predicting the implications of stent designs on the adverse outcomes post-implantation. Such a methodology would need to incorporate most of the factors discussed here, although the extent to which each factor affects the overall result is debateable and currently unknown.

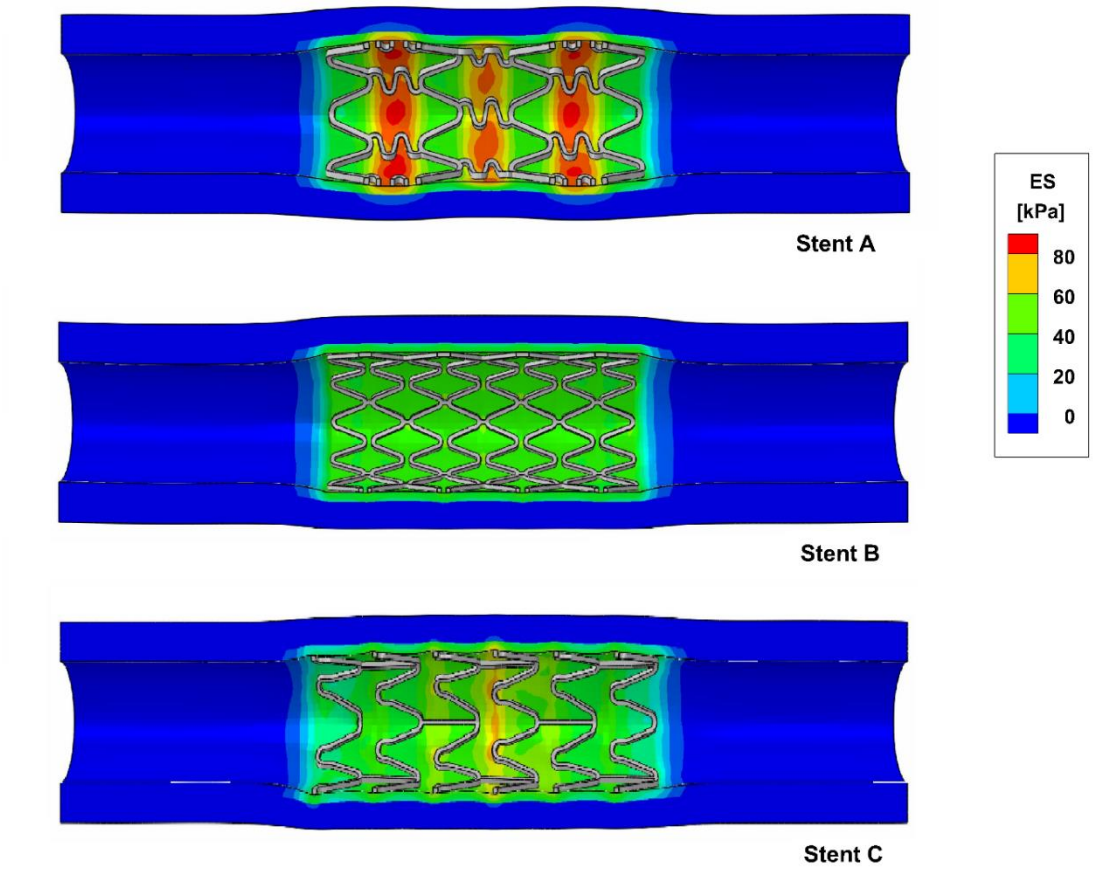

Figure 7.18: Equivalent stress (ES) for each stent design as predicted by Martin.[150]

Note: the adventitia layer is also included in these plots.

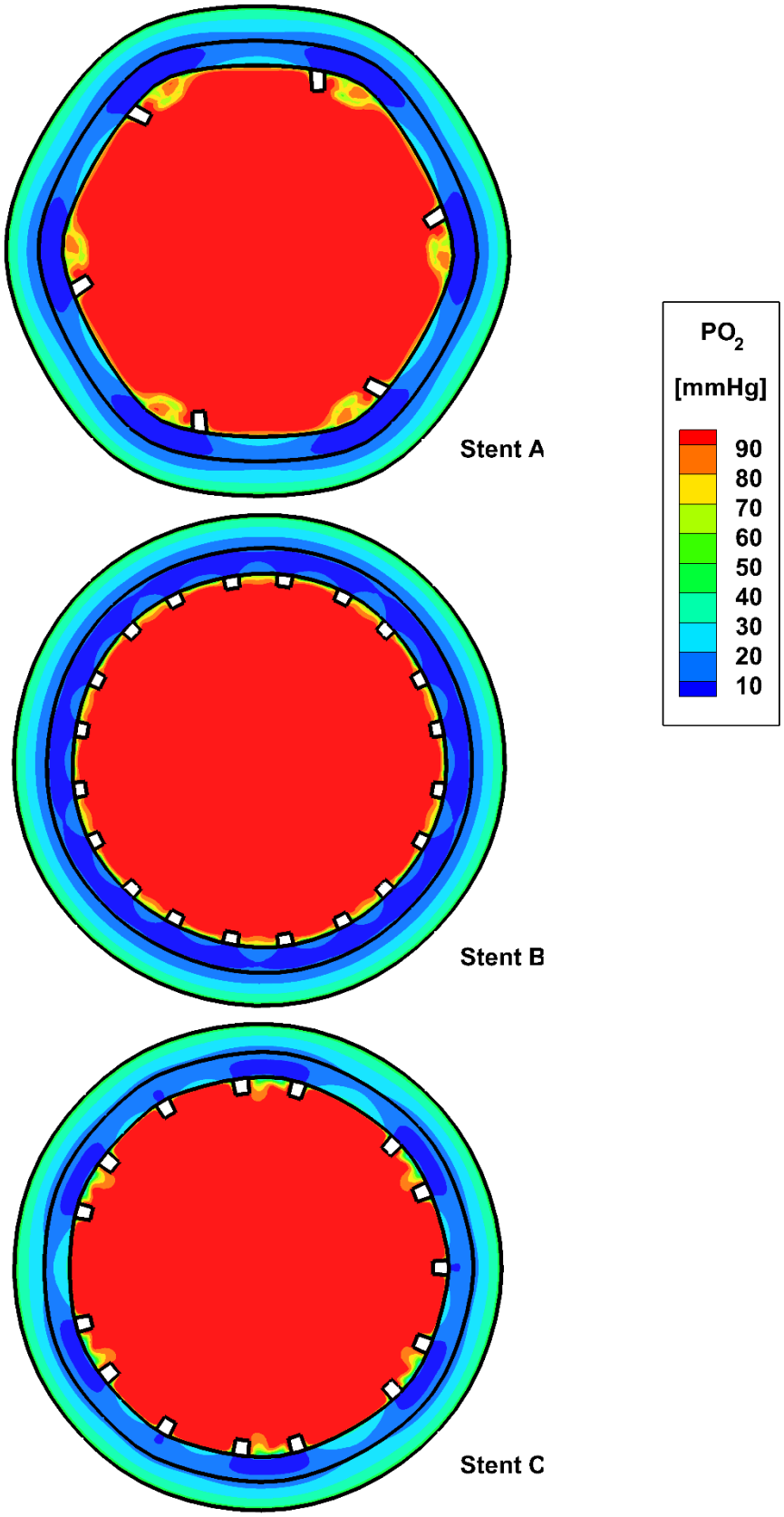

Figure 7.19: Transverse cross-sectional plots for each stent.

7.5 Conclusions

Test Case 2 confirms the limitations of simplifying the blood oxygen transport model, as discussed in Chapter 6, with some additional points to note. The steep PO_2 gradient observed adjacent to the luminal surface at all three locations in Test Case 1 is also visible here in the PO_2 profile plots in Figure 7.5 and significantly, Model 5 fails to predict it again in this test case. Critically, this test case shows that adopting the Sh as a measure of the oxygen flux into the arterial wall can be problematic if using a simplified blood oxygen transport model. This is vividly portrayed in both Figure 7.7 and Figure 7.8. In Figure 7.7 a stark difference is visible between the Sh predicted by Model 1 compared with Model 5 with none of the sharp peaks in Sh downstream of the stent struts predicted by Model 1 visible when Model 5 is used. This is further demonstrated in Figure 7.8 where the line graph of the predicted Sh for Model 5 is flattened in comparison with all the other four models. Therefore, a simplified blood oxygen transport model, as adopted in most oxygen transport studies in the literature, fails to predict these peaks in Sh observed downstream of stent struts. Additionally, some researchers have used the results presented by Moore and Ethier (1997) to justify the use of a correction factor of 2.5 to the Sh when applying a simplified blood oxygen transport model which ignores the bound oxygen.[44,203] As shown clearly in Figure 7.8 this would not suffice in accounting for the use of a simplified model.

Test Case 3 demonstrates that the oxygen transport can be significantly affected by stent design with the three stent designs exhibiting significantly different percentages of the arterial wall exposed to hypoxic PO_2 levels. This is not simply a case of how much of the luminal area is exposed to the blood as shown by the fact that the hypoxic volume percentages do not correlate with the luminal surface interface areas for each stent. Stent struts angled perpendicular to the flow can significantly affect the amount of oxygen

transferred into the arterial wall from the blood flow, which is clearly seen for Stent A in Figure 7.11. Critically, this test case shows the value of an accurate oxygen transport model in improving designs of cardiovascular devices. Additionally, the benefit of using realistically-deformed stented artery geometries, as generated here using FEA, is demonstrated here because some features, such as prolapse and stretching of the arterial wall, which would not be generated accurately otherwise are shown to affect the predicted results. Further investigation is warranted possibly incorporating plaque within the arterial wall or by using a patient-specific geometry which provides an avenue for future study.

7.6 Summary

In Test Case 2, presented here, the five blood oxygen transport models were compared within a realistically-deformed stented geometry.

The results showed that:

- The models that incorporate the bound oxygen again predicts a steep gradient in the PO_2 transarterial profile at the luminal surface that matches well with the experimental data from Santilli et al.
- Model 1 shows the best agreement with regard to the luminal surface value with the experimental data from Santilli et al.
- There are some differences observed in the arterial wall oxygen transport properties possibly because of dissimilarities between species.
- Simplifying the blood oxygen transport model, by ignoring non-linearities and the oxy-haemoglobin, have significant effects on the accuracy of the results generated.

In Test Case 3 the most advanced blood oxygen transport model was used to compare three different stent designs. The results demonstrated that

- There were significant differences between the three stent designs assessed in terms of the oxygen transport into the arterial wall.
- Therefore, stent design affects the amount of oxygen reaching cells within the arterial wall.
- One stent, Stent C, had significantly less of the arterial wall predicted to be exposed to hypoxic PO_2 levels which was caused in part by the stretching of the arterial wall upon implantation as predicted by FEA.
- Another consequence of this was that the amount of the arterial wall exposed to hypoxic PO_2 levels was not correlated with the amount of the luminal surface exposed to hypoxic PO_2 levels.
- This highlights one of the advantages in using realistically-deformed geometries, although computational expense may be an issue.

In the next chapter, the haemodynamics and the oxygen transport, modelled using Model 1, are analysed in helical-flow-inducing stent designs and compared with a straight stent of similar length.

CHAPTER 8

Test Case 4 – Helical-Flow-Inducing Coronary Stents

8.1 Introduction

The local haemodynamics and oxygen transport can both, in theory, affect the long-term outcome of stent implantation, as discussed in Chapter 2, and helical flow has been theorised to improve both, as discussed in Chapter 4. In this chapter Test Case 4 assesses the effects of inducing helical flow on the haemodynamics and oxygen transport in stented coronary arteries. First, the background and justification for a helical-flow-inducing coronary stent are discussed. Second, the methodology for geometry and mesh creation is described briefly. Finally, in the results section both the haemodynamics and the oxygen transport are analysed.

8.2 Background

Helical flow has been theorised to provide several haemodynamic benefits for the reduction of ISR in stented arteries. As described previously in Section 4.4.1 the BioMimics 3D stent is a self-expanding nitinol stent, developed for the treatment of peripheral artery disease, which induces helical flow in a treated artery. Helical-flow-inducing stents have not yet been deployed in coronary arteries; however, there is justification for the use of a similar stent for the treatment of CAD. In theory, a helical-flow-inducing BMS may offer a viable alternative to a DES in cases where it is not

suited and may give additional benefits compared with a conventional BMS, as discussed below.

When a patient is diagnosed with CAD there are recommendations on the best treatment options or pathways. Depending on the severity of the disease a change of diet or statins may be prescribed; however, in cases of acute coronary syndromes, stable angina and myocardial infarction with ST-segment elevation, CABG and angioplasty with stenting are both appropriate treatment options.[180] CABG is generally only undertaken in cases of multi-vessel disease; although, it may not be suitable if the patient is quite frail. When deciding on what stent to implant, DESs are generally recommended given their superior performance in clinical trials when compared with BMSs.[70,181] Clinical scenarios favoring a BMS over a DES are when non-elective surgery is required, expected poor compliance with DAPT, intolerance/allergy to aspirin or clopidogrel/prasugrel/ticagrelor, bleeding risk, and indication for long-term anticoagulation.[14] Patients who have a high bleeding risk are those with a history of congestive heart failure, cerebrovascular disease, hepatic or renal disease, and diabetes mellitus, or simply that they are of advanced age.[229] Both those who have a high bleeding risk and those who will undergo a surgical procedure within the following year may not be able to comply with the one year DAPT required for DES implantation (a BMS only requires one month).[68] Also, in relation to expected poor compliance with DAPT, when an interventional cardiologist is making the decision between a BMS and a DES it is prudent to predict the likelihood that the patient will comply with the long-term DAPT. Current guidelines also recommend avoiding DES implantation in the presence of financial barriers to prolonged DAPT or social barriers that may limit patient compliance.[33] A BMS is seen as a valuable alternative to a DES for large

vessels, for patients with myocardial infarction with ST-elevation, and for saphenous vein graft stenosis.[14] Therefore, there is still a role for BMSs in the treatment of CAD.

In addition to ISR, and late and very late stent thrombosis, neoatherosclerosis is a relatively new observed phenomenon which occurs more frequently and earlier with DESs than with BMSs.[190] One study where the authors reviewed histology findings from 299 autopsy cases (197 BMS and 209 DES lesions) found that the incidence of neoatherosclerosis was greater in DES lesions (31%) than in BMS lesions (16%), although thin-cap fibroatheromas or plaque rupture were more frequent with BMSs than DESs.[177] This is significant because plaque rupture can cause a thrombotic event leading to myocardial infarction. Therefore, beyond the elution period of a DES there is an argument for having a stent in place which not only combats ISR but also produces flow characteristics which are atheroprotective. Additionally, the BioMimics 3D stent is a self-expanding stent and although most current coronary stents are balloon-expandable there are reasons for the use of self-expanding stents in the coronary arteries. Self-expanding stents can have a smaller cross-sectional profile, which can offer an advantage for tortuous vessels, they experience reduced foreshortening in comparison with balloon-expandable stents,[220] and also they can decrease rates of stent malapposition.[19]

Therefore, a self-expanding BMS which is atheroprotective by inducing helical flow would be beneficial for angioplasty procedures in the coronary arteries, particularly for long lesions that are considered a risk factor for ISR.[120] With this justification in mind the following test case was undertaken to see if there are any advantages, in terms of haemodynamics and oxygen transport, to the implantation of a helical-flow-inducing stent in the left coronary artery and to assess the previously theorised benefits of helical flow in this context.

8.3 Methodology

The geometries developed for the assessment of helical-flow-inducing stent designs were based on the BioMimics 3D stent which induces helical flow by imposing a helical shape on the artery. This is different to the other method of a helical ridge within the stented region, as described previously in Section 4.4.1. The BioMimics 3D stent is a self-expanding nitinol stent developed for the treatment of peripheral artery disease, with specific application to the femoral artery. In the case of the popliteal femoral artery, a typical diameter and length of stent required are 6.0mm and 100.0mm, respectively. The BioMimics 3D stent is described as having a central helical region with transition regions either end to help merge the helical region with the straight artery, as shown in Figure 8.1.

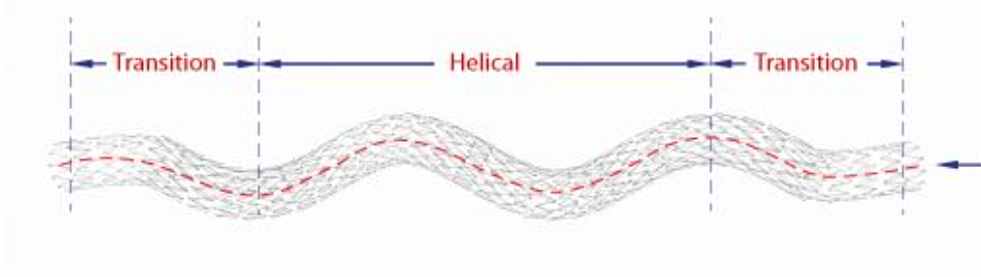

Figure 8.1: Schematic of a typical BioMimics 3D stent.[264]

The same stent configuration was adopted here for assessment of helical flow in a stented coronary artery, with the diameter set at 3.0mm and the length of the stent centreline set at 20.0mm. 20.0mm is considered a long coronary stent that could be used for a correspondingly long atherosclerotic lesion, which is one of the risk factors for ISR in coronary arteries.[60] One straight stent geometry and five helical geometries were constructed with the helical radius increasing from 0.2mm to 1.0mm. The helical section length was set at 10mm with 5mm allowed for the transition regions at either end of the helical section which serve to smoothly change the centreline from a straight

line to a helical shape and visa-versa, as shown in Figure 8.2. The maximum helical radius, given the restrictions on the length of stent, was found to be 1.0mm because any further increase in the helical radius was found to result in an unrealistically deformed outer arterial wall surface within the transition regions. Additionally, for the same reason, the helical section itself consisted of one complete turn. The arterial wall thicknesses adopted were the same as used in the previous coronary artery test cases with the intima and media assigned thicknesses of 0.24 and 0.32mm, respectively, as adopted from Holzapfel et al.[99]

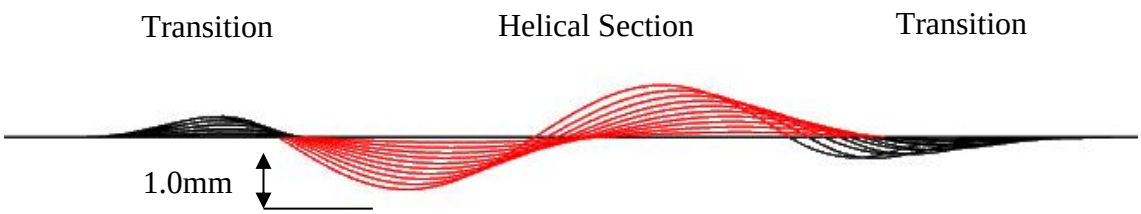

Figure 8.2: Centrelines of the helical stent geometries constructed with a maximum helical radius of 1.0mm. Note the helical section is highlighted in red.

One feature to note is that the length of the centreline was set at 20.0mm; therefore, as the helical radius increased the straight-line distance between the proximal and distal ends decreased accordingly. This can be seen clearly in Figure 8.2 and Figure 8.3. The maximum change in the straight-line distance between the two ends is 2.3mm. Additionally, the artery centreline is shifted by a maximum of 1.0mm from its original position, assuming an initially straight artery. These two geometrical consequences of a helical centreline would have the effect of straining the artery during and after stent implantation and the question arises as to what is a reasonable amount of strain. To answer this one would have to look at how much strain is placed on the arterial wall

during stent implantation in a partially blocked coronary artery. For example, consider a normally 4.0mm diameter coronary artery (luminal cross-sectional area of 12.6mm^2) with a 70% reduction in luminal cross-sectional area due to the presence of an atherosclerotic lesion. The unstented luminal cross-sectional area is 3.8mm^2 which, assuming a circular cross-section, has an unstented diameter, D_u, of approximately 1.1mm. With the further assumption that if the artery was stented the luminal diameter increases to the previous 4.0mm (stented diameter, D_s), then the circumferential strain, ε_c, is as follows:

$$\varepsilon_c = \frac{\Delta D}{D_u} = \frac{2.9}{1.1} \approx 266\% \tag{3.73}$$

Implantation of a helical stent and changing the overall length between the proximal and distal ends by a maximum of 2.3mm (ΔL) over a length of 20mm (L_o) would induce considerably less strain, albeit longitudinal strain, ε_L, i.e.,

$$\varepsilon_L = \frac{\Delta L}{L_o} = \frac{2.3}{20} = 11.5\% \tag{3.74}$$

and consequently stress, on the arterial wall than the strain induced by the change in luminal cross-sectional area. This issue may warrant further investigation using FEA, but is beyond the scope of this work. In total six simulations, i.e one straight stent and five helical stents, were carried out and numbered Stent 1 to Stent 6, with increasing centreline helical radii of 0mm (straight stent), 0.2mm, 0.4mm, 0.6mm, 0.8mm and 1.0mm, respectively, as shown in Figure 8.3.

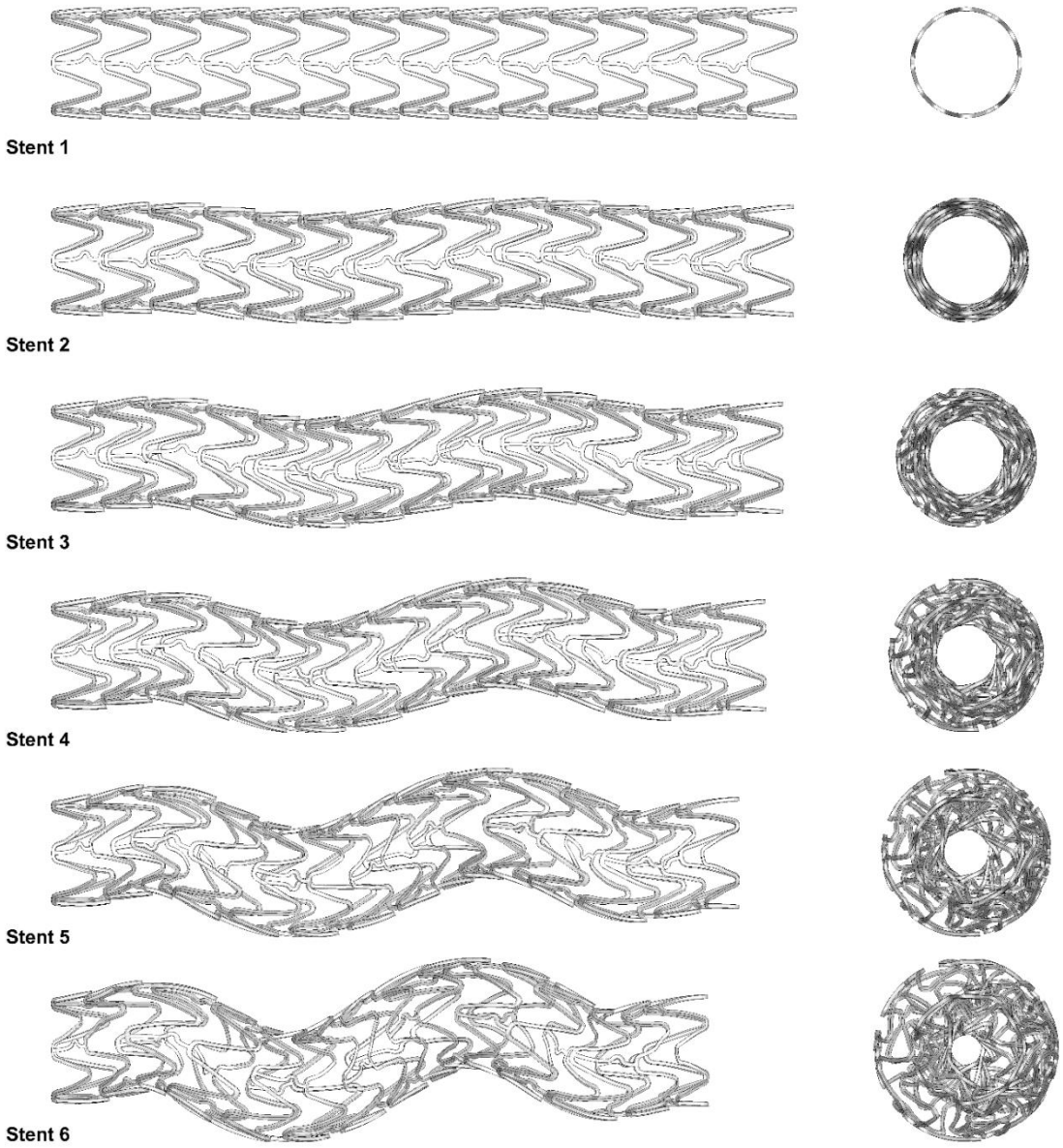

Figure 8.3: Elevation and end views of the geometries of the six stents modelled.

The geometries were created in Rhinoceros 3D and were based on the Multilink Vision (Abbott Laboratories, Lake Bluff, IL, USA) coronary stent strut configuration. This strut configuration was used because the link struts allow for a degree of longitudinal expansion, as needed by the helical stents, the strut configuration is used already in the coronary arteries while the BioMimics 3D configuration is used in the peripheral arteries, and also, exact dimensions of a coronary version of the BioMimics 3D stent are

unknown. To create the stent geometries the strut configuration was first cut from a planar surface, then wrapped into circular form, and finally aligned along the relevant helical centreline. The arterial wall, and entry and exit regions were also created in Rhinoceros 3D.

The completed geometries were imported into ANSYS ICEM, and the same mesh parameters used in Test Cases 2 & 3 were adopted for computational domain discretisation. The typical total node count for each mesh was approximately 14 million, with approximately 2.5, 2.8 and 8.7 million nodes in the media, intima and lumen domains respectively. As an example, Figure 8.4 shows the mesh density used for Stent 6 on the luminal surface and within the arterial wall. The boundary conditions used were the same as those adopted in Test Cases 2 & 3. All simulations were again carried out on the ICHEC Fionn supercomputer using two nodes, each with 2 × 12 2.4 GHz Intel Ivy Bridge core processors and 64 GB of RAM. Approximate time to reach convergence was 1770 CPU hours.

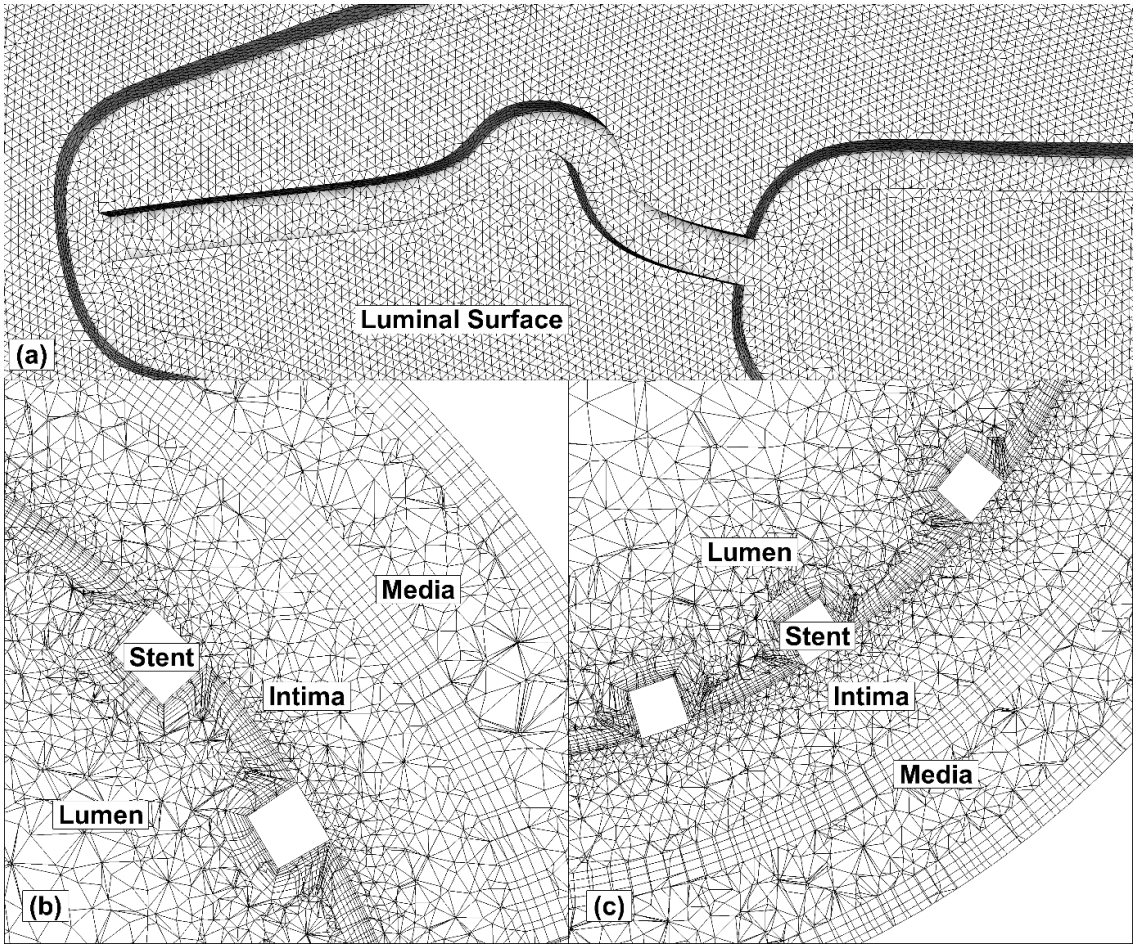

Figure 8.4: Mesh density used for Stent 6 on (a) the luminal surface, and (b & c) within the three volume domains.

8.4 Results

The percentage volumes of the arterial wall within the stented region exposed to low (<30mmHg) and hypoxic (<10mmHg) PO_2 levels for each stent modelled, with helical radii ranging from 0mm to 1.0mm, are plotted in Figure 8.5. It is clear from this graph that there is a downward trend in the percentages as the centreline helical radius increases. Overall, between Stent 1, the straight stent, and Stent 6, the helical stent with a centreline helical radius of 1.0mm, the low PO_2 percentage volume decreases from 75.0% to 68.7% and the hypoxic percentage volume decreases from 28.4% to 22.4%. Although there is only a relatively small reduction, relative to the total amount, in the volume of the arterial wall exposed to low PO_2, the change in volume exposed to hypoxic PO_2 is significant, i.e. a 21.1% reduction within the stented region.

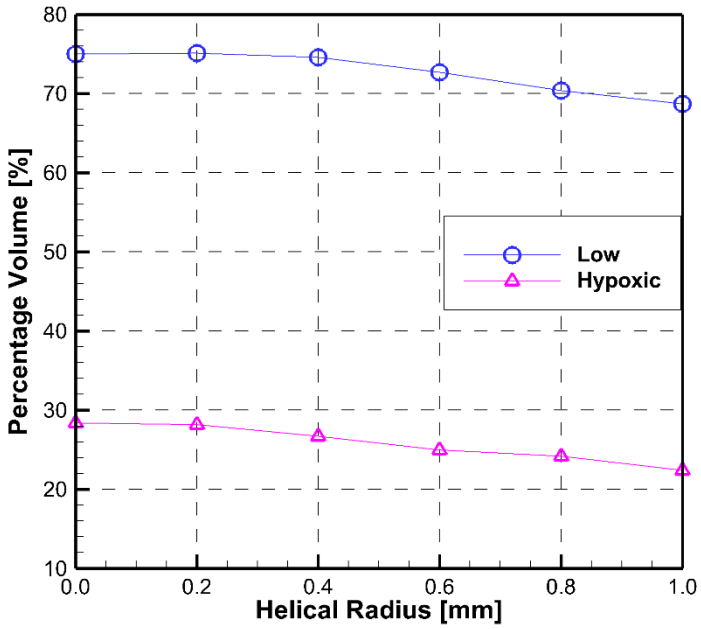

Figure 8.5: Percentage volume of the arterial wall exposed to low and hypoxic PO_2 levels versus helical radius of the stent centreline.

Table 8.1 gives that the luminal-surface area-averaged values of the PO_2, Sh and WSS within the stented region of each stent. Again there is a clear trend in all three variables in that the area-averaged PO_2, Sh and WSS all increase with increasing centreline helical radius. This preliminary analysis of the results appears positive, in terms of reducing the amount of the arterial wall exposed to hypoxic PO_2 levels and reducing adverse WSS conditions; however, it does not give the complete story. Before further analysing the oxygen transport the haemodynamics created by each stent are first analysed, in particular the development of helical flow and its effects on the WSS and WSSG within the stented region.

	Area-Averaged over Stented Luminal Surface		
Stent No	**PO_2 [mmHg]**	**Sh**	**WSS [Pa]**
1	21.1	119	0.60
2	21.3	119	0.60
3	22.1	120.1	0.60
4	24.1	124.4	0.62
5	26.4	131.3	0.64
6	27.9	135.9	0.68

Table 8.1: Area-averaged PO_2, Sh and WSS for the six selected stents. These values were obtained by area-averaging over the luminal surface within the stented region.

8.4.1 Analysis of Haemodynamics

Figure 8.6 and Figure 8.7 show the WSS and WSSG distributions for the six selected stents. Stent 1 produces the lowest area-averaged WSS, as seen in Table 8.1, and in comparison with the other five stents, has the most uniform distribution of WSS within the stented region. As the helical radius increases two distinct ribbons of low and high WSS develop, as shown in Figure 8.6. Also clearly visible in Figure 8.6 is that a large area of low WSS (<0.5Pa) develops in the proximal transition region of Stents 4, 5, and 6, and also in the distal transition region of the three stents, as shown in Figure 8.14(a), Figure 8.15(a), and Figure 8.16(a). These are caused by the sudden change in direction of the flow in the transition regions. Once the helical flow is established between these regions the secondary motion appears to increase the WSS. Physiologically, because there is a concentrated area of the luminal surface exposed to low WSS this could lead to increased NIH within this region.

The histograms presented in Figure 8.8 give a good insight into the change in WSS induced by increasing the helical radius. For Stents 1 – 3 all, or at least 99%, of the luminal surface is exposed to WSS values below the physiological value of 1.5Pa. For Stent 1 particularly, 64% of the luminal surface is exposed to WSS values ranging between 0.5 – 1.0Pa. As the helical radius increases with each successive helical stent the WSS becomes less concentrated within this range as both the maximum WSS increases and the amount of the luminal surface exposed to low WSS also increases. Thus, the range of WSS values that the luminal surface is exposed to broadens when helical flow is induced. This result contradicts the literature which lists a more uniform WSS distribution as one of the benefits of helical flow.[27] Notably, the percentage area exposed to atheroprotective WSS values, i.e. >1.5Pa, increases with helical radius with Stents 4, 5, and 6 exposed to 2.5%, 6.0%, and 7.9%, respectively, as shown in Table

8.2. Conversely, the percentage luminal surface area exposed to low WSS increases from 34.3% for Stent 1 and plateaus at approximately 43% for Stents 4, 5, and 6, as also shown in Table 8.2.

This increase in the range of WSS from Stent 1 to Stent 6 predicted to occur on the luminal surface also results in a relatively small increase in the amount of the luminal surface exposed to high WSSG (>0.85 Pa/mm), as shown in Table 8.2 and Figure 8.7. For the helical stents shown here increasingly high WSSG is present as the helical centreline radius increases, as shown in the histograms in Figure 8.9, with the range of WSSG values steadily rising. High WSSG is commonly observed within a stented artery where the flow separates from and reattaches to the wall upstream and downstream of the stent struts respectively (as demonstrated in Chapter 7). Here, the flow within the helical stented arteries is directed more towards the arterial wall in the high WSS ribbon region. Directing the blood flow towards the arterial wall clearly has benefits in terms of increasing the oxygen transport into the arterial wall, as discussed below; however, increased advection of other elements within the blood would also take place. For instance there would be increased advection of platelets, cytokines and mitogens in the blood towards the wall which could lead to increased NIH in this region. Additionally, the increase in WSSG within the high ribbon could lead to problems with re-endothelialisation and increased inflammation with high WSSG linked to increased inflammatory marker expression by ECs.[211,212]

Helical flow is characterised by a secondary circular motion of the flow on a plane perpendicular to the main flow direction. For the purpose of visualising helical flow the LNH for each stent is presented which gives both a visual representation of the flow vortices, and also an indication as to the degree that the helical flow extends beyond the stented region, as seen in Figure 8.10. Additionally, the contour plots of the velocity

magnitude with the secondary flow streamlines at five slice locations perpendicular to the centreline are presented for each stent in Figure 8.11 to Figure 8.16.

First, in visually analysing the velocity contours and the streamlines at each of the slice locations for Stent 1, see Figure 8.11(h – l), the maximum velocity is seen to remain within the centre of the lumen throughout and the dominant flow disturbances are being caused by stent struts that create small recirculation regions downstream. As the helical centreline radius increases with each subsequent stent the induced secondary flow becomes more prevalent. For Stent 2 there is the clear existence of two vortices on the three slices within the stented region, see Figure 8.12(i – k). Normally these exist in circular conduits with centrelines which curve along a plane where the momentum of the flow carries it towards the outer wall of the curved conduit where it divides into two counter-rotating vortices, known as Dean vortices. In the geometries presented here the secondary flows are established in a different manner. The maximum velocity region maintains its central alignment, with reference to a straight line between the entry and exit regions, driven by its momentum through the helical section, and where the flow deviates the most from this central maximum velocity region is where the secondary flows are strongest, with the slower moving blood recirculating back into this faster region. This secondary flow thus increases mixing within the blood flow which is interpreted as a beneficial effect by not having the same blood within the low velocity region continually along the length of the stent.

For Stent 3 these vortices are also visible in the velocity and streamline plots in Figure 8.13(i – k), and crucially one vortex begins to dominate over the other which is a sign of developing helical flow. The domination of one vortex over the other is clear also in the LNH plot in Figure 8.10, where the only vortex visible, due to its strength, is the clockwise rotating one. Again the maximum velocity skews slightly more towards the

outer surface which in turn further increases the WSS magnitude along this ribbon within the stented region, as shown in Figure 8.13(a). Also visible, in terms of the WSS, is that there is a ribbon of low WSS developing along the inner curve of the stented region, see Figure 8.13(a), as a consequence of the skewed velocity profile, see Figure 8.13(i – k). For Stent 4 the clockwise rotating vortex begins to dominate earlier as the flow transits through the stented region, although the anti-clockwise vortex becomes more visible, and also extends further downstream, as seen in Figure 8.10 and Figure 8.14(i & j). This trend continues which each successive helical stent with the clockwise rotating vortex becoming established earlier in the stented region and extending further beyond it, see Figure 8.10, the velocity skewing more towards the outer wall of the curved artery, and the values of WSS and WSSG increasing within the high ribbon region, as shown in Figure 8.6 and Figure 8.7.

Helical flow is also thought to reduce the size of recirculation zones within a straight stented artery, as discussed in Chapter 4.[36] Recirculation zones are created upstream and downstream of stent struts when the flow separates away from the arterial wall surface and their effects in relation to the biological processes are summarised in Chapter 2. Briefly, recirculation zones create conditions at the arterial wall surface that promote increased thrombus formation, inflammation and NIH within the stented artery. To quantify the volume of the blood within the stented region which undergoes recirculation the volume of the luminal domain experiencing retrograde longitudinal velocity was measured. The results are presented in Table 8.2 where it is apparent that the volume of the stented region experiencing recirculation is doubled for Stent 6 relative to Stent 1. The percentage volume values are all extremely low; however, it should be noted that these recirculation areas are all adjacent to the arterial wall luminal surface and, therefore, could have a considerable effect on the biological processes

within the arterial wall at these locations. This result contradicts the previous literature on this subject which theorises that helical flow reduces recirculation zones.[36]

Stent No	Retrograde Flow [$\times 10^{-10} m^3$]	Retrograde Flow [%]	Low WSS (<0.5Pa) [%]	WSS (>1.5Pa) [%]	WSSG (>0.85Pa/mm) [%]
1	1.5	0.11	34.3	0	68.5
2	1.51	0.11	35.2	0	67.6
3	1.53	0.11	38.5	0	68.4
4	1.63	0.12	42.2	2.5	67.0
5	1.99	0.14	43.8	6.0	71.0
6	3.05	0.22	43.6	7.9	75.4

Table 8.2: Volume and percentage of the stented lumen that experiences retrograde longitudinal velocity, and the percentage of the luminal surface within the stented region that experiences low (<0.5 Pa) WSS, atheroprotective (>1.5 Pa) WSS, and high WSSG (>0.85 Pa/mm).

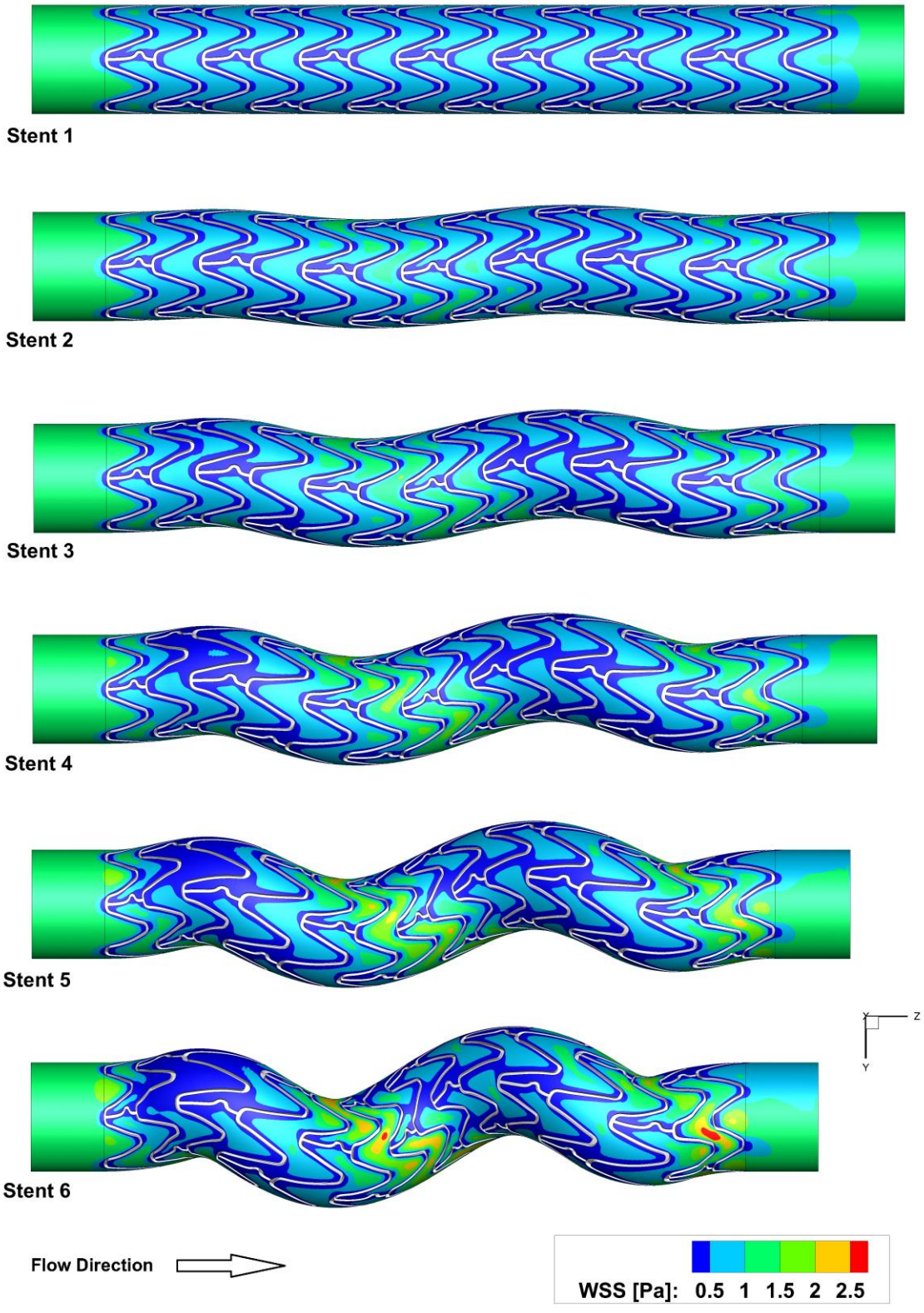

Figure 8.6: Contour plots of WSS within stented region for the six selected stents.

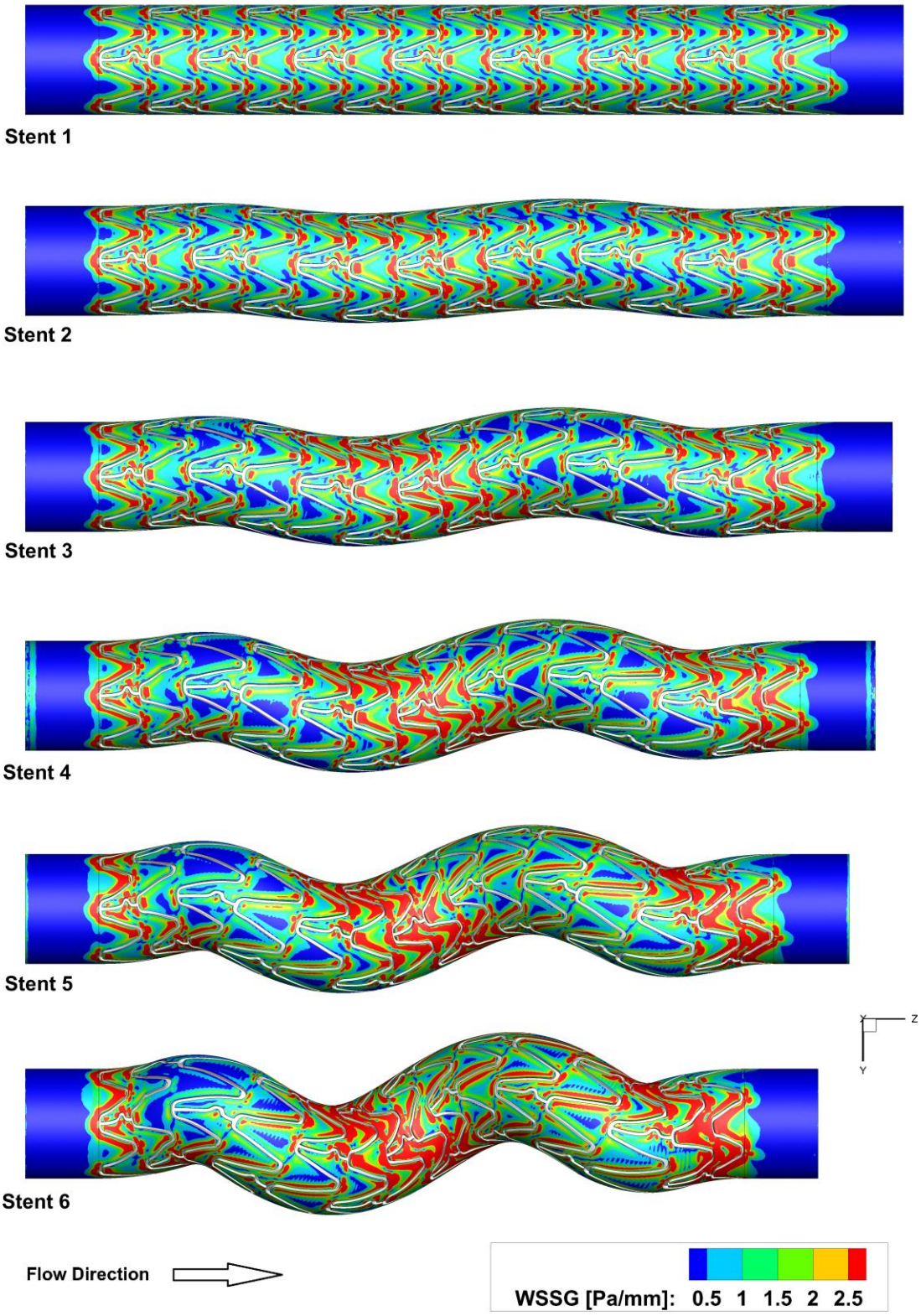

Figure 8.7: Contour plots of WSSG within stented region for the six selected stents

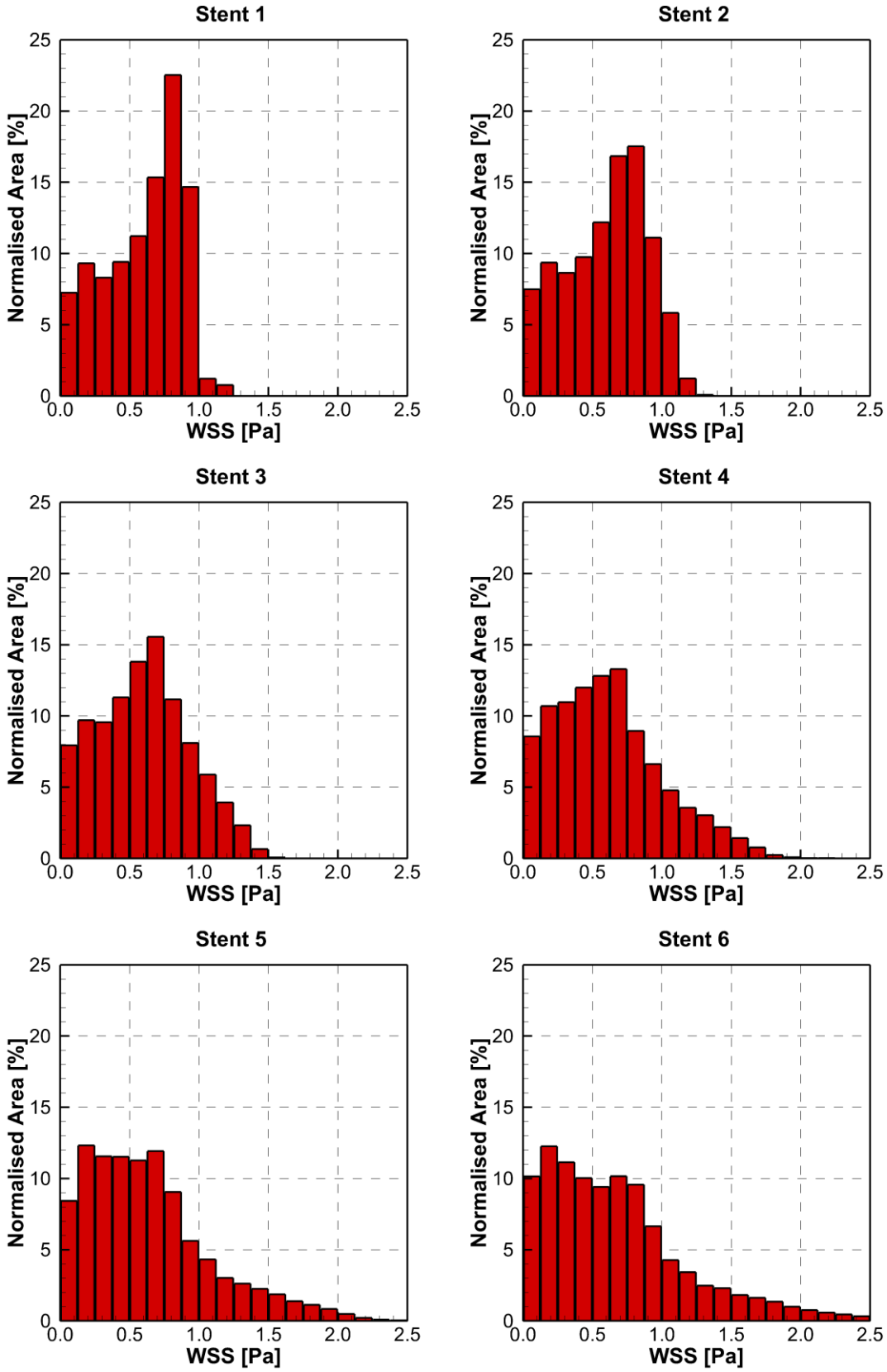

Figure 8.8: Normalised area of the stented luminal surface exposed to a WSS range of 0 – 2.5Pa in bins of 0.125Pa.

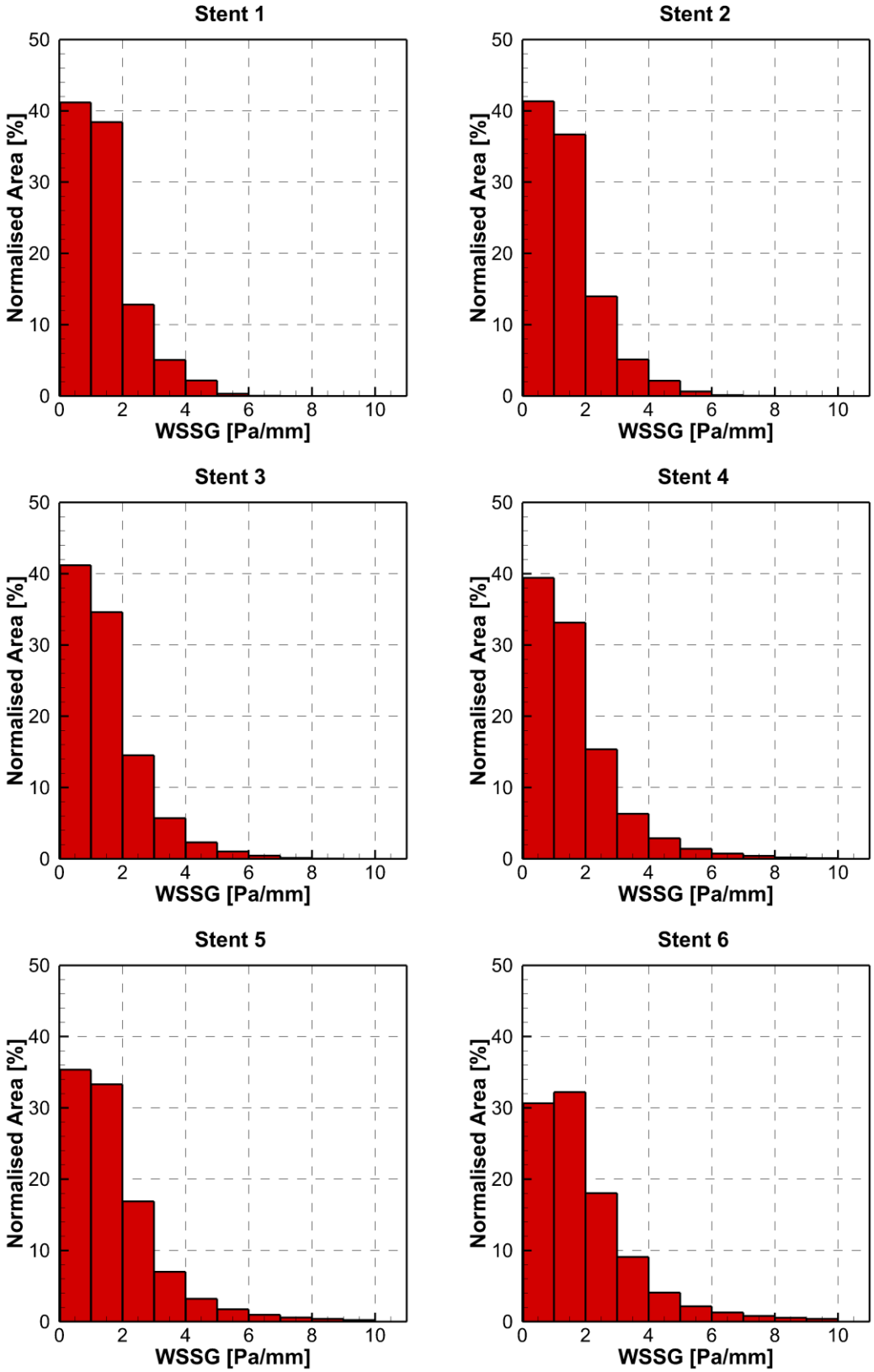

Figure 8.9: Normalised area of the stented luminal surface exposed to a WSSG range of 0 – 10.0Pa/mm in bins of 1.0Pa/mm.

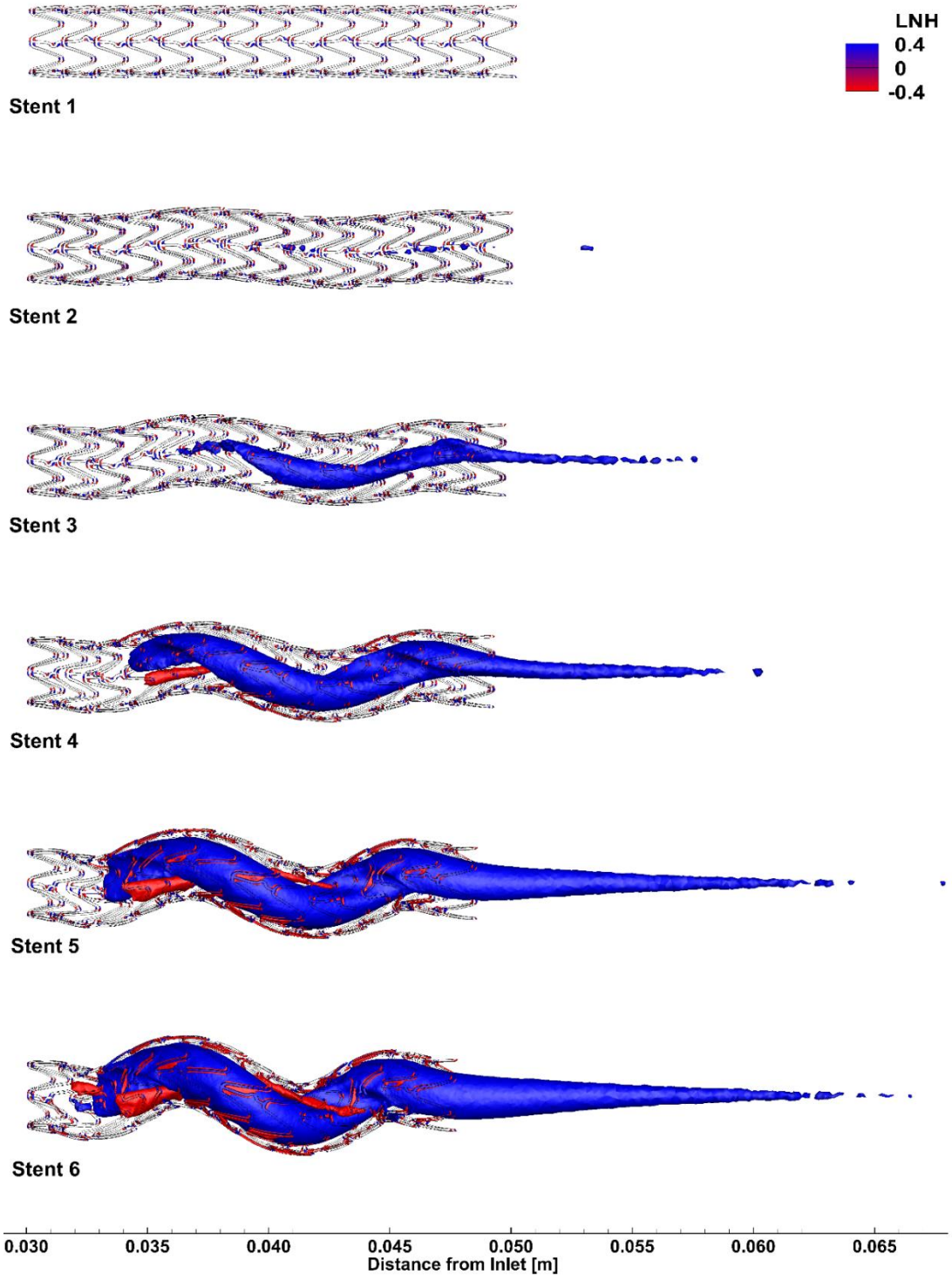

Figure 8.10: Iso-surface plots of LNH for the six selected stents.

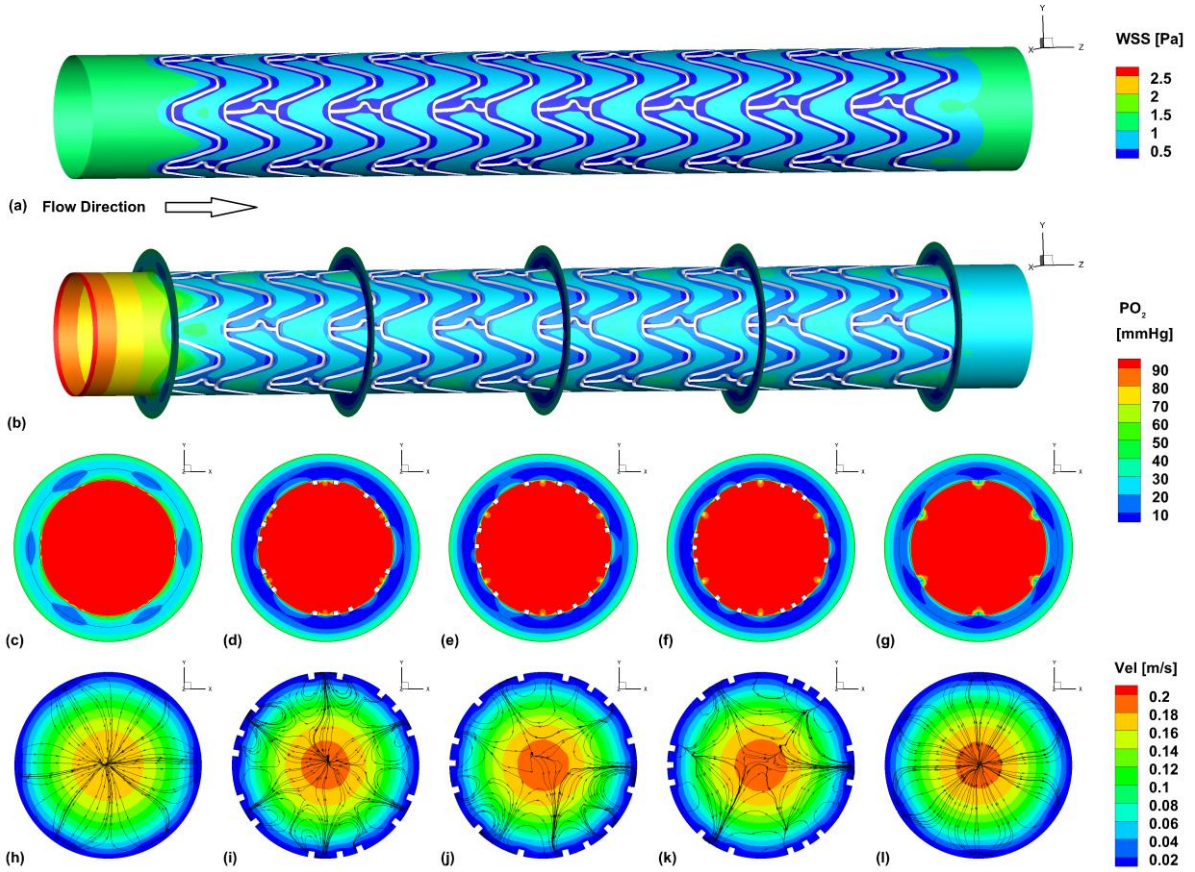

Figure 8.11: Results for Stent 1 – (a) WSS, (b) luminal PO_2 and slice locations, (c-g) PO_2 in lumen, intima and media at each slice location, and (h-l) velocity contours and secondary flow streamlines at each slice location. Note that the main flow direction for slices is towards the reader.

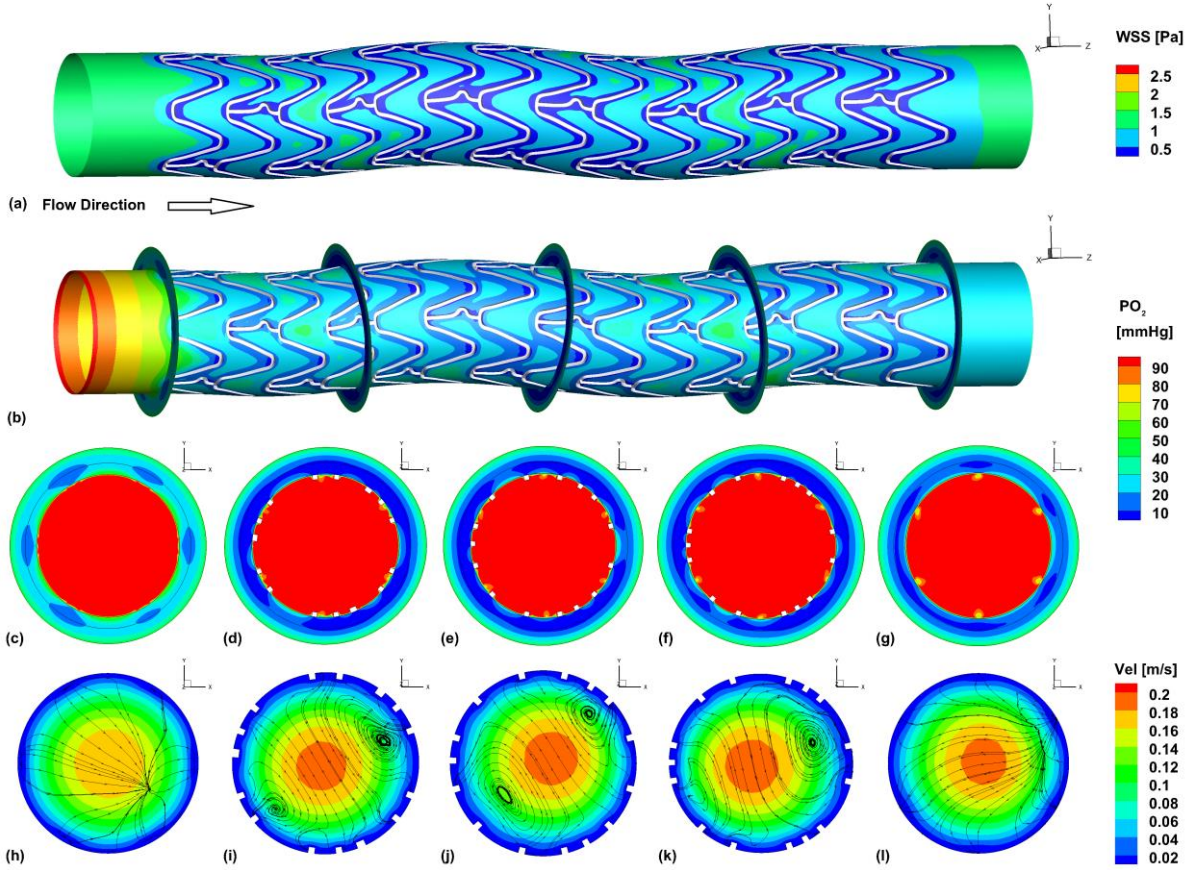

Figure 8.12: Results for Stent 2 – (a) WSS, (b) luminal PO_2 and slice locations, (c-g) PO_2 in lumen, intima and media at each slice location, and (h-l) velocity contours and secondary flow streamlines at each slice location. Note that the main flow direction for slices is towards the reader.

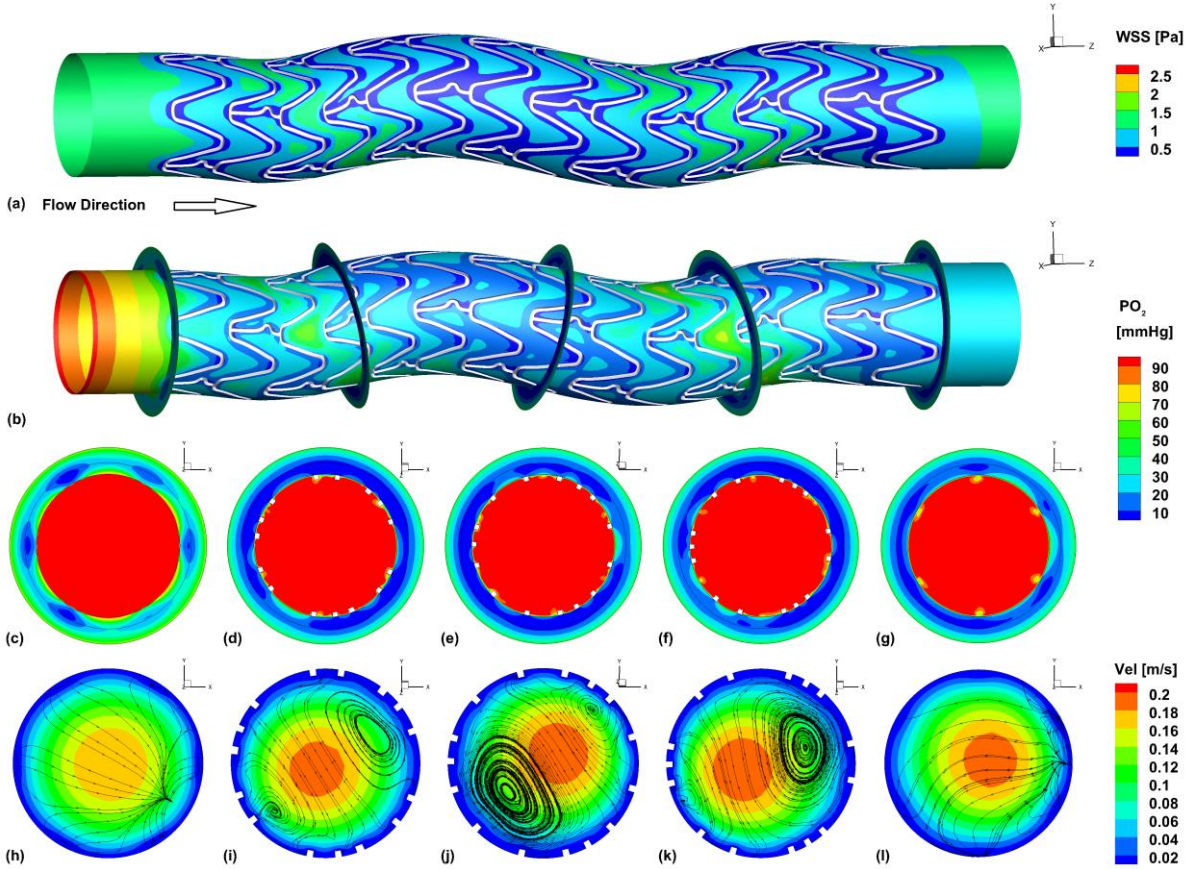

Figure 8.13: Results for Stent 3 – (a) WSS, (b) luminal PO_2 and slice locations, (c-g) PO_2 in lumen, intima and media at each slice location, and (h-l) velocity contours and secondary flow streamlines at each slice location. Note that the main flow direction for slices is towards the reader.

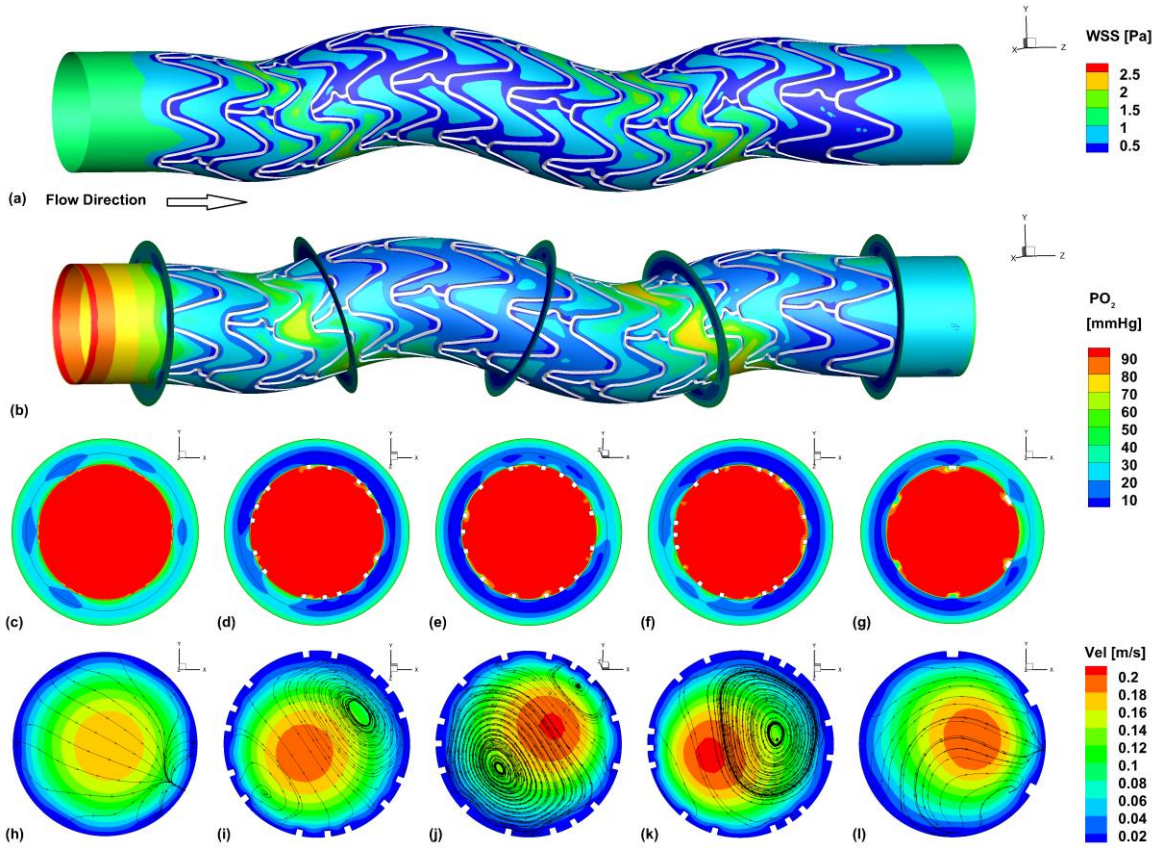

Figure 8.14: Results for Stent 4 – (a) WSS, (b) luminal PO_2 and slice locations, (c-g) PO_2 in lumen, intima and media at each slice location, and (h-l) velocity contours and secondary flow streamlines at each slice location. Note that the main flow direction for slices is towards the reader.

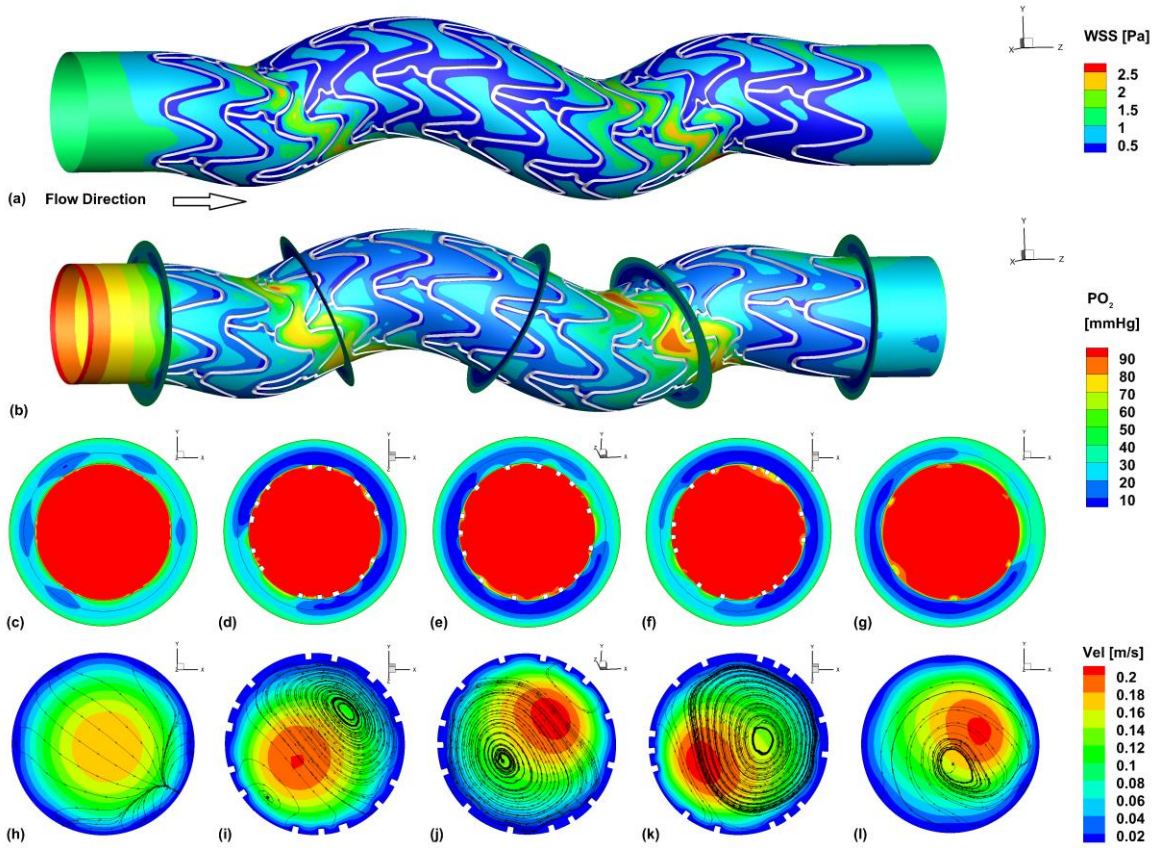

Figure 8.15: Results for Stent 5 – (a) WSS, (b) luminal PO_2 and slice locations, (c-g) PO_2 in lumen, intima and media at each slice location, and (h-l) velocity contours and secondary flow streamlines at each slice location. Note that the main flow direction for slices is towards the reader.

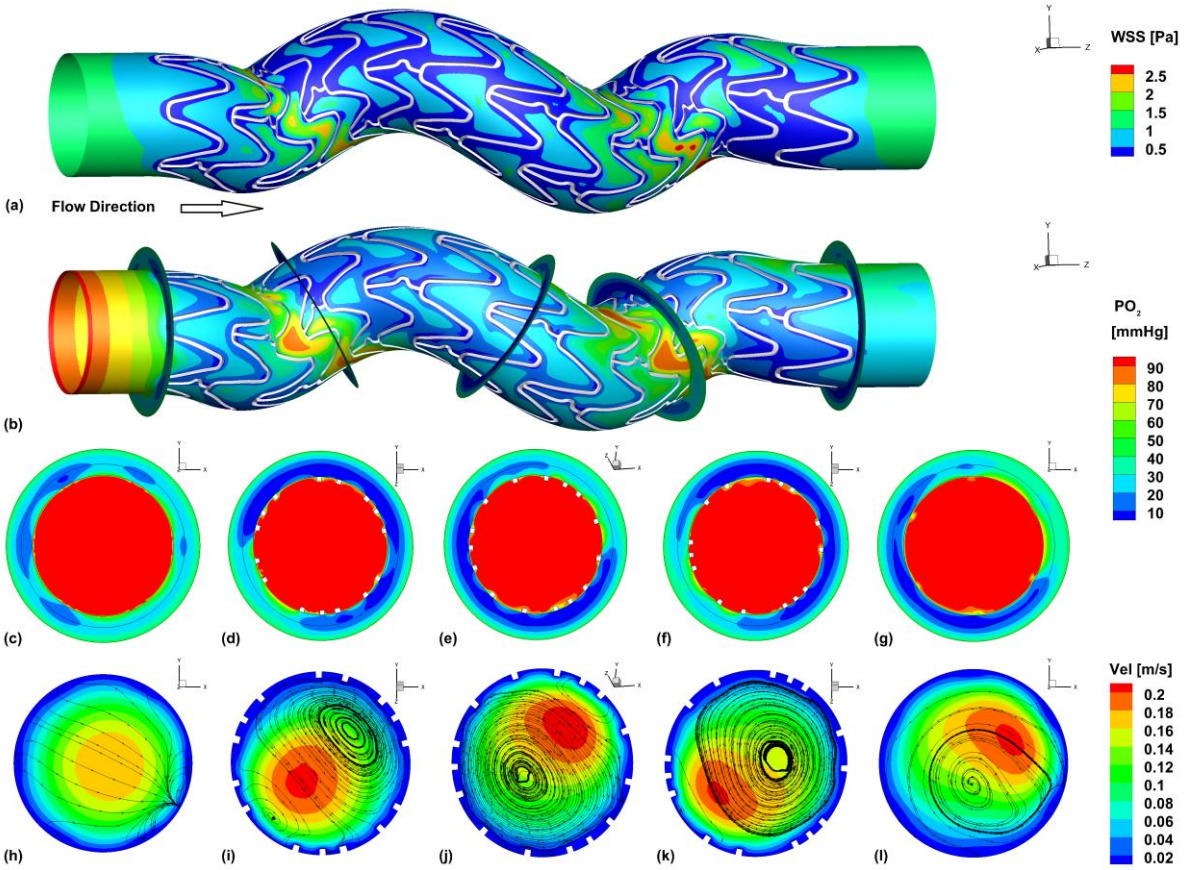

Figure 8.16: Results for Stent 6 – (a) WSS, (b) luminal PO_2 and slice locations, (c-g) PO_2 in lumen, intima and media at each slice location, and (h-l) velocity contours and secondary flow streamlines at each slice location. Note that the main flow direction for slices is towards the reader.

8.4.2 Analysis of Oxygen Transport

The changes in haemodynamics created by inducing helical flow have significant influence on the oxygen transport from the blood into the arterial wall which is apparent when the luminal surface PO_2 and Sh contour plots in Figure 8.17 and Figure 8.18 are analysed. As shown in Figure 8.5, between Stent 1 and Stent 6 the percentage volume of the arterial wall exposed to low PO_2 decreases from 75.0% to 68.7% and the percentage volume exposed to hypoxic PO_2 decreases from 28.4% to 22.4%. It is clear from Figure 8.17 that even though there is an overall reduction in the volume of the arterial wall exposed to hypoxic PO_2 levels the reduction is not uniform on the luminal surface; instead, similar to the WSS, increased oxygen transport is observed in a helical ribbon through the stented region. Looking again at Figure 8.17 there are essentially two helical ribbons of opposing high and low PO_2 levels distributed along the length of the stented region. These high and low helical ribbons are also present in the Sh, WSS and WSSG plots, and are a result of the helical centrelines governing the geometries of the five helical stents, and the induced secondary motion of the flow towards the outside of the curved lumen.

Figure 8.19 shows the percentage volume of the arterial wall exposed to PO_2 values in bins of 5mmHg and also the proportion of each bin that is within the intima. What is clear from this figure is that the impact of helical flow affects the intima and the media disproportionately. For Stent 1 28.4% of the arterial wall is exposed to hypoxic PO_2 levels, but the media only accounts for 4.2% of that. For Stent 6 22.4% of the arterial wall is exposed to hypoxic PO_2 levels with the media proportion only reducing to 3.6%. Conversely, the intima represents 24.2% of that total for Stent 1 and reduces to 18.8% for Stent 6. In Figure 8.19 it can be seen that the percentage of the arterial wall within

the intima that is hypoxic is significantly reduced with relatively slight increases in all bins from 15 – 75mmHg. Contrary to this, the proportion of the arterial wall that is within the media and also hypoxic is not significantly reduced by increasing the helical centreline radius. This can be further seen in Table 8.3, where the individual percentages of the intima, media, and the complete arterial wall exposed to hypoxic and low PO_2 are given. Most tellingly the percentage of the intima exposed to hypoxic PO_2 levels reduces from 62.0% to 48.5%, and the percentage of the media exposed to hypoxic PO_2 levels reduces from 6.9% to 5.9%.

The flow disturbances caused by the stent struts limit the amount of oxygen diffusing in from the lumen in all the stent geometries; however, with the helical stents there is increased advection towards the arterial wall within the high PO_2 ribbon, for example as seen in Figure 8.14(b). Consequently, the high PO_2 ribbon marks the region where the underlying arterial wall experiences higher PO_2 levels which can be seen in the cross-sectional plots shown in Figure 8.14(c – g). Crucially, the low PO_2 ribbon does not have a significant effect on the amount of the arterial wall exposed to hypoxic PO_2 levels for one reason – only the intima is significantly affected by the luminal surface PO_2 levels. The media layer is predominantly supplied with oxygen through diffusion from the outer interface, representing, physiologically, the interface with the adventitia, and the intima layer is supplied through diffusion from the luminal surface, as demonstrated previously in Test Case 3. Following on from this, the intima within the arterial wall in the straight stent model already experiences a considerable amount of hypoxic PO_2 levels (62.0% of the intima for Stent 1) within the stented region due to stent struts disrupting the luminal blood flow. Finally, even though the luminal surface within the high PO_2 ribbon experiences PO_2 levels that reach up to values as high as 80 – 90mmHg in Stent 6, compared with 20 – 40mmHg in Stent 1, the low PO_2 ribbon does not change

to the same degree with a considerable amount of the luminal surface still experiencing PO_2 levels within the 20 – 30mmHg range, similar to the same area within Stent 1.

Therefore, helical flow does improve the oxygen transport into the arterial wall within a stented artery, although not uniformly as it only improves it within a high PO_2 helical ribbon within the stented region. The question arises as to what this might mean physiologically. This is similar to the results seen in the previous test cases where the media remains relatively unaffected, in terms of oxygenation, by changes in haemodynamics within the lumen because of the oxygen supply from the outer interface with the adventitia (as expected). The intima though is affected considerably. Given that in reality stents are placed within arteries that have experienced atherosclerotic plaque build-up, the intima could already have been infiltrated by inflammatory cells and undergone some degree of intimal hyperplasia before stent implantation. Decreasing the percentage volume of the intima exposed to hypoxic PO_2 levels could aid in the healing of this crucial layer, particularly coupled with the potential haemodynamic benefits, as discussed above. However, the degree to which it may aid the healing process post-stent-implantation is debateable and would require further work to elucidate.

Stent	Intima		Media		Arterial Wall	
	Hypoxic [%]	Low [%]	Hypoxic [%]	Low [%]	Hypoxic [%]	Low [%]
1	62.0	92.0	6.9	64.2	28.4	75.0
2	61.4	91.7	7.0	64.4	28.2	75.1
3	57.8	90.8	6.8	64.3	26.7	74.6
4	53.3	87.7	6.9	63.2	25.0	72.7
5	51.5	83.6	6.7	61.9	24.2	70.4
6	48.5	81.3	5.9	60.7	22.4	68.7

Table 8.3: The percentage volume of the intima, media, and arterial wall (both intima and media together) exposed to hypoxic (<10mmHg) and low (<30mmHg) PO_2 levels for six selected stents.

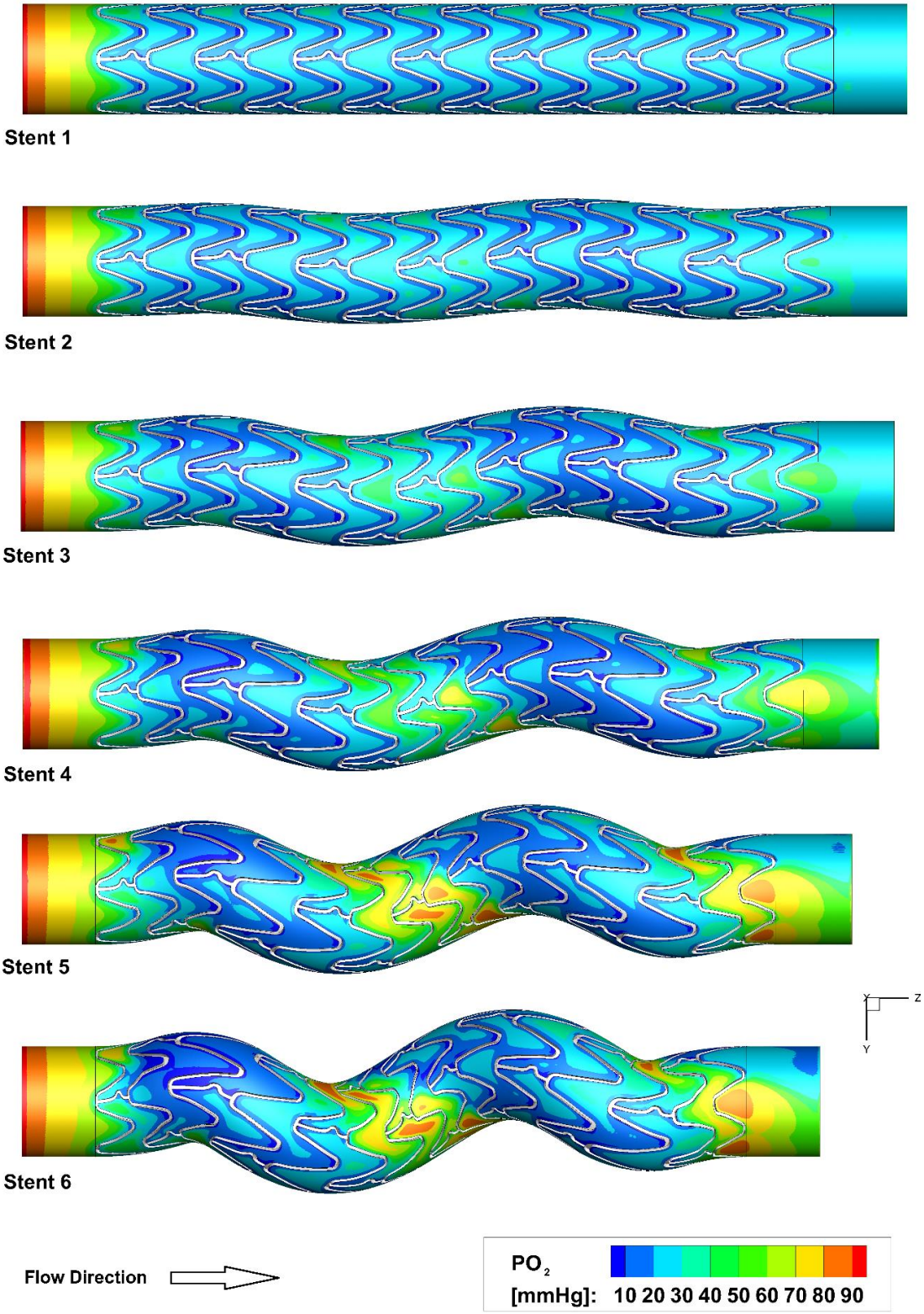

Figure 8.17: PO_2 on the luminal surface within the stented region for the six selected stents.

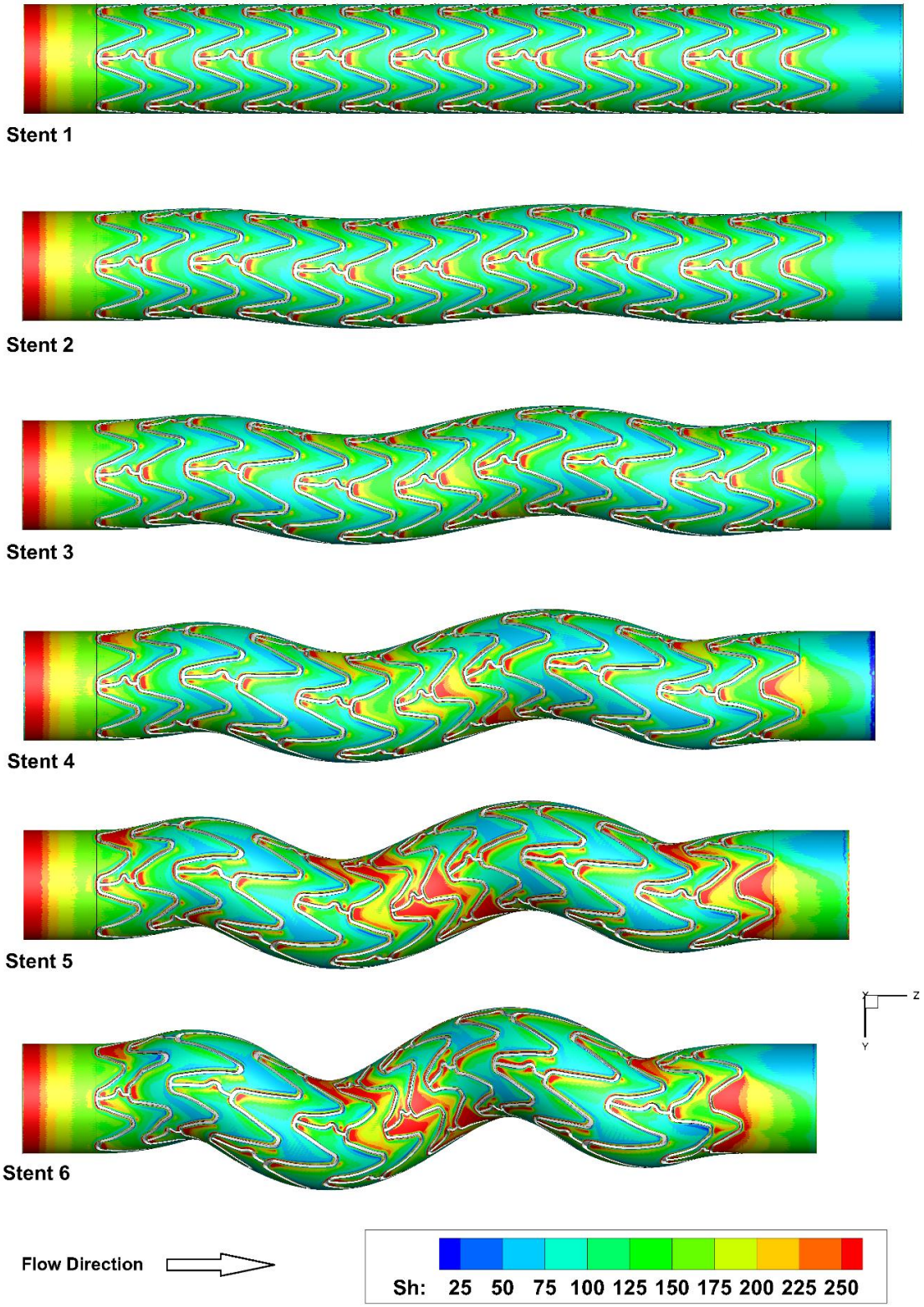

Figure 8.18: Sh on the luminal surface within the stented region for the six selected stents.

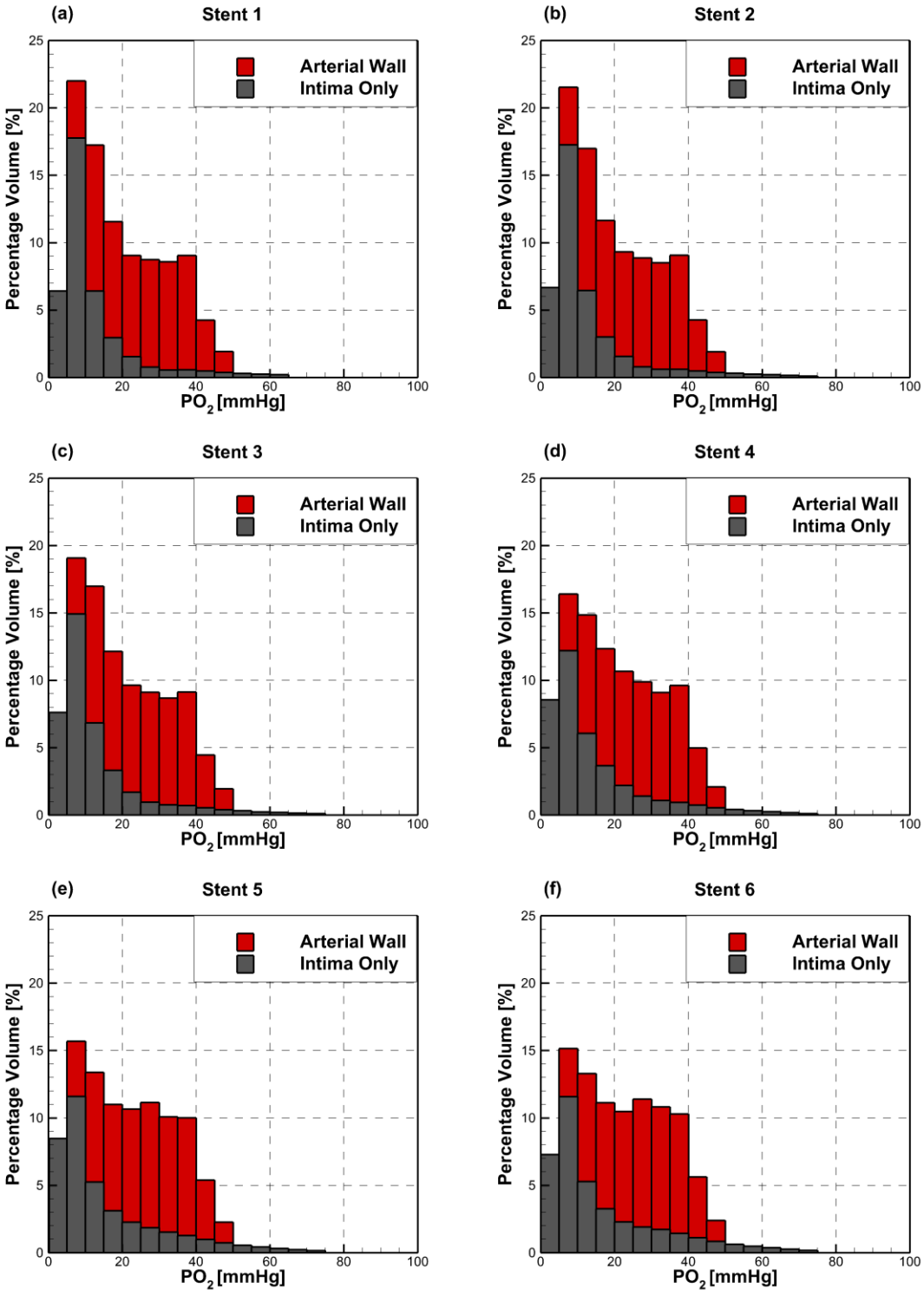

Figure 8.19: Predicted percentage volume of the arterial wall and intima exposed to PO_2 values in bins of 5mmHg for the six selected stents.

8.5 Discussion

Helical flow has been shown here to increase oxygen transport into the arterial wall within a stented coronary artery with the volume of the arterial wall exposed to hypoxic PO_2 levels decreasing by 21.1% between a straight stent (Stent 1) and a stent with helical centreline radius of 1.0mm (Stent 6). This reduction in hypoxic PO_2 levels is not uniform throughout the arterial wall with the region experiencing increased oxygen transport only within a helical ribbon within the stented region that also experiences high WSS and WSSG. Additionally, the intima is significantly more affected by the change in haemodynamics and, consequently, the oxygen transport and reduction in hypoxic PO_2 levels, in comparison with the media. Given that physiologically the intima experiences severe trauma during stent implantation, and also, prior atherosclerotic lesion development, the fact that its oxygenation is also significantly affected by changes in local haemodynamics gives added importance to improving these local haemodynamics. When these local haemodynamics were analysed it was found here that with increasing helical centreline radii the percentage of the luminal surface exposed to atheroprotective WSS, and low WSS both increase. Unfortunately, the region that experiences atheroprotective WSS also experiences high WSSG values that are associated with increased inflammation and difficulties in re-endothelisation. The transition regions within each helical stent geometry are areas that are prone to low WSS due to the change in the flow direction in these regions. A more gradual transition with a longer stent could result in more favourable WSS conditions within this region. The LNH plots show that the helicity of the flow can extend to almost a full stent length beyond the stented region for Stent 6.

8.6 Conclusions

Helical flow, as induced here, is a double-edged sword with increased advection of oxygen towards the luminal surface collocated with a ribbon of high WSSG. Additionally, there is a diametrically opposite ribbon of low WSS which could lead to increased NIH along the length of the stent in this region. Whether or not the added benefit of atheroprotective WSS values and increased intima oxygenation out-weighs the adverse effects of high WSSG is a question that these numerical models cannot answer at present and instead may only come with further *in vitro* and *in vivo* work.

This is the first time the predicted oxygen transport within helical-flow-inducing stent designs has been simulated using an advanced oxygen transport model which incorporates both the free and bound oxygen. Additionally, this is the first time, to the author's knowledge, that the haemodynamics within several helical stents have been analysed where the stent struts have been incorporated in the geometries, thus providing a more realistic representation of a stented artery immediately post-implantation.

8.7 Summary

The results of Test Case 4 were presented here in which the effects of helical-flow-inducing stents on the haemodynamics and oxygen transport within stented coronary arteries were analysed. Six stented coronary artery geometries with increasing helical centreline radii, from 0mm to 1.0mm, were modelled and the results compared. These results indicate that helical flow has potentially beneficial and adverse effects on both the WSS patterns and the oxygen transport within a stented coronary artery. Chapter 9 will summarise the conclusions drawn here from this test case, and those from the previous three test cases, along with the novelty, limitations, and recommendations of this work.

CHAPTER 9

Conclusions

9.1 Introduction

Hypoxia in arterial walls contributes to the formation of foam cells and affects the severity of inflammation in atherosclerotic lesions, causes VSMCs to express growth factors which could lead to increased NIH, and can induce EC apoptosis.[20,134,215,216,252] Rabbits treated with supplemental oxygen following graft-to-artery anastomosis had reduced NIH.[135] The biological processes, thrombosis, inflammation, NIH and re-endothelialisation, instigated following stent implantation can result in ISR and can potentially all be influenced by the amount of oxygen reaching the cells within the arterial wall. Therefore, predicting the amount of oxygen which will reach the tissue cells within the walls of a stented vessel is of benefit in determining how well a stent would perform post-implantation. In fact, predicting oxygen transport in the cardiovascular system has applications beyond stents and could include the modelling of atherosclerotic lesion development and the assessment of other cardiovascular devices. Helical flow has been hypothesised to improve both the local haemodynamics and the arterial wall oxygenation within stented arteries.

The aim of the research undertaken here was to develop an advanced oxygen transport model that incorporates both the free oxygen dissolved in plasma and the bound oxygen contained in RBCs, and also accounts for the shear-induced dispersion of RBCs, which could be used to assess stent designs. As part of this over-arching aim, comparison of

the results generated in 3D geometries using the advanced oxygen transport model and the simpler models with experimental measurements from Santilli et al. was carried out. Showing how this advanced oxygen transport model could then be used to assess three different stent designs demonstrated the importance and viability of the methodology. The advanced oxygen transport model was also used to assess the ability of helical flow to improve oxygenation of the arterial wall in stented coronary arteries. In addition, the effect of helical flow on the local haemodynamics within a stented coronary artery were analysed.

9.2 Novelty

The work undertaken as part of this thesis has several novel aspects that deserve mentioning:

- It is the first time that an advanced blood oxygen transport model has been developed that incorporates both free and bound oxygen, and a shear-dependent RBC dispersion coefficient.
- It is the first time that the simplifications of blood oxygen transport models, which are prevalent in the literature, have been assessed in 3D geometries and their effects on the PO_2 profile within the arterial lumen and wall have been analysed.
- It is the first time that the oxygen transport has been modelled in three different stent designs with the predicted low and hypoxic PO_2 volumes within the arterial wall assessed.
- It is the first time that the oxygen transport within several helical-flow-inducing stent designs has been predicted incorporating a heterogeneous arterial wall.

Although many previous studies analysing the blood flow within a stented vessel have analysed the haemodynamics, predominantly WSS-based variables, this study aimed to elucidate how the haemodynamics affects the oxygen delivery to the arterial wall. Thus, this study goes beyond the luminal surface and shows how the local haemodynamics can have a significant impact on the biological processes within the arterial wall through augmented delivery of oxygen to the cells contained within. For example, Test Case 3 shows how the oxygen transport into the arterial wall can be affected by different stent designs and also, how the WSS, as plotted on the luminal surface within the stented region, does not act as an accurate predictor of the extent of hypoxic regions within the arterial wall. Test Case 4 demonstrates how the methodology developed can be applied to improve coronary stent designs by studying the oxygen transport in several helical-flow-inducing stent designs. This may assist in the design of future cardiovascular devices.

9.3 Limitations

Computational modelling of any sort when dealing with a real-world event/process inevitably incorporates some degree of uncertainty and simplifications based on well-thought-out assumptions. In the case of computational modelling of oxygen transport within the cardiovascular system there are some simplifications made for several reasons, which include a lack of experimental data to confirm what parameter values to adopt, inability of current software to accurately model some aspects of the problem, and computational expense.

Lack of experimental data is an issue in predicting the oxygen transport within the arterial wall which leads to some assumptions, for instance assuming a homogeneous composition. The inability of current software to accurately model some aspects is

exemplified by the fact that current CFD models of blood flow, which generally is composed of several cellular constituents, assume a homogeneous medium (this also falls under computational expense). Without more experimental data and more powerful software and hardware there is little that can be currently done to avoid these limitations and consequently the assumptions made.

In terms of limitations of the methodology presented here, and possible avenues for future work, the shear-dependant dispersion of RBCs is a haemodynamic flow feature that is not fully understood. Additionally, at low shear rates RBCs are known to form rouleaux which could impact both their dispersion and the oxygen transport. Therefore, future studies of this phenomenon may improve the predictive capability of the model. This may be improved by particle based CFD software which could model all the constituent cells of blood including the RBCs. All the simulations carried out as part of this study were steady state with the assumption of rigid arterial walls. The assumption of steady state was used because of the computational cost of transient simulations of the geometries presented here would be extremely high and also, given how low the diffusivity of oxygen is within plasma and within the arterial wall, the effect of pulsatility has been shown to have a minimal effect.[124] Also, the haematocrit is considered to be constant throughout the fluid domain when in reality there is a reduced haematocrit within the plasma skimming layer at the luminal surface. This could affect the predicted steep gradient in the PO_2 levels within the blood adjacent to the luminal surface, although to what extent would need further investigation. Some numerical work undertaken by Krüger (2016) modelling a suspension of deformable RBCs and nearly rigid platelets using a combination of the lattice-Boltzmann, immersed boundary and finite element methods produced results where the plasma skimming layer was

observable.[126] This type of work could serve as a basis for future work looking at the effect of the plasma skimming layer on the oxygen transport into the arterial wall.

One aspect which was not varied was the parameters defining the oxygen transport within the arterial wall. In reality, for stented arteries the presence of plaque, and additionally, the structural damage caused to the arterial wall by stent implantation, could result in a much higher oxygen demand within the arterial wall. Thus, the values shown here in this study are conservative estimates of the PO_2 levels and in reality the situation could be significantly worse. Clearly, as shown by the results at Location 2 in Test Case 1, more accurate representations of each layer of the arterial wall, including plaque, and their diffusion/reaction parameters based on cellular composition would be required for more patient-specific analysis; unfortunately, these are not available at present. Additionally, given the complexity of the biological processes that can lead to ISR, as described in Chapter 2, the power of the predictive models presented here is limited. In truth they only present an idealised snap-shot of the stented artery. Thrombus formation and inflammation begin to occur immediately upon stent implantation, but given their scale at which they occur modelling them in the geometries presented here would be extremely computationally expensive. As such the models presented here assume uniform oxygen consumption throughout the arterial wall, when in reality with leukocytes transmigrating into the arterial wall these would increase the oxygen consumption.[157] With this in mind the simulations presented here, even though they are designed at a larger scale than the biological processes take place, do serve to give an indication of the oxygen levels and highlight areas of potential hypoxia. This provides an important step in reaching more accurate, patient-specific models that could be improved with advanced imaging techniques such as optical coherence tomography and

elastography which potentially could provide information at close to a cellular level in patient-specific arteries that may aid in the design of future more discrete models.

The presence of malapposed struts was not considered in the test cases presented here. Previous studies have found that malapposed struts can affect the local haemodynamics within the stented region;[12] therefore, consequently they would affect the oxygen transport. This limitation may be addressed in future work using patient-specific geometries. Additionally, although current medical imaging technology has allowed the acquisition of patient-specific geometries, attaining the governing transport parameters would be very challenging. Given the aforementioned correlations between hypoxia and IH, with the addition of patient-specific geometries and parameters this methodology could be a considerable aid to the both the design of future implantable devices and also to the tailored analysis of the impact of these devices on individual patients.

9.4 Main Conclusions/Recommendations

The conclusions/recommendations of this study can be divided into two separate categories:

- Conclusions/recommendations for oxygen transport modelling
- Conclusions/recommendations for stent design

9.4.1 Oxygen Transport Modelling

Three important conclusions for future analyses of oxygen transport modelling are inferred by this study.

First, ignoring the oxyhaemoglobin content within the RBCs leads to large errors in the PO_2 gradient within the MTBL and, consequently, the prediction of hypoxic regions within the arterial wall. The standard simplified model which ignores oxyhaemoglobin,

i.e. Model 5, and is crucially the most commonly-used model in the literature, over-predicts the PO_2 levels in both the carotid bifurcation and stented coronary artery test cases presented here. It therefore presents an overly optimistic view of the risk of IH caused by low and hypoxic PO_2 levels.

Second, neglecting the shear-induced dispersion of RBCs also affects the accuracy of the predicted results which is also shown in Test Cases 1 and 2.

Third, the use of a correction factor in the Sh results when neglecting the bound oxygen in the blood oxygen transport model can lead to inaccurate results in comparison with a more advanced model, i.e. Model 1.

The first conclusion deserves elaborating on further as the PO_2 gradient within the MTBL has been a source of controversy in the area of oxygen transport modelling which remains unresolved at present. The steep PO_2 gradient, seen in Figures 6.10, 6.16, 6.20, and 7.5, which has been observed in experimental measurements, has led to a debate as to the role of the endothelium in oxygen transport as highlighted by Tsai et al. (2010).[258] In this study here the diffusion across the lumen/arterial wall interface has been modelled with no resistance and no additional consumption in line with other studies in oxygen transport in arteries.[23,203,248] According to *in vivo* measurements of the PO_2 across the arteriole and arterial walls in animals, there is a high PO_2 gradient at the wall going from the lumen into the arterial wall.[217,218] Previous studies have concluded that this gradient is due to extremely high oxygen consumption by the endothelial cells, for example in the study by Shibata et al.[226], which have been thoroughly reviewed by Tsai et al.[259] However, when ECs have been cultured and studied *in vitro* the consumption levels predicted have not matched with levels recorded by these studies.[169,192] Thus, the mismatch between *in vivo* and *in vitro* measurements has led to

uncertainty as to what effect the endothelium has on PO_2 gradients. The results presented in this study would suggest that the endothelium does not consume a significantly higher proportion of the oxygen being transferred into the wall than other cells in arteries, in agreement with *in vitro* measurements using cultured ECs. Instead the steep gradient is caused by the balance between the free and bound oxygen with the bound oxygen acting a large store/sink for oxygen.

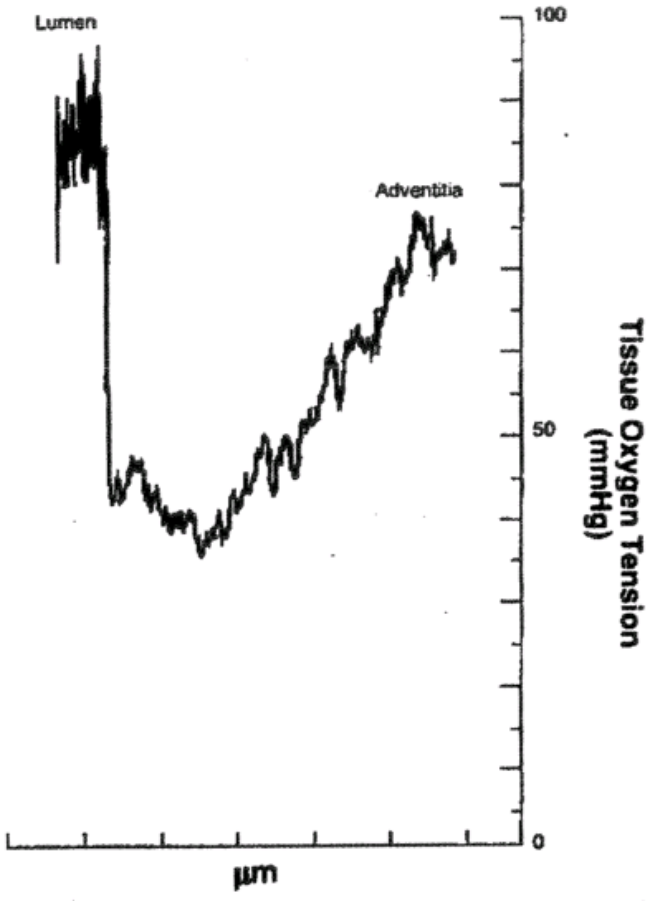

Figure 9.1: Artist's representation of a transarterial wall PO_2 profile as measured using an electrode probe at Location 1 (in line with the locations described in Chapter 6) within a dog carotid artery by Santilli et al.[217]

In addition, it is assumed by previous studies that the luminal measurements taken from Santilli et al. are just inside the lumen as the probe is advanced through the arterial wall.

In actuality, Santilli et al. give an artist's representation of the transarterial wall oxygen profile as recorded by the chart recorder from Location 1, as shown in Figure 9.1. In their study it is mentioned that there is "a combination of respiratory movement, pulsatile blood flow, electrode movement and electrical noise" which causes this saw-toothed pattern.[217] These effects, combined with the accuracy of the electrode probe used, i.e. its sphere of influence, is discussed by Tsai et al.[259] In their review on the subject, they suggest that it is doubtful that the PO_2 value given is representative of the actual value on the luminal surface and more likely an average of the PO_2 value within a volume around the probe which could include the MTBL.

From the results for Models 1 – 4 presented in Test Case 1 and 2, which include the bound oxygen, the high PO_2 gradient that is recorded by *in vivo* studies is reproduced in the predicted PO_2 transarterial profiles. This would lead to the conclusion that it is not the consumption or resistance of the endothelium which creates the high gradient seen *in vivo*, but the properties of the blood itself. Specifically, because of the slope of the oxyhaemoglobin curve between 10 and 40mmHg, the RBCs act as both a sizeable source and a sink for free oxygen. Thus, physiologically, the interaction between both the free and bound oxygen within the MTBL can significantly affect how much oxygen is delivered to the arterial wall.

Critically, in the studies which conclude that the endothelium must consume vastly higher amount of oxygen than what is seen *in vitro*, this conclusion is based on evaluation of oxygen mass transport from the lumen into the arterial wall using simple diffusion calculations similar to Model 5, as presented in Chapter 3. Additionally, a study by Vadapalli et al. concluded that most of the reported values of intravascular oxygen flux are overestimated, which could explain some of the differences seen *in vivo*.[261] Additionally, it should be noted that many of the studies which support the high

oxygen consumption of the endothelium were carried out in arterioles and capillaries, and possibly the endothelium consumption would vary with the size of the vessel. Therefore, consideration of the findings presented here may be important for future studies of this area. This is clearly an area where future study is needed to fully understand the processes taking place and more work, which would include *in vivo, in vitro,* and numerical simulation, could shed light on these issues.

The second and third conclusions are related to the simplifications made in the blood oxygen transport model, as detailed in Chapter 3, in previous studies. These are made to reduce the computational expense of the simulations. For instance, by neglecting the bound oxygen, and consequently, the shear-dependent nature of the RBC dispersion, reduces the complexity and ensures convergence of simulations with larger timesteps, and therefore, are less computationally expensive. However, as demonstrated here in Test Cases 1 and 2 neglecting the bound oxygen in the blood oxygen transport model leads to large errors which cannot be accounted for using a simple correction factor. Therefore, some of these long-standing simplifications must be called into question when the results generated could be significantly different from the actual physiological process. More work is needed in this area.

9.4.2 Stent Design

From Test Case 3 it is clear that stent strut configuration can have a considerable impact on the amount of oxygen reaching the underlying arterial wall cells. Stent A was predicted to perform the worst which is predominantly caused by the N-shaped link struts. These link struts, which are aligned perpendicular to the main blood flow, create large volumes of hypoxic zones adjacent to the recirculation zones upstream and downstream of the struts. Stent B suffers slightly from a decreased interface area caused by the amount of struts present in the design. Stent C has the combination of both large

intra-strut areas and also less low WSS zones caused by struts aligned perpendicular to the main blood flow. It is clear from the results of Test Case 3 that the predicted oxygenation levels within the arterial wall are not predictable by the interface area presented to the luminal blood or by the WSS values plotted on the luminal surface within the stented region. Additionally, in terms of assessing stent designs the benefit of realistically-deformed stented arteries, as derived using FEA, is demonstrated in this test case because some features, such as prolapse and stretching of the arterial wall, which would not be generated accurately otherwise are shown to affect the predicted results.

Helical flow has been hypothesised to help reduce ISR when induced within a stented region, as reviewed in Chapter 4. It presents certain theoretical benefits such as reduced recirculation zones, more uniform WSS, and increased oxygen transport into the arterial wall. Test Case 4 aimed to assess these benefits for a specific well-defined application, i.e. a 20mm stent with a 10mm one-turn helical section. Briefly, the results presented in Chapter 8 indicate that helical-flow-inducing stents do increase the overall amount of oxygen transfer into the arterial wall; although, only in a helical ribbon within the stented region. This is also true in relation to the WSS with two diametrically-opposite ribbons; one high, one low, present within the stented region. The WSSG shows a similar distribution which could lead to adverse consequences in terms of re-endothelialisation and inflammation. Additionally, the amount of the blood flow experiencing retrograde flow, which would signify recirculation zones, is shown to increase with increasing helical centreline radius. Therefore, helical flow in stent designs is beneficial to some extent for oxygen transfer into the arterial wall, but could have adverse effects with increased WSSG and recirculation zones. How influential one aspect is in comparison to the other would require further research. Because of the specific restraints placed on the geometry, for instance the length and only one helical

turn, some of the benefits of helical flow found by other researchers may not exist in this specific test case but may appear with the longer stents that are used in peripheral arteries.

9.5 Future Work

As detailed in the limitations section above, the parameters defining the oxygen transport within the arterial wall need to be better defined with more experimental work. Specifically, the effects of an atherosclerotic lesion on the parameters governing oxygen transport would be beneficial for predicting necrosis in affected arteries. The blood oxygen transport model needs further validation with simple comparison test cases between *in vitro* measurements and *in silico* results. A comparison of the effects of geometry simplifications used commonly in CFD studies on the predicted oxygen transport within stented arteries would be of benefit. This study would take a similar form to a study by Martin et al. (2014) whereby the arterial wall oxygenation predicted using realistically-deformed stent geometries, as presented here in Chapter 7, could be compared with the arterial wall oxygenation predicted using non-deformed, simplified stent geometries.[153]

Bibliography

1. Al-Roubaie S, Jahnsen ED, Mohammed M, Henderson-Toth C, Jones EA V. Rheology of embryonic avian blood. *Am J Physiol Heart Circ Physiol*. 301, H2473-81, 2011.

2. Ammirati E, Moroni F, Magnoni M, Camici PG. The role of T and B cells in human atherosclerosis and atherothrombosis. *Clin Exp Immunol*. 179, 173-187, 2015.

3. Anderson JM, Rodrigruez A, Change DT. Foreign body reaction to biomaterials. *Semin Immunol*. 20, 86-100, 2008.

4. ANSYS Inc. ANSYS Acadenmic Research, Release 15, Help System, Linear Equation Solution.

5. Back LH, Radbill JR, Crawford DW. Analysis of oxygen transport from pulsatile, viscous blood flow to diseased coronary arteries of man. *J Biomech*. 10, 763-774, 1977.

6. Balossino R, Gervaso F, Migliavacca F, Dubini G. Effects of different stent designs on local hemodynamics in stented arteries. *J Biomech*. 41, 1053-1061, 2008.

7. Banerjee RK, Kwon O, Vaidya VS, Back LH. Coupled oxygen transport analysis in the avascular wall of a coronary artery stenosis during angioplasty. *J Biomech*. 41, 475-479, 2008.

8. Barth T, Jespersen D. The design and application of upwind schemes on

unstructured meshes. American Institute of Aeronautics and Astronautics; 1989, .

9. Bassiouny HS, Song RH, Kocharyan H, Kins E, Glagov S. Low flow enhances platelet activation after acute experimental arterial injury. *J Vasc Surg Off Publ Soc Vasc Surg [and] Int Soc Cardiovasc Surgery, North Am Chapter*. 27, 910-918, 1998.

10. Bassiouny HS, White S, Glagov S, Choi E, Giddens DP, Zarins CK. Anastomotic intimal hyperplasia: mechanical injury or flow induced. *J Vasc Surg*. 15, 708-716, 1992.

11. Bayes-Genis a, Camrud a R, Jorgenson M, et al. Pressure rinsing of coronary stents immediately before implantation reduces inflammation and neointimal hyperplasia. *J Am Coll Cardiol*. 38, 562-568, 2001.

12. Beier S, Ormiston J, Webster M, et al. Hemodynamics in Idealized Stented Coronary Arteries: Important Stent Design Considerations. *Ann Biomed Eng*. 44, 315-329, 2015.

13. Beijk MAM, Klomp M, Verouden NJW, et al. Genous endothelial progenitor cell capturing stent vs. the Taxus Liberté stent in patients with de novo coronary lesions with a high-risk of coronary restenosis: a randomized, single-centre, pilot study. *Eur Heart J*. 2009.

14. Ben-Dor I, Waksman R, Pichard AD, Lindsay J, Satler LF. The Current Role of Bare-Metal Stents. *Card Interv Today*. , 40-46, 2011.

15. Bharadvaj BK, Mabon RF, Giddens DP. Steady flow in a model of the human carotid bifurcation. Part I--flow visualization. *J Biomech*. 15, 349-362, 1982.

16. Bharadvaj BK, Mabon RF, Giddens DP. Steady flow in a model of the human carotid bifurcation. Part II--flow visualization. *J Biomech*. 15, 349-362, 1982.

17. Bhargava B, Reddy NK, Karthikeyan G, et al. A novel paclitaxel-eluting porous carbon–carbon nanoparticle coated, nonpolymeric cobalt–chromium stent: Evaluation in a porcine model. *Catheter Cardiovasc Interv*. 67, 698-702, 2006.

18. Biasetti J, Spazzini PG, Hedin U, Gasser CT. Synergy between shear-induced migration and secondary flows on red blood cells transport in arteries: considerations on oxygen transport. *J R Soc Interface*. 112014.

19. Boddu AR, Balmuri AR, Kamalesh M. Clinical utility of self-expanding stents in coronary artery disease. *Res Reports Clin Cardiol*. 6, 117-122, 2015.

20. Boström P, Magnusson B, Svensson PA, et al. Hypoxia converts human macrophages into triglyceride-loaded foam cells. *Arterioscler Thromb Vasc Biol*. 26, 1871-1876, 2006.

21. Brecher GA. Experimental evidence of ventricular diastolic suction. *Circ Res*. 4, 513-518, 1956.

22. Bricker JM. Rheology fo noncolloidal suspensions of spheres in oscillatory shear flow and the dynamics of suspensions of rigid fibers. 2007.

23. Caputo M, Chiastra C, Cianciolo C, et al. Simulation of oxygen transfer in stented arteries and correlation with in-stent restenosis. *Int j numer method biomed eng*. 29, 1373-1387, 2013.

24. Caro CG. Discovery of the role of wall shear in atherosclerosis. *Arterioscler Thromb Vasc Biol*. 29, 158-161, 2009.

25. Caro CG. The dispersion of indicator flowing through simplified models of the circulation and its relevance to velocity profile in blood vessels. *J Physiol*. 185, 501-519, 1966.

26. Caro CG, Cheshire NJ, Watkins N. Preliminary comparative study of small amplitude helical and conventional ePTFE arteriovenous shunts in pigs. *J R Soc Interface*. 2, 261-266, 2005.

27. Caro CG, Doorly DJ, Tarnawski M, Scott KT, Long Q, Dumoulin CL. Non-Planar Curvature and Branching of Arteries and Non-Planar-Type Flow. *Proc Math Phys Eng Sci*. 452, 185-197, 1996.

28. Caro CG, Pedley TJ, Schroter RC, Seed WA. *Mechanics of the Circulation*. Oxford University Press; 1978, .

29. Carroll GT, Devereux PD, Ku DN, McGloughlin TM, Walsh MT. Experimental validation of convection-diffusion discretisation scheme employed for computational modelling of biological mass transport. *Biomed Eng Online*. 9, 34, 2010.

30. Cha W, Beissinger RL. Evaluation of shear-induced particle diffusivity in red cell ghosts suspensions. *Korean J Chem Eng*. 18, 479-485, 2001.

31. Chandran KB, Yoganathan AP, Rittgers SE. *Biofluid Mechanics: The Human Circulation*. Vol 1st ed. CRC Press; 2006, .

32. Chatzizisis YS, Coskun AU, Jonas M, Edelman ER, Feldman CL, Stone PH. Role of endothelial shear stress in the natural history of coronary atherosclerosis and vascular remodeling: molecular, cellular, and vascular behavior. *J Am Coll*

Cardiol. 49, 2379-2393, 2007.

33. Chavez JF, Doll JA, Mediratta A, et al. Factors Associated with the Use of Drug-Eluting Stents in Patients Presenting with Acute ST-Segment Elevation Myocardial Infarction. *Cardiol Res Pract*. 2015.

34. Cheema AN, Hong T, Nili N, et al. Adventitial microvessel formation after coronary stenting and the effects of SU11218, a tyrosine kinase inhibitor. *J Am Coll Cardiol*. 47, 1067-1075, 2006.

35. Chen HY, Hermiller J, Sinha AK, Sturek M, Zhu L, Kassab GS. Effects of stent sizing on endothelial and vessel wall stress: potential mechanisms for in-stent restenosis. *J Appl Physiol*. 106, 1686-1691, 2009.

36. Chen Z, Fan Y, Deng X, Xu Z. Swirling flow can suppress flow disturbances in endovascular stents: a numerical study. *ASAIO J*. 55, 543-549, .

37. Cheng C, Helderman F, Tempel D, et al. Large variations in absolute wall shear stress levels within one species and between species. *Atherosclerosis*. 195, 225-235, 2007.

38. Chiastra C, Morlacchi S, Gallo D, Morbiducci U, Cárdenes R, Migliavacca F. Computational fluid dynamic simulations of image-based stented coronary bifurcation models. 2013.

39. Chiastra C, Morlacchi S, Pereira S, Dubini G, Migliavacca F. Computational fluid dynamics of stented coronary bifurcations studied with a hybrid discretization method. *Eur J Mech - B/Fluids*. 35, 76-84, 2012.

40. Chow MJ, Turcotte R, Lin CP, Zhang Y. Arterial extracellular matrix: A

mechanobiological study of the contributions and interactions of elastin and collagen. *Biophys J*. 106, 2684-2692, 2014.

41. Cookson AN. Computational Investigation of Helical Pipe Geometries From a Mixing Perspective. 2009.

42. Cookson AN, Doorly DJ, Sherwin SJ. Using coordinate transformation of Navier–Stokes equations to solve flow in multiple helical geometries. *J Comput Appl Math*. 234, 2069-2079, 2010.

43. Coppola G, Caro CG. Oxygen mass transfer in a model three-dimensional artery. *J R Soc Interface*. 5, 1067-1075, 2008.

44. Coppola G, Caro CG. Oxygen mass transfer in a model three-dimensional artery. *J R Soc Interface*. 5, 1067-1075, 2008.

45. Coppola G, Caro CG. Arterial geometry, flow pattern, wall shear and mass transport: potential physiological significance. *J R Soc Interface*. 6, 519-528, 2009.

46. Coughlin MF, Schmid-Schönbein GW. Pseudopod projection and cell spreading of passive leukocytes in response to fluid shear stress. *Biophys J*. 87, 2035-2042, 2004.

47. Depaola N, Gimbrone MA, Davies PF, Dewey CF. Vascular endothelium responds to fluid shear stress gradients [published erratum appears in Arterioscler Thromb 1993 Mar;13(3):465]. *Arterioscler Thromb Vasc Biol*. 12, 1254-1257, 1993.

48. Dichek D a, Neville RF, Zwiebel J a, Freeman SM, Leon MB, Anderson WF.

Seeding of intravascular stents with genetically engineered endothelial cells. *Circulation*. 80, 1347-1353, 1989.

49. Ding Z, Friedman MH. Dynamics of Human Coronary Arterial Motion and Its Potential Role in Coronary Atherogenesis. *J Biomech Eng*. 122, 488-492, 2000.

50. Ding Z, Friedman MH. Quantification of 3-D coronary arterial motion using clinical biplane cineangiograms. *Int J Card Imaging*. 16, 331-346, 2000.

51. Ding Z, Zhu H, Friedman MH. Coronary Artery Dynamics In Vivo. *Ann Biomed Eng*. 30, 419-429, 2002.

52. Doorly DJ, Peiró J, Sherwin SJ, et al. Helix and model graft flows: MRI measurement and CFD simulations. *FEDSM*. 1997.

53. Doorly DJ, Sherwin SJ, Franke PT, Peiró J. Vortical flow structure identification and flow transport in arteries. *Comput Methods Biomech Biomed Engin*. 5, 261-273, 2002.

54. Dotter CT, Judkins MP. Transluminal Treatment of Arteriosclerotic Obstruction: Description of a New Technic and a Preliminary Report of Its Application. *Circulation*. 30, 654-670, 1964.

55. Dumoulin C, Cochelin B. Mechanical behaviour modelling of balloon-expandable stents. *J Biomech*. 33, 1461-1470, 2000.

56. Duraiswamy N, Cesar JM, Schoephoerster RT, Moore JJE. Effects of stent geometry on local flow dynamics and resulting platelet deposition in an in vitro model. *Biorheology-Oxford-*. 45, 547-562, 2008.

57. Esmon CT. Inflammation and thrombosis. *J Thromb Haemost*. 1, 1343-1348, 2003.

58. Faller D V. Endothelial cell responses to hypoxic stress. *Clin Exp Pharmacol Physiol*. 26, 74-84, 1999.

59. Farb a, Sangiorgi G, Carter a J, et al. Pathology of acute and chronic coronary stenting in humans. *Circulation*. 99, 44-52, 1999.

60. Farooq V, Gogas BD, Serruys PW. Restenosis: Delineating the numerous causes of drug-eluting stent restenosis. *Circ Cardiovasc Interv*. 4, 195-205, 2011.

61. Fischman DL, Leon MB, Baim DS, et al. A randomized comparison of coronary-stent placement and balloon angioplasty in the treatment of coronary artery disease. *N Engl J Med*. 331, 496–501, 1994.

62. Frazin LJ, Lanza G, Vonesh M, et al. Functional chiral asymmetry in descending thoracic aorta. *Circulation*. 82, 1985-1994, 1990.

63. Frazin LJ, Vonesh MJ, Chandran KB, Shipkowitz T, Yaacoub AS, McPherson DD. Confirmation and Initial Documentation of Thoracic and Abdominal Aortic Helical Flow: An Ultrasound Study. *ASAIO J*. 42, 951-956, 1996.

64. Friedman MH, Ehrlich LW. Effect of spatial variations in shear on diffusion at the wall of an arterial branch. *Circ Res*. 37, 446-454, 1975.

65. Fukuda S, Yasu T, Predescu DN, Schmid-Schönbein GW. Mechanisms for regulation of fluid shear stress response in circulating leukocytes. *Circ Res*. 86, e13–e18, 2000.

66. Fung YC. *Biomechanics: Circulation*. Springer New York; 1996, .

67. Gaglia M a, Torguson R, Xue Z, et al. Insurance type influences the use of drug-eluting stents. *JACC Cardiovasc Interv*. 3, 773-779, 2010.

68. Gara PTO, Kushner FG, Ascheim DD, et al. ACCF / AHA Guideline 2013 ACCF / AHA Guideline for the Management of ST-Elevation Myocardial Infarction : Executive Summary A Report of the American College of Cardiology Foundation / American Heart Association Task Force on Practice Guidelines. , 529-555, 2016.

69. Garasic JM, Edelman ER, Squire JC, Seifert P, Williams MS, Rogers C. Stent and artery geometry determine intimal thickening independent of arterial injury. *Circulation*. 101, 812-818, 2000.

70. Garg S, Serruys PW. Coronary stents: current status. *J Am Coll Cardiol*. 56, S1-42, 2010.

71. Garg S, Serruys PW. Coronary stents: looking forward. *J Am Coll Cardiol*. 56, S43-78, 2010.

72. Gasser CT, Ogden RW, Holzapfel GA. Hyperelastic modelling of arterial layers with distributed collagen fibre orientations. *J R Soc Interface*. 3, 15-35, 2006.

73. Geary RL, Clowes AW, Cannon CP. Epidemiology and Pathogenesis of Restenosis. Vol (Duckers HJ, Nabel EG, Serruys PW, eds.). Humana Press; 2007, .

74. Geary RL, Kohler TR, Vergel S, Kirkman TR, Clowes a W. Time course of flow-induced smooth muscle cell proliferation and intimal thickening in

endothelialized baboon vascular grafts. *Circ Res*. 74, 14-23, 1994.

75. van der Giessen WJ, Lincoff AM, Schwartz RS, et al. Marked Inflammatory Sequelae to Implantation of Biodegradable and Nonbiodegradable Polymers in Porcine Coronary Arteries. *Circ* . 94, 1690-1697, 1996.

76. Glagov S, Weisenberg E, Zarins CK, Stankunavicius R, Kolettis GJ. Compensatory Enlargement of Human Atherosclerotic Coronary Arteries. *N Engl J Med*. 316, 1371-1375, 1987.

77. Go AS, Mozaffarian D, Roger VL, et al. *Heart Disease and Stroke Statistics - 2014 Update: A Report from the American Heart Association*. Vol 129. 2014, .

78. Goldman D. Theoretical models of microvascular oxygen transport to tissue. *Microcirculation*. 15, 795-811, 2008.

79. Goldsmith H. Red cell motions and wall interactions in tube flow. *Fed Proc*. 30, 1578-1590, 1971.

80. Goldsmith H., Marlow J. Flow behavior of erythrocytes. II. Particle motions in concentrated suspensions of ghost cells. *J Colloid Interface Sci*. 71, 383-407, 1979.

81. Gorbet MB, Sefton M V. Biomaterial-associated thrombosis: roles of coagulation factors, complement, platelets and leukocytes. *Biomaterials*. 25, 5681-5703, 2004.

82. Grotendorst GR, Chang T, Seppä HEJ, Kleinman HK, Martin GR. Platelet-derived growth factor is a chemoattractant for vascular smooth muscle cells. *J Cell Physiol*. 113, 261-266, 1982.

83. Grüntzig A. Transluminal dilation of coronary-artery stenosis. *Lancet*. 311, 263, 1978.

84. Grüntzig A, Kumpe DA. Technique of percutaneous transluminal angioplasty with the Gruntzig ballon catheter. *Am J Roentgenol*. 132, 547-552, 1979.

85. Grüntzig A, Vetter W, Meier B, Kuhlmann U, Lüolf U, Siegenthaler W. Treatment of renovascular hypertension with percutaneous transluminal dilation of a renal-artery stenosis. *Lancet*. 311, 801-802, 1978.

86. Gyongyosi M, Yang P, Khorsand A, Glogar D, on behalf of the Austrian Wiktor Stent Study Group, European Paragon Stent Investigators. Longitudinal straightening effect of stents is an additional predictor for major adverse cardiac events. *J Am Coll Cardiol*. 35, 1580-1589, 2000.

87. Habib RH, Dimitrova KR, Badour SA, et al. CABG Versus PCI: Greater Benefit in Long-Term Outcomes With Multiple Arterial Bypass Grafting. *J Am Coll Cardiol*. 66, 1417-1427, 2015.

88. Hamilton C, Steinlechner B, Gruber E, Simon P, Wollenek G. The oxygen dissociation curve: quantifying the shift. *Perfusion*. 19, 141-144, 2004.

89. Han CI, Campbell GR, Campbell JH. Circulating Bone Marrow Cells Can Contribute to Neointimal Formation. *J Vasc Res*. 38, 113-119, 2001.

90. Harnek J, Zoucas E, Carlemalm E, Cwikiel W. Differences in Endothelial Injury After Balloon Angioplasty, Insertion of Balloon-Expanded Stents or Release of Self-Expanding Stents: An Electron Microscopic Experimental Study. *Cardiovasc Intervent Radiol*. 22, 56-61, 1999.

91. Haruguchi H, Teraoka S. Intimal hyperplasia and hemodynamic factors in arterial bypass and arteriovenous grafts: a review. *J Artif Organs*. 6, 227-235, 2003.

92. Haude M, Erbel R, Issa H, Meyer J. Quantitative analysis of elastic recoil after balloon angioplasty and after intracoronary implantation of balloon-expandable Palmaz-Schatz stents. *J Am Coll Cardiol*. 21, 26-34, 1993.

93. He Y, Duraiswamy N, Frank AO, Moore JJE. Blood Flow in Stented Arteries: A Parametric Comparison of Strut Design Patterns in Three Dimensions. *J Biomech Eng*. 127, 637-647, 2005.

94. Helmlinger G, Geifer R V, Schreck S, Nerem RM. Effects of pulsatile flow on cultured vascular endothelial cell morphology. *J Biomech Eng*. 113, 123-131, 1991.

95. Heppner BT, Morgan LW. Plasma oxygen permeability may be a factor in atherosclerosis. *J Atheroscler Thromb*. 11, 49-55, 2004.

96. Hill A V. The possible effects of the aggregation of the molecules of haemoglobin on its dissociation curve. *J Physiol*. 41,1910.

97. Hofer M, Rappitsch G, Perktold K, Trubel W, Schima H. Numerical study of wall mechanics and fluid dynamics in end-to-side anastomoses and correlation to intimal hyperplasia. *J Biomech*. 29, 1297-1308, 1996.

98. Holmes Jr DR, Kereiakes DJ, Garg S, et al. Stent Thrombosis. *J Am Coll Cardiol*. 56, 1357-1365, 2010.

99. Holzapfel GA, Ogden RW, Lally C, Prendergast PJ. Simulation of In-stent Restenosis for the Design of Cardiovascular Stents. Springer Berlin Heidelberg;

2006, pp. 255-267.

100. Holzapfel GA, Sommer G, Gasser CT, Regitnig P. Determination of layer-specific mechanical properties of human coronary arteries with nonatherosclerotic intimal thickening and related constitutive modeling. *Am J Physiol Heart Circ Physiol*. 289, H2048-H2058, 2005.

101. Hong M-K, Park S-W, Lee CW, et al. Long-term outcomes of minor plaque prolapsed within stents documented with intravascular ultrasound. *Catheter Cardiovasc Interv*. 51, 22-26, 2000.

102. Houston JG, Bonneau M, Kang C, Stonebridge PA, Dick J. Reducing intimal thickening and arterial wall stresses downstream to a spiral flow inducing stent in a carotid arterial stenosis porcine model. *CIRSE 2008*. 2008.

103. Houston JG, Gandy SJ, Milne W, Dick JBC, Belch JJF, Stonebridge PA. Spiral laminar flow in the abdominal aorta: a predictor of renal impairment deterioration in patients with renal artery stenosis? *Nephrol Dial Transplant*. 19, 1786-1791, 2004.

104. Houston JG, Hood RG, Stonebridge PA, Thomson A. Method of determining the helix angle of a helical formation for a conduit. May 2010.

105. Houston JG, Stonebridge PA, Dick JBC, et al. An insert for a stent. July 2007.

106. Hsu P-P, Li S, Li Y-S, et al. Effects of Flow Patterns on Endothelial Cell Migration into a Zone of Mechanical Denudation. *Biochem Biophys Res Commun*. 285, 751-759, 2001.

107. Huijbregts HJTAM, Blankestijn PJ, Caro CG, et al. A Helical PTFE

Arteriovenous Access Graft to Swirl Flow Across the Distal Anastomosis: Results of a Preliminary Clinical Study. *Eur J Vasc Endovasc Surg*. 33, 472-475, 2007.

108. Inoue T, Croce K, Morooka T, Sakuma M, Node K, Simon DI. Vascular inflammation and repair implications for re-endothelialization, restenosis, and stent thrombosis. *JACC Cardiovasc Interv*. 4, 1057-1066, 2011.

109. Inoue T, Sata M, Hikichi Y, et al. Mobilization of CD34-Positive Bone Marrow-Derived Cells After Coronary Stent Implantation. *Circulation*. 115, 553-561, 2007.

110. Jang IK, Tearney G, Bouma B. Visualization of tissue prolapse between coronary stent struts by optical coherence tomography: comparison with intravascular ultrasound. *Circulation*. 104, 2754, 2001.

111. Jiménez J, Davies PF. Hemodynamically Driven Stent Strut Design. *Ann Biomed Eng*. 37, 1483-1494, 2009.

112. Johnson K, Sharma P, Oshinski J. Coronary Artery Flow Measurement Using Navigator Echo Gated Phase Contrast Magnetic Resonance Velocity Mapping at 3.0 Tesla. 41, 595-602, 2008.

113. Joner M, Finn A V, Farb A, et al. Pathology of drug-eluting stents in humans: delayed healing and late thrombotic risk. *J Am Coll Cardiol*. 48, 193-202, 2006.

114. Joner M, Nakazawa G, Finn A V., et al. Endothelial Cell Recovery Between Comparator Polymer-Based Drug-Eluting Stents. *J Am Coll Cardiol*. 52, 333-342, 2008.

115. Jung H, Choi JW, Park CG. Asymmetric flows of non-Newtonian fluids in symmetric stenosed artery. *Korea Aust Rheol J*. 16, 101-108, 2004.

116. Kaazempur-Mofrad MR, Ethier CR. Mass transport in an anatomically realistic human right coronary artery. *Ann Biomed Eng*. 29, 121-127, 2001.

117. Kaazempur-Mofrad MR, Wada S, Myers JG, Ethier CR. Mass transport and fluid flow in stenotic arteries: Axisymmetric and asymmetric models. *Int J Heat Mass Transf*. 48, 4510-4517, 2005.

118. Kastrati A, Mehilli J, Dirschinger J, et al. Restenosis after coronary placement of various stent types. *Am J Cardiol*. 87, 34-39, 2001.

119. Kilner PJ, Yang GZ, Mohiaddin RH, Firmin DN, Longmore DB. Helical and retrograde secondary flow patterns in the aortic arch studied by three-directional magnetic resonance velocity mapping. *Circulation*. 88, 2235-2247, 1993.

120. Kim MS, Dean LS. In-stent restenosis. *Cardiovasc Ther*. 29, 190-198, 2011.

121. Kleinstreuer C. *Biofluid Dynamics: Principles and Selected Applications*. Taylor & Francis Group ; 2006, .

122. Kleinstreuer C, Hyun S, Buchanan JR, Longest PW, Archie JP, Truskey GA. Hemodynamic parameters and early intimal thickening in branching blood vessels. *Crit Rev Biomed Eng*. 29, 1-64, 2001.

123. Koenig W, Khuseyinova N. Biomarkers of atherosclerotic plaque instability and rupture. *Arterioscler Thromb Vasc Biol*. 27, 15-26, 2007.

124. Kolandavel MK, Fruend E-T, Ringgaard S, Walker PG. The effects of time

varying curvature on species transport in coronary arteries. *Ann Biomed Eng*. 34, 1820-1832, 2006.

125. Krone RJ, Rao S V, Dai D, et al. Acceptance, panic, and partial recovery the pattern of usage of drug-eluting stents after introduction in the U.S. (a report from the American College of Cardiology/National Cardiovascular Data Registry). *JACC Cardiovasc Interv*. 3, 902-910, 2010.

126. Krüger T. Effect of tube diameter and capillary number on platelet margination and near-wall dynamics. *Rheol Acta*. 55, 511-526, 2016.

127. Ku DN. Blood flow in arteries. *Annu Rev Fluid Mech*. 29, 399-434, 1997.

128. Ku DN, Giddens DP, Zarins CK, Glagov S. Pulsatile flow and atherosclerosis in the human carotid bifurcation. Positive correlation between plaque location and low oscillating shear stress. *Arteriosclerosis*. 5, 293-302, 1985.

129. Kute SM, Vorp DA. The effect of proximal artery flow on the hemodynamics at the distal anastomosis of a vascular bypass graft: computational study. *J Biomech Eng*. 123, 277-283, 2001.

130. LaDisa Jr. JF, Guler I, Olson L, et al. Three-Dimensional Computational Fluid Dynamics Modeling of Alterations in Coronary Wall Shear Stress Produced by Stent Implantation. *Ann Biomed Eng*. 31, 972-980, 2003.

131. LaDisa Jr. JF, Hettrick D a, Olson LE, et al. Stent implantation alters coronary artery hemodynamics and wall shear stress during maximal vasodilation. *J Appl Physiol*. 93, 1939-1946, 2002.

132. LaDisa Jr. JF, Olson LE, Guler I, et al. Stent design properties and deployment

ratio influence indexes of wall shear stress: a three-dimensional computational fluid dynamics investigation within a normal artery. *J Appl Physiol*. 97, 424-430, 2004.

133. LaDisa Jr. JF, Olson L, Hettrick D, Warltier D, Kersten J, Pagel P. Axial stent strut angle influences wall shear stress after stent implantation: analysis using 3D computational fluid dynamics models of stent foreshortening. *Biomed Eng Online*. 4, 59, 2005.

134. Lee ES, Bauer GE, Caldwell MP, Santilli SM. Association of artery wall hypoxia and cellular proliferation at a vascular anastomosis. *J Surg Res*. 91, 32-37, 2000.

135. Lee ES, Caldwell MP, Tretinyak a S, Santilli SM. Supplemental oxygen controls cellular proliferation and anastomotic intimal hyperplasia at a vascular graft-to-artery anastomosis in the rabbit. *J Vasc Surg Off Publ Soc Vasc Surg [and] Int Soc Cardiovasc Surgery, North Am Chapter*. 33, 608-613, 2001.

136. Lei M, Kleinstreuer C, Truskey GA. A focal stress gradient-dependent mass transfer mechanism for atherogenesis in branching arteries. *Med Eng Phys*. 18, 326-332, 1996.

137. Leung DY, Glagov S, Mathews MB. Cyclic stretching stimulates synthesis of matrix components by arterial smooth muscle cells in vitro. *Science (80-).* 191, 475-477, 1976.

138. Li Y, Neoh KG, Kang E-T. Plasma protein adsorption and thrombus formation on surface functionalized polypyrrole with and without electrical stimulation. *J Colloid Interface Sci*. 275, 488-495, 2004.

139. Lima R, Ishikawa T, Imai Y, Takeda M, Wada S, Yamaguchi T. Radial dispersion of red blood cells in blood flowing through glass capillaries: the role of hematocrit and geometry. *J Biomech*. 41, 2188-2196, 2008.

140. Liu X, Fan Y, Deng X. Effect of Spiral Flow on the Transport of Oxygen in the Aorta: A Numerical Study. *Ann Biomed Eng*. 38, 917-926, 2010.

141. Liu X, Pu F, Fan Y, Deng X, Li D, Li S. A numerical study on the flow of blood and the transport of LDL in the human aorta: the physiological significance of the helical flow in the aortic arch. *Am J Physiol Hear Circ Physiol*. 297, 163-170, 2009.

142. Ma P, Li X, Ku DN. Convective mass transfer at the carotid bifurcation. *J Biomech*. 30, 565-571, 1997.

143. Ma P, Li X, Ku DN. Convective mass transfer at the carotid bifurcation. *J Biomech*. 30, 565-571, 1997.

144. Malek AM, Alper SL, Izumo S. Hemodynamic Shear Stress and Its Role in Atherosclerosis. *JAMA J Am Med Assoc*. 282, 2035-2042, 1999.

145. Malek AM, Izumo S. Mechanism of endothelial cell shape change and cytoskeletal remodeling in response to fluid shear stress. *J Cell Sci*. 109 (Pt 4), 713-726, 1996.

146. Mallinger F, Drikakis D. Laminar-to-turbulent transition in pulsatile flow through a stenosis. *Biorheology*. 39, 437-441, 2002.

147. Mani G, Feldman MD, Patel D, Agrawal CM. Coronary stents: A materials perspective. *Biomaterials*. 28, 1689-1710, 2007.

148. Marinelli R, Furst B, van der Zee H, McGinn A, Marinelli W. The heart is not a pump: A refutation of the pressure propulsion premise of heart function. *Front Perspect*. 5, 15–24, 1995.

149. Marinelli R, Penney DG, Marinelli W, Baciewicz Jr. FA. Rotary motion in the heart and blood vessels: A review. *J Appl Cardiol*. 6, 421-431, 1991.

150. Martin DM. Sequential Structural and Fluid Dynamics Analysis of Balloon-Expandable Coronary Stents: A Multivariable Statistical Analysis. 2015.

151. Martin DM, Boyle FJ. Drug-Eluting Stents for Coronary Artery Disease : a Review. *Med Eng Phys*. 33, 148-163, 2011.

152. Martin DM, Boyle FJ. Finite element analysis of balloon-expandable coronary stent deployment: Influence of angioplasty balloon configuration. *Int j numer method biomed eng*. 29, 1161-1175, 2013.

153. Martin DM, Murphy EA, Boyle FJ. Computational fluid dynamics analysis of balloon-expandable coronary stents: influence of stent and vessel deformation. *Med Eng Phys*. 36, 1047-1056, 2014.

154. Martini F, Nath JL, Bartholomew EF. *Fundamentals of Anatomy & Physiology*. San Francisco: Benjamin Cummings; 2012, .

155. Massai D, Soloperto G, Gallo D, Xu XY, Morbiducci U. Shear-induced platelet activation and its relationship with blood flow topology in a numerical model of stenosed carotid bifurcation. *Eur J Mech B/Fluids*. 35, 92-101, 2012.

156. Mayr M, Sidibe A, Zampetaki A. The Paradox of Hypoxic and Oxidative Stress in Atherosclerosis**Editorials published in the Journal of the American College

of Cardiology reflect the views of the authors and do not necessarily represent the views of JACC or the American College of Cardio. *J Am Coll Cardiol*. 51, 1266-1267, 2008.

157. Mayr M, Sidibe A, Zampetaki A. The paradox of hypoxic and oxidative stress in atherosclerosis. *J Am Coll Cardiol*. 51, 1266-1267, 2008.

158. Mclaren M. Endothelium II : inflammatory response. *Vasc Dis*. , 1-6, 2005.

159. Mehran R, Dangas G, Abizaid AS, et al. Angiographic Patterns of In-Stent Restenosis : Classification and Implications for Long-Term Outcome. *Circulation*. 100, 1872-1878, 1999.

160. Moazzam F, DeLano F a, Zweifach BW, Schmid-Schönbein GW. The leukocyte response to fluid stress. *Proc Natl Acad Sci U S A*. 94, 5338-5343, 1997.

161. Mohamied Y, Rowland EM, Bailey EL, Sherwin SJ, Schwartz MA, Weinberg PD. Change of Direction in the Biomechanics of Atherosclerosis. *Ann Biomed Eng*. 43, 16-25, 2014.

162. Moore JA, Ethier CR. Oxygen mass transfer calculations in large arteries. *J Biomech Eng*. 119, 469-475, 1997.

163. Moore JJE, Soares J, Rajagopal K. Biodegradable Stents: Biomechanical Modeling Challenges and Opportunities. *Cardiovasc Eng Technol*. 1, 52-65, 2010.

164. Morbiducci U, Ponzini R, Grigioni M, Redaelli A. Helical flow as fluid dynamic signature for atherogenesis risk in aortocoronary bypass. A numeric study. *J Biomech*. 40, 519-534, 2007.

165. Morbiducci U, Ponzini R, Nobili M, et al. Blood damage safety of prosthetic heart valves. Shear-induced platelet activation and local flow dynamics: a fluid-structure interaction approach. *J Biomech*. 42, 1952-1960, 2009.

166. Morbiducci U, Ponzini R, Rizzo G, et al. Mechanistic insight into the physiological relevance of helical blood flow in the human aorta: an in vivo study. *Biomech Model Mechanobiol*. 10, 339-355, 2011.

167. Mortier P, Holzapfel GA, De Beule M, et al. A novel simulation strategy for stent insertion and deployment in curved coronary bifurcations: Comparison of three drug-eluting stents. *Ann Biomed Eng*. 38, 88-99, 2010.

168. Motomiya M, Karino T. Flow patterns in the human carotid artery bifurcation. *Stroke*. 15, 50-56, 1984.

169. Motterlini R, Kerger H, Green CJ, Winslow RM, Intaglietta M. Depression of endothelial and smooth muscle cell oxygen consumption by endotoxin. *Am J Physiol*. 275, H776-H782, 1998.

170. Murphy BP, Savage P, McHugh PE, Quinn DF. The stress-strain behavior of coronary stent struts is size dependent. *Ann Biomed Eng*. 31, 686-691, 2003.

171. Murphy EA, Boyle FJ. Reducing in-stent restenosis through novel stent flow field augmentation. *Cardiovasc Eng Technol*. 3, 353-373, 2012.

172. Murphy JB, Boyle FJ. A full-range, multi-variable, CFD-based methodology to identify abnormal near-wall hemodynamics in a stented coronary artery. *Biorheology*. 47, 117-132, 2010.

173. Murphy JB, Boyle FJ. A Numerical Methodology to Fully Elucidate the Altered

Wall Shear Stress in a Stented Coronary Artery. *Cardiovasc Eng Technol*. 1, 256-268, 2010.

174. Naeraa N, Petersen ES, Boye E, et al. pH and molecular CO2 components of the Bohr effect in human blood. *Scand J Clin Lab Invest*. 18, 96-102, 1966.

175. Naghavi M, Libby P, Falk E, et al. From Vulnerable Plaque to Vulnerable Patient: A Call for New Definitions and Risk Assessment Strategies: Part I . *Circ* . 108, 1664-1672, 2003.

176. Nakamura M, Yock PG, Bonneau HN, et al. Impact of Peri-Stent Remodeling on Restenosis : A Volumetric Intravascular Ultrasound Study. *Circulation*. 103, 2130-2132, 2001.

177. Nakazawa G, Otsuka F, Nakano M, et al. The pathology of neoatherosclerosis in human coronary implants: Bare-metal and drug-eluting stents. *J Am Coll Cardiol*. 57, 1314-1322, 2011.

178. National Institute for Health and Care Excellence. Early management of unstable angina and NSTEMI. *NICE Pathways*. 2015.

179. National Institute for Health and Care Excellence. *Managing Stable Angina*.; 2015, .

180. National Institute for Health and Care Excellence. *Guidance on the Use of Coronary Artery Stents*.; 2003, .

181. National Institute for Health and Care Excellence. *Drug-Eluting Stents for the Treatment of Coronary Artery Disease*.; 2008, .

182. Nebeker JR, Virmani R, Bennett CL, et al. Hypersensitivity cases associated with drug-eluting coronary stents: A review of available cases from the Research on Adverse Drug Events and Reports (RADAR) project. *J Am Coll Cardiol*. 47, 175-181, 2006.

183. Nelson R. Spiral Flow. 2011.

184. Newman VS, Berry JL, Routh WD, Ferrario CM, Dean RH. Effects of vascular stent surface area and hemodynamics on intimal thickening. *J Vasc Interv Radiol*. 7, 387-393, 1996.

185. Niccoli G, Sgueglia GA, Crea F. The emerging role of allergic inflammation in adverse reactions after coronary stent implantation. *Atherosclerosis*. 217, 70-71, 2011.

186. Padfield GJ, Newby DE, Mills NL. Understanding the role of endothelial progenitor cells in percutaneous coronary intervention. *J Am Coll Cardiol*. 55, 1553-1565, 2010.

187. Papadaki M, McIntire L V, Eskin SG. Effects of shear stress on the growth kinetics of human aortic smooth muscle cells in vitro. *Biotechnol Bioeng*. 50, 555-561, 1996.

188. Papafaklis MI, Bourantas C V, Theodorakis PE, Katsouras CS, Fotiadis DI, Michalis LK. Relationship of shear stress with in-stent restenosis: bare metal stenting and the effect of brachytherapy. *Int J Cardiol*. 134, 25-32, 2009.

189. Papaharilaou Y, Doorly DJ, Sherwin SJ. The influence of out-of-plane geometry on pulsatile flow within a distal end-to-side anastomosis. *J Biomech*. 35, 1225-

1239, 2002.

190. Park SJ, Kang SJ, Virmani R, Nakano M, Ueda Y. In-stent neoatherosclerosis: A final common pathway of late stent failure. *J Am Coll Cardiol*. 59, 2051-2057, 2012.

191. Paul MC, Larman A. Investigation of spiral blood flow in a model of arterial stenosis. *Med Eng Phys*. 31, 1195-1203, 2009.

192. Paul RJ. Smooth muscle energetics and theories of cross-bridge regulation. *Am J Physiol - Cell Physiol*. 258, C369-C375, 1990.

193. Perktold K, Leuprecht A, Prosi M, et al. Fluid Dynamics, Wall Mechanics, and Oxygen Transfer in Peripheral Bypass Anastomoses. *Ann Biomed Eng*. 30, 447-460, 2002.

194. Perktold K, Rappitsch G. Computer simulation of local blood flow and vessel mechanics in a compliant carotid artery bifurcation model. *J Biomech*. 28, 845-856, 1995.

195. Phelps JE, DePaola N. Spatial variations in endothelial barrier function in disturbed flows in vitro. *Am J Physiol - Hear Circ Physiol*. 278, H469-H476, 2000.

196. Phillips RJ, Armstrong RC, Brown RA, Graham AL, Abbott JR. A constitutive equation for concentrated suspensions that accounts for shear-induced particle migration. *Phys Fluids A*. 41992.

197. Pittman RN. *Oxygen Transport in the Microcirculation and Its Regulation*. Vol 20. 2013, .

198. Pittman RN. Regulation of tissue oxygenation. *Colloq Ser Integr Syst Physiol From Mol to Funct*. 3, 1-100, 2011.

199. Ponde CK, Aroney CN, McEniery PT, Bett JHN. Plaque prolapse between the struts of the intracoronary Palmaz-Schatz stent: Report of two cases with a novel treatment of this unusual problem. *Cathet Cardiovasc Diagn*. 40, 353-357, 1997.

200. Popel AS. Theory of oxygen transport to tissue. *Crit Rev Biomed Eng*. 17, 257-321, 1989.

201. Pritchard WF, Davies PF, Derafshi Z, et al. Effects of wall shear stress and fluid recirculation on the localization of circulating monocytes in a three-dimensional flow model. *J Biomech*. 28, 1459-1469, 1995.

202. Qiu Y, Tarbell JM. Numerical simulation of pulsatile flow in a compliant curved tube model of a coronary artery. *J Biomech Eng*. 122, 77-85, 2000.

203. Qiu Y, Tarbell JM. Numerical Simulation of Oxygen Mass Transfer in a Compliant Curved Tube Model of a Coronary Artery. *Ann Biomed Eng*. 28, 26-38, 2000.

204. Rappitsch G, Perktold K, Pernkopf E. Numerical Modelling of Shear-Dependent Mass Transfer in Large Arteries. 857, 847-857, 1997.

205. Resnick N, Yahav H, Shay-Salit A, et al. Fluid shear stress and the vascular endothelium: for better and for worse. *Prog Biophys Mol Biol*. 81, 177-199, 2003.

206. Richardson RB. Age-dependent changes in oxygen tension, radiation dose and sensitivity within normal and diseased coronary arteries-Part B: modeling oxygen

diffusion into vessel walls. *Int J Radiat Biol*. 84, 849-857, 2008.

207. Rogers C, Edelman ER. Endovascular Stent Design Dictates Experimental Restenosis and Thrombosis. *Circ* . 91, 2995-3001, 1995.

208. Rogers C, Parikh S, Seifert P, Edelman ER. Endogenous Cell Seeding: Remnant Endothelium After Stenting Enhances Vascular Repair. *Circulation*. 94, 2909-2914, 1996.

209. Rogers C, Tseng DY, Squire JC, Edelman ER. Balloon-Artery Interactions During Stent Placement : A Finite Element Analysis Approach to Pressure, Compliance, and Stent Design as Contributors to Vascular Injury. *Circ Res*. 84, 378-383, 1999.

210. Ross R, Glomset JA. The Pathogenesis of Atherosclerosis. *N Engl J Med*. 295, 369-377, 1976.

211. Rouleau L, Copland IB, Tardif J-C, Mongrain R, Leask RL. Neutrophil adhesion on endothelial cells in a novel asymmetric stenosis model: effect of wall shear stress gradients. *Ann Biomed Eng*. 38, 2791-2804, 2010.

212. Rouleau L, Farcas M, Tardif J-C, Mongrain R, Leask RL. Endothelial cell morphologic response to asymmetric stenosis hemodynamics: effects of spatial wall shear stress gradients. *J Biomech Eng*. 132, 81013, 2010.

213. Rouleau L, Rossi J, Leask RL. The response of human aortic endothelial cells in a stenotic hemodynamic environment: effect of duration, magnitude, and spatial gradients in wall shear stress. *J Biomech Eng*. 132, 71015, 2010.

214. Rubanyi G. The role of endothelium in cardiovascular homeostasis and diseases.

J Cardiovasc Pharmacol. 1993.

215. Rydberg EK, Salomonsson L, Hultén LM, et al. Hypoxia increases 25-hydroxycholesterol-induced interleukin-8 protein secretion in human macrophages. *Atherosclerosis*. 170, 245-252, 2003.

216. Sanada J-I, Matsui O, Yoshikawa J, Matsuoka T. An experimental study of endovascular stenting with special reference to the effects on the aortic vasa vasorum. *Cardiovasc Intervent Radiol*. 21, 45-49, 1998.

217. Santilli SM, Stevens RB, Anderson JG, Payne WD, Caldwell MD. Transarterial wall oxygen gradients at the dog carotid bifurcation. *Am J Physiol - Hear Circ Physiol*. 268, H155-H161, 1995.

218. Santilli SM, Tretinyak a S, Lee ES. Transarterial wall oxygen gradients at the deployment site of an intra-arterial stent in the rabbit. *Am J Physiol Heart Circ Physiol*. 279, H1518-25, 2000.

219. Scheinert D, Scheinert S, Sax J, et al. Prevalence and clinical impact of stent fractures after femoropopliteal stenting. *J Am Coll Cardiol*. 45, 312-315, 2005.

220. Schillinger M, Sabeti S, Loewe C, et al. Balloon angioplasty versus implantation of nitinol stents in the superficial femoral artery. *N Engl J Med*. 354, 1879-1888, 2006.

221. Schoephoerster RT, Oynes F, Nunez G, Kapadvanjwala M, Dewanjee MK. Effects of local geometry and fluid dynamics on regional platelet deposition on artificial surfaces. *Arterioscler Thromb Vasc Biol*. 13, 1806–1813, 1993.

222. Segadal L, Matre K. Blood velocity distribution in the human ascending aorta.

Circulation. 76, 90-100, 1987.

223. Serruys PW, de Jaegere P, Kiemeneij F, et al. A comparison of balloon-expandable-stent implantation with balloon angioplasty in patients with coronary artery disease. *N Engl J Med*. 331, 489–495, 1994.

224. Shi H-J, Cao A-H, Teng G-J. Seeding Endothelial Progenitor Cells on a Self-expanding Metal Stent: An in Vitro Study. *J Vasc Interv Radiol*. 21, 1061-1065, 2010.

225. Shi Z-D, Abraham G, Tarbell JM. Shear stress modulation of smooth muscle cell marker genes in 2-D and 3-D depends on mechanotransduction by heparan sulfate proteoglycans and ERK1/2. *PLoS One*. 5, e12196, 2010.

226. Shibata M, Ichioka S, Kamiya A. Estimating oxygen consumption rates of arteriolar walls under physiological conditions in rat skeletal muscle. *Am J Physiol Heart Circ Physiol*. 289, H295-H300, 2005.

227. Shigematsu K, Yasuhara H, Shigematsu H, Muto T. Direct and indirect effects of pulsatile shear stress on the smooth muscle cell. *Int Angiol a J Int Union Angiol*. 19, 39-46, 2000.

228. Shinke T, Robinson K, Burke MG, et al. Abstract 6059: Novel Helical Stent Design Elicits Swirling Blood Flow Pattern And Inhibits Neointima Formation In Porcine Carotid Arteries. *Circulation*. 118, S_1054-, 2008.

229. Shoeb M, Fang MC. Assessing Bleeding Risk in Patients Taking Anticoagulants. *J Thromb Thrombolysis*. 35, 312-319, 2013.

230. Sigwart U, Puel J, Mirkovitch V, Joffre F, Kappenberger L. Intravascular Stents

to Prevent Occlusion and Re-Stenosis after Transluminal Angioplasty. *N Engl J Med*. 316, 701-706, 1987.

231. Simanonok JP. Non-ischemic hypoxia of the arterial wall is a primary cause of atherosclerosis. *Med Hypotheses*. 46, 155-161, 1996.

232. Simper D, Stalboerger PG, Panetta CJ, Wang S, Caplice NM. Smooth Muscle Progenitor Cells in Human Blood. *Circulation*. 106, 1199-1204, 2002.

233. Sipahi I, Akay MH, Dagdelen S, Blitz A, Alhan C. Coronary Artery Bypass Grafting vs Percutaneous Coronary Intervention and Long-term Mortality and Morbidity in Multivessel Disease: Meta-analysis of Randomized Clinical Trials of the Arterial Grafting and Stenting Era. *JAMA Intern Med*. 174, 223-230, 2013.

234. Sprague EA, Luo J, Palmaz JC. Human Aortic Endothelial Cell Migration onto Stent Surfaces under Static and Flow Conditions. *J Vasc Interv Radiol*. 8, 83-92, 1997.

235. Sprague EA, Palmaz JC. A Model System to Assess Key Vascular Responses to Biomaterials. *J Endovasc Ther*. 12, 594-604, 2005.

236. Spranger K, Capelli C, Bosi GM, Schievano S, Ventikos Y. Comparison and Calibration of a Real- time Virtual Stenting Algorithm Using Finite Element Analysis and Genetic Algorithms. *Comput Methods Appl Mech Eng*. 293, 462-480, 2015.

237. Stangeby DK, Ethier CR. Computational analysis of coupled blood-wall arterial LDL transport. *J Biomech Eng*. 124, 1-8, 2002.

238. Stary HC, Chandler AB, Dinsmore RE, et al. A Definition of Advanced Types of

Atherosclerotic Lesions and a Histological Classification of Atherosclerosis: A Report From the Committee on Vascular Lesions of the Council on Arteriosclerosis, American Heart Association . *Circ* . 92, 1355-1374, 1995.

239. Sterpetti A V, Cucina A, Fragale A, Lepidi S, Cavallaro A, Santoro-D'Angelo L. Shear stress influences the release of platelet derived growth factor and basic fibroblast growth factor by arterial smooth muscle cells. *Eur J Vasc Surg*. 8, 138-142, 1994.

240. Stone GW, Moses JW, Ellis SG, et al. Safety and efficacy of sirolimus- and paclitaxel-eluting coronary stents. *N Engl J Med*. 356, 998-1008, 2007.

241. Stonebridge PA, Brophy C. Spiral laminar flow in arteries? *Lancet*. 338, 1360–1361, 1991.

242. Stonebridge PA, Buckley C, Thompson A, et al. Non spiral and spiral (helical) flow patterns in stenoses. In vitro observations using spin and gradient echo magnetic resonance imaging (MRI) and computational fluid dynamics modeling. *Int Angiol*. 23, 276-283, 2004.

243. Stonebridge PA, Buckley C, Thompson A, et al. Non spiral and spiral (helical) flow patterns in stenoses. In vitro observations using spin and gradient echo magnetic resonance imaging (MRI) and computable fluid dynamics modeling. *Int Angiol*. 23, 276-283, 2004.

244. Stonebridge PA, Ch M. Three-Dimensional Blood Flow Dynamics : Spiral / Helical Laminar Flow. *Methodist Debakey Cardiovasc J*. 7, 21-26, 2011.

245. Stonebridge PA, Hoskins PR, Allan P, Belch J, others. Spiral laminar flow in

vivo. *Clin Sci*. 91, 17–22, 1996.

246. Sumagin R, Lamkin-Kennard KA, Sarelius IH. A separate role for ICAM-1 and fluid shear in regulating leukocyte interactions with straight regions of venular wall and venular convergences. *Microcirculation*. 16, 508–520, 2009.

247. Suo J. Investigation of Blood Flow Patterns and Hemodynamics in the Human Ascending Aorta and Major Trucks of the Right and Left Coronary Arteries using Magnetic resonance Imaging and Computational Fluid Dynamics. *Biomed Eng (NY)*. Ph.D.2005.

248. Tada S. Numerical study of oxygen transport in a carotid bifurcation. *Phys Med Biol*. 55, 3993-4010, 2010.

249. Tada S, Tarbell JM. A computational study of flow in a compliant carotid bifurcation–stress phase angle correlation with shear stress. *Ann Biomed Eng*. 33, 1202-1212, 2005.

250. Tada S, Tarbell JM. Oxygen mass transport in a compliant carotid bifurcation model. *Ann Biomed Eng*. 34, 1389-1399, 2006.

251. Tammareddi S, Sun G, Li Q. Multiobjective robust optimization of coronary stents. *Jmade*. 90, 682-692, 2016.

252. Tarbell JM. Mass transport in arteries and the localization of atherosclerosis. *Annu Rev Biomed Eng*. 5, 79-118, 2003.

253. Tarbell JM, Qiu Y. Arterial wall mass transport: the possible role of blood phase resistance in the localization of arterial disease. Vol (Bronzino EJD, ed.). Boca Raton: CRC Press LLC; 2000, .

254. Tarbell JM, Shi Z-D, Dunn J, Jo H. Fluid Mechanics, Arterial Disease, and Gene Expression. *Annu Rev Fluid Mech*. 46, 591-614, 2014.

255. Tardy Y, Resnick N, Nagel T, Gimbrone Jr MA, Dewey Jr CF. Shear Stress Gradients Remodel Endothelial Monolayers in Vitro via a Cell Proliferation-Migration-Loss Cycle. *Arter Thromb Vasc Biol*. 17, 3102-3106, 1997.

256. Texon M. Hemodynamic Basis of Atherosclerosis with Critique of the Cholesterol-Heart Disease Hypothesis. *Cardiovasc Eng An Int J*. 1, 57-58, 2001.

257. Torrent-Guasp F, Ballester M, Buckberg GD, et al. Spatial orientation of the ventricular muscle band: physiologic contribution and surgical implications. *J Thorac Cardiovasc Surg*. 122, 389-392, 2001.

258. Tsai AG, Cabrales P, Intaglietta M. The physics of oxygen delivery: facts and controversies. *Antioxidants Redox Signal*. 12, 683-691, 2010.

259. Tsai AG, Johnson PC, Intaglietta M. Oxygen gradients in the microcirculation. *Physiol Rev*. 83, 933-963, 2003.

260. Ueba H, Kawakami M, Yaginuma T. Shear Stress as an Inhibitor of Vascular Smooth Muscle Cell Proliferation : Role of Transforming Growth Factor-Beta1 and Tissue-Type Plasminogen Activator. *Arterioscler Thromb Vasc Biol*. 17, 1512-1516, 1997.

261. Vadapalli A, Pittman RN, Popel AS. Estimating oxygen transport resistance of the microvascular wall. *Am J Physiol Heart Circ Physiol*. 279, H657-71, 2000.

262. Vavuranakis M, Sigala F, Vrachatis D a, et al. Quantitative analysis of carotid plaque vasa vasorum by CEUS and correlation with histology after

endarterectomy. *Vasa*. 42, 184-195, 2013.

263. Vermassen F, Stonebridge PA. Spiral laminar flow arterial grafts: improved early clinical results and theoretical basis. *36th Annu Symp Vasc Endovasc Issues*. 2008.

264. Veryan. Veryan Medical Ltd - Anatomy of the BioMimics 3D vascular biomimetic stent. 2014.

265. Virmani R, Guagliumi G, Farb A, et al. Localized Hypersensitivity and Late Coronary Thrombosis Secondary to a Sirolimus-Eluting Stent: Should We Be Cautious? *Circulation*. 109, 701-705, 2004.

266. Wang H, Yan S, Chai H, et al. Shear stress induces endothelial transdifferentiation from mouse smooth muscle cells. *Biochem Biophys Res Commun*. 346, 860-865, 2006.

267. Whitcher FD. Simulation of in vivo loading conditions of nitinol vascular stent structures. *Comput Struct*. 64, 1005-1011, 1997.

268. White FM. *Fluid Mechanics S1.2*.; 2010, .

269. Wijesinghe M, Perrin K, Ranchord A, Simmonds M, Weatherall M, Beasley R. Routine use of oxygen in the treatment of myocardial infarction: systematic review. *Heart*. 95, 198-202, 2009.

270. Windecker S, Mayer I, De Pasquale G, et al. Stent Coating With Titanium-Nitride-Oxide for Reduction of Neointimal Hyperplasia. *Circulation*. 104, 928-933, 2001.

271. Zabielski L, Mestel a J. Helical flow around arterial bends for varying body mass. *J Biomech Eng*. 122, 135-142, 2000.

272. Zeller T, Gaines PA, Ansel GM, Caro CG. Helical Centerline Stent Improves Patency: Two-Year Results From the Randomized Mimics Trial . *Circ Cardiovasc Interv* . 92016.

273. Zhan F, Fan Y, Deng X. Swirling flow created in a glass tube suppressed platelet adhesion to the surface of the tube: Its implication in the design of small-caliber arterial grafts. *Thromb Res*. 125, 413-418, 2010.

274. Zheng T, Fan Y, Xiong Y, Jiang W, Deng X. Hemodynamic performance study on small diameter helical grafts. *ASAIO J*. 55, 192-199, 2008.

275. Zierenberg JR, Fujioka H, Hirschl RB, Bartlett RH, Grotberg JB. Pulsatile blood flow and oxygen transport past a circular cylinder. *J Biomech Eng*. 129, 202-215, 2007.

APPENDIX A

Validation of ANSYS Software

A.1 Introduction

To validate the accuracy of the WSS values predicted by the ANSYS CFX 15.0 software used in this study Validation Test Case 1 was devised. Validation Test Case 1 compares the normalised velocity profile and WSS values predicted using the ANSYS CFX 15.0 to those calculated from the Blasius solution for laminar flow over a flat plate. In addition to this, Validation Test Case 2 was designed to validate the transport equation used in ANSYS CFX 15.0 to model the oxygen transport in the blood. This validation test case compares the Sh predicted using ANSYS CFX 15.0 to the Lévêque analytical solution of the Graetz-Nusselt problem. First, the boundary layer theory is discussed below followed by the derivation of the boundary layer equations.

A.1.1 Boundary Layer Theory

Consider the 2D incompressible viscous flow over a flat plate, as shown in Figure A.1, where the inlet velocity of the fluid is U_{∞}. This inlet velocity is constant, with no vertical gradient, in the entry region before the fluid meets the leading edge of the flat plate. When the fluid meets the front edge and flows along the flat plate, the fluid particles directly adjacent to its surface are slowed to a stop, because of frictional forces, which numerically is modelled as a “no-slip” boundary condition. The fluid particles neighbouring these particles are then in turn slowed by the viscous force between them and the stationary fluid particles. Each layer of neighbouring fluid particles, with

increasing distance normal to the surface, travels at a slightly higher velocity in comparison with the preceding layer. This results in the characteristic velocity profile, as shown in Figure A.1, with the velocity increasing until it reaches the free-stream velocity, U_∞. The thickness of the boundary layer, δ, is defined as the vertical distance extending from the flat plate surface, where the fluid is stationary, to the point where u is 99% of U_∞. As the flow moves along a flat plate the boundary layer grows with more fluid particles retarded by their neighbouring slower particles. Eventually the boundary layer transitions from laminar to turbulent. To help predict where this transition may occur the Reynolds Number, Re, is used which is defined as the ratio of inertial forces to viscous forces. For a flat plate the local Re at any position, x, along the plate is calculated as follows:

$$Re_x = \frac{\rho U x}{\mu} \tag{A.1}$$

where ρ is the density of the fluid, x is the distance from the leading edge of the plate and μ is the dynamic viscosity of the fluid. The flow within the boundary layer exhibits different characteristics at different Re with approximate ranges and characteristics given in Table A.1.

As listed by White (2010), there are three techniques for analysing flows over a flat plate: CFD, experimentation and boundary layer theory. The third technique, boundary layer theory, was first formulated by Ludwig Prandtl in 1904 and the resulting boundary layer equations were solved, only for laminar flow, by his student Heinrich Blasius in 1908. The derivation of the boundary layer equations is presented below.

Re Range	Description of Flow Characteristics
$0 < Re < 1$	Highly viscous laminar "creeping motion
$1 < Re < 100$	Laminar, strong Re dependence
$100 < Re < 10^3$	Laminar, boundary-layer theory useful
$10^3 < Re < 10^4$	Transition to turbulence
$10^4 < Re < 10^6$	Turbulent, moderate Re dependence
$10^6 < Re < \infty$	Turbulent, slight Re dependence

Table A.1: Re ranges and the flow characteristics exhibited within the boundary layer. Adapted from White (2010).[268]

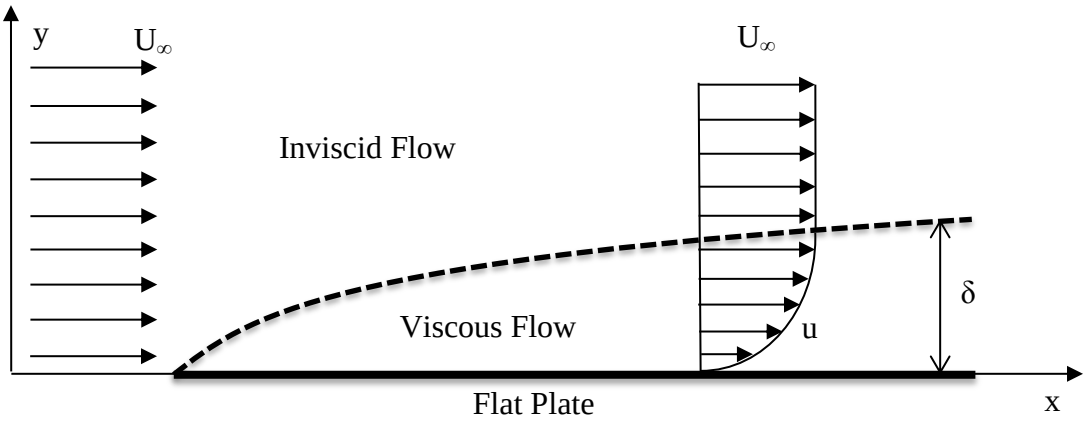

Figure A.1: Typical boundary layer development along a flat plate within a 2D flow example.

Within the boundary layer viscous forces exert an influence over the velocity profile while outside of the boundary layer the flow is considered inviscid where viscous forces are small relative to inertial forces.

A.1.2 Derivation of the Boundary Layer Equations

To analyse the 2D incompressible viscous flow over a flat plate, as described above, the continuity equation and the momentum equations are needed:

$$\frac{\partial u}{\partial x}+\frac{\partial v}{\partial y}=0 \tag{A.2}$$

$$\rho\left(u\frac{\partial u}{\partial x}+v\frac{\partial u}{\partial y}\right)=-\frac{\partial P}{\partial x}+\mu\left(\frac{\partial^2 u}{\partial x^2}+\frac{\partial^2 u}{\partial y^2}\right) \tag{A.3}$$

$$\rho\left(u\frac{\partial v}{\partial x}+v\frac{\partial v}{\partial y}\right)=-\frac{\partial P}{\partial x}+\mu\left(\frac{\partial^2 v}{\partial x^2}+\frac{\partial^2 v}{\partial y^2}\right) \tag{A.4}$$

These should be solved for u, v and P with the imposed typical boundary conditions: no-slip at the plate surface, an inlet velocity, and an outlet zero pressure boundary. To solve these equations is actually too difficult in their present form, so some approximations need to be made. First, Prandtl deduced that if the characteristic Reynolds Number, Re_L, is very large then the shear layer must be very thin resulting in the following approximations:

$$v \ll u \tag{A.5}$$

$$\frac{\partial u}{\partial x} \ll \frac{\partial u}{\partial y} \tag{A.6}$$

$$\frac{\partial v}{\partial x} \ll \frac{\partial v}{\partial y} \tag{A.7}$$

When applied to the y-momentum equation, Equation (A.4), this results in the simplification:

$$\frac{\partial P}{\partial y} \approx 0 \tag{A.8}$$

which essentially means the pressure only varies with respect to x, and the y-momentum equation can be neglected entirely. In the x-momentum equation, Equation (3.57), the pressure gradient term can be calculated using Bernoulli's equation as applied to the outer inviscid flow, i.e.

$$\frac{\partial P}{\partial x} = \frac{dP}{dx} = -\rho U \frac{dU}{dx} \tag{A.9}$$

Additionally, one of the second derivatives within Equation (3.57) can be neglected due to the previous approximations, i.e.

$$\frac{\partial^2 u}{\partial x^2} \ll \frac{\partial^2 u}{\partial y^2} \tag{A.10}$$

All of these assumptions and simplifications results in the three equations of motion being reduced down to Prandtl's two boundary layer equations:

$$\frac{\partial u}{\partial x} + \frac{\partial v}{\partial y} = 0 \tag{A.11}$$

$$u\frac{\partial u}{\partial x} + v\frac{\partial u}{\partial y} \approx U\frac{dU}{dx} + \frac{1}{\rho}\frac{\partial \tau}{\partial y} \tag{A.12}$$

where τ is the shear stress and is given by:

$$\tau = \mu \frac{\partial u}{\partial y} \quad \text{for laminar flow} \tag{A.13}$$

$$\tau = \mu \frac{\partial u}{\partial y} - \rho \overline{u'v'} \quad \text{for turbulent flow} \tag{A.14}$$

where these are solved for u and v, which are both functions of x and y within the boundary layer, with the following boundary conditions imposed:

$$\text{At } y=0 \text{ (flat plate surface)} \qquad u = v = 0 \quad \text{(no-slip condition)} \tag{A.15}$$

At y=δ (outer edge of boundary layer) $u = U(x)$ (A.16)

The boundary layer equations for laminar flow are mathematically parabolic and are solved numerically by beginning at the leading edge and marched downstream.[268] Blasius conceived the analytical solution to the equations in 1908 by showing that the dimensionless velocity profile, u/U, is a function of a single composite dimensionless variable, η:

$$\frac{u}{U} = f'(\eta) \tag{A.17}$$

$$\eta = y\left(\frac{U}{\nu x}\right)^{1/2} \tag{A.18}$$

where the prime denotes differentiation with respect to η, and ν is the kinematic viscosity. Once Equations (A.17) and (A.18) are substituted into the boundary layer equations the problem can be reduced to a single third-order non-linear ordinary differential equation for f:

$$f''' + \frac{1}{2} ff'' = 0 \tag{A.19}$$

where the boundary conditions become:

At y = 0: $f(0) = f'(0) = 0$ (A.20)

As $y \to \infty$: $f'(\infty) \to 1.0$ (A.21)

Equation (A.19) is known as the Blasius equation and can be solved for the velocity profile within the boundary layer.

Based on this solution of the velocity profile within the boundary layer the WSS along the flat plate can also be subsequently predicted. WSS, τ_w, for laminar flow is defined as:

$$\tau_w = \mu \frac{\partial u}{\partial y}_{y=0} \tag{A.22}$$

To put this in terms of η, from Equation (A.17):

$$u = U_\infty f'(\eta) \tag{A.23}$$

$$\frac{\partial u}{\partial \eta} = U_\infty f''(\eta) \tag{A.24}$$

From Equation (A.18):

$$\frac{\partial \eta}{\partial y} = \left(\frac{U_\infty}{\nu x} \right)^{1/2} \tag{A.25}$$

Therefore, using the chain rule:

$$\tau_w = \mu \left(\frac{\partial u}{\partial \eta} \cdot \frac{\partial \eta}{\partial y} \right)_{y=0} = \mu \left(U_\infty f''(\eta) \left(\frac{U_\infty}{\nu x} \right)^{1/2} \right)\Bigg|_{\eta=0} \tag{A.26}$$

From Table A.2: $f''(\eta)$ =0.332 at η=0, and thus, the WSS, $\tau_w(x)$, can be calculated using:

$$\tau_w(x) = \frac{0.332 \rho^{1/2} \mu^{1/2} U^{1.5}}{x^{1/2}} \tag{A.27}$$

η	$f(\eta)$	$f'(\eta)$	$f''(\eta)$
0.00000	0.00000	0.00000	0.33203
0.20000	0.00664	0.06640	0.33196
0.40000	0.02656	0.13275	0.33144
0.60000	0.05973	0.19892	0.33005
0.80000	0.10610	0.26469	0.32736
1.00000	0.16556	0.32975	0.32298
1.50000	0.37011	0.48675	0.30256
2.00000	0.64997	0.62972	0.26674
2.50000	0.99624	0.75121	0.21740
3.00000	1.39671	0.84599	0.16136
3.50000	1.83757	0.91298	0.10777
4.00000	2.30559	0.95546	0.06424
4.50000	2.78995	0.97946	0.03398
5.00000	3.28306	0.99149	0.01591
∞	∞	1	0

Table A.2: Blasius solution in terms of η.

A.2 Validation Test Case 1

In order to validate the ANSYS CFX 15.0 software a validation test case was constructed. The velocity profiles and WSS values along a flat plate predicted by ANSYS CFX 15.0 were compared with the Blasius solution. First, a 3D geometry of a fluid domain with a flat plate along one face was constructed, with dimensions as shown in Figure A.2. The flat plate was 1.0m long with a no-slip boundary condition imposed on the surface. The domain was given a height of 1.6m with an opening boundary

condition placed on the upper surface to allow for unrestricted development of the boundary layer. An entry region was added upstream of the flat plate 0.1m long which ensures the inlet boundary condition does not interfere with the solution along the flat plate. A velocity of 0.5m/s (U_∞) was placed at the inlet and water was used as the domain fluid with a density of 998kg/m^3 and a kinematic viscosity of 8.899×10^{-4} Pa.s. The geometry was discretised using a hexahedral mesh with 85626 nodes as shown in Figure A.3. Inflation mesh refinement was designated at the front edge of, and along, the flat plate to ensure accurate capture of the boundary layer. The convergence criterion for the solution was a maximum residual of 1×10^{-6} with a high resolution advection scheme used.

To compare the results predicted by ANSYS CFX 15.0 and the Blasius solution three variables were analysed: u*, v*, and WSS, where the relevant calculations are shown in Table A.3:

	ANSYS CFX 15.0	Blasius Solution	
u* =	$\frac{u}{U_\infty}$	$f'(\eta)$	(11.1)
v* =	$\frac{v}{\left(\frac{\nu}{U_\infty x}\right)^{1/2} U_\infty}$	$\frac{1}{2}\left(\eta f'(\eta) - f(\eta)\right)$	(11.2)
WSS=	$\mathbf{n}_i \cdot \tau_{ij}$	$\frac{0.332\rho^{1/2}\mu^{1/2}U^{1.5}}{x^{1/2}}$	(11.3)

Table A.3: The relevant calculations for u*, v*, and WSS within ANSYS CFX 15.0 and according to the Blasius solution.

The results were imported into TecPlot 360 2012 for post-processing. Both u* and v* were sampled at three locations at distances 0.25m, 0.50m and 0.75m from the leading edge of the flat plate, and these were compared with the values calculated using the

Blasius solution. Additionally, the WSS predicted by ANSYS CFX 15.0 along the flat plate was compared with the WSS calculated using the Blasius solution. The boundary layer velocity profiles, Figure A.4 and Figure A.5, and the WSS, Figure A.6, predicted by ANSYS CFX 15.0 show good agreement with the Blasius solution. This validates the WSS predicted by ANSYS CFX 15.0 and shows that the program is behaving as expected in this regard.

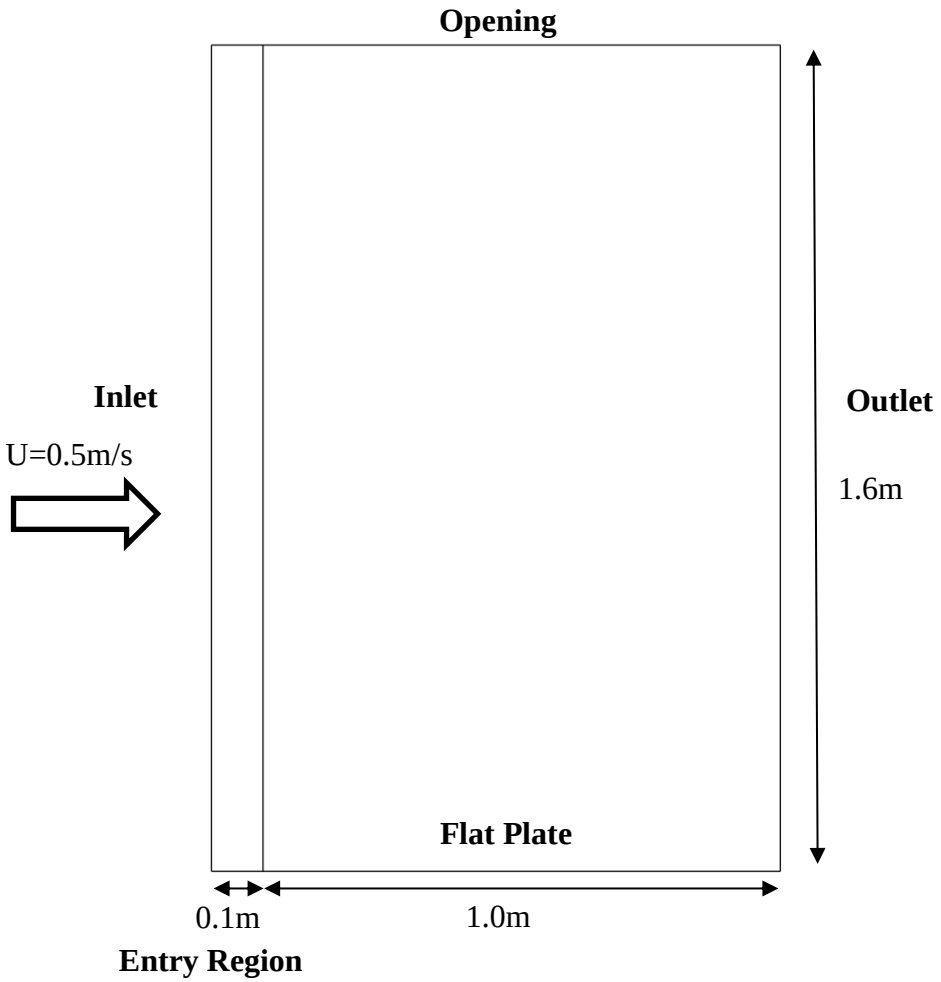

Figure A.2: Details of the computational domain geometry created for Validation Test Case 1.

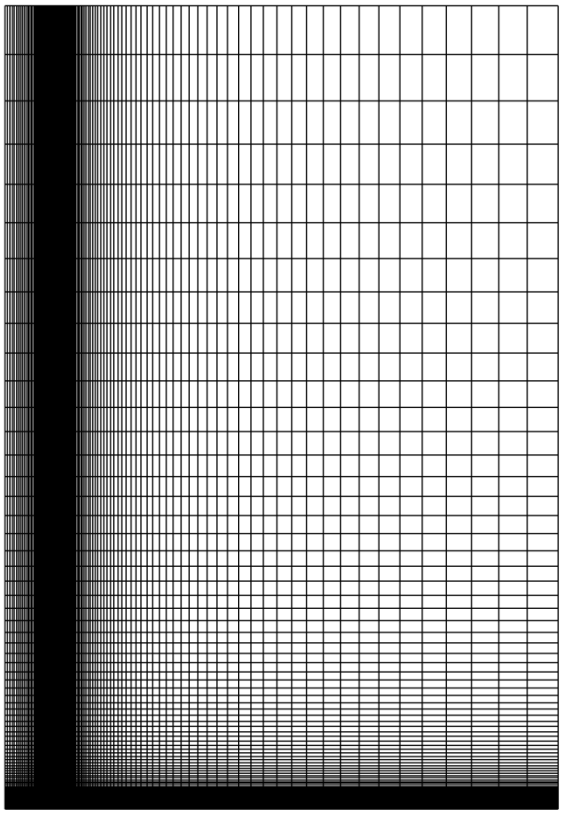

Figure A.3: Mesh created for Validation Test Case 1.

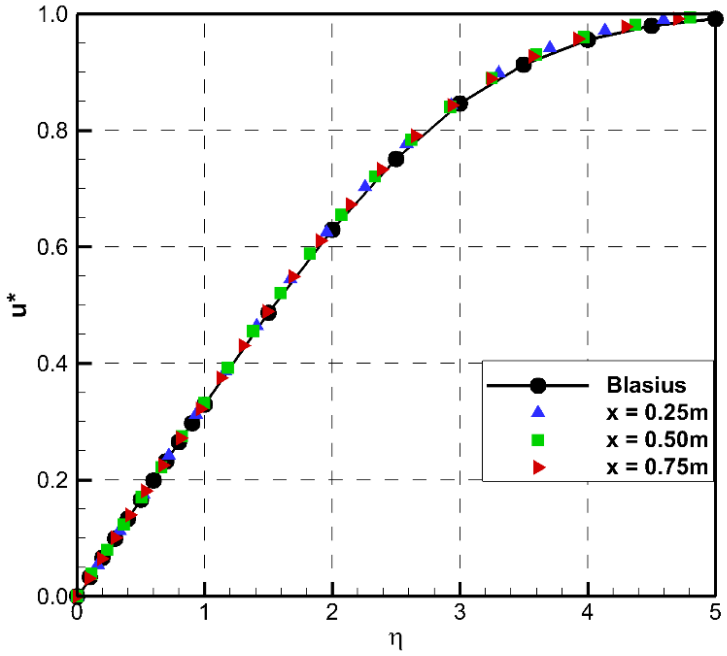

Figure A.4: Boundary layer velocity profiles, u* vs η, predicted by ANSYS CFX 15.0 at three locations with distances from the leading edge of the flat plate of 0.25m, 0.50m and 0.75m. The Blasius solution is shown for comparison.

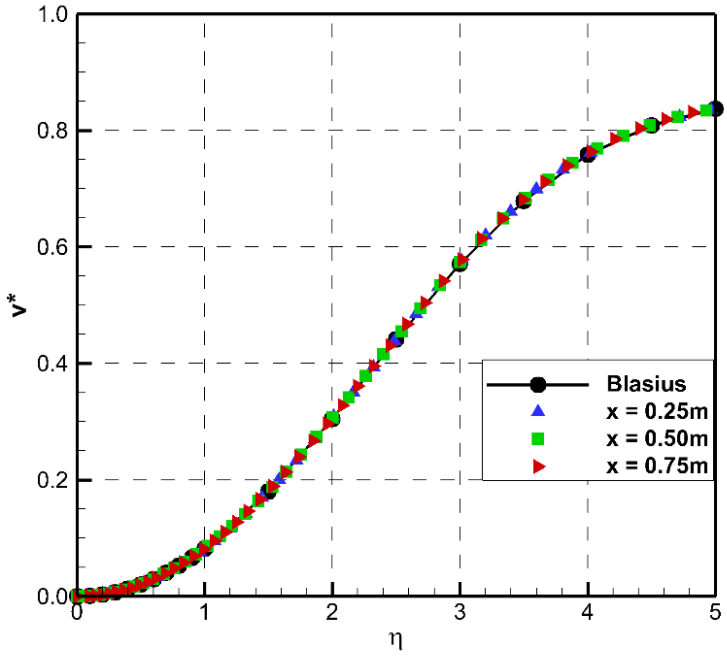

Figure A.5: Boundary layer vertical velocity profiles, v* vs η, predicted by ANSYS CFX 15.0 at three locations with distances from the leading edge of the flat plate of 0.25m, 0.50m and 0.75m. The Blasius solution is shown for comparison.

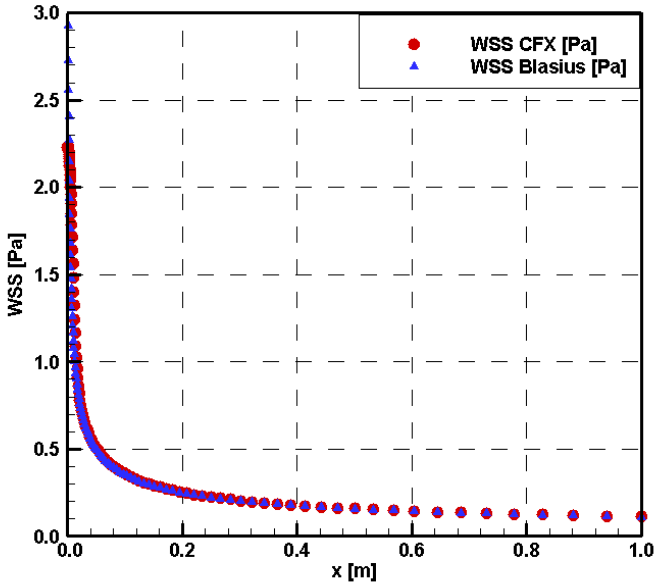

Figure A.6: WSS values predicted along the flat plate by ANSYS CFX 15.0 plotted against the distance from the leading edge of the flat plate, x. The WSS predicted by the Blasius solution is shown for comparison.

A.3 Validation Test Case 2

As a validation of the transport equations used in ANSYS CFX 15.0, results from a simulation of the developing PO_2 boundary layer in a straight tube using Model 5 were compared with the Lévêque analytical solution of the Graetz-Nusselt problem for the development of a thermal boundary layer in a straight tube. This problem is analogous to the developing mass transport boundary layer in fully developed laminar flow in a straight tube. This is a standard validation test case, as used in previous studies, where the local Sh predicted along the tube wall, with a constant PO_2 boundary condition, is compared with the Sh as calculated using the Lévêque analytical solution.[117,248] For the simulation a five degree circumferential wedge of the tube was modelled, as shown in Figure A.7(a). The mesh was generated in ANSYS Meshing with refinement at the start of the tube wall and prism layers inflated off the tube wall to accurately capture the MTBL. The following boundary conditions were applied: a fully-developed Hagen-Poiseuille velocity profile, with mean velocity V_{mean}=0.116m/s, applied at the inlet with $PO_{2,in}$=100mmHg, a zero pressure entrainment at the outlet, and a no-slip boundary condition set on the tube wall with $PO_{2,w}$=0. The diameter of the tube, Dia=2.7mm, is equivalent to the average diameter of the unstented LAD geometries modelled for Test Cases 2 and 3.

The Lévêque solution was calculated based on a Reynolds number Re=75, typical of the left coronary artery, and Sc=3538 as calculated using:

$$Sc = \frac{\mu}{\rho D_b} \tag{A.31}$$

where the dynamic viscosity μ=0.0044Pa.s (volume-averaged for the domain). The Sh for the Lévêque analytical solution was calculated for a constant wall boundary condition using:

$$x^* = \frac{x/Dia}{ReSc} \tag{A.32}$$

$$Sh_{Lévêque} = 1.08(x^*)^{-1/3} \tag{A.33}$$

where x* is a dimensionless axial distance which accounts for differing rates of concentration boundary layer growth due to convection and diffusion[253] and x is the axial distance from the inlet.

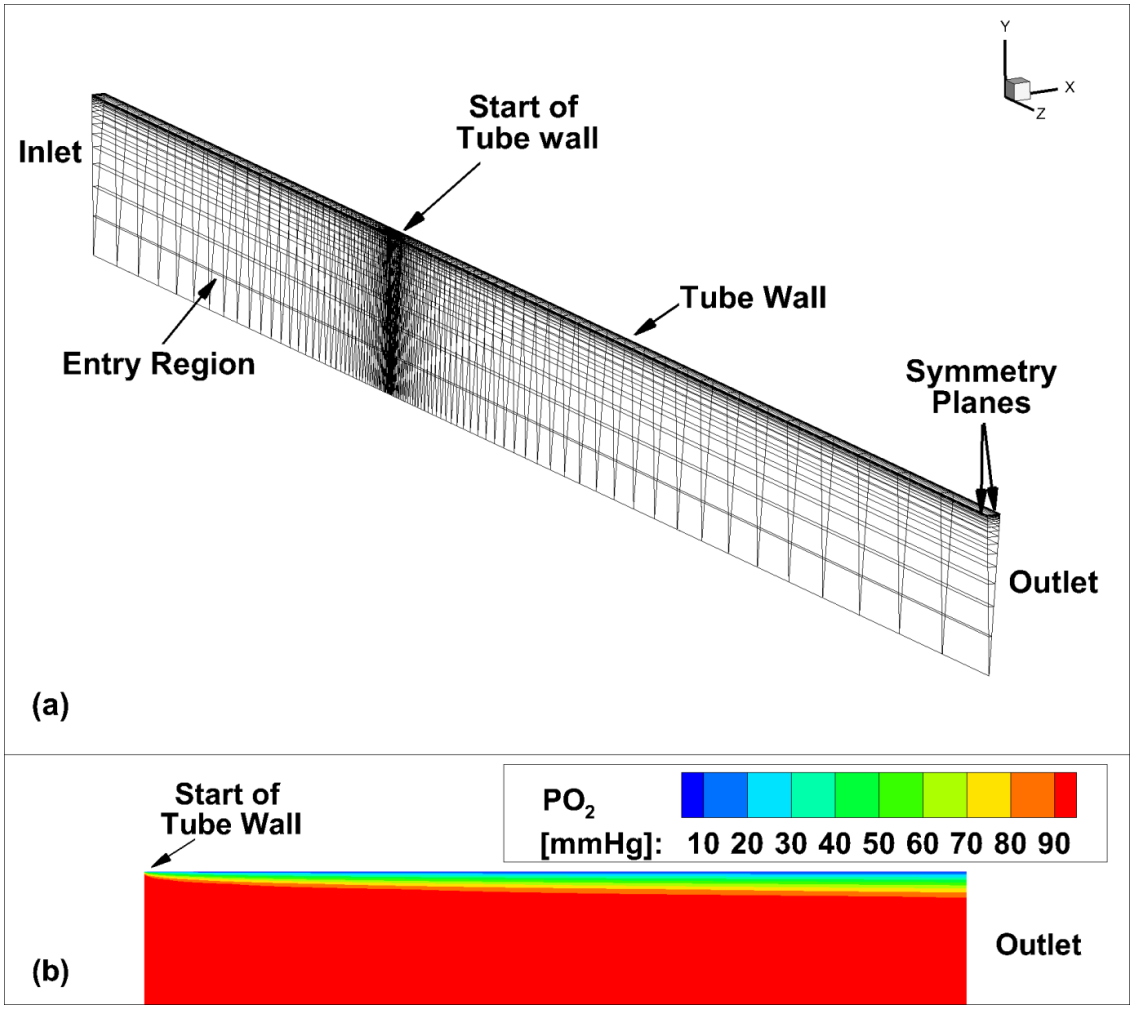

Figure A.7: (a) The mesh employed for Validation Test Case 2, (b) the PO_2 boundary layer in a tube using Model 5 in an axial cross-section.

A comparison of the predicted and calculated Sh is shown in Figure A.8. The Lévêque analytical solution and the predicted results using Model 5 compare very well, which

confirms that Model 5 is producing the expected results and that the mesh density is sufficient for capturing the flow and oxygen transport accurately.

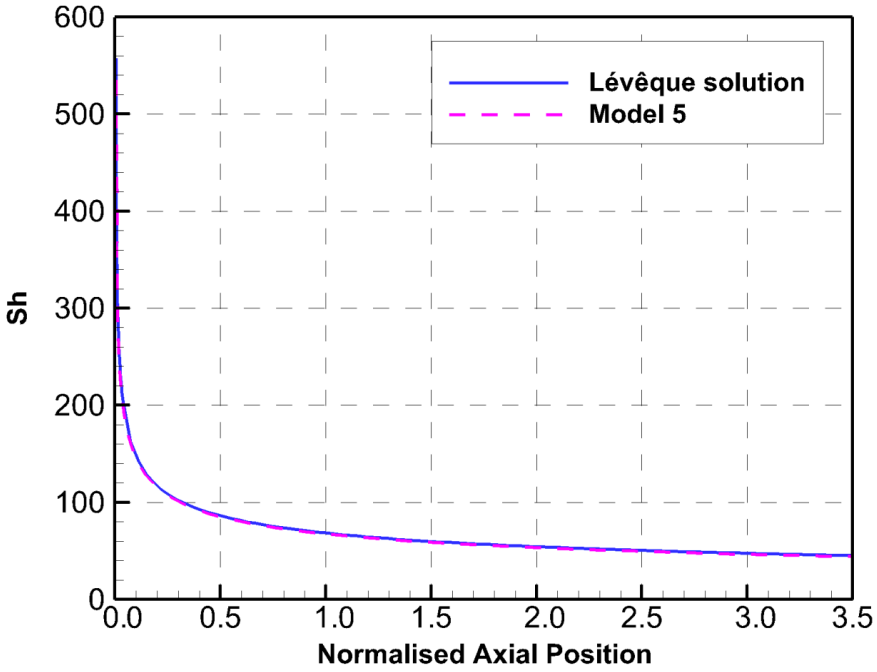

Figure A.8: Comparison of the predicted Sh using Model 5 with the Lévêque analytical solution of the Graetz-Nusselt problem. The axial distance is normalised with respect to the diameter of the tube with zero corresponding to the start of the tube wall.

A.4 Summary

Both validation cases presented in this appendix serve to demonstrate that the commercial software, ANSYS CFX 15.0, is accurately predicting the fluid dynamics and the mass transport. Both validation cases show good agreement with analytical solutions, Blasius and Lévêque.

APPENDIX B
Mesh Convergence

B.1 Introduction

In this appendix the mesh convergence studies undertaken for all four test cases, Chapters 6-8, are described. Mesh convergence studies comprise of refining a mesh until the results are considered mesh independent, i.e. when the results do not change by a user-specified tolerance with further refinement of the mesh. Accurate capture of the MTBL for this work was one crucial aspect of the mesh convergence. Model 1 was used for all the mesh convergence studies as it includes all non-linearities, and also because the MTBL observed, as demonstrated in Chapters 6 and 7, has an extremely steep gradient, which make the results susceptible to adverse effects from poor meshing. Following the mesh convergence studies the details of the meshes employed for each test case are listed along with figures to visually demonstrate the mesh densities used.

B.2 Mesh Convergence 1 – Prism Layers to Capture MTBL

Critical to accurate modelling of the oxygen transport is the refinement of the mesh within the MTBL, which is thinner than the velocity boundary layer. The geometry used was a 5° wedge with three domains: lumen, intima, and media, as shown in Figure B.1(a). The meshes used for the Validation Test Case 2 (Lévêque solution) and Test Case 1 (carotid bifurcation) are both hexa-dominant meshes and also, for this mesh convergence study. Three meshes were created and the only parameter that was varied was the height of the first layer inflated off the luminal wall surface: Mesh 1 – 6.7μm,

Mesh 2 – 3.8µm, and Mesh 3 – 1.2µm. An inflation rate of 1.2 was used in all three meshes. Mesh 3 is shown in Figure B.1(b) to demonstrate the structure of the mesh used with refinement at the wall and the beginning of the arterial wall segment.

The boundary conditions used were a parabolic velocity profile with a maximum velocity of 0.2313m/s and $PO_{2,in}$=100mmHg set at the inlet, entrainment with a 0Pa relative pressure and $PO_{2,out}$=0mmHg set at the outlet, symmetry conditions set on the wedge sides, free slip and zero PO_2 flux set at entry wall, PO_2=45mmHg set at media outer wall, and free PO_2 flux set across all domain interfaces.

B.2.1 Results

Figure B.1(c) shows a contour plot of the PO_2 across a longitudinal slice within all three domains. A line plot of the PO_2 along the arterial wall luminal surface for each mesh from the start of the wall surface to the end of the domain is shown in Figure B.2. As can be seen from this figure the difference between Mesh 2 and Mesh 3 is minimal and within a tolerance of 5%, with a maximum difference of 0.7%. From this mesh convergence study the height of the first inflation layer for all meshes was set at 3µm.

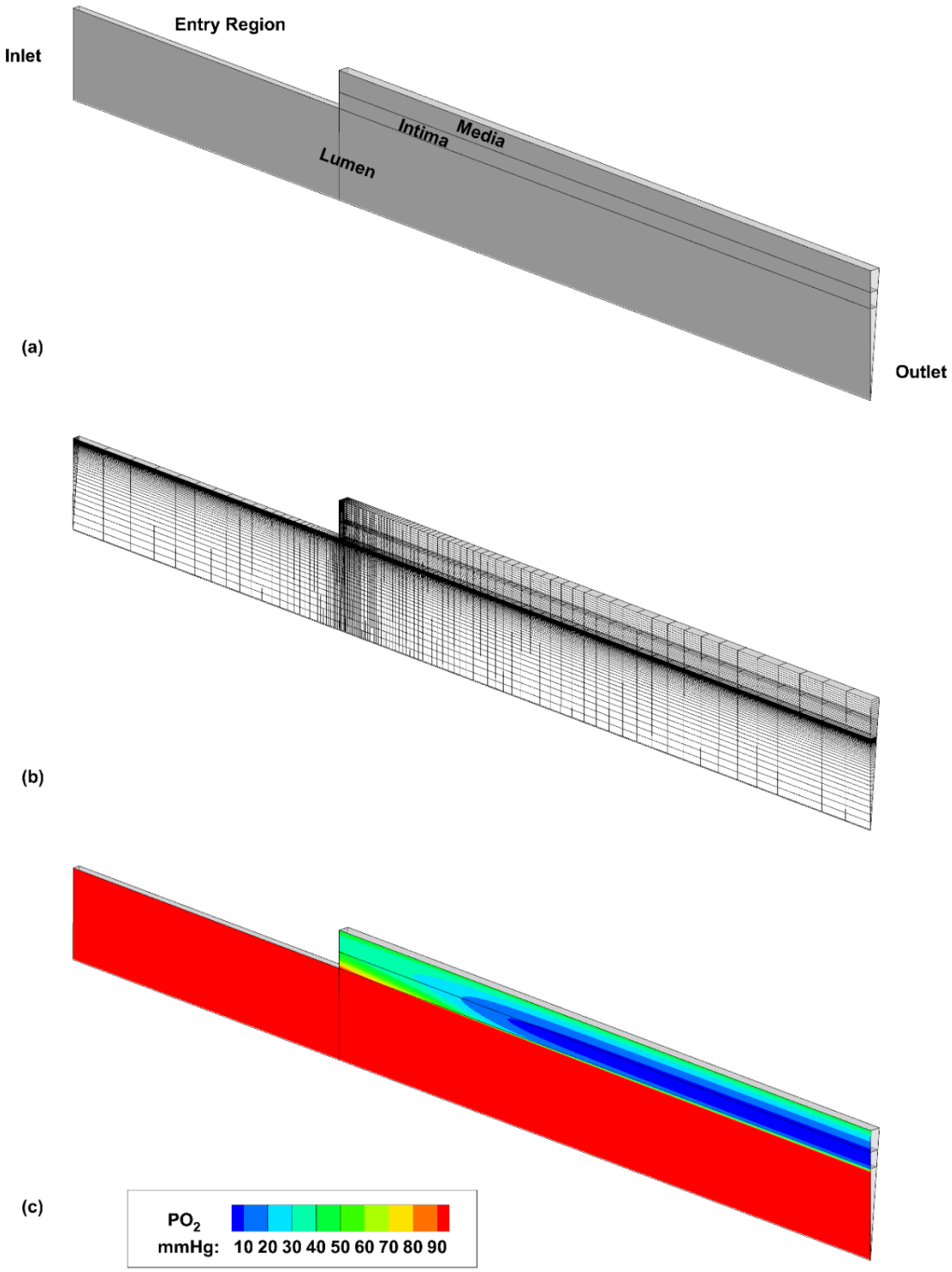

Figure B.1: (a) Diagram of set-up for Mesh Convergence Study 1, (b) Mesh 3 outline, and (c) contour plot of PO_2 along slice within all three domains showing how the MTBL develops.

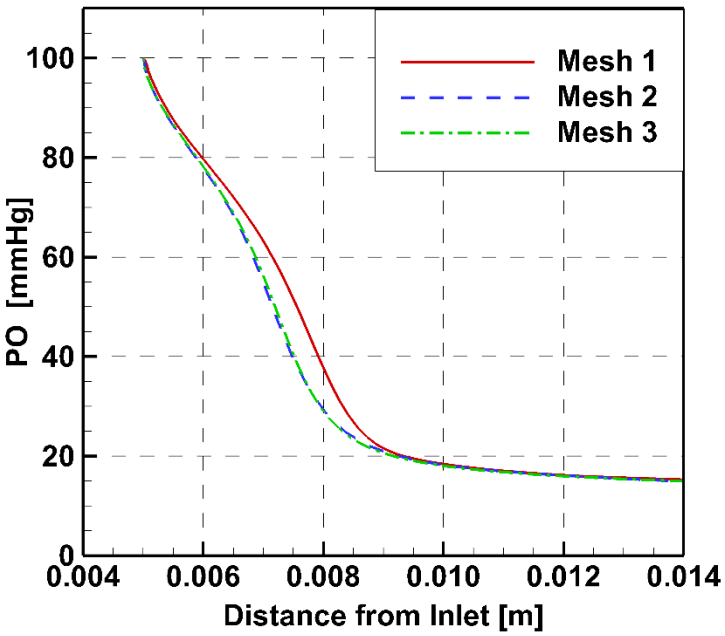

Figure B.2: Line plot of PO_2 along the arterial wall luminal surface from the start of the arterial wall to the end of the domain.

B.3 Mesh Convergence 2 – Carotid Artery

This mesh convergence study was undertaken with the same carotid artery geometry, created using Rhinoceros 3D, with the measurements as discussed in Chapter 6. For Test Case 1 the transarterial wall PO_2 profiles at three locations, as shown in Figure B.3, were the results of interest. Thus, these results were monitored for two different mesh densities which are referred to as Carotid Mesh 1 and Carotid Mesh 2. The mesh statistics for both meshes are displayed in Table B.1, and Figure B.4 and Figure B.5 are presented to give an indication of the mesh densities adopted for both meshes.

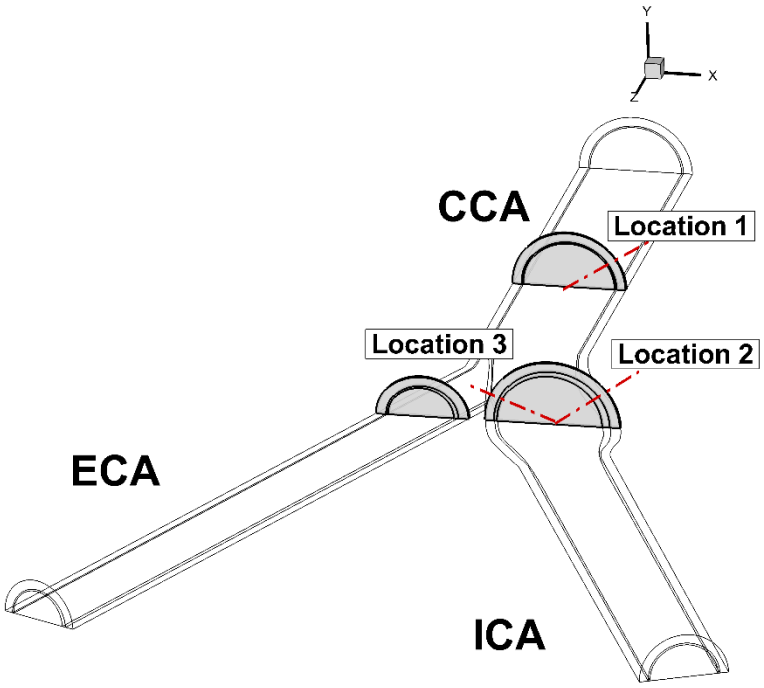

Figure B.3: Carotid bifurcation model with locations of transarterial wall PO_2 profiles of interest highlighted.

Number of Nodes	Carotid Mesh 1	Carotid Mesh 2
Lumen	501546	2604504
Intima	295075	429200
Media	176500	635284
Total	973121	3668988

Table B.1: Node counts for the three domains (lumen, intima, and media) within the two carotid meshes adopted for the mesh convergence.

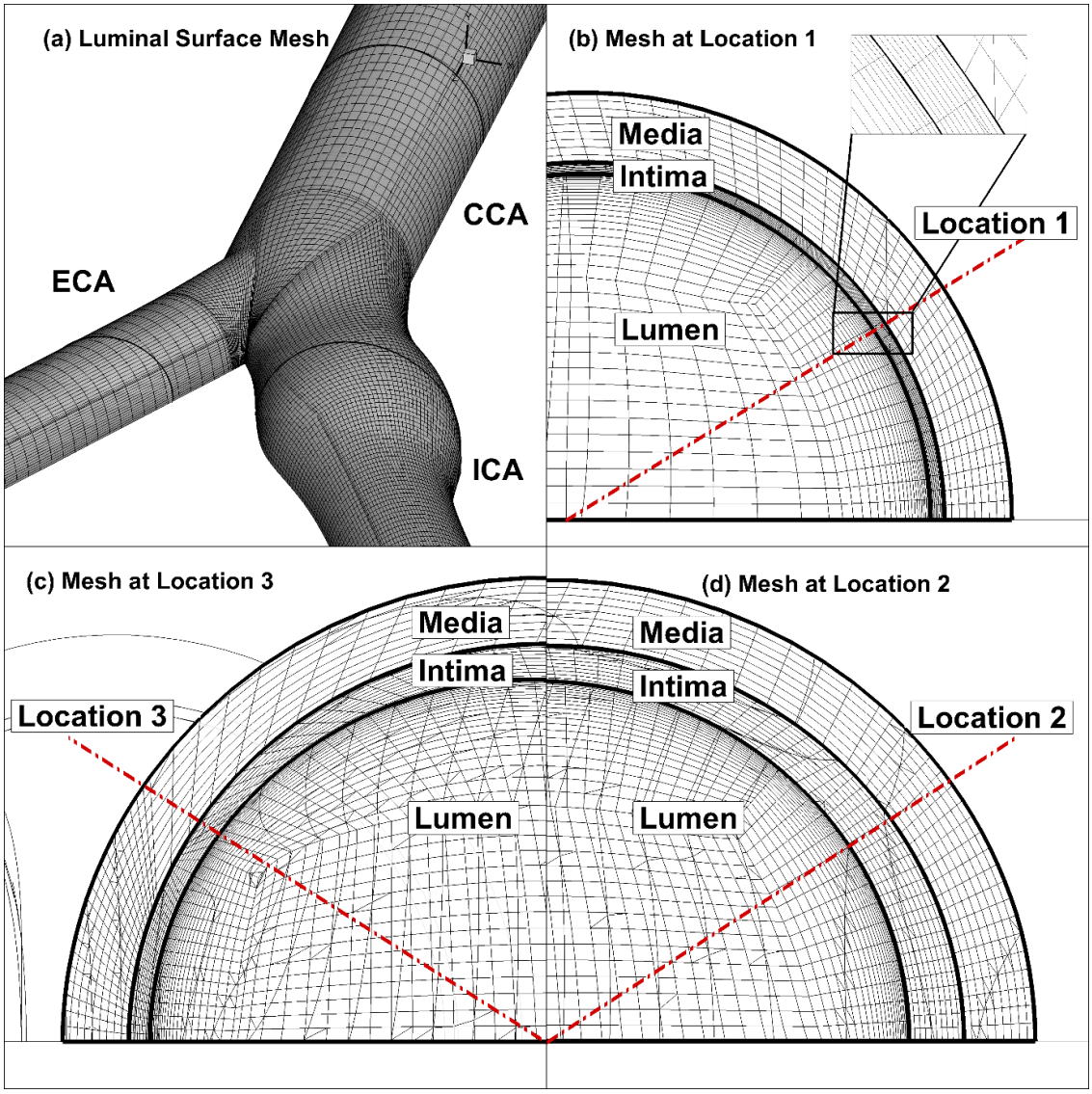

Figure B.4: (a) The luminal surface mesh and (b-d) cross-sectional views of the volume mesh at the three locations for Carotid Mesh 1.

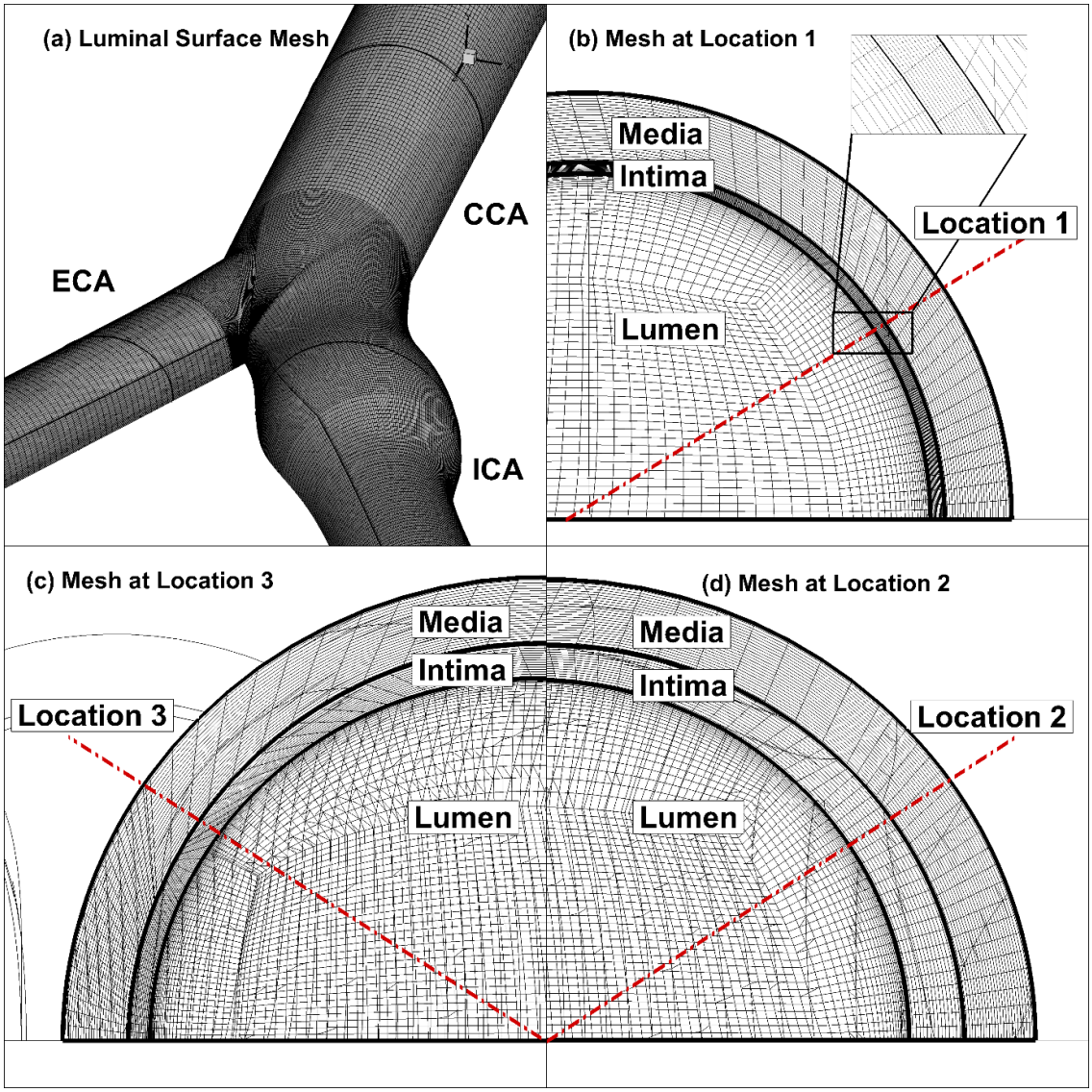

Figure B.5: (a) The luminal surface mesh and (b-d) cross-sectional views of the volume mesh at the three locations for Carotid Mesh 2.

B.3.1 Results

The transarterial wall PO_2 profiles at each location for both meshes are presented in Figure B.6, and it is clear from this figure that there is no significant difference between the results at these three locations with the maximum deviation seen at Location 3 with a percentage difference between the luminal surface PO_2 value of 2.1% (1.4mmHg

difference). Thus, Carotid Mesh 1 was adopted for all simulations undertaken for Test Case 1.

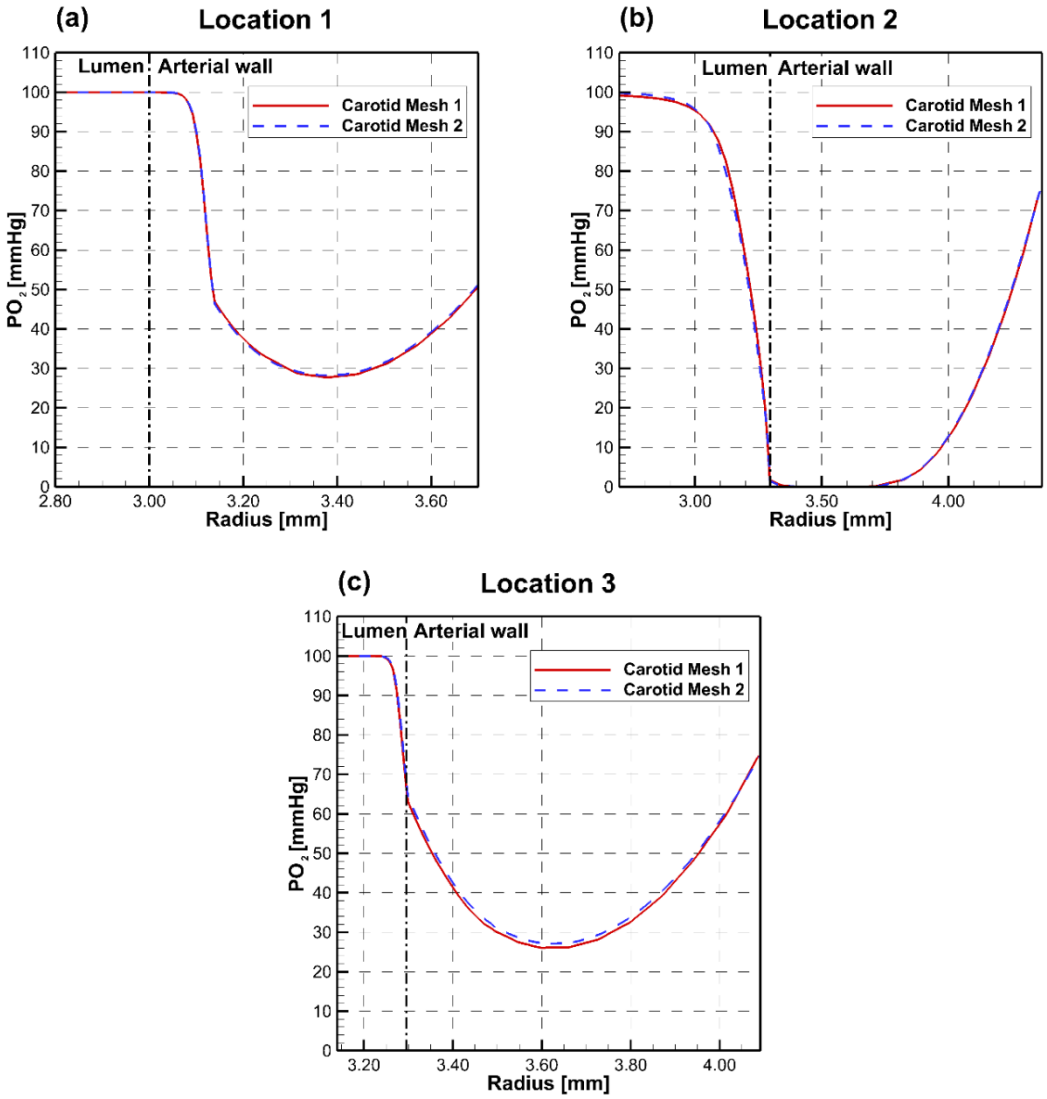

Figure B.6: Transarterial wall PO_2 profiles at all three locations for Carotid Mesh 1 and Carotid Mesh 2.

B.4 Mesh Convergence 3 – Stented Coronary Artery

This mesh convergence study was undertaken to elucidate the mesh parameters to be adopted for Test Cases 2, 3 and 4 in which stented coronary artery geometries were used.

B.4.1 Geometry

A smaller stent geometry was used for the mesh convergence study, as shown in Figure B.7, which is shorter than the stents used in all the test cases and differs in several ways to the stent geometries used in Test Cases 2 and 3 in Chapter 7. First, the geometry was not generated using FEA and therefore, there is no deformation of the stent or arterial wall surface. Additionally, there is no over-expansion of the stent which would cause the stented region to have a larger diameter than the unstented artery. This was done so that the effect of the overexpansion would not impact the results; therefore, keeping the geometry as simple as possible with the focus on the refinement of the MTBL on the stented arterial wall luminal surface, and accurate capture of the diffusion within the arterial wall. The stent design used resembles the Multilink Vision coronary stent (Abbott Laboratories, North Chicago, IL, USA) with a 3.0mm internal diameter.

B.4.2 Geometry Discretisation

The meshing methodology adopted is the same as mentioned in Chapter 7; a volume mesh was created using the Delaunay Method, which ensures smooth transition from small to larger cells, from a surface mesh which was created using the Octree Method. Prism layers (eight) were created along luminal and stent surfaces to accurately capture the MTBL. Prism layers were also used within the arterial wall to ensure accurate capture of the transarterial wall PO_2 profiles.

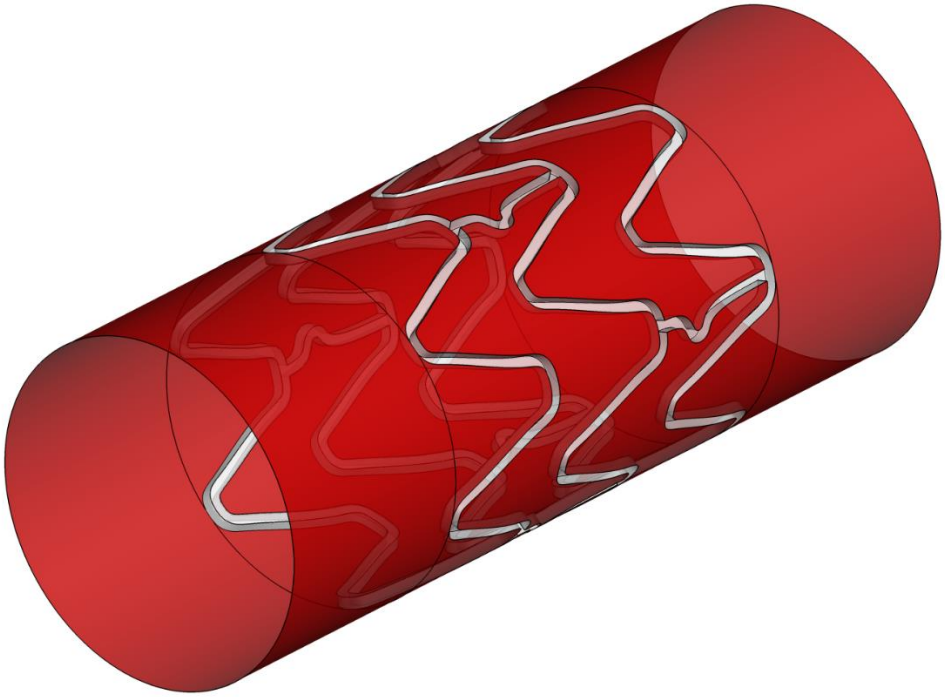

Figure B.7: Idealised stent geometry used for mesh convergence study (a segment of the stent geometry used for Test Case 4). Note: additional entry and exit regions (each 32mm long) are not shown.

B.4.3 Test 1 - Luminal Surface

With the size of the initial prism layer adjacent to the luminal surface fixed from the first mesh convergence study described in Section B.2, the next sizing parameter to refine for the stented coronary artery geometries was the luminal surface and stent strut element size within the stented region. Thus, to ensure mesh convergence of the oxygen transport results three separate meshes were generated where only the luminal surface and stent strut element size within the stented region was varied, with the smallest cell size implemented in Mesh 3. This resulted in three separate meshes, numbered one to three, with node counts of 34232, 75518, and 91637 on the luminal surface within the stented region. The three meshes are shown in Figure B.8.

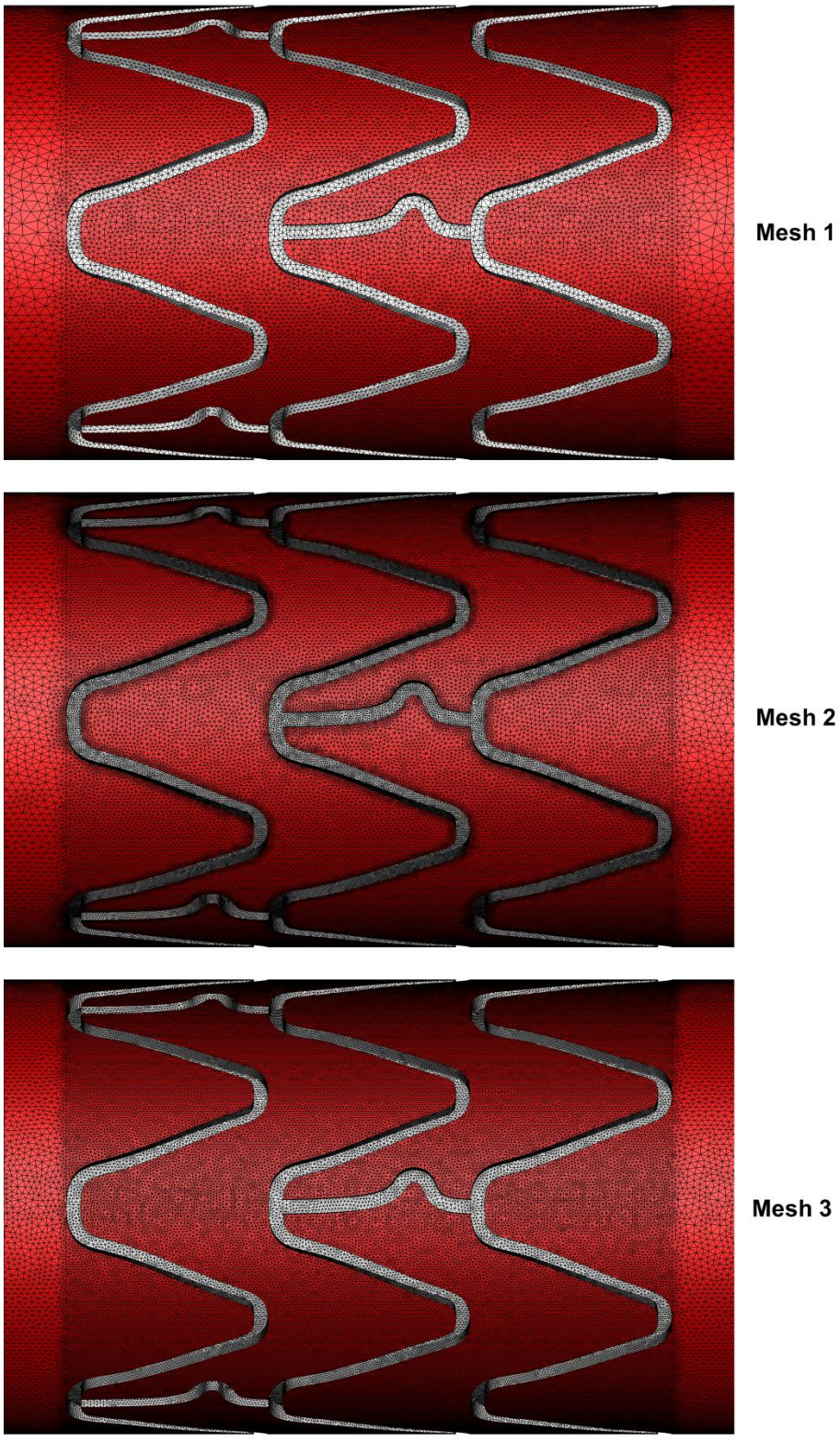

Figure B.8: Meshes 1, 2, and 3 with stented region luminal surface node counts of 34232, 75518, and 91637 respectively.

B.4.3.1 Test 1 – Results

First, to confirm that the WSS values on the luminal surface of the stented region are converged Table B.2 presents the area-averaged (AA), maximum and minimum WSS, and WSSG values predicted on the luminal surface for each mesh, along with Figure B.9 and Figure B.10 which show the WSS and WSSG distribution on the luminal surface. Given that an accepted user-specified tolerance for the percentage change in values between meshes is 5.0%, it is clear from both the table and figures that the WSS and WSSG are converged on the luminal surface for all the meshes. This is expected because the mesh refinement required for the haemodynamic variables would not be as high as for the oxygen transport. The WSSG shows a slight variability in the maximum value, but this has no significant effect on the AA WSSG value.

Table B.3 details the AA, maximum and minimum PO_2 and Sh values predicted on the luminal surface for each mesh, while Figure B.11 and Figure B.12 show the PO_2 and Sh distributions on the luminal surface. The PO_2 values can be considered converged in Mesh 2 as further refinement results in no significant difference in the AA, maximum or minimum PO_2 values predicted on the luminal surface. This is supported by the PO_2 distribution plots presented in Figure B.11.

For the Sh there is a large variation in the maximum and minimum values. This is because the Sh is calculated using the normal gradient in PO_2 off the luminal surface, as shown in Equation (3.54) in Chapter 3. Any slight variation in the PO_2 gradient normal to the wall produces a noticeable effect on the Sh value. What is clear from the 1% difference in the AA Sh on the luminal surface between Meshes 2 and 3 is that the minimum and maximum values are extreme outliers which do not affect the overall

distribution significantly. This is also demonstrated clearly by analysing the predicted Sh distribution in Figure B.12, which shows little difference in the predicted contour levels on the luminal surface for Meshes 2 and 3.

To demonstrate that the prism layers implemented in the mesh generation accurately capture the MTBL Figure B.13 shows the PO_2 distribution around a stent strut and across the intima for Mesh 2. The mesh is also displayed. As shown, eight layers were inflated off the luminal and stent surfaces with at least three or four prism layers falling within the MTBL. Three layers is the minimum required to accurately capture the high PO_2 gradient, as seen in Test Cases 1 and 2.

WSS [Pa]	1	Diff. (1-2)	2	Diff. (2-3)	3
Max	1.22	1%	1.21	0%	1.21
AA	0.67	0%	0.67	1%	0.66
Min	0.00	0%	0.00	0%	0.00
WSSG [Pa/mm]	**1**	**Diff. (1-2)**	**2**	**Diff. (2-3)**	**3**
Max	12.00	47%	6.33	-84%	11.66
AA	1.38	1%	1.37	-3%	1.41
Min	0.00	0%	0.00	0%	0.00

Table B.2: The predicted maximum, area-averaged, and minimum WSS and WSSG values calculated on the luminal surface of the stented region for Meshes 1, 2, and 3.

Sh [-]	1	Diff. (1-2)	2	Diff. (2-3)	3
Max	465.37	-47%	248.38	50%	372.07
AA	129.34	-14%	111.77	-1%	110.84
Min	18.14	-11%	16.11	-66%	5.45
PO_2 [mmHg]	**1**	**Diff. (1-2)**	**2**	**Diff. (2-3)**	**3**
Max	71.34	-15%	60.54	0%	60.55
AA	32.30	-19%	26.02	0%	26.02
Min	12.30	-35%	7.95	0%	7.95

Table B.3: The predicted maximum, area-averaged, and minimum Sh and PO_2 values calculated on the luminal surface of the stented region for Meshes 1, 2, and 3.

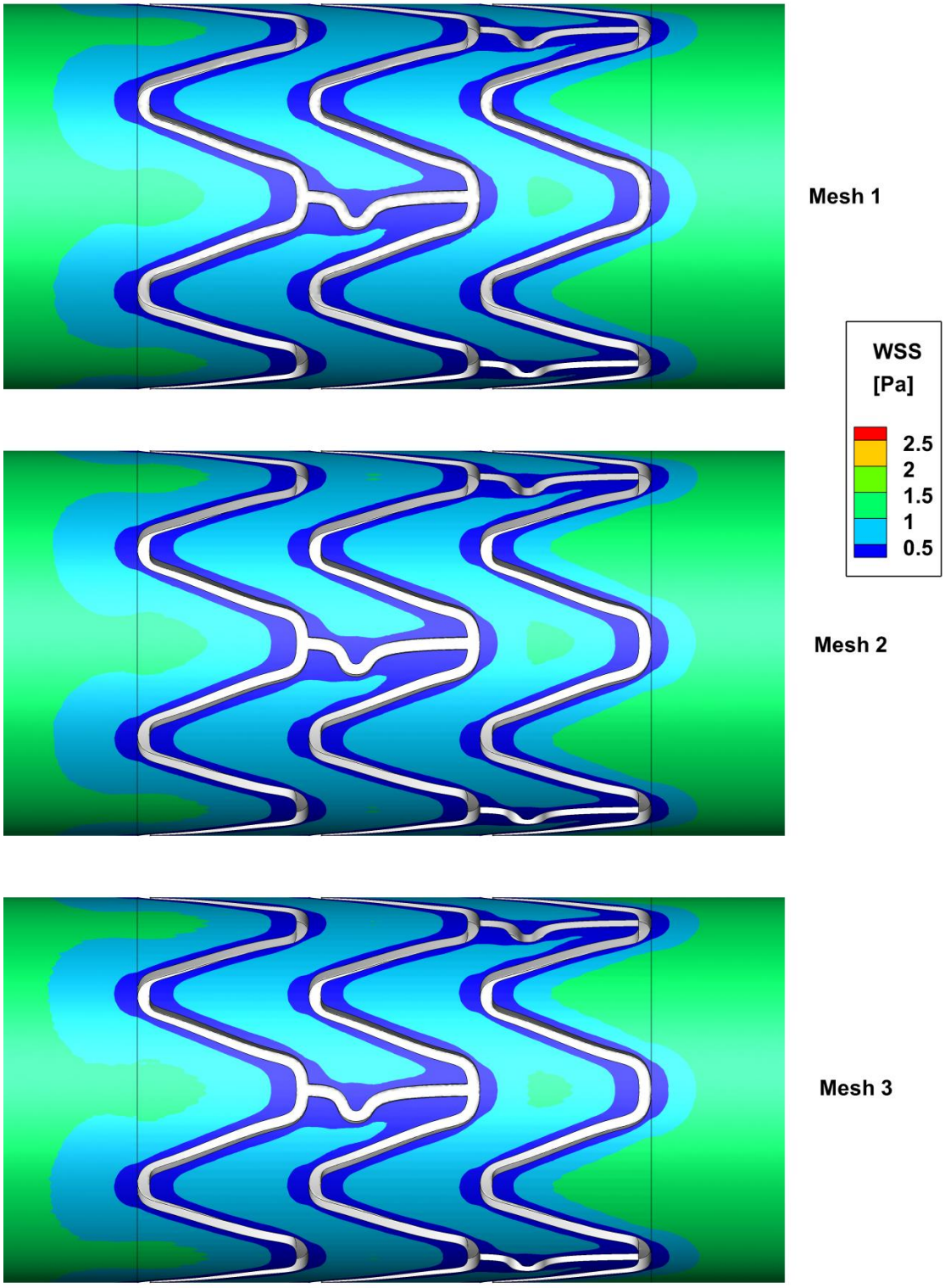

Figure B.9: Predicted WSS distribution for Meshes 1, 2, and 3.

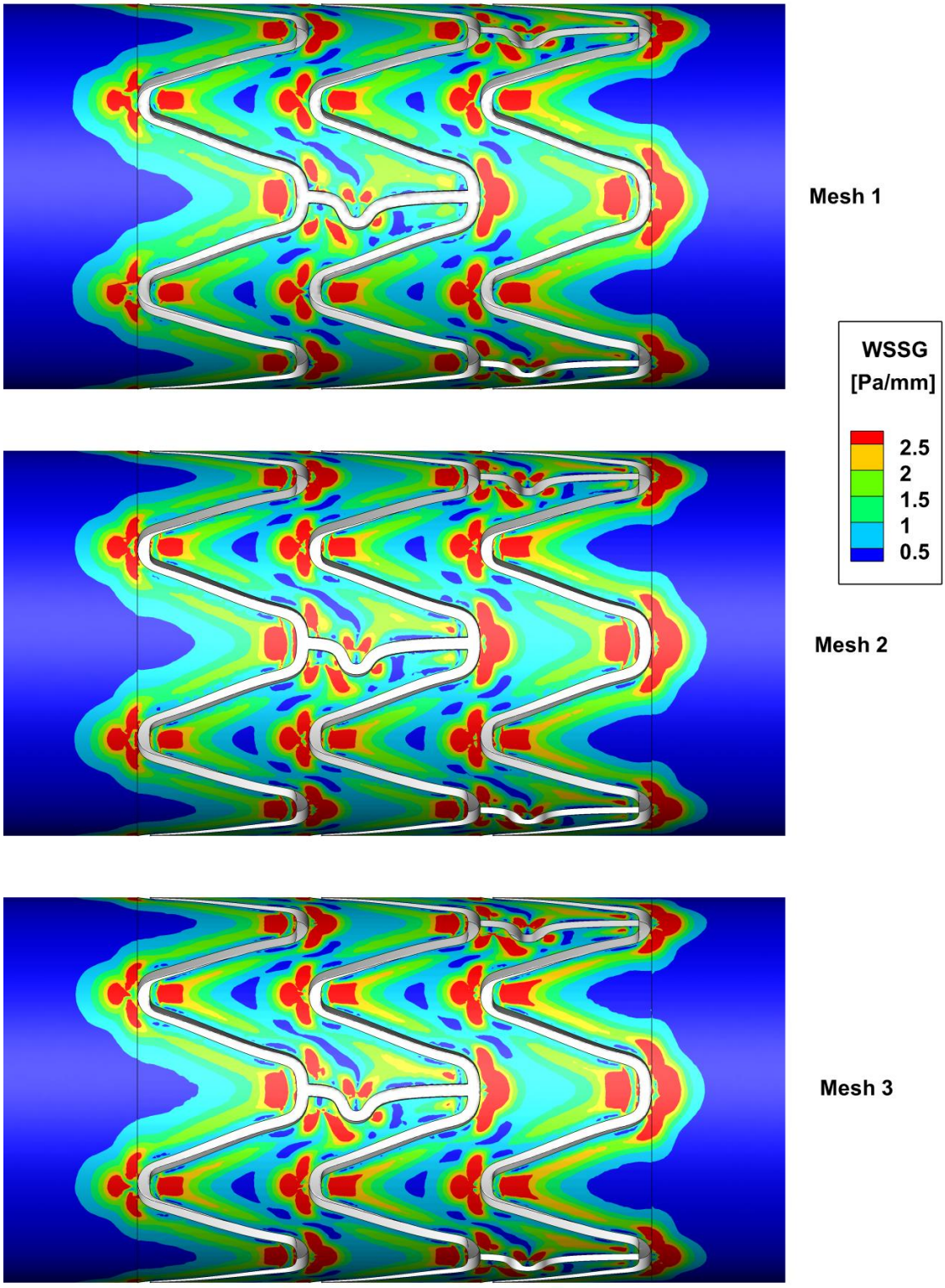

Figure B.10: Predicted WSSG distribution for Meshes 1, 2, and 3.

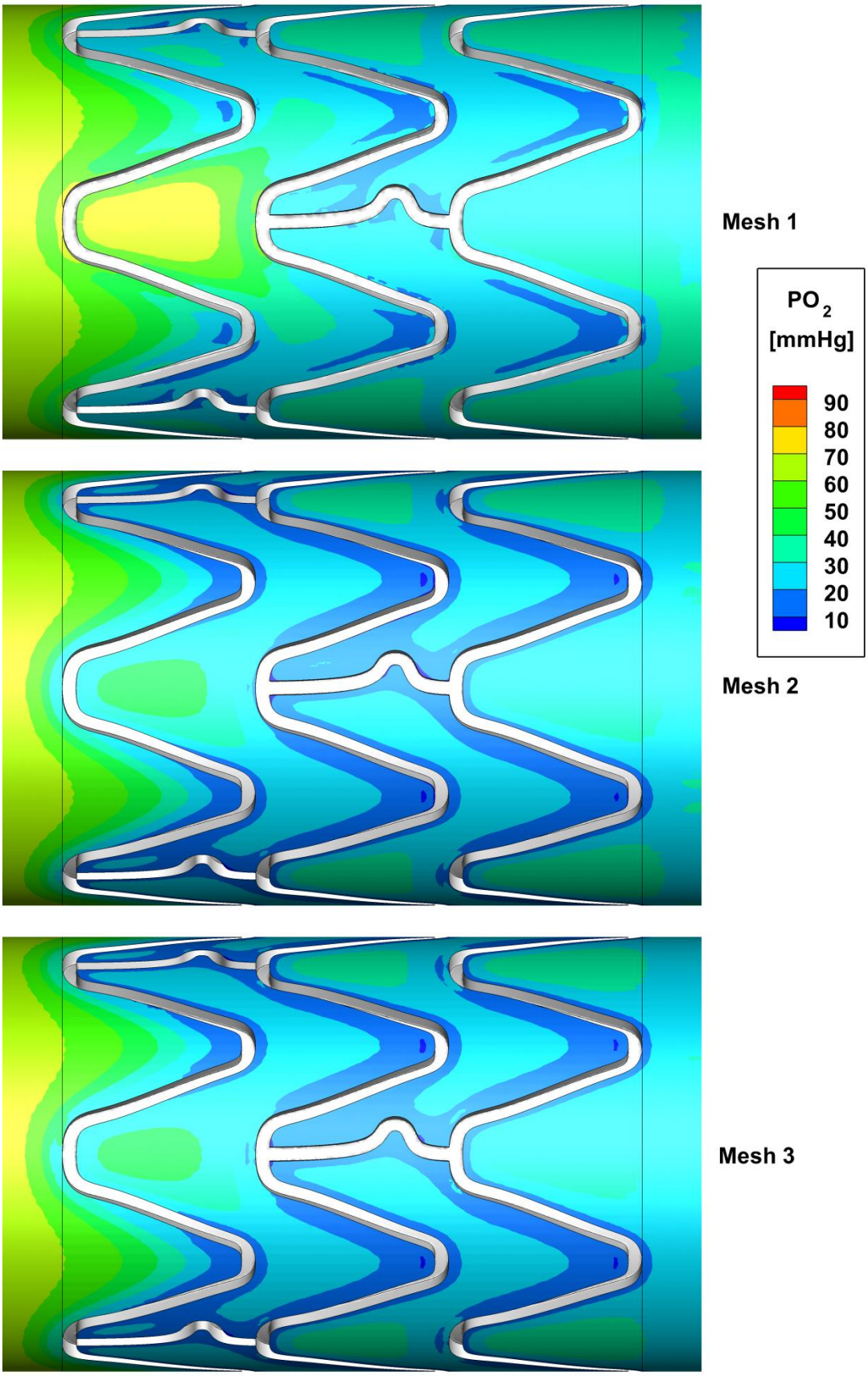

Figure B.11: Predicted PO_2 distribution for Meshes 1, 2, and 3.

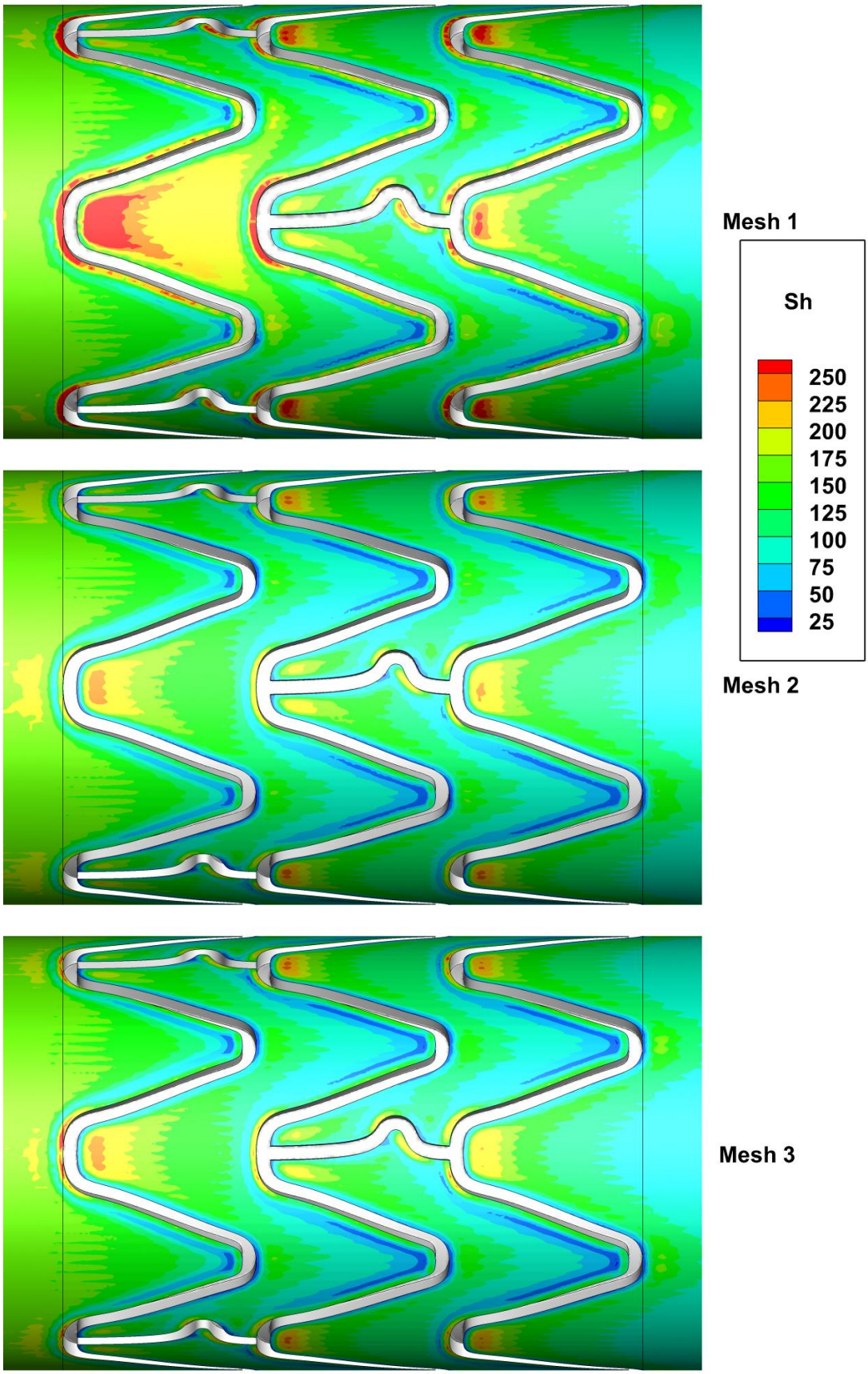

Figure B.12: Predicted Sh distribution for Meshes 1, 2, and 3.

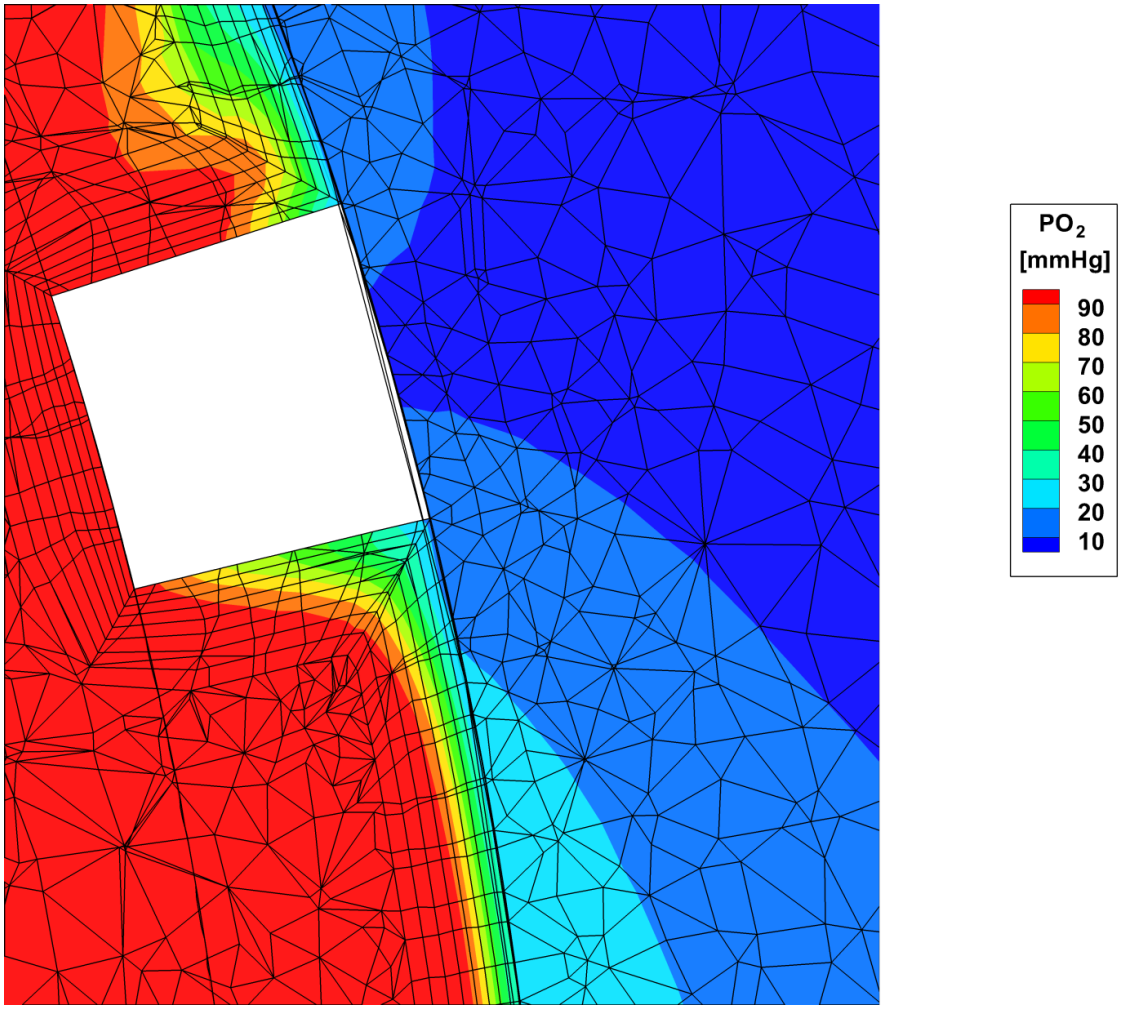

Figure B.13: Typical prism layers mesh used on the luminal surface to capture the MTBL, which is seen as the region lower than 90mmHg at the luminal surface.

B.4.4 Test 2 – Arterial Wall

The percentages of the arterial wall exposed to low PO_2 (<30mmHg) and hypoxic PO_2 (<10mmHg) are needed for Test Cases 2, 3, and 4, therefore, in addition to the previous test, two additional tests were undertaken to ensure that the mesh refinement was appropriate.

First, the effect of refinement of the luminal surface mesh outside of the stented region on the results within the stented region was assessed. Figure B.14 shows the two meshes used to assess if increasing the mesh density on the luminal surface upstream and downstream of the stented region, i.e. the region of interest, produced any significant effect on the predicted oxygen transport. This refinement had the effect of increasing the node count within the lumen for Mesh 2 and Mesh 2a were 2308558 and 2761248, respectively.

Second, the effect of further refinement of the intima layer was assessed. Cross-sectional views of the meshes employed in the second test are shown in Figure B.15 with Mesh 2b having the increased intima mesh density provided by prism layers on the inner and outer surface of the intima. The node count within the intima for Mesh 2 and Mesh 2b were 634154 and 1510538, respectively.

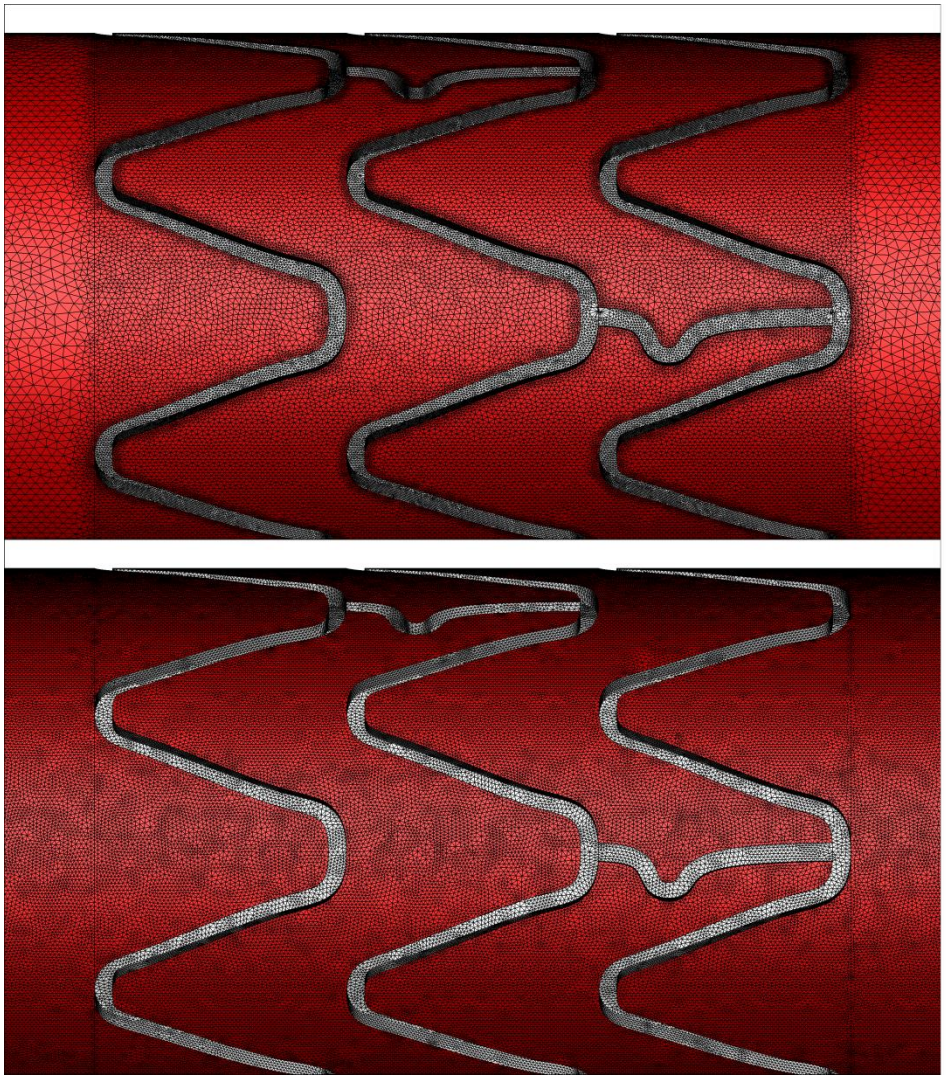

Figure B.14: Mesh density on the luminal surface for Meshes 2 and 2a.

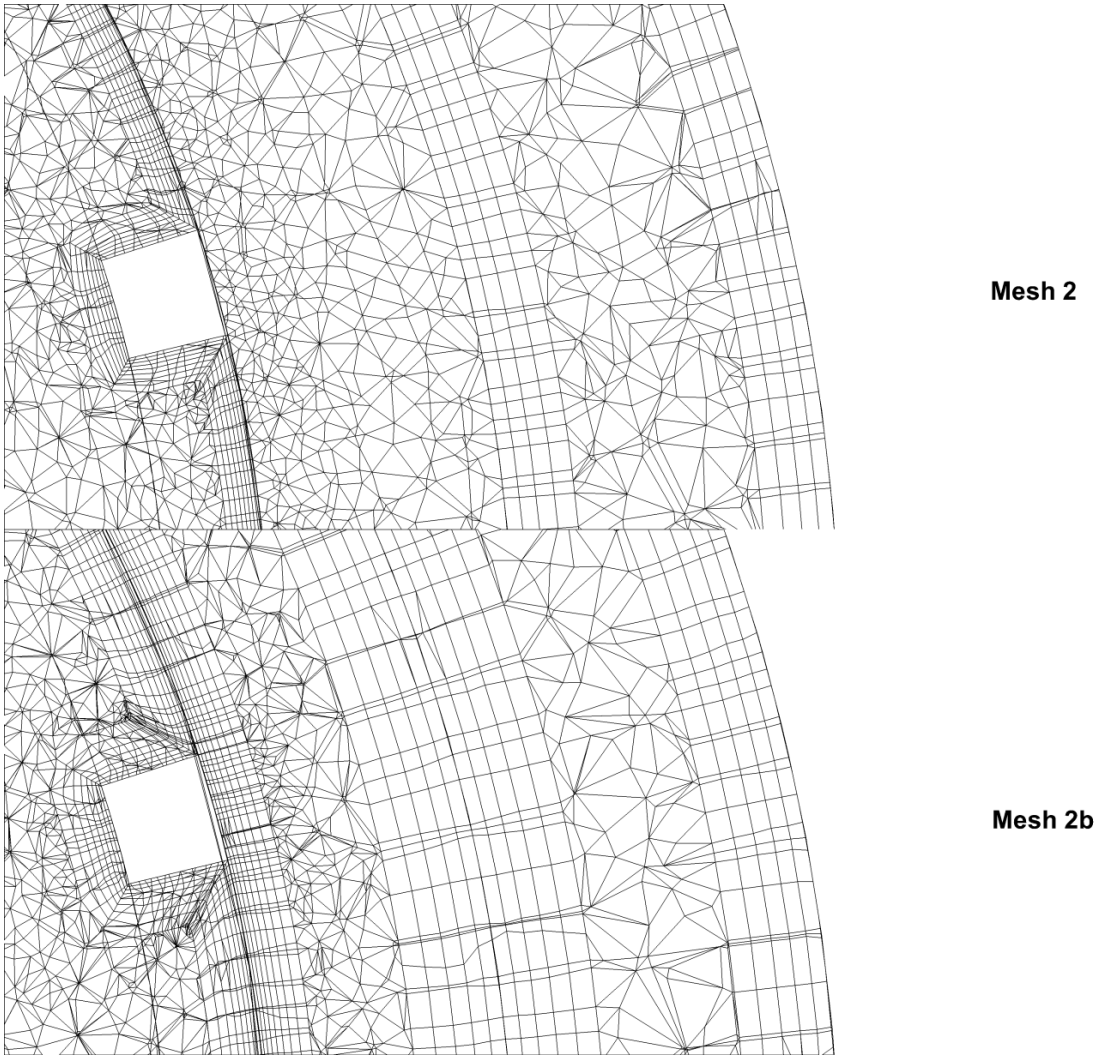

Figure B.15: Cross-sections of Mesh 2 and Mesh 2b showing the mesh density within the arterial wall and around a stent strut within the lumen.

B.4.4.1 Test 2 – Results

The results of the additional tests conducted to ensure mesh convergence are presented in Table B.4 which shows the predicted percentage volume of the intima exposed to PO_2 values over a range of 0-30mmHg for Meshes 2, 2a, and 2b. The media was not included in this as the PO_2 levels within the intima are more strongly influenced by the luminal surface PO_2 values (as discussed in Chapters 7 – 9). The additional refinement of the intima or the refinement of the luminal surface mesh outside of the stented region does not produce any significant change in the predicted PO_2 levels within the intima.

PO_2 [mmHg]	Mesh 2 [%]	Diff. (2-2a)	Mesh 2a [%]	Diff. (2-2b)	Mesh 2b [%]
0-5	6.8	0.1	6.7	1.3	5.5
5-10	46.1	-0.2	46.4	0.6	45.6
10-15	22.3	-0.4	22.7	-0.4	22.7
15-20	11.7	0.1	11.6	-0.4	12.1
20-25	6.6	0.1	6.5	-0.3	6.9
25-30	3.3	0.1	3.2	-0.3	3.6
Total <30	96.77	-0.2	96.96	0.4	96.38
Total <10	52.91	-0.2	53.07	1.8	51.08

Table B.4: Percentage volumes of intima exposed to PO_2 range 0-30mmHg and the totals <30mmHg and <10mmHg for Meshes 2, 2a, and 2b, along with the difference between them.

B.5 Meshes Employed in Test Cases 2 and 3

The node counts for the three stent geometries used in Test Cases 2 and 3 are shown in Table B.5. Additionally, Figure B.16 to Figure B.21 show the mesh density on the luminal surface and within the three volume domains for each stented coronary artery geometry analysed in Test Cases 2 and 3.

Mesh	Stent A	Stent B	Stent C
Lumen	5148910	5030463	5084752
Intima	1703823	1699687	1696288
Media	1687966	1661928	1645520
Total	8540699	8392078	8426560

Table B.5: Node counts for the three stent geometries used for Test Cases 2 and 3.

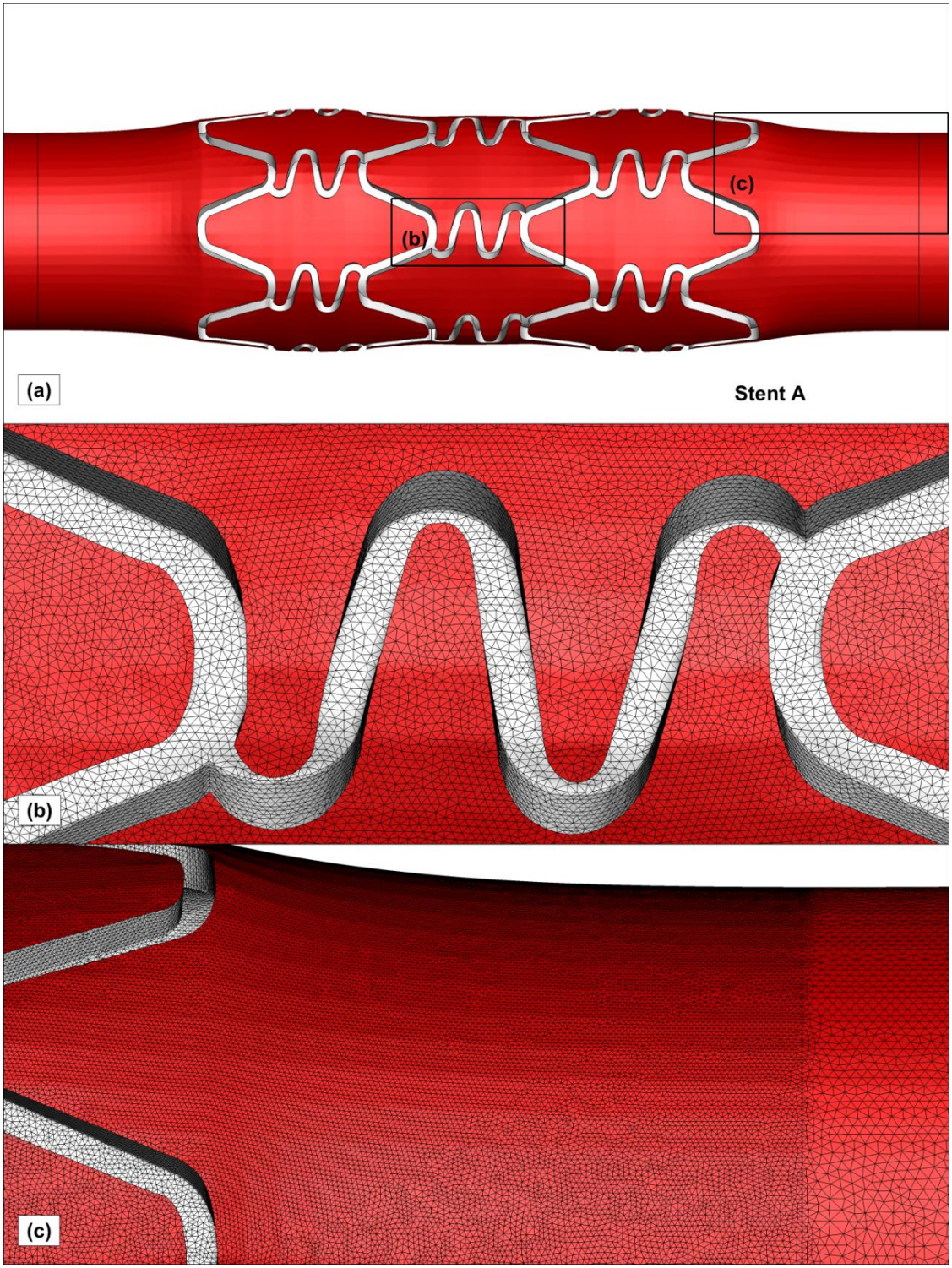

Figure B.16: (a) Geometry of Stent A with the two areas highlighted to shown where (b) and (c) are located. (b) Mesh density around stent struts, (c) Mesh density transitioning from stented region to unstented region.

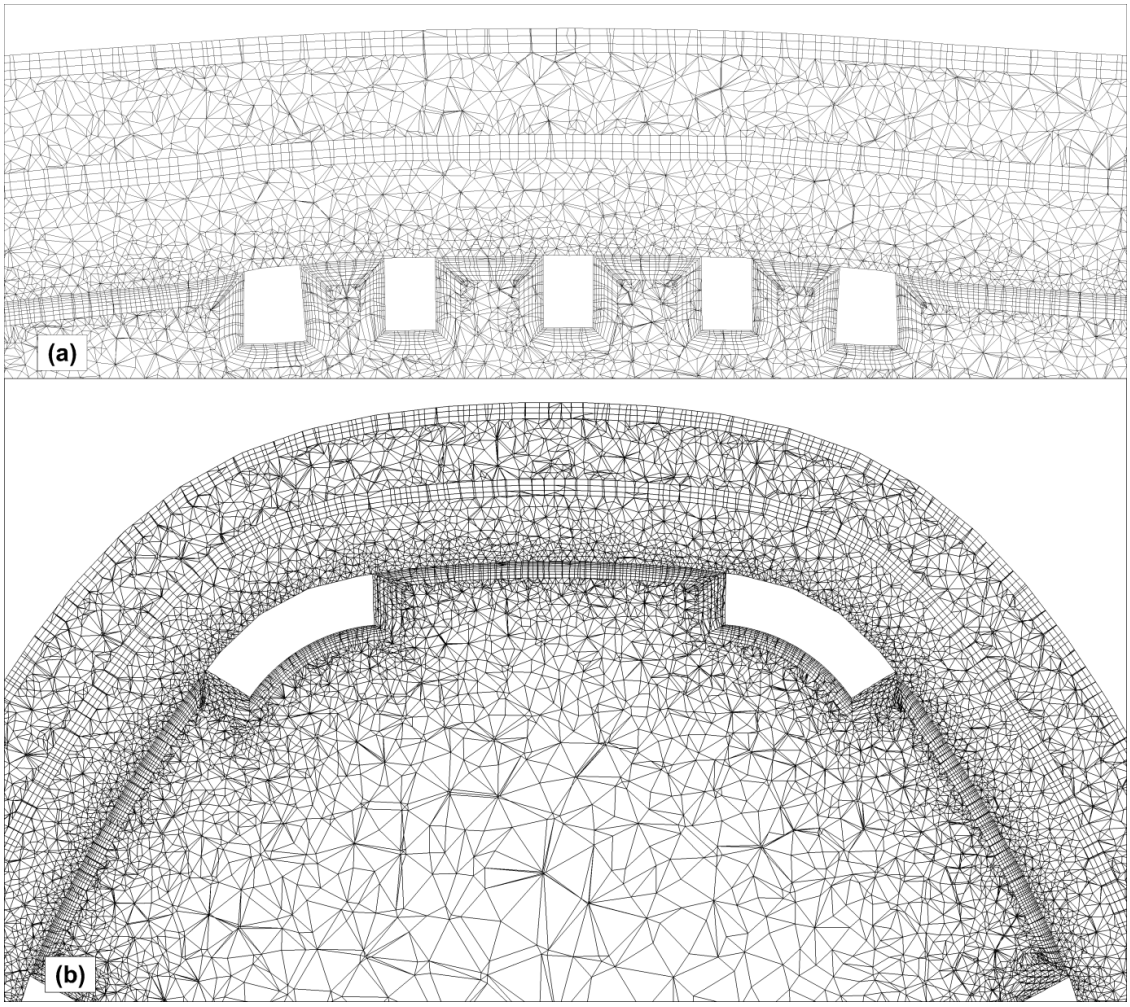

Figure B.17: (a) Longitudinal cross-section and (b) transverse cross-section showing the mesh density at the luminal surface and across the arterial wall for Stent A.

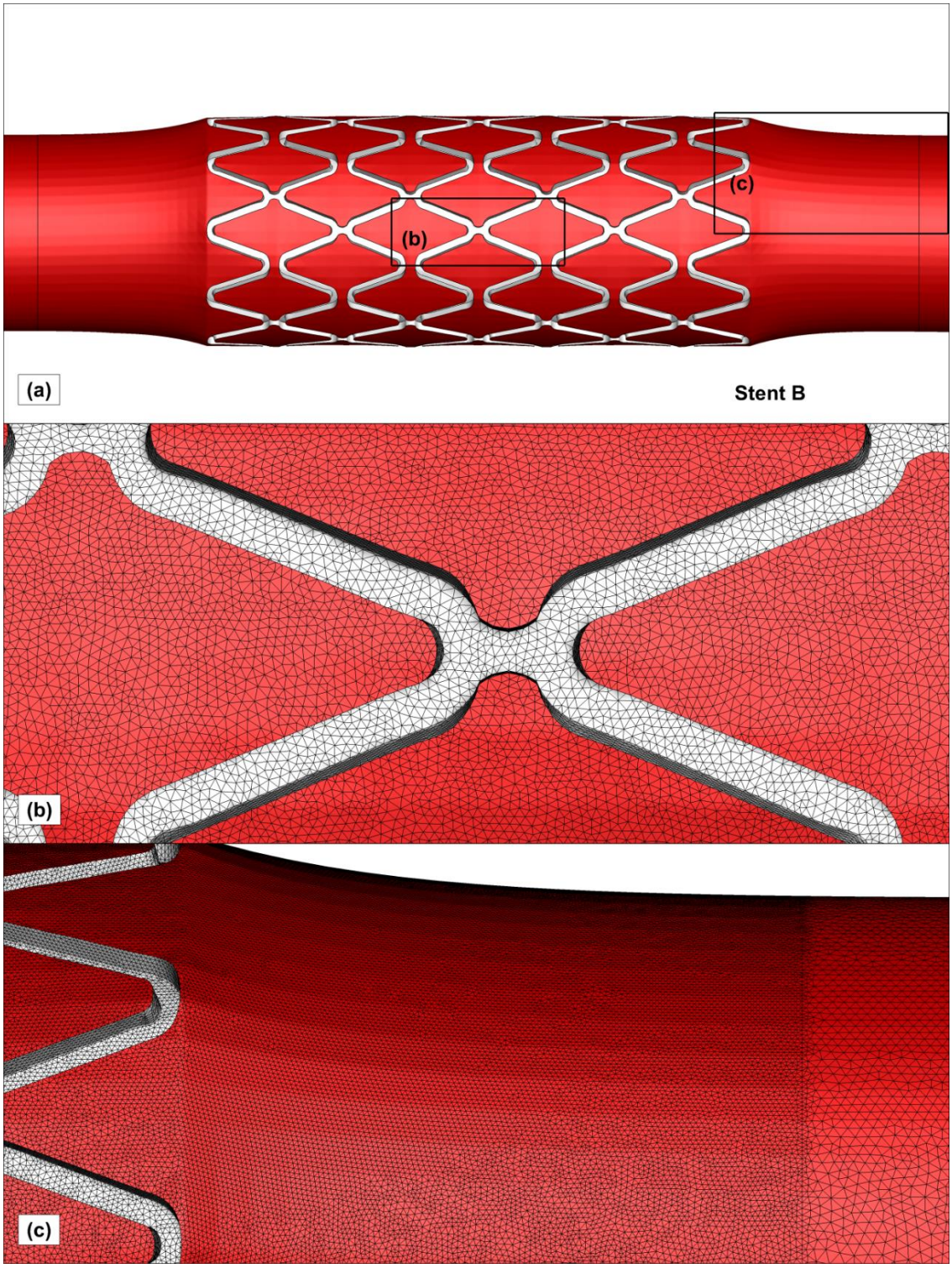

Figure B.18: (a) Geometry of Stent B with the two areas highlighted to shown where (b) and (c) are located. (b) Mesh density around stent struts, (c) Mesh density transitioning from stented region to unstented region.

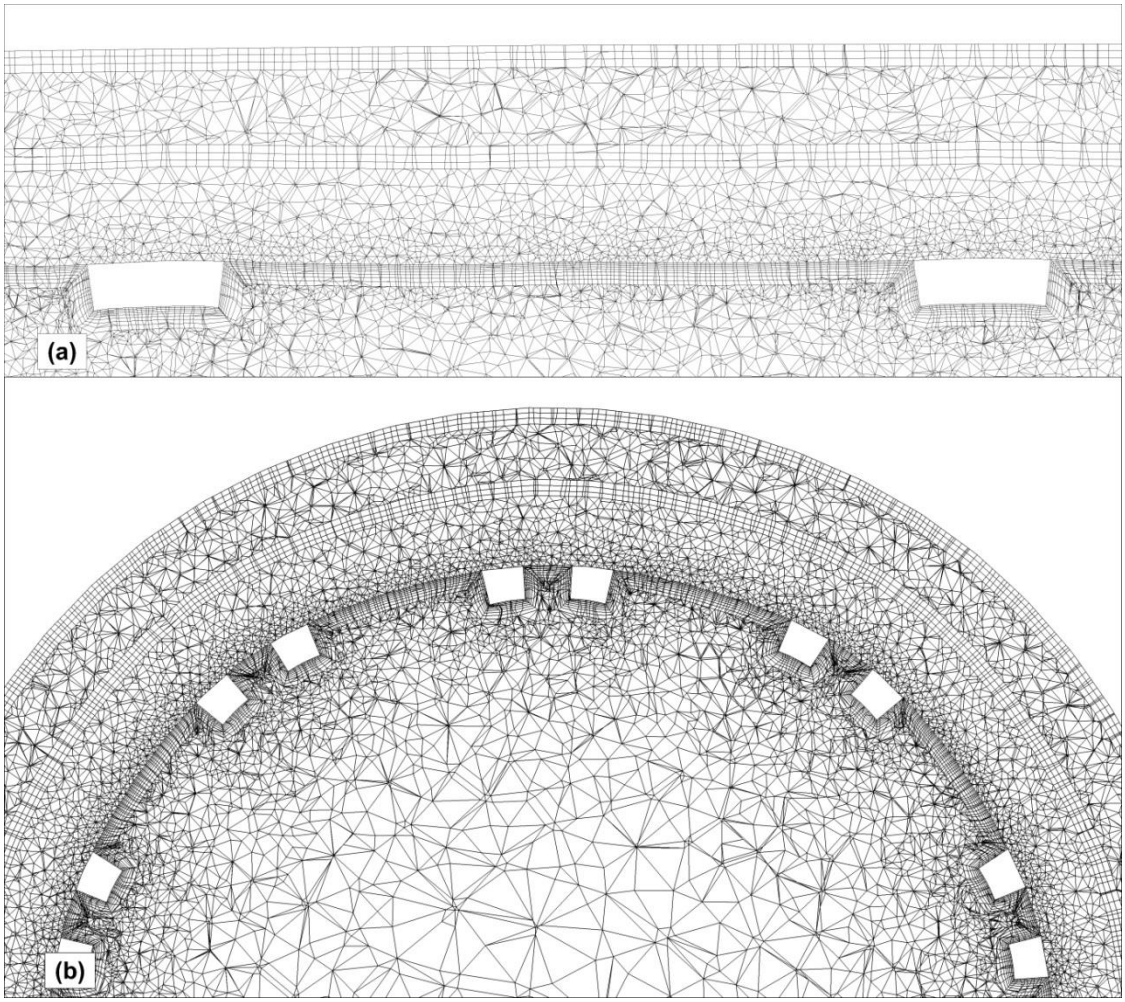

Figure B.19: (a) Longitudinal cross-section and (b) transverse cross-section showing the mesh density at the luminal surface and across the arterial wall for Stent B.

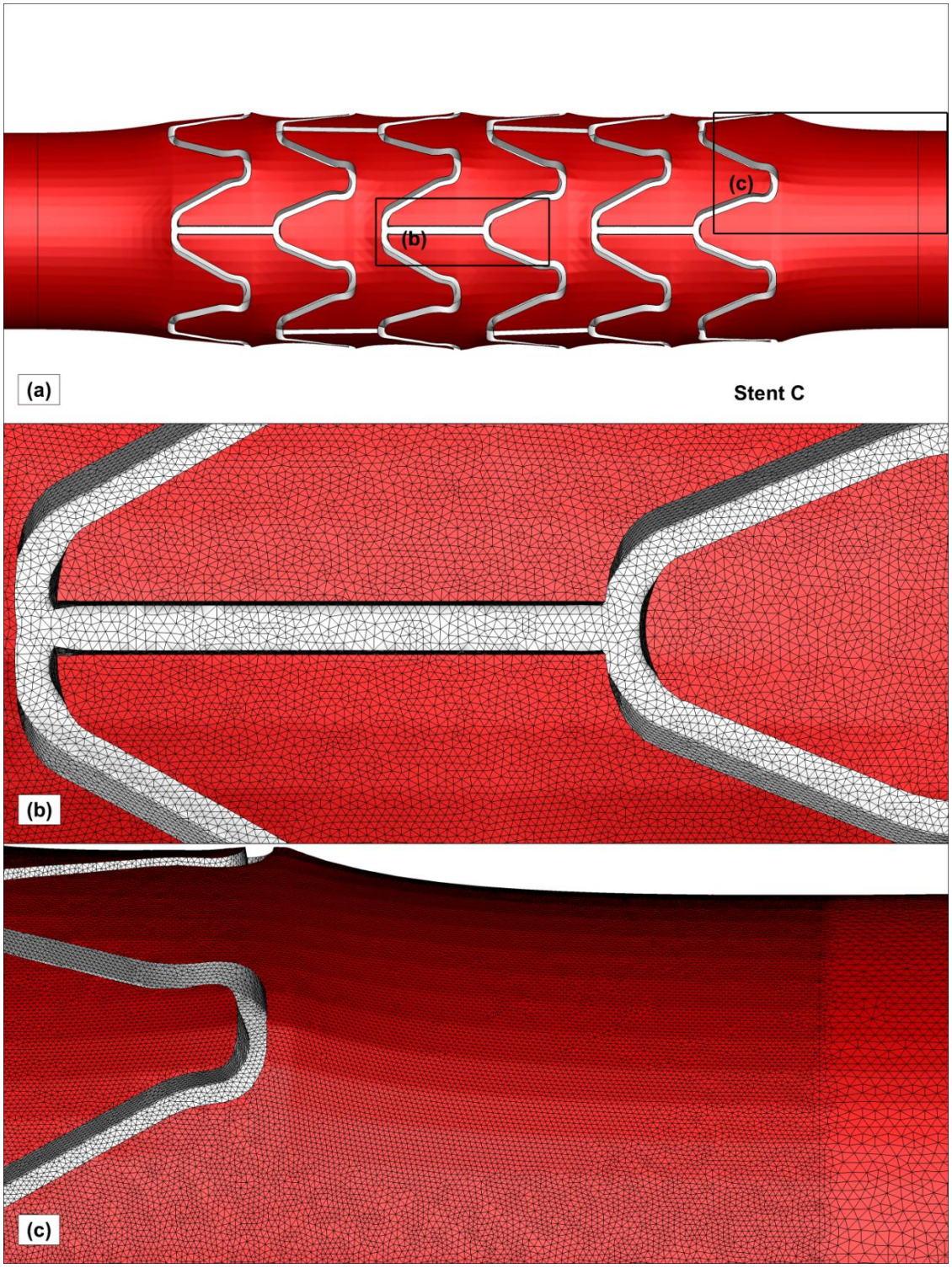

Figure B.20: (a) Geometry of Stent C with the two areas highlighted to shown where (b) and (c) are located. (b) Mesh density around stent struts, (c) Mesh density transitioning from stented region to unstented region.

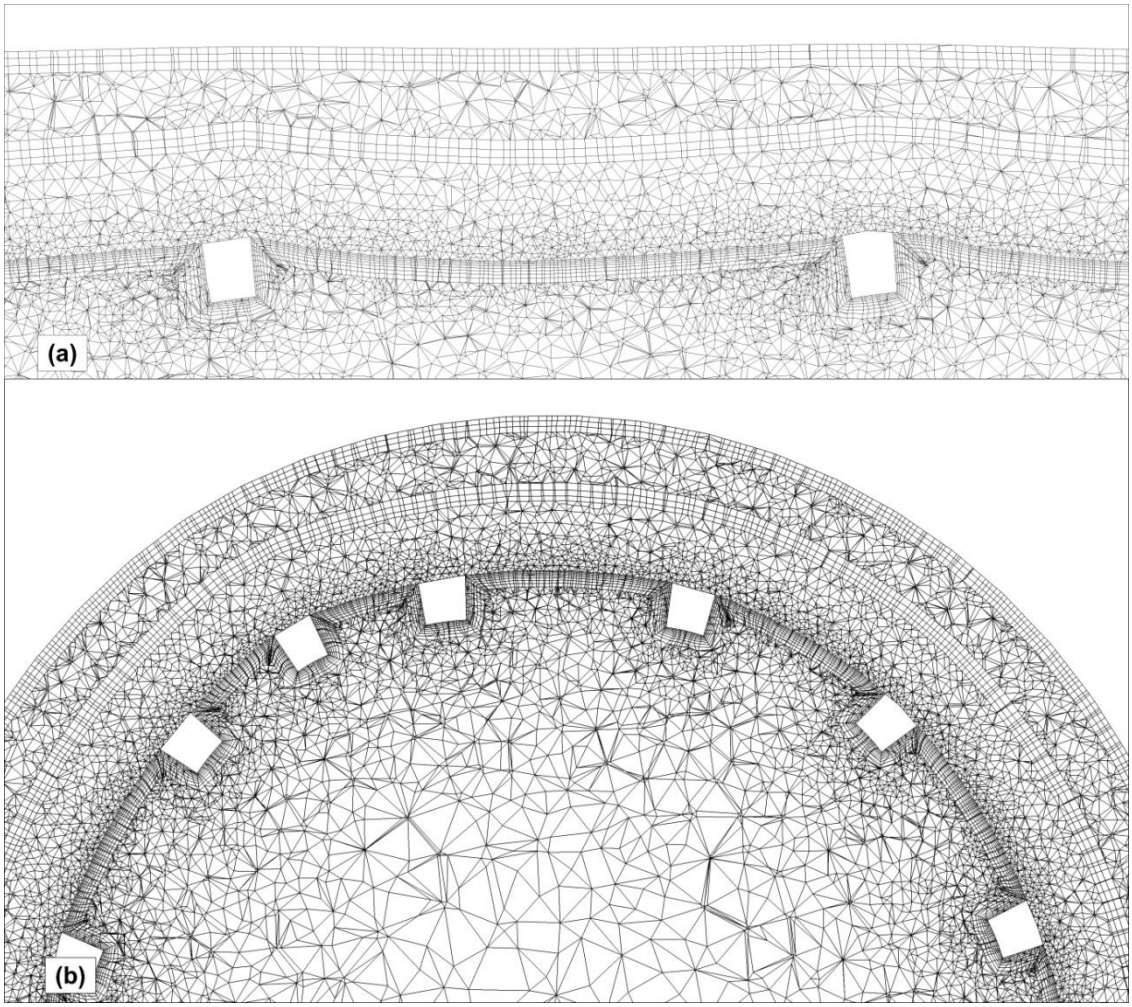

Figure B.21: (a) Longitudinal cross-section and (b) transverse cross-section showing the mesh density at the luminal surface and across the arterial wall for Stent C.

B.6 Meshes Employed in Test Case 4

The node counts for the six stents used in Test Case 4 are shown in Table B.6 Additionally, Figure B.22 and Figure B.23 show the mesh density on the luminal surface and within the three volume domains for just one of the helical stent geometries analysed in Test Case 4.

Mesh	HS 01	HS 02	HS 03	HS 04	HS 05	HS 06
Lumen	8132554	8292765	8442955	8545144	8686147	8766917
Intima	2512188	2573811	2627794	2672542	2731482	2768639
Media	2264040	3083466	2443055	2504670	2543354	2566802
Total	12908782	13950042	13513804	13722356	13960983	14102358

Table B.6: Node counts for the six helical stent meshes used in Test Case 4.

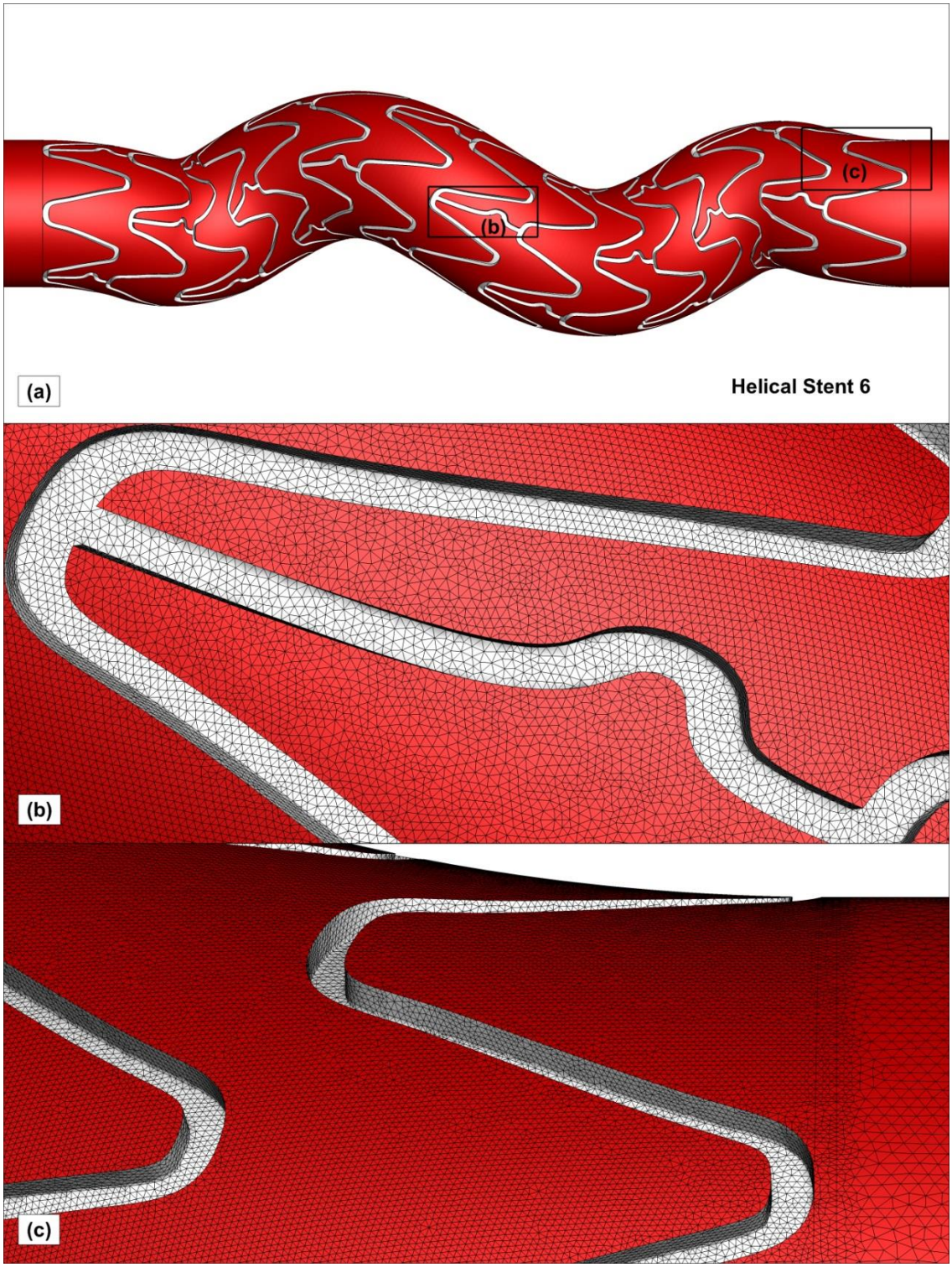

Figure B.22: (a) Geometry of Helical Stent 6 with the two areas highlighted to shown where (b) and (c) are located. (b) Mesh density around stent struts, (c) Mesh density transitioning from stented region to unstented region.

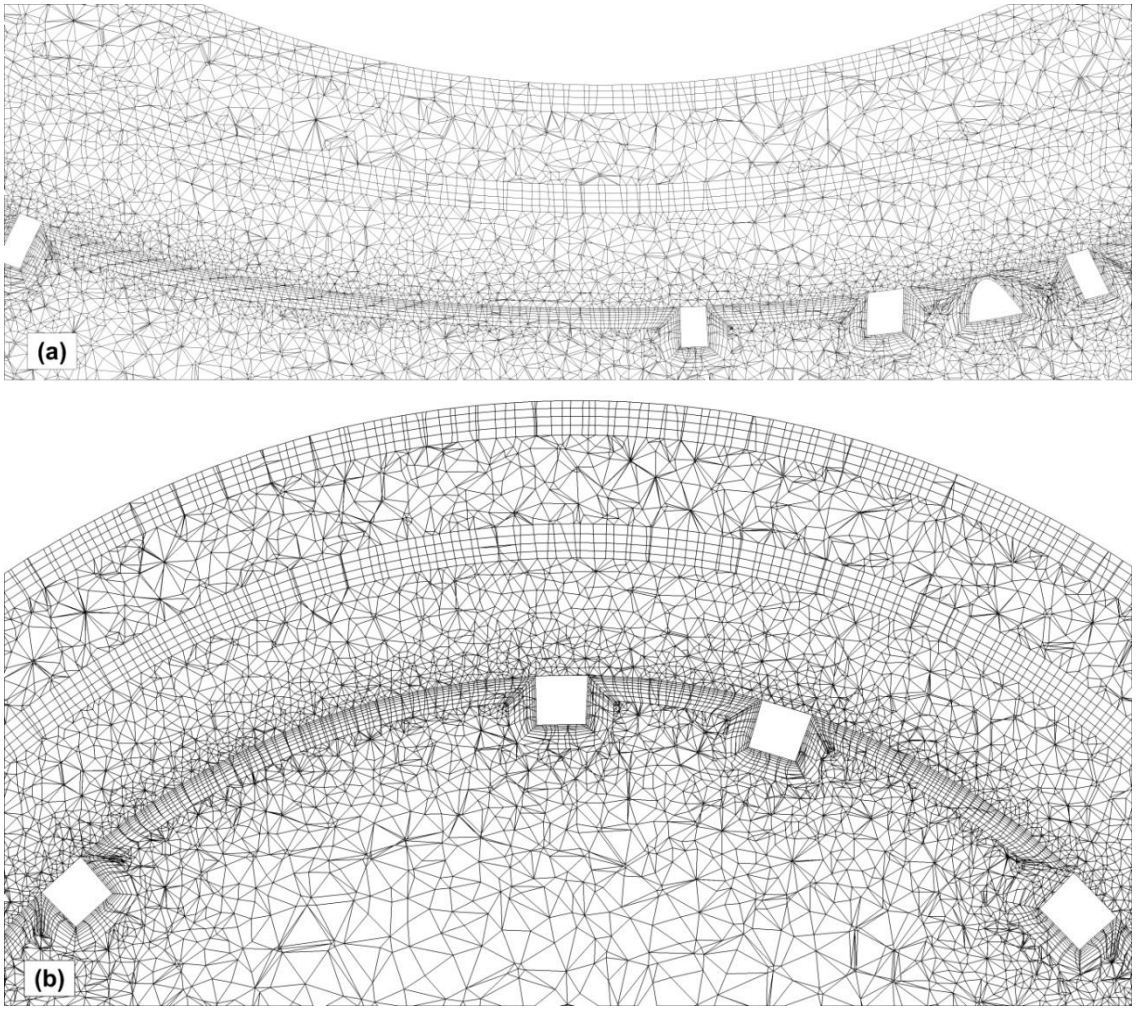

Figure B.23: (a) Longitudinal cross-section and (b) transverse cross-section showing the mesh density at the luminal surface and across the arterial wall for Helical Stent 6.

B.7 Conclusions

Following the mesh convergence studies presented in this appendix the mesh parameters were set for each simulation analysed in the four test cases. Accurate capture of the MTBL was ensured with at least three prism layers within MTBL, as described in Section B.2. In comparison with previous studies of haemodynamic variables a more refined luminal surface mesh was required to accurately capture the oxygen transport. As a side note, this, along with the low diffusivity used, makes the analysis of oxygen transport much more computationally expensive.